Investigation of Fracture in Polymeric Coatings

Soratos Tantideeravit

February 2013

Mechanics of Materials

Department of Mechanical Engineering

Imperial College London

A thesis submitted for the degree of Doctor of Philosophy of

Imperial College London and the Diploma of Imperial College

Abstract

The objective of this study is to quantify the effect of low amplitude cyclic stresses, such as those induced by environmental condition fluctuations and transportation, on multilayer paint systems found in works of art. A model was developed to establish criteria for damage, which take into account viscoelastic fatigue, and to establish safe rates of change for environmental parameters. To establish the methodology, the investigation focused on modern paintings executed in mixed media. In particular, acrylic gesso grounds with superimposed alkyd paint layers on canvas were investigated, which have been found to be vulnerable to stresses and delamination. Data from uniaxial testing of free-standing paint films were used to determine the constitutive properties of the paint. The effects of temperature, strain rate and age on the tensile properties were investigated. Results from peel tests, performed to determine the energy release rate of the interface between the paint and gesso layers, are reported.

The peel tests were modelled using Finite Element Analysis with cohesive zone elements at the interface in a commercial finite element software Abaqus. The value of the maximum traction in the traction-separation law was determined by comparing numerical and experimental peel loads and the cohesive energy was determined using an established analytical method. The cohesive zone properties determined from the peel tests, and the calibrated constitutive model for the alkyd paint, were used in a separate finite element model of a coating on a primed canvas substrate subjected to combined cyclic hygrothermal and static mechanical loadings typically experienced by fine art paintings; interface separation was controlled by an irreversible cohesive zone model that includes damage accumulation due to cyclic loading. Fatigue crack initiation times in years, and crack propagation rates, are predicted under various conditions including ordinary and extreme histories that paintings may experience in museum and conservation settings.

Acknowledgement

I would like to take this opportunity to thank many people who have supported me throughout this project. Firstly I wish to thank my supervisors, Dr Maria Charalambides and Dr Daniel Balint who have continuously offered their guidance and encouragement throughout this project. I would like to thank Dr Christina Young for the useful input and trainings. I am grateful to Prof. Thomas Siegmund, Purdue University, USA, for the provision of the original Abaqus User-Subroutine script for the Irreversible Cohesive Zone Model and his helpful advice. I am thankful for the financial support provided by the Royal Thai Government as well as the friendship from the staffs of the Royal Thai Embassy and the Office of Educational Affairs in London. I also would like to show my appreciation to the members of Mechanics of Material section, in particular Dr Chaiwut Gamonpilas, Dr Edmund Tarleton, Dr Idris Mohammed, Dr Mohd Afandi P Mohammed, Dr Hari Arora, Dr Diego Alvarez Feito, Dr Ioannis Giannakopoulos, Dr Judith Thei, Miss Rangsinee Piyasombatkul. I would finally like to thank my family, my friends and especially Miss Prattana Kaewpet, for the encouragement over the past several years.

Declaration of Originality

This work is my own and all else is appropriately referenced.

Copyright Declaration

Table of Contents

List of Figures

List of Tables

1. Introduction

Polymeric coatings are extensively used in many industries for several purposes. For example, polymeric paints are used as chemical/corrosion or mechanical protection layers in power or chemical plants. In the automotive and construction industries, coatings are also used for the same purposes; however the coating layer in these applications is also expected to be aesthetically pleasing and increase the value of the product. Similar applications are found in household and daily life products. As for purely decorative coatings as in fine art applications, polymeric paint is the most common medium for artists where countless types of coatings and supports are used and created to achieve the desired visual effects.

One of the major concerns in the usage of polymeric coatings is durability. Manufacturing technology and polymeric coating chemistry have changed over time in order to improve the durability of modern coatings. Depending upon the application, designs for durability, i.e. to withstand mechanical failure over a sustained loading, would be different. For instance, for coatings used on household or disposable products, the selected polymer would only be expected to last a few months or years, whereas coatings for cars and buildings are most likely required to last at least ten years, or longer. If a coating type is used to create valuable objects, e.g. antiques and artist paintings, it would be expected to have an even longer lifetime, or ideally last indefinitely.

1.1 Artists' paintings: compositions, durability and conservations

Artists' paintings are usually made of layers of polymeric coatings. Myriads of different materials are used by artists to produce the texture and appearance of modern and contemporary paintings. For those working on canvas there is also a choice of binder for the pigmented paint layers, and the underlying ground layer, if one is used. In the nineteenth century, paints would have been typically bound in oils such as linseed, poppy or walnut (1). Other fillers or extenders would also have been added. However, in the 1940's alkyd paints were first introduced to the market as interior/exterior

house paints, especially for wood and metal (1). These paints were adopted by artists, such as Jackson Pollock, because they had the texture and handling properties of oil paint but dried much faster and were available in large quantities (2). In the 1960's acrylic household paints became available; they were also produced as artist's paints. Thus from the 1960's to the present day there has been much experimentation with all three media (oils, alkyds and acrylics) and paintings can contain layers and areas with all three types of paint present (mixed media).

The fact that some paintings can be considered priceless makes durability one of the most important concerns. Paintings in museums are important artefacts that must be kept and handled under controlled conditions in order to preserve them for as long as possible. Experience gained from conservation of such works has highlighted one problem associated with some mixed media paintings, which is an apparent lack of adhesion between different layers of paint. This is thought to be exacerbated by fluctuating temperature and humidity, (3), eventually leading to delamination and loss of the image and meaning of the work, an example of which is shown in Figure 1-1 below.

Figure 1-1, crack defects in artist paints: through thickness and delamination; Sun, Church in Zeeland, 1909-10, oil on canvas

It is known that the risk of deterioration of paint can be reduced by keeping paintings within controlled temperature and humidity. Since paintings are made up of multiple layers of paint, they are very sensitive to the surrounding environment, hence variations in temperature and relative

humidity can cause expansion/contraction mismatch between these layers. Subsequently, mechanical failures caused by cracking or delamination within the multilayer will occur. Hence, artist paint technology is continuously seeking ways to make these paintings impervious to potential damage caused by changes in the surrounding environment. Inside museums, the temperature and relative humidity are maintained at approximately 24°C and 50% RH respectively as summarised in Table 1-1, (4), (5).

Table 1-1, Class 1 environmental control specifications for museums and galleries. From Thomson (4).

Relative Humidity
Day and night throughout the year: 50 or 55 ± 5% RH Note: The level may be fixed higher or lower, but for mixed collections should be in the range 45-60% RH.
Temperature
Winter: 19 ± 1 °C Summer: up to 24 ± 1 °C Note 1: Temperature must be controlled to control RH, but the level is dictated by human comfort. For fuel economy different winter and summer levels are suggested. Note 2: In storage areas or buildings closed to the public in winter, temperature can be allowed to fall, but not to the point where condensation may occur on cold or unventilated surfaces. A lower limit of 10 °C is suggested.

However in some situations it is not possible to maintain the conditions above, for example when paintings have to be exposed to the outside environment during transits. Figure 1-2 shows the variation of temperature over time during the transportation of art paintings from London's museums to several distant locations (6). It can be seen from the chart that the temperature can vary up to 5°C with 48 hours.

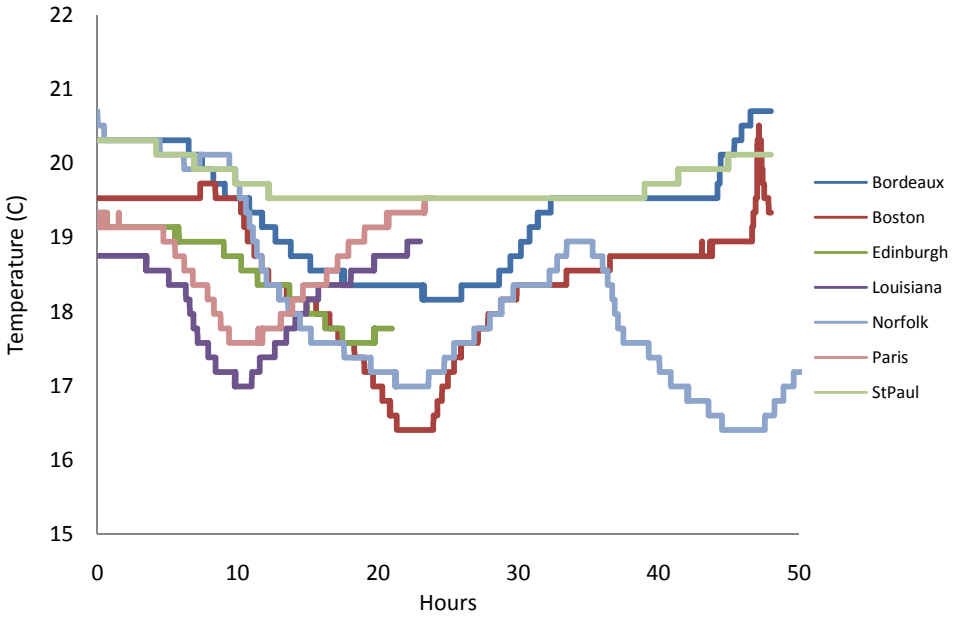

Figure 1-2, temperature versus time during the transportation of paintings from London to various destinations

The failure mechanisms in multilayer paints and coatings are very complex. As each painting is a unique combination of layers, and each colour of paint contains different vehicles and pigments, establishing the exact cause of damage and failure based on the works themselves has proven to be difficult, especially as removal of original material for analytical identification is not usually possible. In earlier studies, constitutive relationships for the adhesion between paint layers were successfully established and mechanical tests were developed for the determination of adhesive strength. Nevertheless, many failure mechanisms, including fatigue crack growth and mixed mode cracking between interfaces, is not yet fully captured by any standardised techniques.

In many recent studies on fracture mechanics, finite element (FE) analysis has played an important role. It is promising that many crack initiation and propagation simulation techniques, including those developed for nonlinear viscoelastic analysis available in commercial FE software, can be used to accurately predict fracture in adhesive/multilayer materials. In conjunction with mechanical test methods, computational and analytical models can provide useful predictions not only for the field

of artist paints conservation, but also in the design and utilisation of polymeric coatings in other industries.

1.2 Objectives

The first objective of this thesis is to investigate the mechanical properties of free standing films of pthalo blue alkyd and an acrylic gesso paint, and the adhesive strength between them when used in a multilayer. The tensile properties and the fracture toughness will be determined through uniaxial tensile tests and T-peel tests, respectively. The second objective is to use finite element simulation techniques to characterise the deformation and damage of the paint during the mechanical tests. The final objective is to model the effect of low amplitude cyclic stresses, induced by environmental conditions, on multilayer paint systems found in works of art. Information from the peel and tensile tests will be used in finite element simulations to make a fatigue life prediction for an alkyd paint on a primed canvas.

Once the fracture properties of artists' paints are known, paintings can be improved to withstand a wider range of environmental conditions outside of museums without undergoing deterioration. Furthermore, as institutions re-evaluate their environmental control policies in the light of the need to conserve energy, prediction of the degradation of works of art becomes more pertinent. Thus, the development of a representative model will serve to aid risk management of collections.

1.3 Outline of this thesis

Chapters 2 through 4 will provide the background for this research, specifically on alkyd and acrylic paints compositions, stress analysis for hyperelastic and viscoelastic material and fracture mechanics in layered materials, respectively. Experimental work is explained in Chapter 5. This will include test methods, analytical solutions and test results. In Chapter 6, finite element techniques related to stress analysis and fracture for layered materials are reviewed, with parametric studies for each technique reported. Chapter 7 outlines the development of a fatigue life prediction model for a

paint film on a canvas using the information from Chapters 5 and 6, with predictions of the fatigue life model also presented. Conclusions of this thesis are provided in Chapter 8, and possible areas for future work are discussed.

2. Artist Paints

This chapter provides information on the artists' paints and pigments used in this project, as well as an introduction on the durability of paints and a summary of previous studies on this topic.

Three types of artists' paints currently dominate the market. These are drying oils, acrylics and alkyds, categorised by the types of their binders. Oil paint was the first to be utilised by artists. The application of oils began in the 12th century, when artists started to use oil paints for decoration. Later in the 15th century, oil paint was adopted as an artistic medium and by the 16th century, oils became universal to all artists. Oil paints are among the easier paints to produce by using natural drying oils such as linseed oil (steamed-pressed linseed oil is the most common in oil paint manufacturing) or soybean oil as binder. Semi-drying oil such as safflower and poppyseed oil are usually added by 5 to 10 percent of the total volume of the paint, normally in a lighter colour, as a modifier to reduce the tendency for yellowing. Oil paint is still widely used nowadays due to its unique visual properties, richness in colour, glossiness, ease of adaptability and longevity.

Synthetic paints such as acrylics have become increasingly popular among modern artists since the 1940s due to their advantages over oil paints including a lower susceptibility to cracking even as a thick layer, better ageing, a shorter drying time and an ability to be easily cleaned up. Presently, approximately half of artist paints in the market are graded as acrylics. Alkyd paints also make use of a synthetic binder, however the latter is combined with oils or fatty acids which act as modifiers. Alkyd paint has gained popularity among artists due to the fact that it produces a similar final result of colour richness and glossiness to oil paint but with the benefit of a faster drying time. Nevertheless, it has also been shown to become more brittle with age than oil paint (7). Alkyd paint was initially available for interior/exterior household use, especially for wood and metal, before the introduction of the Griffin artists' alkyd paint series by Winsor & Newton, Middlesex, England. A

comparison of the physical properties and durability of common binders used by artists is provided by Gottsegen (1); those of oil, acrylic and alkyd paint are shown in Table 2-1.

Table 2-1, comparison of properties of paint binders (1); *Exc = excellent.

Common name	**Steam-pressed linseed oil**	**Acrylic Resins**	**Alkyd resins**
Type	Natural drying oil, alkaline refined	Synthetic resins	Synthetic resins
Source	Linum usitatissimum, flaxseed, steam-pressed	Vinyl resins; large variety	Condensed ester of a polyhydric alcohol and a polybasic acid
Colour/Appearance	Pale yellow to darker yellow-orange	Large clear lumps or white powder; in water dispersion, milky white	Yellow to yellow-red, depending on modifier
Use	Binder; ingredient in mediums	Varies	Major industrial use as a paint binder
Refractive index	Relatively low	Low, depending on form	Low to medium
Viscosity	Low to medium	Low to medium in solution or water dispersion	High, but in artists' paint vehicle, low to medium
Thinner/Solvent	Mineral spirits, gum, turpentine, stronger	Aliphatics for most solutions; water for dispersions unless dry	Varies, but in artists' binders mineral spirits; higher aromatics for dried films
Reversibility	Not with original thinner	Good in solution; poor in dispersion	Poor; aromatic solvents will destroy,

			not reverse
pH	Slightly acidic; refining reduces acidity	Neutral in solution; alkaline in dispersion	Oil-modified: slightly acidic
Durability Interior Exterior Rigid support Flexible support	 Good-excellent Fair Good-excellent Fair	Solution: Dispersion: Excellent Good-Exc* Good Fair Excellent Excellent Fair Good-Exc*	 Excellent Good Excellent Good-excellent
Resistance to Water Acid Alkali Pollutants Ultraviolet light Decay	 Good Poor Fair Fair Fair Good	Solution: Dispersion: Excellent Fair Fair Poor Fair Poor Fair-Good Fair Fair Fair Excellent Excellent	 Excellent Fair Fair Good Good Excellent
Hazards Health Fire (flash point)	N/A Over 260˚C	Solvents are a major hazard Varies with solvent	N/A, except if misused or abused Very high
Other comments	Most used for commercial and studio-based paint makings; average drier; less costly; only a fair binder, but in use for more than 500 years,	Solution hazardous because of solvents, but can make good paints; use only solutions that can be thinned with mineral spirits; see Material Safety Data	With more than 50% oil in vehicle, paint are really oil paints; versatile, non-yellowing (depending on oil), quick-drying, less apt to crack than

	reliable	Sheets (MSDS) for hazards	linseed oil binders; better colour development than acrylic dispersion binders

Thus far, an introduction to the type and physical properties of artists' paint has been given. The next sections of this chapter will focus on the production and application of acrylic paint; alkyd paint will be discussed in section 2.2. Information on pigments used in paint manufacturing and further details on the colouring materials used in the samples of this project are provided in section 2.3. The importance of durability of paints is discussed in section 2.4. Finally, the last section, 2.5, will provide details on the paints used in the mechanical tests of this project.

2.1 Acrylic paint

When latex paint was first introduced in 1940, the earlier formulae used polyvinyl acetate as the binder until later when acrylic copolymer became more common, hence the name of acrylic paint or acrylic solution paint. Initially acrylic paint was used for exterior decoration because of its durability Shortly after, acrylic paints for artists were developed by using acrylic resins dissolved in solvent. One of the earliest formulae was created by Bocour and Golden by using the solutions of poly(n-butyl methacrylate) in organic solvents as the vehicle of the paint (8). The application and final appearance of these solution paints were similar to oil paint. They were superior as they did not yellow but they were more brittle than oil (1).

An attempt to increase the use of synthetic paints by artists led to the introduction of acrylic dispersion paints or water-based acrylic paints in the early 1950's. The vehicle of the paint was acrylic resin dispersed in water or so-called acrylic polymer emulsion, the paint also being thinned with water again after pigments are added. The performance of this paint is rather different from oil

and acrylic solution paint, with many advantages including versatility, flexibility, faster drying time and better ability to withstand environmental changes (9), which make this paint the most popular among modern artists, currently dominating the artists' paints market.

The process of making modern acrylic dispersion vehicles is considered to be the most complex of all synthetic paint vehicles. Firstly, surfactant is added to water in enough quantity to form micelles, which is the spherical cluster of surfactant molecules with the polar end of the molecules towards the perimeter and the non-polar ends towards the centre of the sphere. Monomers, which in most modern formulae are n-butyl methacrylate (nBA) (molecular structure shown in Figure 2-1), are then added along with an initiator, which starts and maintains the polymerization process.

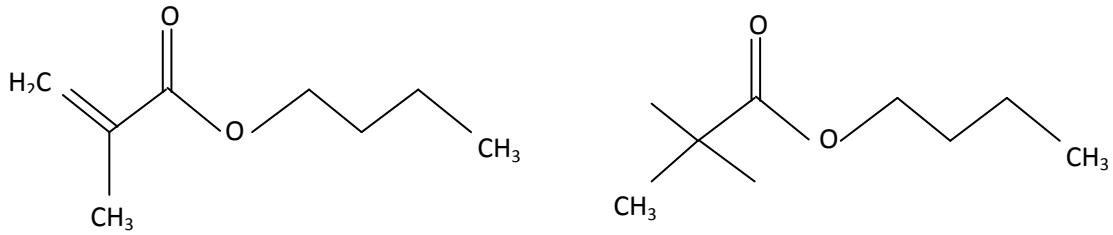

Figure 2-1, molecular structure of n-butyl methacrylate; left) as monomer, right) as polymer.

Varieties of additives including dispersants, defoamers, preservatives, glycols, thickeners and pH balancers, are often mixed into the vehicle after the polymerisation process. Finally, pigments are added into the vehicle. However, a smaller amount of pigment can be added to acrylic dispersion vehicle than in oils, alkyd or acrylic solution vehicles due to the nature of particles when suspended in liquid (1). This is the main reason why acrylic dispersion paints usually have less richness in colour than oils and alkyds. Nevertheless, the chroma of the paint improves when it is dried (1). The drying and adhering process in acrylic dispersion paints has been discussed by Brown (10). The process is illustrated in Figure 2-2 starting with the paint composed of particles of plastic acrylic resin dispersed in water and pigment. As the water gradually evaporates, the resin particles converge and are forced into a hexagonal shape, trapping the pigment particles. Finally, the resin particles are bonded by inter-diffusion (coalescence) of the polymer, forming a homogeneous, durable paint.

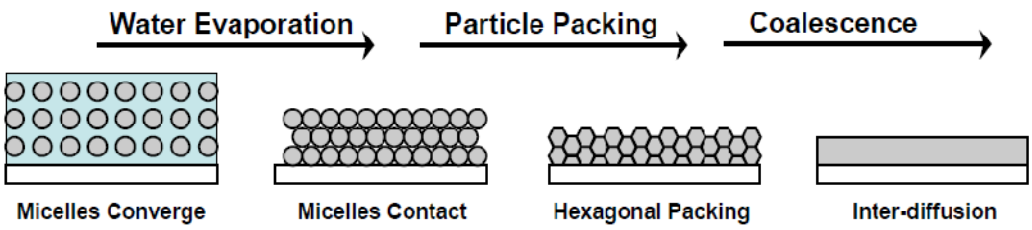

Figure 2-2, formation of acrylic paint film (11).

2.2 Alkyd paint

Alkyds or oil-modified alkyd paints use a combination of an oil or a fatty acid and polyesters, which are chemically constructed from a non-catalysed esterification reaction between acid and alcohol. Typically, phthalic anhydride or maleic anhydride is combined with glycerine or pentaerythritol as shown in Figure 2-3.

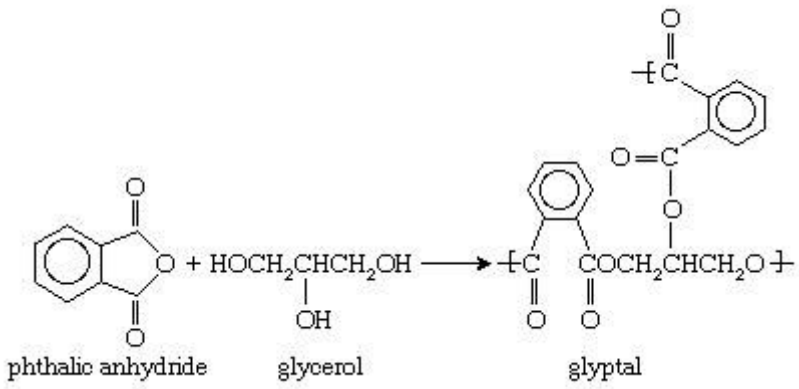

Figure 2-3, esterification of alkyd resin (12).

The product of the polymerisation is called an alkyd resin. In the making of alkyd paint, the resin is mixed with a suitable unsaturated drying oil, such as linseed oil or castor oil, resulting in a branched polyester with fatty acid side groups. The mixture has the properties of a coating agent where in the presence of oxygen, the cross-linking process of the polyester occurs. As it dries, it forms a solid film.

Before being adopted as a durable artists' medium, alkyd in fact had been utilised in the coating industry since it was first developed around 1901. Its applications are mainly as exterior coatings for woods and metal such as house and automobile paints.

There are three classes of alkyd resins classified by the percentage of drying oil content in the paint known as oil-length (wt% oil/ wt% resin), which are long-oil, medium-oil and short-oil. Long oil alkyds contain a high percentage of >60% drying oil, which has a faster drying time, and are suitable for moderate duty coatings. Medium oil alkyds contain approximately 40-60% drying oil and are used in high gloss applications and wood surfaces finishes. Lastly, short oil alkyds with a drying oil content less than 40% and the longest drying time, are typically used as baking enamels for metals and heating is required to dry the alkyds. A higher percentage of drying oil reduces the drying time by reacting with oxygen in the air, which polymerises the oils and speeds up the cross-linking process; this therefore increases the flexibility and the brushability of the paint.

Artist series alkyd paints belong to the long-oil category as they contain approximately 56–70 weight per cent oil. Among synthetic paints, alkyd paint is considered to have the most similar visual properties to oil paints (13). Another advantage of alkyd paint over traditional oil paint is its higher speed of drying, i.e. it takes approximately 18–24 hours for a typical thickness oil paint layer to feel touch dry (14). This is due to the high molecular weight alkyd resin and the need for fewer crosslinks for film formation.

Two techniques of adding oil to the polymer in the manufacturing of alkyds are the fatty acid method and monoglyceride (alcoholysis) method (15). The first method is achieved by heating fatty acids with the phthalic anhydride and polyol during esterification. This method provides better control over the final chemical structure of the resins. The latter method involves an extra step where triglycerides are heated with the polyol prior to the ester formation. This technique is more common in the making of long-oil alkyd due to the lower cost of production (16).

2.3 Materials

This work focuses on the mechanical behaviour of individual paint layers of acrylic and alkyd and multilayers of acrylic/alkyd for conservation of modern artists' works. Two commercial paints were used in this work. They were chosen to be representatives of artist practice and because previous data had shown such combinations can result in cracking of the upper layer under bending (7). The first paint layer was an acrylic gesso primer manufactured by Golden. It is made from acrylic resin dispersed in water with $CaCO_3$ and TiO_2 white pigments. Acrylic gesso is recommended for use on solid and flexible supports, and is widely used as a base layer for painting on canvas. The second paint was an artists' alkyd (oil based polyester) with phthalocyanine blue pigment (Griffin series) manufactured by Winsor & Newton.

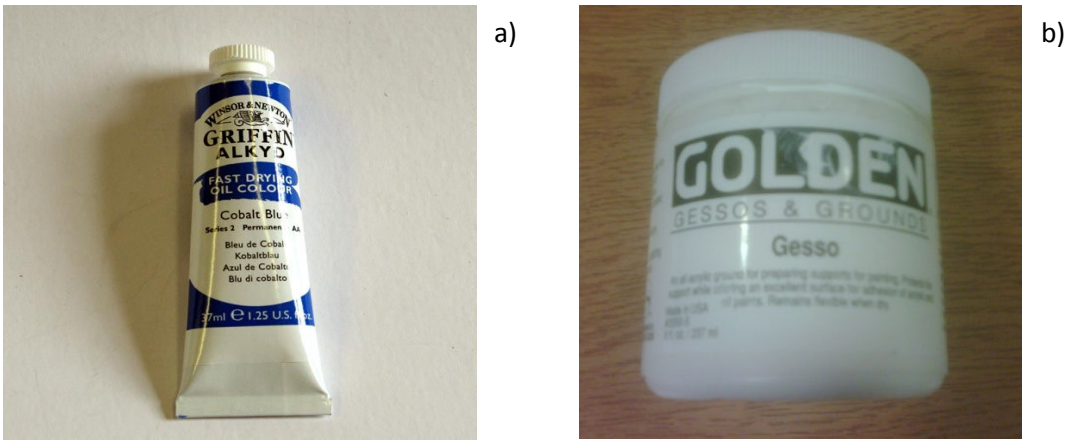

Figure 2-4, test material a) Winsor & Newton blue phthalo Alkyd b) Golden acrylic gesso.

2.4 Pigments and colouring material of titanium white acrylic gesso and phthalo blue alkyd

A general introduction to the pigments used in artists' paints is given in the first part of this section. In the latter part of the section, details of the pigments used in the specific paints under study, namely acrylic dispersion gesso and phthalo blue alkyd paint, are provided.

Two types of colouring materials are pigments and dyes. Dyes are soluble material and most are non-permanent; therefore they are used only in the manufacturing industry and not in artists' paints

which need to be of higher quality. Pigments, unlike dye, are insoluble particles added during the manufacturing of artists' paints to create colours. They are expected to maintain their durability over a very long period of time. Gottsegen (1) has provided the qualifications the pigments in artist paints must meet as listed below.

1) They should be in the form of a fine and smooth powder
2) They should have a good lightfastness property, meaning that their chroma and hue should not change after a certain period of exposure to normal light; usually measured by a 100-year equivalent real-time exposure test.
3) They should not react chemically or physically with other mediums including binder, thinner, ground or supports.
4) They should not react to normal atmospheric changes.
5) They should form a smooth film layer when the paint is dried.
6) Pigments should not migrate or bleed through the paint layer after the paint is dried.
7) They should not be mixed with ingredients that affect their colour and handling.
8) They should be non-toxic under normal use.
9) They should be supplied by a manufacturer who can provide the information on their origin, quality and other relevant properties.

Most pigments remain in the paint layer after the paint has dried and have a pronounced influence on the mechanical properties of the coating layer as reported in the work of Hagan et al. (11),(17). Generally, the same colour pigments used in oil paint can also be added into acrylic and alkyd binder.

As already mentioned in section 2.3, the paints that were studied in this section are titanium white acrylic dispersion gesso and phthalo blue alkyd. The first material, titanium white acrylic dispersion gesso, obtains its opaque white optical properties from a high concentration of titanium dioxide (TiO_2), with pigment usually more than 30% by volume. TiO_2 has a high refractive index and low

toxicity. It has therefore replaced lead carbonate, which had been used to produce a thick white opaque effect since the 1920's. $CaCO_3$, or kaolin, is also added as additional white particles. They have a lower optical quality than TiO_2 but a significantly lower cost.

The second paint, phthalo blue, also called phthalocyanine blue or monastral blue alkyd, is a mixture of alkyd resin with synthetic phthalocyanine blue pigment. The pigment was firstly introduced in the mid 1930's. It is a complex structure of copper phthalocyanine ($C_{32}H_{16}N_8Cu$), shown in Figure 2-5, synthesised by reacting copper with phthalimide. Copper phthalocyanine is considered to be a good quality pigment because it is insoluble in water, is very stable under heat, is chemically stable and lightfast.

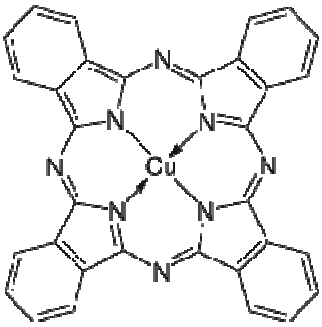

Figure 2-5, molecular structure of phthalocyanine blue.

2.5 Durability of paints

Polymeric coatings are extensively used in many applications. For example, they are frequently used as chemical/mechanical protection layers and as decorative coatings. Based on the application, the design for durability to withstand mechanical failure would be different. For coatings used in household or disposable products, the selected polymer would only be expected to last a few months or years. Coatings for cars and buildings are most likely required to last at least ten years or longer. If a coating is used to create valuable objects, for example, antiques and artist paintings, it would be expected to have even longer usage life or ideally last forever. An artist's painting is made of layers of paint. The fact that some paintings can be considered priceless makes durability one of

the most important concerns in the design of artists' paints. It is known that the risk of paint deterioration can be reduced by keeping paintings in a controlled temperature and humidity environment, although, in some situations this is difficult to ensure and will require a large amount of energy consumption. As institutions re-evaluate their environmental control policies in light of the need to conserve energy, prediction of the degradation of works of art becomes more pertinent. Thus, the development of a representative model will serve to aid risk management of collections.

Cracking in polymeric coatings and specifically paints is a topic that has been studied previously, though not extensively. Mecklenburg (18) studied the mechanical behaviour of paint films on supports under low temperature and severe changes in relative humidity. The study confirms the changes in stress-strain responses under different environmental conditions and also shows the evidence of through-thickness and interfacial cracks in paintings under mechanical stresses, and the delamination between oil and acrylic paints. Delamination between alkyd and acrylic paints is shown in the recent work by Young (19), although there is still uncertainty whether the cracks that form on such coatings are 'through-thickness' cracks formed by tensile or flexural loading, or delaminations that occur at the interface which then spread and lead to spallation of the coating. Kim and Nairn (20), (21), measured the through-thickness crack density as a function of energy release in automotive paints under tension and bending. Cracking in paints on substrates was also studied by Nichols et al. (22) where a tensile test was used to study the initiation of a channelling crack, i.e. a through-thickness crack, in thin paint layers on a thick substrate as used in the automotive industry. This work showed that the critical energy release rate, G_C, can be accurately computed using linear elastic theories as long as the cracking process involves no plastic deformation and the plasticity of the film due to the tensile loading can be ignored. In (23), the same test procedure was used to examine the effect of weathering, due to environmental exposure, on the fracture toughness of thin coatings. All of these studies made the assumption of linear elasticity and did not consider the effect of cyclic loading on the integrity of the paints.

Measurements of the flexibility and adhesion of two-layer mixed media films have been reported (19). However, the study only measured the paint loss using the bend test method and did not investigate peel strength or fracture energy. Adhesive fracture energy, G_C, of various combinations of multi-layered paints is reported by Song (24) and Valkana (25). The effect of age on the fracture toughness has also been studied in the same reports, however the maximum storage life of the paint in the studies is less than 60 days which is a relatively short period for the paint layer to become fully dry. Finite element analysis for oil paints on canvas has been performed by Mecklenburg and Tumosa (26) using a linear-elastic model to predict the stresses that develop during changes in temperature and relative humidity. The study did not include the prediction of cracks forming in such paints as a result of these stresses.

The aim of this work is to investigate the durability of an alkyd on acrylic gesso paint combination in the extent of its resistance to delamination due to environmental fatigue. The interfacial fracture energy between the two paints was determined through tensile and T-peel tests. Based on the information from the mechanical tests, predictions of delamination between the two paints due to environmental fatigue were then made using finite element techniques.

In summary, an introduction on artists' acrylic and alkyd paints and pigments has been provided in this chapter. The importance of durability of paint has been addressed. The type of paints used in this project has been introduced. Samples made from these paints will be used in the mechanical tests reported in chapter 5 of this thesis.

3. Mechanical properties of artist paints

The aim of this chapter is to provide the background theory and literature review on the topic of the mechanical behaviour of polymeric coatings, particularly artists' paints. The constitutive equations are outlined, and the implementation of the nonlinear viscoelastic equations into a commercial finite elemental software package (Abaqus) is also presented in this chapter.

The mechanical properties of artists' paints, and especially acrylics, have been studied as single thin films by Erlerbacher et al. (27) who showed that the stiffness of acrylic paints is significantly higher at 5% Relative Humidity (RH) than at 50% RH; however, it was found that the paints had lost their ductility at the lower humidity. Material models for acrylic and polyester based paints have been investigated by Hagan et al. (17),(28) (29), and Giannakopoulos (30), respectively, where the studies showed that the mechanical response of paints under load can be described using the stress-strain relationship developed for rubber, known as hyperelasticity, which exhibits high nonlinearity at large strains without yielding (see Figure 3-1a), combined with a time-dependent viscoelastic behaviour. The material properties were measured as a function of relative humidity, temperature, test rate and pigment volume fraction. The same studies also showed that whilst a higher modulus or glassy behaviour can be observed at lower temperatures or higher strain rates, rubbery behaviour can be found under the opposite conditions. Figure 3-1b illustrates the rate dependence of a latex paint film subjected to tensile load. The effect of loading rate is highlighted by comparing curves 2, 3 and 4 while the effect of temperature can be observed by comparing curves 1 to 4 and 2 to 5. It is also worth noting that curves 1 and 2 are similar which points to the principle of time-temperature superposition being valid.

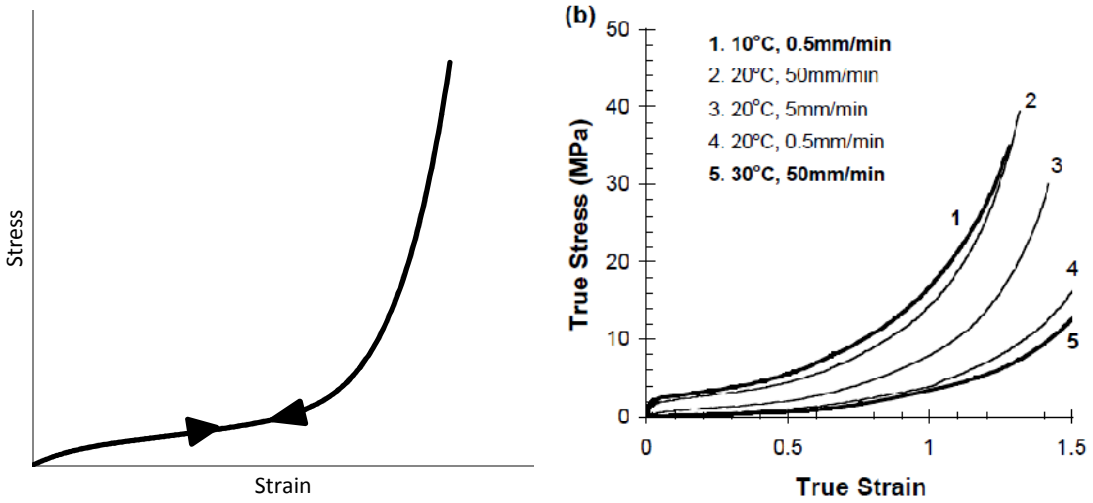

Figure 3-1, a) stress-strain curve of a hyperelastic material, b) stress-strain curves for the latex films under different test conditions (11)**.**

Mechanical testing techniques have been used in many studies to determine the mechanical properties of paints and coatings. These mechanical properties are necessary when analysing the fracture of coatings, which will be discussed later in the next chapter. Combinations of time-independent hyperelastic models, i.e. Ogden (31) and van der Waals (32), and time-dependent viscoelastic models, i.e. Prony series, are used to describe the mechanical response of paints in this project.

The development of the time-independent hyperelastic models will be outlined in section 3.1 of this chapter where the derivation of the stress function for the Ogden and van der Waals models for uniaxial tension is discussed. In section 3.2, the theory of viscoelasticity including the derivation of the stress function of the Prony series and the hyperviscoelastic model is provided. Section 3.3 outlines the implementation of the viscohyperelastic model in Abaqus, the commercial finite element software used in this project. A discussion on the quasi-static analysis method is given. The difference in the numerical results for viscoelastic materials between two versions of the software, version 6.8 and 6.9, is also discussed in this section. Section 3.4 provides a discussion on the time-temperature superposition behaviour of polymeric materials.

3.1 Time-independent behaviour

Using classic theories of non-linear elasticity, material models have been proposed to fit hyperelastic material testing data. Table 3-1 (11), originally created by Marckmann and Verron(33), illustrates the history of the development of hyperelastic models and techniques with the last column indicating the models that are supported by Abaqus.

Table 3-1, list of strain-energy potential based models modified from Marckmann and Verron,(11), (33).

Model	Year	Physically Based (A) Phenomenological (B)	Abaqus Supported
Mooney	1940	B	Yes
Gaussian	1943	A	Yes
3-Chain	1943	A	
Ishihara	1951	B	
Biderman	1958	B	
Gent-Thonmas	1958	B	
Hart-Smith	1966	B	
Valanis-Landel	1967	B	
Ogden	1972	B	Yes
Haines-Wilson	1975	B	
Slip-link	1981	A	
Constrained Junction	1982	A	
Van der Waals	1986	A	Yes
8-Chain	1993	A	Yes
Gent	1996	B	
Yeoh-Fleming	1997	B	Yes
Tube	1997	A	
Extended-tube	1999	A	
Shariff	2000	B	
Microsphere	2004	A	

This section will provide a brief discussion on the development of hyperelastic models that relate to this work. A comprehensive summary of the available hyperelastic models is provided in the work by Hagan (11). From Table 3-1, the hyperelastic models are divided into those that are physically based, also called statistical, and those that are phenomenological. The phenomenological models make use of the continuum mechanics principle, based on the work of deformation or strain energy

potential (W), which is characterised in terms of the principal stretch ratios (λ). The original nonlinear elastic model, proposed by Mooney (34), was derived in terms of the Cauchy Green stretch Tensor (C),

$$C = F^T \cdot F = \begin{bmatrix} \lambda_1 & 0 & 0 \\ 0 & \lambda_2 & 0 \\ 0 & 0 & \lambda_3 \end{bmatrix} \cdot \begin{bmatrix} \lambda_1 & 0 & 0 \\ 0 & \lambda_2 & 0 \\ 0 & 0 & \lambda_3 \end{bmatrix} = \begin{bmatrix} \lambda_1^2 & 0 & 0 \\ 0 & \lambda_2^2 & 0 \\ 0 & 0 & \lambda_3^2 \end{bmatrix} \quad 3\text{-}1$$

where the strain energy potential is given by

$$W_{MR} = C_{10}\,(I_1 - 3) + C_{01}(I_2 - 3) \quad 3\text{-}2$$

where $C_{10} = \lambda_1^2$ and $C_{01} = \lambda_3^2$ from equation 3-1

The invariants, which are functions of λ, are defined as

$$I_1 = \mathrm{tr}C = \lambda_1^2 + \lambda_2^2 + \lambda_3^2$$

$$I_2 = \frac{1}{2}(\mathrm{tr(C)}^2 - \mathrm{tr(C}^2)) = \lambda_1^2\lambda_2^2 + \lambda_2^2\lambda_3^2 + \lambda_3^2\lambda_1^2 \quad 3\text{-}3$$

$$I_3 = \mathrm{det}C = \lambda_1^2\lambda_2^2\lambda_3^2$$

The first invariant, I_1, represents the influence of the chain length defined by the sum of the square of the stretch ratios in the principal directions whilst the second and the third invariants combine the influences of area and volume changes of the element, respectively. In a rubbery polymer, conservation of volume or incompressibility is commonly assumed (35), which results in the third invariant being equal to unity and the other invariants being written as:

$$I_1 = \lambda_1^2 + \lambda_2^2 + \lambda_3^2$$

$$I_2 = \frac{1}{\lambda_1^2} + \frac{1}{\lambda_2^2} + \frac{1}{\lambda_3^2} \quad 3\text{-}4$$

$$I_3 = 1$$

The Mooney-Rivlin model is a widely accepted hyperelastic model and has been shown to provide good predictions at medium to high deformations. A more general form of this model has been proposed by Rivlin (36) using an infinite series of terms:

$$W_R = \sum_{i,j=0}^{\infty} C_{ij}(I_1 - 3)^i \, (I_2 - 3)^j \qquad 3\text{-}5$$

where the first two terms (i=1, j=0 and j=1, i=0) will produce the original Mooney-Rivlin model whilst using only the single term of i=1, j=0 results in the neo-Hookean model which is written as :

$$W_{NH} = C_{10} \, (I_1 - 3) \qquad 3\text{-}6$$

The obvious advantage of the Mooney-Rivlin over the neo-Hookean is that the second invariant term will improve the accuracy of biaxial predictions. Nevertheless, both models were found to be inaccurate at very large deformations due to the fact that the limiting chain extensibility or the effect of the locking stretch are not taken into account.

An improvement has been made by Gent (37) where the effect of the limiting chain extensibility was incorporated by introducing two extra parameters: the initial modulus, μ_0, and the locking stretch, J_m, where the model is defined as

$$W_G = -\frac{\mu_0}{2} J_m \ln\left(1 - \frac{I_1 - 3}{J_m}\right) \qquad 3\text{-}7$$

It can be seen from equation 3-7 that the value of I_1-3 is limited by the value of J_m as the value in the parenthesis is always positive.

Ogden(38) later proposed a modified model where the strain energy only depends on the exponent of the stretch ratios, removing the invariant (*I*) dependence:

$$W_O = \sum_i \frac{\mu_i}{\alpha_i}\left(\lambda_1^{\alpha_i} + \lambda_2^{\alpha_i} + \lambda_3^{\alpha_i} - 3\right) \qquad 3\text{-}8$$

where the material's initial shear modulus μ_0 is defined as $\mu_0 = \sum_i \mu_i$

Ogden has proven that the model is capable of capturing the S-shape of the hyperelastic stress-strain curves without incorporating a locking stretch parameter. Increasing the number of terms, *i*, allows the model to accurately predict larger deformation. This model is supported by Abaqus (39),(40), and was used to model the hyperviscoelastic behaviour in artists' paints in the works by Hagan (11) and Hagan et al (17),(29).

The physically-based models, on the other hand, use the principle of entropy change due to the stretching of the polymer chain. The change can be used to calculate the work of deformation, also called the strain energy potential. The first models introduced for rubber elasticity (41), (42), were developed using a Gaussian probability distribution where one end of the polymer chains is assumed fixed and the distribution is used to describe the probability density of the other ends of the chains at the coordinate (x,y,z) away from the fixed end. This is given by:

$$p(x,y,z) = \left(\frac{b^3}{\pi^{3/2}}\right) \exp\left(-b^2 r^2\right) \qquad 3\text{-}9$$

where *b* is related to the number of links in the chain, *n*, and the link length, *l*, and *r* is the direct distance between endpoints of the chain where the mean value is given by

$$\bar{r}^2 = \frac{3}{2} b^2 = nl^2 \qquad 3\text{-}10$$

Using Boltzman's thermodynamic principle,

$$s = k\{\ln p(x,y,z) d\tau\} \qquad 3\text{-}11$$

the entropy changes ($\Delta s = s\text{-}s_0$) due to the extension of polymer chains can be obtained as:

$$\Delta S = \sum \Delta s = -\frac{1}{2} Nk(\lambda_1^2 + \lambda_2^2 + \lambda_3^2 - 3) \qquad 3\text{-}12$$

where λ is the extension or the stretch ratio defined by l/l_0, *N* is the number of polymer chains, $d\tau$ is the volume element and *k* is the Boltzmann constant. The work, *W*, is then obtained by using the thermodynamic principle, $W=-T\Delta S$, where *T* is the temperature in Kelvin:

$$W = \frac{1}{2}NkT(\lambda_1^2 + \lambda_2^2 + \lambda_3^2 - 3) \quad 3\text{-}13$$

At large deformations, the Gaussian probability distribution may prove to be inaccurate, especially when the maximum extension of the polymer chain is approached. Several models developed later (43) use the modified or non-Gaussian distribution to expand the model's versatility and improve accuracy. The maximum chain extension or locking stretch, λ_L, was therefore introduced, defined as:

$$\lambda_L = \sqrt{n} \quad 3\text{-}14$$

The accuracy at large deformation has been improved; however, there was still the issue of anisotropic behaviour due to the small number of oriented chains in the unit cell. Using a similar approach, Arruda and Boyce (43) later proposed the 8-chain model which effectively eliminates this behaviour. The work of deformation for this model is given as:

$$W_{8Ch} = NkT\lambda_L(\beta_{Ch}\lambda_{Ch} + \lambda_L \ln\left(\frac{\beta_{Ch}}{\sinh \beta_{Ch}}\right) \quad 3\text{-}15$$

where

$$\beta_{Ch} = \mathcal{L}^{-1}\left(\frac{\lambda_{Ch}}{\lambda_L}\right) \quad 3\text{-}16$$

$$\lambda_{Ch} = \left(\frac{\lambda_1^2+\lambda_2^2+\lambda_3^2}{3}\right)^{1/2} \quad 3\text{-}17$$

where $\mathcal{L}$ is the Langevin function

$$\mathcal{L}(x) = \coth(x) - \left(\frac{1}{x}\right) \quad 3\text{-}18$$

As an alternative to solving the inverse Langevin function, an approximate form of the equation was proposed by Cohen (44), as:

$$W_{8Ch} = \mu\left[\frac{(I_1-3)}{2} + \frac{(I_1^2-9)}{20\lambda_L^2} + \frac{11(I_1^3-27)}{1050\lambda_L^4} + \frac{19(I_1^4-27)}{7000\lambda_L^6} + \frac{519(I_1^5-243)}{673750\lambda_L^8}\right] \quad 3\text{-}19$$

where $I_1 = \lambda_1^2 + \lambda_2^2 + \lambda_3^2$, and μ_0 is introduced as the initial shear modulus and is related to μ by:

$$\mu_0 = \mu\left[1 + \frac{3}{5\lambda_L^2} + \frac{99}{175\lambda_L^4} + \frac{513}{875\lambda_L^6} + \frac{42039}{67375\lambda_L^8}\right] \qquad 3\text{-}20$$

Later, an additional parameter, a, was included to account for the interaction between polymer chains in the model for rubber elasticity by Kilian (45),(46) and Enderle(46). The equation of state for an ideal gas was used in the derivation, hence the name van der Waals model. The strain energy potential form as below:

$$W_{vdW} = \mu\left\{-(\lambda_m^2 - 3)\left[\ln\left(1 - \sqrt{\frac{\bar{I}-3}{\lambda_m^2-3}}\right) + \sqrt{\frac{\bar{I}-3}{\lambda_m^2-3}}\right] - \frac{2}{3}a\left(\frac{\bar{I}-3}{2}\right)^{\frac{3}{2}}\right\} \qquad 3\text{-}21$$

where

$$\bar{I} = (1-\beta)I_1 + \beta I_2 \quad ; \qquad 0 \le \beta \le 1$$

and β is used as a linear scaling factor determining the influence of the first and second invariants. It is worth noting that, in the case of β=0 when $\bar{I} - 3 = \lambda_m^2 - 3$, a singularity is observed, therefore in this case λ_m determines the locking stretch. The Van der Waals model was used in this study. The implementation of the model will be explained in the next section.

3.1.1 van der Waals model for uniaxial tension

The hyperelastic models introduced earlier in this chapter can be used to fit the stress-strain curve data from actual experiments. The most common experiments used for fitting are the uniaxial tensile, pure shear and biaxial tests, and the experimental data are usually approximated using the least squares fitting method. Consider the deformation in these three tests shown in Figure 3-2, below:

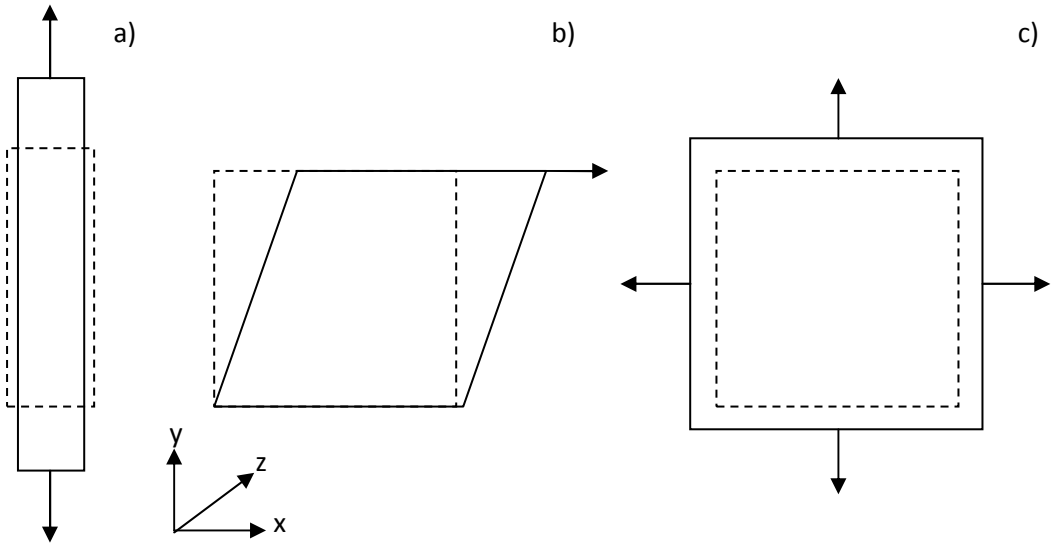

Figure 3-2, deformation in mechanical tests; a) uniaxial tension, b) pure shear, c) biaxial tension.

The stretch ratios for each test can be written as:

For uniaxial tension $\lambda_1 = \lambda$ and $\lambda_2 = \lambda_3 = \lambda^{-1/2}$

pure shear $\lambda_1 = \lambda$, $\lambda_2 = 1$ and $\lambda_3 = \lambda^{-1}$

biaxial tension $\lambda_1 = \lambda_2 = \lambda$ and $\lambda_3 = \lambda^{-2}$

The stretch invariant can be calculated from these stretch ratios:

For uniaxial tension $I_1 = \lambda^2 + 2\lambda^{-1}$ and $I_2 = 2\lambda + \lambda^{-2}$

pure shear $I_1 = I_2 = 1 + \lambda^2 + \lambda^{-2}$

biaxial tension $I_1 = 2\lambda^2 + \lambda^{-4}$ and $I_2 = 2\lambda^{-2} + \lambda^4$

where $I_3 = 1$ as incompressibility is assumed.

Consider the case of uniaxial tension for the van der Waals model [22] given by equation 3-21. The invariant $\bar{I}$ used in the model can be determined as follows. Assuming $\beta = 0$, where the influence of changes in area and volume is ignored, gives $\bar{I}$ equal to I_1, therefore:

$$\bar{I} = \lambda^2 + \lambda^{-1} \qquad 3\text{-}22$$

The stress as a function of λ corresponding to uniaxial loading can then be derived as follows:

$$\sigma_0 = \lambda f = \lambda \frac{dW}{d\lambda} = \lambda\mu(1-\lambda^{-3})\left[1 - \left(\frac{\lambda^2+2\lambda^{-1}-3}{\lambda_m^2-3}\right)^{-0.5} - \alpha\left(\frac{\lambda^2+2\lambda^{-1}-3}{2}\right)^{0.5}\right] \qquad 3\text{-}23$$

where *f* is the nominal stress-stretch function, *dw/dλ*.

3.1.2 Ogden model for uniaxial tension

The second hyperelastic model used in this work is the Odgen model. Consider the Ogden strain energy function under uniaxial tension. By substitution of the uniaxial tension stretch ratios the following is derived:

$$W_0 = \sum_i \frac{\mu_i}{\alpha_i}\left(\lambda^{\alpha_i} + 2\lambda^{\frac{-\alpha_i}{2}} - 3\right) \qquad 3\text{-}24$$

Differentiating equation 3-24 with respect to *λ* gives the nominal stress *f*:

$$f = \sum_{i=1}^{M} \frac{2\mu_i}{\alpha_i}(\lambda^{\alpha-1} - \lambda^{-0.5\alpha-1}), \quad \text{where} \quad \mu_0 = \sum_{i=1}^{M} \mu_i \qquad 3\text{-}25$$

Then the true stress in the applied direction can be obtained using the relationship, σ = *f*λ. This gives the stress function:

$$\sigma_0 = f\lambda = \lambda \frac{dw}{d\lambda} = \frac{l}{l_0}\sum_{i=1}^{M} \frac{2\mu_i}{\alpha_i}\,(\lambda^{\alpha-1} - \lambda^{-0.5\alpha-1}) \qquad 3\text{-}26$$

The Ogden stress function introduced in this section and the van der Waals stress function introduced in section 3.1.1 will be used as the instantaneous stress functions in the hyperviscoelastic model which will be discussed in the next section.

3.2 Time dependent behaviour

Time dependent behaviour is commonly described using diagram models incorporating combinations of springs (time independent elements) and dashpots (time dependent elements), which are able to capture the unique character of a viscoelastic material(47), including:

1) Creep; the increase in strain with time whilst the stress is held at a constant value
2) Relaxation; the decrease in stress with time whilst the displacement is held constant
3) Recovery; the decrease of strain as a function of time after the stress is removed
4) Constant rate stressing; the non-linear increase in strain as the stress is applied at a constant rate
5) Constant rate straining; the non-linear increase in stress as the strain is applied at a constant rate

Viscoelastic behaviour can be modelled using simple combinations of a single spring and a dashpot connected in series or parallel, called the Maxwell and Voigt elements, respectively, as shown in Figure 3-3.

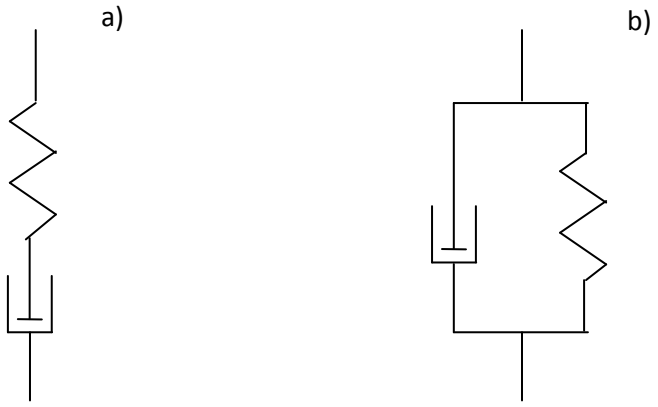

Figure 3-3, a) Maxwell element, b) Voigt element.

The Maxwell element is suitable for describing the relaxation behaviour. The constitutive relationship of the element is written as:

$$M(t) = \frac{p(t)}{e_0} = E\exp\left(-\frac{t}{\tau_0}\right) \quad \text{3-27}$$

where *M(t)* is the relaxation modulus, e_0 is the constant applied strain and τ_0 is the relaxation time, which is equal to the ratio between the viscosity of the dashpot and the elastic modulus, η/E.

The Voigt element, on the contrary, is suitable for the modelling of creep behaviour with the constitutive relationship written as:

$$C(t) = \frac{e(t)}{p_0} = \frac{1}{E}\left[1 - \exp\left(-\frac{t}{\tau_0}\right)\right] \quad \text{3-28}$$

The relationship between the relaxation modulus, *M(t)*, and the creep compliance, *C(t)*, is defined using a linear viscoelastic theory known as the Boltzmann superposition integral:

$$\int_0^t M(t-\tau)C(\tau)d\tau = t \qquad \text{and}$$

$$\int_0^t C(t-\tau)M(\tau)d\tau = t \quad \text{3-29}$$

If one of *M(t)* or *C(t)* is known, the other may be derived using Laplace transforms for the solution of the integral equation. The full derivation of this method can be found in (47). These relationships are fundamental to all viscoelastic analyses.

Considering a homogeneous and isotropic linear viscoelastic material, Goh et al (48), (49) and Charalambides et al (50) proposed that the relaxation stress of the material can be written as a product of a stress function of strain and a function of time given by

$$\sigma(t) = \sigma_0 g(t) \quad \text{3-30}$$

where σ_0 is the instantaneous stress function of strain and *g(t)* is the stress function of time.

Whilst the strain function is the Hookean linear elastic relationship for linear viscoelasticity, the time function can be expressed as the Prony series, which is the combination of a set of Maxwell elements and a spring (see Figure 3-4).

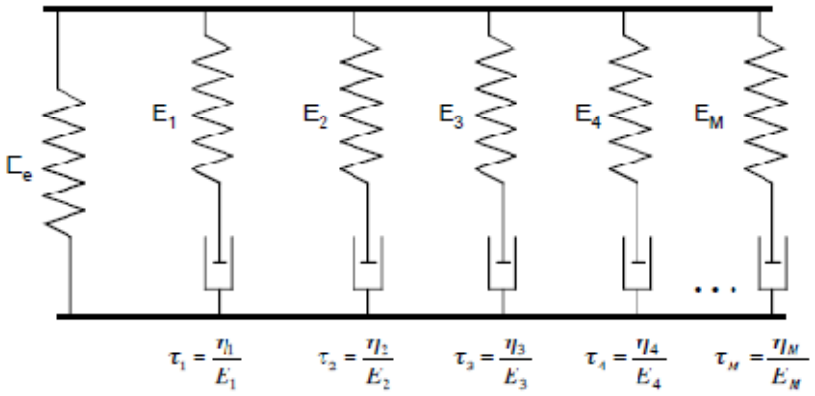

Figure 3-4, Prony series model for a one dimensional linear viscoelastic material.

Consider the simple combination of a Maxwell element placed in parallel with an equilibrium spring, as shown in Figure 3-5 where the stress of the Maxwell element is governed by the stress function of strain and the stress function of time whilst the stress in the spring element is only a function of strain.

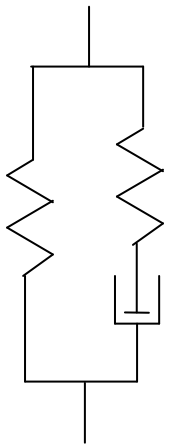

Figure 3-5, linear viscoelastic element.

The relaxation stress of the Maxwell element was given by Williams (47), which can be written as

$$\sigma_1(t) = \varepsilon_0 M(t) = E_1 \varepsilon_0 (e^{-t/\tau}) \qquad 3\text{-}31$$

The contribution of the stress in the spring can be included in the model by simply adding the stress function to the previous equation 3-31, resulting in the total stress equation written as:

$$\sigma(t) = \sigma_e + \sigma_1(t) = E_e\varepsilon_e + E_1\varepsilon_0(e^{-t/\tau}) \qquad 3\text{-}32$$

where σ_e and E_e are the stress and the modulus of the equilibrium spring, respectively.

A single Maxwell element is not able to model the stress relaxation in high molecular weight polymers as the stress relaxation occurs over a broad range of time (s), therefore several Maxwell element models are required. The Prony series, as illustrated earlier in Figure 3-4, is used to model the distribution of the relaxation times as described by Weichert (51). A useful review of this technique has been provided by Leaderman (52).

Each Maxwell element is used to represent a relaxation time, τ_i, where

$$\tau_i = \frac{\eta_i}{E_i} \; ; \qquad i=1..M \qquad 3\text{-}33$$

where E_i and η_i are, respectively, the modulus of elasticity and the viscosity of each Maxwell element. Non-dimensional parameters g_e and g_i are introduced, which represent the ratio of the modulus of the equilibrium spring element and each Maxwell element to the instantaneous modulus, E_o, as shown below:

$$g_e = \frac{E_e}{E_e + \sum_{i=1}^{M} E_i} \qquad \text{and}$$

$$g_i = \frac{E_i}{E_e + \sum_{i=1}^{M} E_i} \qquad \text{where } i = 1..M \qquad 3\text{-}34$$

It can be seen that these parameters define the relaxation of stress for the time range represented by the Maxwell elements. This requires that

$$g_e + \sum_{i=1}^{M} g_i = 1 \qquad 3\text{-}35$$

where the time-dependent stress at step strain is defined as:

$$\sigma(t) = E_0 \varepsilon_0 \left(g_e + \sum_{i=1}^{M} g_i e^{-\frac{t}{\tau_i}} \right) \quad \text{3-36}$$

By adding the equilibrium element and by using the convolution integral form as suggested by Leaderman (52) and Williams (47), the total stress is calculated from the continuous strain history through

$$\sigma(t) = \sigma_0 g_e + \int_0^t \sum_{i=1}^{M} g_i e^{-(t-s)/\tau_i} \frac{d\sigma_0}{ds} ds \quad \text{3-37}$$

where σ_0 is the time independent stress function which can be defined using linear elastic or hyperelastic models.

Goh et al (48) have suggested a method of solving the convolution integrals originally proposed by Taylor (53). The method uses finite time increments as an accurate approximation for solving the integral in equation 3-37. The time increment Δt is written as $\Delta t = t_{n+1} - t_n$ leading to:

$$e^{\frac{-t_{n+1}}{\tau_i}} = e^{\frac{-t_n}{\tau_i}} e^{\frac{-\Delta t}{\tau_i}} \quad \text{3-38}$$

Substituting equation 3-38 into equation 3-37, the second term of equation 3-37 for each Maxwell element can be rewritten as:

$$\begin{aligned} \sigma_i(t_{n+1}) &= \int_0^{t_{n+1}} g_i e^{-(t_{n+1}-s)/\tau_i} \frac{d\sigma_0(S)}{ds} ds \\ &= e^{-\frac{t_{n+1}}{\tau_i}} \int_0^{t_{n+1}} g_i e^{s/\tau_i} \frac{d\sigma_0(S)}{ds} ds \quad \text{3-39} \\ &= e^{-\frac{t_n}{\tau_i}} e^{-\frac{\Delta t}{\tau_i}} \int_0^{t_{n+1}} g_i e^{s/\tau_i} \frac{d\sigma_0(S)}{ds} ds \end{aligned}$$

The integral is separated into two parts: the first part covers the interval $0 \le s \le t_n$ whilst the second part covers the interval $t_n \le s \le t_{n+1}$. Equation 3-39 therefore becomes:

$$\sigma_i(t_{n+1}) = e^{-\frac{t_n}{\tau_i}} e^{-\frac{\Delta t}{\tau_i}} \int_0^{t_n} g_i e^{s/\tau_i} \frac{d\sigma_0(S)}{ds} ds + e^{-\frac{t_n}{\tau_i}} e^{-\frac{\Delta t}{\tau_i}} \int_n^{t_{n+1}} g_i e^{s/\tau_i} \frac{d\sigma_0(S)}{ds} ds \quad 3\text{-}40$$

Similar to equation 3-39, considering the integral from 0 to t_n:

$$\sigma_i(t_n) = \int_0^{t_n} g_i e^{-(t_n - s)/\tau_i} \frac{d\sigma_0(S)}{ds} ds = e^{-\frac{t_n}{\tau_i}} \int_0^{t_n} g_i e^{s/\tau_i} \frac{d\sigma_0(S)}{ds} ds \quad 3\text{-}41$$

Substituting equation 3-41 into equation 3-40 gives:

$$\sigma_i(t_{n+1}) = e^{-\frac{\Delta t}{\tau_i}} \sigma_i(t_n) + g_i \int_n^{t_{n+1}} e^{-(t_{n+1} - s)/\tau_i} \frac{d\sigma_0(S)}{ds} ds \quad 3\text{-}42$$

The derivative term $\frac{d\sigma_0(S)}{ds}$ can be defined using a finite difference scheme as:

$$\frac{d\sigma_0(S)}{ds} = \lim_{\Delta s \to 0} \frac{\Delta \sigma_0(s)}{\Delta s} = \lim_{\Delta t \to 0} \frac{\sigma_0(t+\Delta t) - \sigma_0(t)}{\Delta t} \quad 3\text{-}43$$

Substituting the limit into equation 3-43 gives the time-dependent stress function of a Maxwell element:

$$\sigma_i(t + \Delta t) = e^{-\Delta t/\tau_i} \sigma_i(t) + g_i \frac{1 - e^{-\Delta t/\tau_i}}{\Delta t/\tau_i} [\sigma_0(t + \Delta t) - \sigma_0(t)] \quad 3\text{-}44$$

Combining the equilibrium element with M Maxwell elements, the total stress equation can be written as:

$$\sigma(t + \Delta t) = g_e \sigma_0(t + \Delta t) + \sum_{i=1}^{M} \left[e^{-\Delta t/\tau_i} \sigma_i(t) + g_i \frac{1 - e^{-\Delta t/\tau_i}}{\Delta t/\tau_i} [\sigma_0(t + \Delta t) - \sigma_0(t)] \right] \quad 3\text{-}45$$

This numerical approximation was based on a finite time increment formulation that enables the derivation of an analytical expression for the stress at any time, and the corresponding strain. This allowed the model to be calibrated using the experimental data and the numerical least squares optimisation method. The calculation of stress from this equation can be simply performed in an Excel spreadsheet and will be used as an analytical solution for this project.

3.3 Numerical implementation of viscoelastic analysis in Abaqus

The commercial finite element software Abaqus provides the option of modelling hyperviscoelastic materials where the parameters of six hyperelastic models indicated in can be used directly as the time independent parameters and the parameters of the Prony series can be used directly to define the time dependent behaviour of the material.

3.3.1 Hyperviscoelastic definition in Abaqus

The strain energy potential functions for the models used in this project, Ogden and van der Waals, are defined in Abaqus in the form shown below (40):

van der Waals model:

$$W_{vdW} = \mu\left\{-(\lambda_m^2 - 3)\left[\ln\left(1 - \sqrt{\frac{\bar{I}-3}{\lambda_m^2-3}}\right) + \sqrt{\frac{\bar{I}-3}{\lambda_m^2-3}}\right] - \frac{2}{3}a\left(\frac{\bar{I}-3}{2}\right)^{\frac{3}{2}}\right\} + \frac{1}{D}\left(\frac{J_{el}^2-1}{2} - \ln J_{el}\right) \quad \text{3-46}$$

where

$$\bar{I} = (1-\beta)\bar{I}_1 + \beta\bar{I}_2$$

$$\bar{I}_1 = \bar{\lambda}_1^2 + \bar{\lambda}_2^2 + \bar{\lambda}_3^2 \quad \text{and} \quad \bar{I}_2 = \frac{1}{\bar{\lambda}_1^2} + \frac{1}{\bar{\lambda}_2^2} + \frac{1}{\bar{\lambda}_3^2}$$

Ogden model:

$$W_O = \sum_i \frac{\mu_i}{\alpha_i}\left(\bar{\lambda}_1^{\alpha_i} + \bar{\lambda}_2^{\alpha_i} + \bar{\lambda}_3^{\alpha_i} - 3\right) + \sum_{i=1}^{N}\frac{1}{D_i}(J_{el}-1)^{2i} \quad \text{3-47}$$

where J_{el} is the elastic volume ratio defined by

$$J_{el} = \frac{J}{\left(1+\varepsilon^{th}\right)^3} \quad \text{3-48}$$

where J is the current volume/original volume and ε^{th} is the isotropic linear thermal expansion strain.

It is worth noting that the possible change in volume is also included in the strain energy potential functions in Abaqus through the relationship:

$$\bar{\lambda}_i = J^{-\frac{1}{3}}\lambda_i \qquad 3\text{-}49$$

where $\bar{\lambda}_i$ is the deviatoric principal stretch and λ_i are the principal stretches.

All the material parameters, including μ, λ_m, and a from the van der Waals model and μ_i and α_i from the Ogden model, can be specified directly in Abaqus.

For the time domain viscoelastic material model definition, the users can define the Prony series parameters directly in Abaqus. There is no limit to the number of Prony series term, *M*, that can be employed, although the higher the number, the less meaningful these values are in terms of physical significance. The total sum of the input parameters, g_i, must be less than 1 where g_e is automatically calculated from

$$g_e + \sum_{i=1}^{M} g_i = 1 \qquad 3\text{-}50$$

3.3.2 Solution accuracy and stability control

A quasi-static analysis approach is utilized by Abaqus/Standard for both linear and non linear viscoelastic problems. The accuracy of the analysis is controlled by a user specified parameter, *CETOL*, which is the maximum difference between the creep strain at the beginning and the end of the increment given as

$$CETOL = tolerance \geq (\dot{\bar{\varepsilon}}^{cr}|_{t+\Delta t} - \dot{\bar{\varepsilon}}^{cr}|_{t})\Delta t \qquad 3\text{-}51$$

It can be seen from the equation above that the value of the time increment of the analysis, Δt, is limited by the *CETOL* parameter. A calibration for the value of *CETOL* is necessary for each quasi-static analysis. A large *CETOL* value implies a looser tolerance which may result in an inaccurate or

fluctuating result; however, a very small value may result in excessive requirements regarding analysis time and computational resources.

A numerical instability can occur in nonlinear quasi-static analyses involving large deformations such as in simulations of the peel test. In such situations, Abaqus automatically reduces the size of the time increment from the initial one suggested by the user, until the converged solution is obtained. However, in highly nonlinear problems, the time increment size required for convergence can be very small, resulting in excessive analysis time, or in many situations, the solution cannot be obtained, which leads to the termination of the analysis after 15 iterations due to a the default setting of the software. Also, there is a possibility that the first increment of the analysis is unstable due to a rigid body mode and the analysis is terminated at the first increment.

One of the solutions to the problem mentioned above is to use the automatic stabilisation scheme which enables the user to specify a damping factor in the model. This scheme is the same as that commonly used in nonlinear problems. The damping value should be sufficiently large to prevent instantaneous collapse of heavily distorted elements, however it should not significantly affect the accuracy of the calculation. Three additional Abaqus commands are introduced with this scheme. The first one is STABILIZE, which is used to activate the stabilisation algorithm, the second is FACTOR, which can be set equal to the damping factor, and the third is ALLSDTOL, which is used to define the maximum allowable ratio of the stabilisation energy to the total strain energy.

Consider a nonlinear response of a body as shown in Figure 3-6, where *F* is the applied force acting on a body and *I* is the internal force of the body.

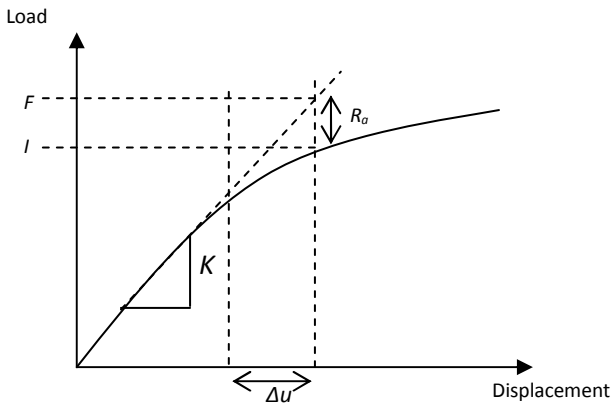

Figure 3-6, nonlinear response of a body.

Abaqus uses a linear relationship with a stiffness *K* to determine the force and displacement, *Δu*, within the iteration. This therefore results in a difference between the determined force and the internal force. The difference is defined as a residual force, *R*. The relationship between the three forces, *F*, *I* and *R,* provides the state of equilibrium in the body as shown in the equation below:

$$R_a = F - I_a \qquad 3\text{-}52$$

where the subscript *a* denotes the current iteration. If R_a is smaller than the tolerance (the default tolerance value is 0.5 per cent of the average force in the body) the solution is considered to be in equilibrium. However, if this criterion is not met, Abaqus restarts the increment with an increment time size reduced by a factor of 75%. If the analysis does not converge after five repeats, the analysis is terminated.

In the case that the residual force is large and a solution is unobtainable, the stabilization scheme can be activated by using the STABILIZE command where there are two possible ways of defining the damping factor for this scheme. The first is using a constant viscous damping factor where the user can set the FACTOR command equal to the damping factor, *c.* This factor is used to calculate the viscous force in the form of

$$F_v = cM^* v \quad \text{3-53}$$

which is then added to the equilibrium equation below:

$$F - I_a - F_v = R_a \quad \text{3-54}$$

where *M** is a mass matrix with unit density, *c* is a user defined damping factor and *v* is the nodal velocity vector = *Δu/Δt.* This method reduces the size of the residual force, R_a, and increases the chance of obtaining a stable solution, which allows the analysis to continue. However, it should be noted that the value of the damping factor could have a major effect on the accuracy of the results.

The second method to define the energy of viscous damping is from the dissipated strain energy during the first increment of the analysis step; in most cases the response is stable and linear. The STABILIZE can be set equal to a fraction of the dissipated energy. The default value is 0.02% of the energy, and this is set equal to the damping energy. In cases when a converged solution is not obtained even in the first increment, a constant damping factor is still required. If this happens, the adaptive automatic stabilization scheme is enabled by default.

During the adaptive automatic stabilization scheme, the damping factor is varied based on the convergence history in a way that the factor may increase if extra iterations are required due to severe instabilities or a rigid body mode. The size of viscous damping energy must always be lower than the user-defined tolerance, ALLSDTOL, multiplied by the total strain energy.

The stabilisation scheme with constant damping factor is used in the peel test and the environmental fatigue models in chapter 7. This is because both models are highly nonlinear where the convergence of the first increment cannot be obtained if the stabilised scheme is not enabled.

3.3.2.1 Viscoelastic formulations in Abaqus 6.8 and 6.9 version

Recent work by Mohammed (54) has reviewed the differences between the viscoelastic stress analysis in Abaqus 6.8 (39) and Abaqus 6.9 (40). It was found that the true stress, σ, in equation 3-37 in Abaqus 6.8 was replaced by the nominal stress, P, in version 6.9, which leads to:

$$\sigma(t) = \lambda(t)P_0 g_e + \lambda(t)\int_0^t \sum_{i=1}^{M} g_i e^{-(t-s)/\tau_i} \frac{dP_0}{ds} ds \qquad 3\text{-}55$$

Notice that the stretch ratio, $\lambda(t)$, is introduced in the equation to convert the nominal stress into true, outside of the second term integral. The relationship between nominal and true stress is:

$$\sigma_0(t_n) = P_0(t_n) \cdot \lambda(t_n) \qquad 3\text{-}56$$

Using the same integral approximation method as in the previous section, the stress function in Abaqus 6.9 becomes:

$$\sigma(t+\Delta t) = g_e \sigma_0(t+\Delta t) + \lambda(t+\Delta t)\sum_{i=1}^{M} e^{-\Delta t/\tau_i}\sigma_i(t) + g_i \frac{1-e^{-\Delta t/\tau_i}}{\Delta t/\tau_i}[P_0(t+\Delta t) - P_0(t)] \qquad 3\text{-}57$$

Mohammed (54) showed that there is a noticeable difference between the value of stress in the uniaxial tension stress strain curve predicted by Abaqus 6.8 and those from 6.9 at strains larger than 50%. The difference is less than 5% at 50% true strain and approximately 8% at 100% true strain.

3.4 Time-temperature superposition

It is known from the work of Hagan et al. (17) that, for acrylic paints, increasing the strain rate has a similar effect as decreasing the temperature (see Figure 3-1). A similar behaviour in polyester-based paints has been reported by Giannakopoulos (30). This enabled a time-temperature superposition approach such that modelling the effect of both strain rate and temperature on the paints' mechanical behaviour could be achieved.

Early studies by Tolbolsky and Andrews (55), Leaderman (56) and Williams et al(57), investigated the mathematical relationships between the temperature of a polymer and the shift of the relaxation time distribution. The relaxation time of the Prony series can be shifted simply by introducing the shift factor, a_T, to the relationship below.

$$\tau_i = a_T \tau_{i(ref)} \qquad 3\text{-}58$$

where τ_i is the discrete relaxation time at the shifted temperature and $\tau_{i(ref)}$ is the discrete relaxation time at the reference temperature. A similar relationship can be used in the case of a continuous distribution of relaxation time, where the discrete relaxation time is replaced by the mean relaxation time, τ_m, given as

$$\tau_m = a_T \tau_{m(ref)} \qquad 3\text{-}59$$

A frequently cited empirical equation for the shift factor at temperatures above the glass transition temperature, T_g, was given by Williams, Landel and Ferry (WLF) (57) which is written as:

$$\log(a_T) = \left(-\frac{C_1(T-T_{ref})}{C_2+(T-T_{ref})}\right) \qquad 3\text{-}60$$

For most amorphous polymers above T_g, the values of the parameters C_1 and C_2 are normally 17.4 and 51.6, respectively. Another theoretical relationship commonly used for the relaxation at a temperature below T_g is given by the Arrhenius equation (58):

$$\ln(a_T) = \left(\frac{\Delta Q}{R_{IG}}\right)\left(\frac{1}{T} - \frac{1}{T_{ref}}\right) \qquad 3\text{-}61$$

where ΔQ and R_{IG} are the activation energy and the ideal gas constant = 8.31 J/K/mol, respectively.

The time-temperature superposition is very useful for the determination of the modulus of a polymer at very high rates where the test speed is limited by the ability of the instrument, or at a very low strain rate where the length of time required for the experiment is prohibitive.

Several experimental techniques can be used to study the effects of time and temperature on the mechanical behaviour. One of the most popular techniques, especially for studying thermal and humidity effects, is Dynamic Mechanical Analysis (DMA). A thorough explanation of the technique can be found in (58). DMA is very useful for characterising the mechanical behaviour of a viscoelastic solid under an applied tension, or shear at small strains. Under larger strain, tensile tests are frequently used in the literature for the characterisation of a paint film's behaviour. Experimental studies on the effect of time and temperature on acrylic paints has been reported by Hagan (11). The study involved the construction of a master logarithmic curve of the secant modulus versus the inverse of strain rates by using uniaxial tensile test results. Similar studies on polyester-based paints have been reported by Giannakopoulos (30). It is noted here that the construction of such master curves involves extensive experimentation, i.e. paints need to be tested at various strain rates at each temperature.

In summary, the theoretical background on the mechanical behaviour of artists' paints has been presented in this chapter. A review of hyperelastic models has been provided with the derivations of van der Waals and Ogden models for uniaxial tensile loading. The theory of time-dependent, viscoelastic behaviour has been outlined. The definition of the stress relaxation time distribution using the Prony series has been discussed and the combination of the hyperelastic model with the time-independent behaviour has been outlined. An integral approximation using the Taylor numerical method can be used to solve the convolution integral. This enables the determination of the Prony series and hyperelastic parameters that can then be used directly within Abaqus. The implementation method of the hyperviscoelastic model in Abaqus and the method of controlling the numerical accuracy have been discussed. A brief introduction to the time temperature superposition theory including related work using this technique on artist's paints has been presented. The next chapter will focus on the fracture mechanics theories relevant to this work. Also included in chapter 4, is the summary of previous literature work on the topic of fracture in thin films.

4. Fracture Mechanics of Multi-Layered Films

This chapter provides the background theory and literature review concerning fracture in polymeric coatings, particularly artists' paints. First, the analytical solutions for a channelling crack and delamination in a film on a rigid substrate are presented in section 4.1, followed by a review of experimental techniques for characterising fracture in multilayered materials in section 4.2. In section 4.3, the prediction of fatigue crack initiation and propagation are discussed, including the well-known Paris law (59), (60). Finally, in section 4.4, various simulation techniques suitable for fracture problems are discussed. Both monotonic and fatigue loading situations in multi-layered materials are considered, including the predictions of crack initiation as well as crack propagation.

4.1 Fracture mechanics of layered materials

Mixed-mode fracture problems in multilayered materials are a widely studied subject in Fracture Mechanics. The solutions for the stress field near a crack-tip and the calculation of the stress intensity factor at bi-material interfaces have been thoroughly investigated by Rice (61). Hutchinson (62) reviewed and derived the analytical solutions for the fracture phenomena at the interface between two different elastic materials which required the solution of stresses acting at the crack-tip and the phase transformation of the stress intensity factor under mixed-mode loading, where ψ is used to defined the ratio between K_I and K_{II}, written by $\psi = tan^{-1}(K_{II}/K_I)$ where K_I and K_{II} are the stress intensity factors of Mode I and Mode II fracture, respectively. Suo (63) has described the analytical solutions for the fracture behaviour and calculated the energy release rate for a thin film on a rigid substrate under tension and considered the case of a channelling crack as well as decohesion (delamination) of the film. While most fracture analysis models are based on the assumption of linear elastic behaviour, Schapery (64) has proposed a calculation procedure for the total energy release rate for a viscoelastic solid using the correspondence principle. Liang et al. (65)

used Schapery's procedure to calculate the energy release rate during crack initiation and propagation, and also the crack propagation rate. The model was verified with data obtained from standard test geometries including an infinite plate with a central crack under tension, a semi-infinite plate with an edge crack and a single edge notched bend sample of PMMA. However, as yet this has not been validated for interfacial fracture.

Decorative and artists' paints can be susceptible to fracture even under low magnitude cyclic loading such as environmental loading, thermal and/or hygrothermal, and loading during transportation of works of art. Hutchinson (62) and Suo (63) have described several modes of failure in both the thin film and the substrate. In this chapter, the focus is only on channeling cracks and cracks along the film and substrate interface (delamination), under tensile loading. In many situations complex cracking can be observed as shown in Figure 4-1, where both channeling crack growth and delamination can occur simultaneously.

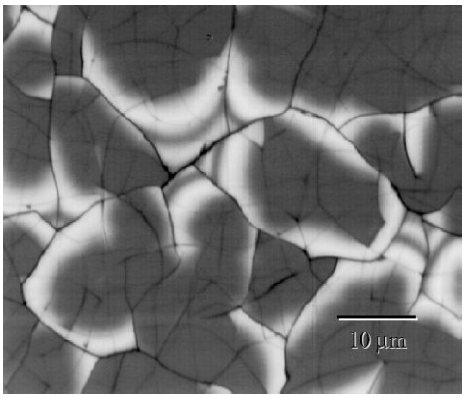

Figure 4-1, X-ray picture showing cracks in coating materials: white colour area is the location where the film was delaminated from the substrate. Black lines are channeling cracks within the film layer (63).

4.1.1 Origin of stress in thin films

Even without an external mechanical load, internal stresses can originate in thin films in many cases. Defects after the deposition process, epitaxial growth phase transformation and mismatch of the strain fields during film growth due to thermal expansion, can create internal stresses and initial

crack sites in the film. Exposure of the film-substrate geometry to the environment can produce stress. During a temperature change, the difference in strain between the film and the substrate is defined (with the assumptions that the substrate is flat and stress free and the expansion of the film is uniform in an in-plane direction) as:

$$\varepsilon_T = \int_{T_0}^{T} (\alpha_f - \alpha_s) dT \qquad 4\text{-}1$$

where α_f and α_s are the thermal expansion coefficients of the film and substrate, respectively. T_0 and T are the initial temperature and the final temperature, respectively.

If the substrate thickness is much greater than the film thickness, the assumption that the substrate can be assumed to be stress free is accurate. The elastic stress in the film due to the thermal strain is then given by:

$$\sigma_T = \frac{E_f \varepsilon_T}{1-\nu_f} \qquad 4\text{-}2$$

The total stress in the film is the sum of the thermal stress, σ_T, and the applied stresses (external mechanical loading).

4.1.2 Channeling crack during tensile testing of a film on a substrate

Considering a linear elastic film under tension, a crack in the film layer is likely to occur as shown in Figure 4-2. According to Hutchinson (62) and Suo (63), the crack growth mechanism starts when the crack driving force is larger than the crack resistance of the film.

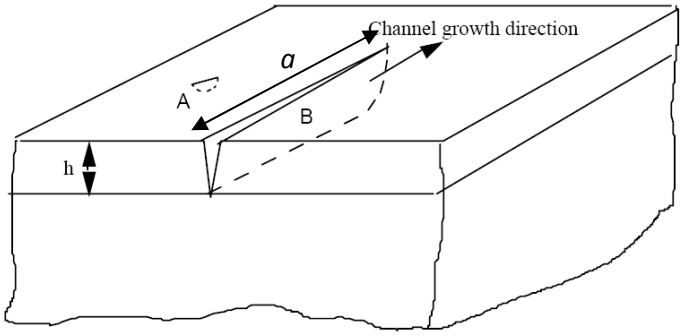

Figure 4-2, an Illustration of a channeling crack: A is the for the case that *a* << *h*, B is for a > h [10].

Let *a* be the cracklength and *h* be the film thickness. In the case that *a* << *h*, the crack can propagate in both the lateral direction and through the film thickness. The energy release rate can then be calculated using equation 4-3, below:

$$G = 3.94\frac{\left(1-\nu_f^2\right)\sigma^2 a}{E_f} \qquad 4\text{-}3$$

where σ is the applied tensile stress, E_f and ν_f are the Young's modulus and Poisson's ratio of the film, respectively. It can be observed that the size of the crack has an influence on the crack driving force.

On the other hand, if the cracklength is comparable to the film thickness, $a \approx h$, the crack can grow only in the lateral direction within the film. The effect of the crack size is then eliminated. A dimensionless parameter, β, that depends on the geometry of the crack, is then introduced into equation 4-4, (63).

$$G = \beta\frac{\left(1-\nu_f^2\right)\sigma^2 h}{E_f} \qquad 4\text{-}4$$

If the substrate is stiffer than the film, β is between 1 and 2. When the substrate is considerably more compliant than the film, β can become very large which will increase the value of *G*. This equation can be used as a conservative design rule, as *G* calculated with this equation can be larger than the actual value.

4.1.3 Interface cracking (delamination) of a film on a substrate under peeling loads

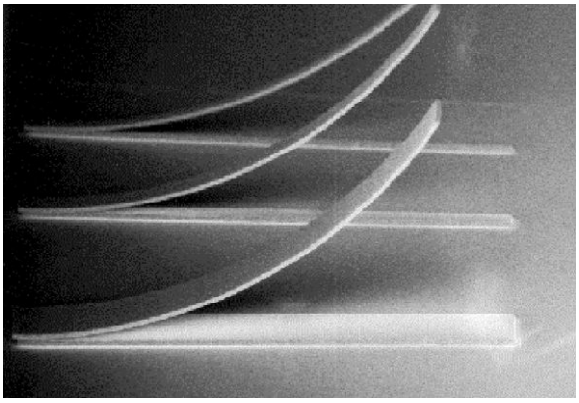

Figure 4-3, illustration of film delamination under tension (63).

Interfacial fracture or delamination as shown in Figure 4-3 is inherent in mixed-mode fracture problems where Mode I, the opening load, and Mode II, the in-plane shearing load, can both be presented. If a crack cannot freely propagate in one direction, asymmetry in loading and elastic response occurs. Also, plasticity and friction can alter the mixed mode behavior. Delamination can start either at the root of the channeling crack or the edge of the film.

Hutchinson (62) explains that the interfacial toughness, G, can be expressed as a function of the stress intensity factors for mode I and II, K_I and K_{II}. If the value of $\psi = tan^{-1}(K_{II}/K_I)$ is defined then the critical interfacial toughness for crack advance is defined as a function of ψ:

$$G = G_c(\psi) \qquad 4\text{-}5$$

where G_C is the energy required to create two unit areas of free surface from an ideally brittle interface.

Considering a delaminating film on a substrate with the debond length (crack length) much longer than the thickness of the film, the energy release rate becomes independent of the crack length and can be calculated using equation 4-6.

$$G = \frac{\left(1-\nu_f^2\right)\sigma^2 h}{2E_f} \qquad 4\text{-}6$$

where σ is the applied tensile stress and h is the film thickness. E_f and v_f are the Young's modulus and Poisson's ratio of the film, respectively. If G is equal to $G_C(\psi)$, steady state crack propagation occurs.

4.2 Experimental considerations for multilayer coatings

Many specimen geometries were proposed for investigating interfacial fracture of coatings and laminate composite materials for different modes of loading. Moore et al. (66) gave an overview of the Mode I, Mode II and mixed-mode test standards used in delamination fracture tests of fibre composites. Most of the standard test geometries such as Double Cantilever Beam (DCB), End Notched Flexure (ENF) and End Loaded Split (ELS) can be performed using rather stiff materials such as metals and fibre reinforced polymers. However, for soft, thin solids such as multilayer paints, these test geometries would not be practical to implement.

Mixed–mode testing methods that would be suitable for interfacial fracture testing involving thin polymer coatings are the Cracked Lap Shear (CLS) and the Notched Coating Adhesion (NCA) tests. The CLS specimen, an example of which is shown in Figure 4-4, is widely used in mixed mode testing of adhesive joints and composite laminates. Various analytical solutions of the specimen can be found in (67) where a round-robin was conducted using 9 techniques and 4 different approaches. Nevertheless, the ratio between G_I and G_{II} for this specimen cannot be concluded from the current literature. Poursartip and Chinatambi (68) applied tensile loading to a CLS specimen to study fatigue and deflection in Carbon Fibre Reinforced Plastic (CFRP) laminates. The study reports the occurrence of fibre bridging which is a mechanism that reduces the compliance of the specimen and can lead to crack arrest in fatigue crack growth. Also, the crack opening displacement and deflection were measured using a Linear Voltage Differential Transducer. Chang (69) suggested the NCA specimen, shown in Figure 4-4, in his study on the effect of moisture on adhesive strength, as a modification of the CLS specimen with the aim to reduce the required preconditioning time for adhesive specimens. The specimen was loaded under tension to determine the mixed-mode energy release rate. The

Mode I portion of the determined energy release rate (37% of the total) is in good agreement (approximately less than 10% different) with the results from DCB samples (100 per cent Mode I). The analytical solutions of NCA were based on the assumption that the material is linear elastic and the substrate is significantly thicker than the coating (70). A comparison with numerical results using the J-contour integral technique was performed in the same work (70); a very good agreement was observed in the comparison.

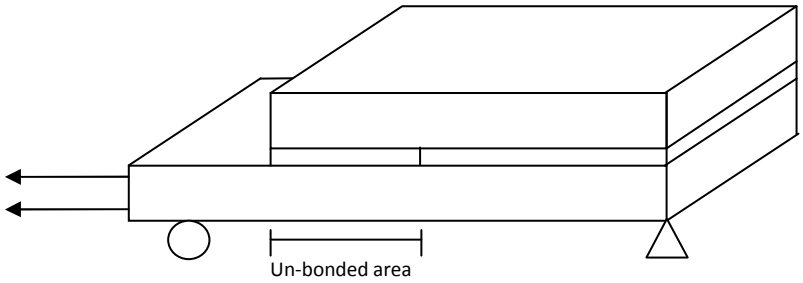

Figure 4-4, cracked lap shear specimen.

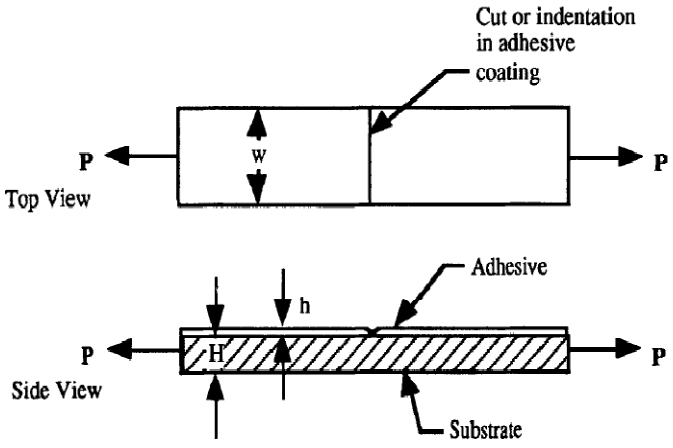

Figure 4-4, notched coating adhesion specimen [15].

Cracking in coatings was also studied by Nichols et al. (71), where a uniaxial tensile test setup was used to study the initiation of a channelling crack in thin paint layers on a thick substrate, shown in Figure 4-5, as used in the automotive industry.

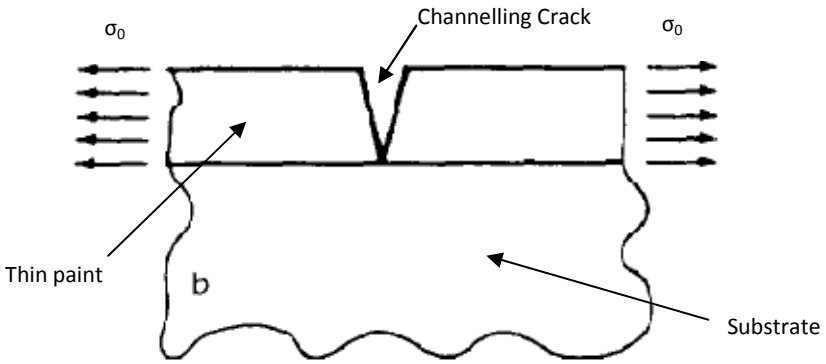

Figure 4-5, initiation of channelling crack in a thin coating on a thick substrate under uniaxial tensile test of (71).

This work showed that the critical energy release rate (G_{IC}) can be accurately computed using linear elastic theories as long as the cracking process involves no plastic deformation and the plasticity of the film due to the tensile loading can be ignored. In another paper from the same author (72), the same test procedure was used to examine the effect of weathering, due to environmental exposure, on the fracture toughness of thin coatings.

Finally, the peel test is a test geometry widely used in characterising adhesive strength and Mode I toughness of soft thin coatings on either a thick substrate, the fixed arm peel (73), or a thin substrate with its thickness comparable to the coating, T-peel (74). As shown by Kinloch et al. (75), peel strength and the adhesive fracture energy, G_a, of flexible laminates do not depend on the peel angle and test geometry but relies on the rate and the temperature of the test only. The true value of G_a can be determined by subtracting from the external energy the elastic stored strain energy, plastic energy due to tension and plastic energy due to bending, although the elastic strain energy and plastic energy due to tension are relatively small and can be neglected. Thouless (76) later performed a parametric study using numerical techniques that indicated the steady state peel force is also dominated by the thickness of the film. In a thin peel arm, the amount of plastic deformation

increases with the thickness due to more bending at the crack tip and results in an increase of the peel force. However, as the peel arm becomes thicker, the deformation in the arm also becomes more elastic and the toughness of the interface starts to dominate the peel force, therefore the force is decreased. As a result of a mixing between these two situations, the peel force is maximised in the medium thickness peel arm and is reduced as the arm becomes thinner or thicker. Peel test data and the age effect on the adhesive strength of modern artist acrylic paints can also be found in recent work by Song (24) and Valkana (25).

4.3 Fatigue in polymer coatings

Fatigue failures occur under the application of repetitive dynamic loading (cyclic loading), after a definite period of time. Fatigue failure can occur without obvious signs of deformation before failure. The fracture surface exhibits a smooth, brittle fracture appearance normal to the loading direction. For soft materials such as rubber, analytical approaches for predicting fatigue crack nucleation and propagation have been reviewed by Mars and Fatemi (77). Failure in paints due to fatigue has been observed by Mecklenburg (78) where the mechanical behaviour of paint films on supports under low temperature and severe changes in relative humidity were studied. The study confirms changes in the stress-strain response of paints due to fluctuations in environmental conditions. It also shows evidence of through thickness and interfacial cracks in paintings under mechanical stresses, as well as the delamination between oil and acrylic paints. Nevertheless, the information on this fatigue failure is qualitative and is still unable to be used for life prediction of multilayered paints.

4.3.1 The S-N curve

Cyclic loading can be described using the stress parameters σ_a, σ_m and $\Delta\sigma$, which are stress amplitude, mean stress and stress range, respectively. These are related through:

$$\Delta\sigma = \sigma_{max} - \sigma_{min},\ \sigma_m = \frac{\sigma_{max}+\sigma_{min}}{2},\ \sigma_a = \frac{\Delta\sigma}{2}$$

where σ is normally taken to be the local stress, in the case of a notched specimen, or when the stress raisers are present in a structure, the stress concentration factor (k) is introduced which provides the relationship between nominal stress (S) and local stress as shown below:

$$\sigma = kS \qquad 4\text{-}7$$

The nominal stress (S) or the stress amplitude, σ_a, is normally plotted versus the number of cycles to failure in order to illustrate the life of a specimen from a specific material and test geometry. The data can be obtained from various types of test, ranging from rotating bending to temperature cycling. In the case of an un-notched specimen, the value of the nominal stress, S, and the local stress, σ, would be the same.

The equation that is frequently used to represent the logarithmic plot of the S-N curve is:

$$S = C + D \log N_f \qquad 4\text{-}8$$

where C and D are fitting constants and N_f is the number of cycles to failure.

Most fatigue data is determined from a complete reversed loading i.e., $\sigma_m = 0$. However, if σ_m is in the tensile range, $\sigma_m > 0$, the allowable stress range, $\Delta\sigma$, is smaller because the maximum stress is limited by the yield stress or the ultimate tensile strength. Furthermore, the number of cycles to failure needs to be reduced relative to the original S-N curve of the same material in order to sustain the same fatigue life.

4.3.2 Fatigue Crack Growth

Cyclic loading can cause crack propagation in materials; the phenomenon is called fatigue crack growth. The extended length of the crack (Δa) is related to the number of cycles (N) while the fatigue crack growth rate is defined as da/dN.

4.3.2.1 Paris law

Defining a relation between the stress intensity factor and fatigue crack propagation rate (da/dN) provides the ability to predict the increase in crack length under cyclic loading.

The same concepts as in the previous section can be used to relate stress intensity factor to crack growth rate for many loading conditions and sample geometries. In the case where plastic deformation is small, the stress intensity factor can be used to express the relationship between crack growth rate and K_{min} and K_{max}:

$$\frac{da}{dN} = f(\Delta K, R) \qquad \text{where } \Delta K = (K_{max} - K_{min}) \qquad 4\text{-}9$$

$$R = K_{min}/K_{max} \qquad 4\text{-}10$$

A schematic of a typical Log-Log plot of the relationship between da/dN and ΔK is shown in Figure 4-7 below. The fatigue crack growth rate behaviour is divided into three regions: I, II and III as shown.

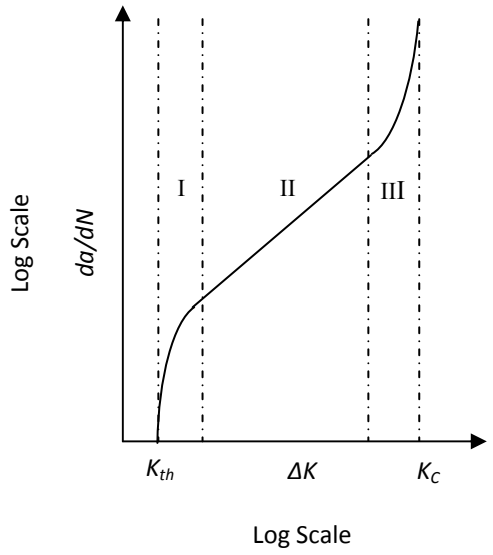

Figure 4-7, da/dN versus ΔK plot.

At low ΔK, i.e. in region I, the crack growth rate approaches zero, which implies that the crack will not grow if ΔK is below ΔK_{th}. On the opposite side of the curve, region III, the rate approaches infinity. This is where the unstable crack propagation occurs due to the fact that the value of K_{max} approaches K_c.

In region II, a linear relationship is observed which can be represented by the following equation, which is known as Paris' Law.

$$\log \frac{da}{dN} = m \log \Delta K + \log C \qquad 4\text{-}11$$

which can be re-arranged as:

$$\frac{da}{dN} = C \Delta K^m \qquad 4\text{-}12$$

Paris' Law is an empirical equation, where C and m are obtained from experimental data.

Many researchers have been trying to extend the power-law dependence in equation 4-12 to the other two regions by adding the effect of R and K_c. However, by using K, which is a linear elastic parameter, the effect of large-scale plastic deformation in region III cannot be represented. Dowling and Begley (79) implemented the J-integral into the Paris law in an attempt to solve the problem with large scale yielding. Nevertheless, limitations still remain which will be explained in the next section.

4.3.2.2 Fatigue crack growth for elastic-plastic materials

In the case of large plasticity due to fatigue, the use of ΔK in the Paris law can result in an inaccurate prediction. Under nonlinear elasticity, the J-integral is a more suitable parameter in fracture mechanics than K, which can be used to characterise the fatigue crack growth under small scale yielding only. As mentioned above, Dowling and Begley (79) applied the J-integral concept to the Paris law as shown below:

$$\frac{da}{dN} = C\Delta J^m \quad \text{4-13}$$

Nevertheless, thus far there is no strong evidence that proves the validity of equation 4-13 for cases where excessive plastic deformation is taking place at the crack tip.

4.4 Finite Element techniques for fracture mechanics

The Finite Element Method (FEM) is a versatile tool for solving nonlinear stress analysis and fracture mechanics problems. This work uses Abaqus, which is a commercial finite element software capable of solving visco-hyperelastic problems with several hyperelastic options including van der Waals and Ogden models. Special purpose techniques for fracture mechanics problems are also available in the software. The techniques include the J-contour integral calculation and the Virtual Crack Closure Technique (VCCT), for the study of crack initiation and debonding, while direct cyclic fatigue and cohesive zone models are suited for the study of crack propagation. Each technique is explained individually in the following section. The software also provides the option to implement user subroutines that enable users to write or modify algorithms for solutions to specific problems.

4.4.1 Crack initiation simulation technique

In dealing with crack initiation problems, as reviewed by Anderson (80), two approaches are used in the finite element method for the calculation of the Stress Intensity Factor (SIF) at the crack-tip. The first one is the point matching method where the SIF is calculated directly from the stress or displacement field at the crack tip. The second method is the Energy method where SIFs are inferred from the energy release rate (*G*). The advantage of the point matching method over the energy method is that it can separately calculate the SIF of each mode for mixed-mode problems separately, which is more complicated when using the energy method. Nevertheless, problems involving elastic-plastic materials can only be analysed by using the energy release rate. In several earlier studies, the Crack Opening Displacement and the Virtual Crack Extension methods introduced by Helen (81) and Park (82) were frequently used and complicated numerical procedures to extract

the SIF values were required. In this project, two energy methods for calculating *G* for a bi-material interface at crack initiation will be used. The first method is the J-contour integral, which is provided in Abaqus as a special purpose analysis tool, and the second is the Virtual Crack Closure Technique, VCCT, used as a tool in the post-processing step.

The J-contour integral has been used in simulations of many fracture mechanics problems. Wilson and Yu (83) introduced the modified J-contour integral in the analysis of a thermal loading problem. Shih et al. (84) and Stern (85) expanded the capability into 3-dimensions and bi-material interface fracture problems, respectively. Aside from the bi-material delamination crack problem, Chen et al. (86) have proposed J_R and K_B as modified *J* and *K* parameters for cracks growing perpendicular to an interface (channeling crack). Khandelwal and Chandra-Kishen (87) have proposed an analytical solution for bi-material fracture under thermal stress and analysed the problem with a modified J-contour integral implemented into a commercial finite element software.

Although the energy method is useful in calculating the total energy release rate for both LEFM and EPFM materials, the downside of the method is the difficulty to extract the SIF in a mixed–mode crack situation. In 1977, the Modified Crack Closure integral technique was introduced by Kanninen (88) as an effective tool for the calculation of the stress intensity factor. The method has the capability to separately calculate the SIF of Mode I (K_I) and Mode II (K_{II}) by using only nodal forces and displacements and with only one analysis. The comparisons presented in (88) between the energy release rate in Mode I from this method and the J-contour integral method were within 4.5% from each other for linear-elastic problems.

Furthermore, another advantage of VCCT was demonstrated by Viswanath et al. (89). They considered the model of a plate with a through-thickness crack under a bending load, without any special stress singular elements around the crack field. Good accuracy was obtained even with the use of a coarse mesh and conventional element types. VCCT can be applied to finite element calculations, not only with solid and shell elements but also with anisotropic and bi-material models

without any need to modify the finite element analysis code. The method can be implemented in the Abaqus with a user defined subroutine as described in the literature by Krueger (90), and the Abaqus user manual (40). In this project, the VCCT method was employed as a post-process analysis which uses output data from the finite element simulations of crack initiation problems. It was also used as one of the fracture criteria in crack propagation problems using the "Debond" capability of Abaqus. The J-integral and the VCCT are described in more detail in sections 4.4.1.1 and 4.4.1.2 below, respectively.

4.4.1.1 J-contour integral Method

The J-integral was proposed by Rice (91), Cherapanov (92) and was first implemented to a 2-dimensional finite element analysis through the virtual crack extension method by Shih, et al. (84). The J-integral is a versatile tool in the characterisation of fracture in both linear and nonlinear elastic and plastic fracture mechanics problems. The J-integral is given by:

$$J = \int_{\tau} \left[w dy - T_i \frac{\partial u_i}{\partial x} ds \right] \qquad 4\text{-}14$$

where w is the strain energy density, T_i are the components of the traction vector, u_i are the displacement vector components and ds is the length increment along the contour Γ as shown in Figure 4-6.

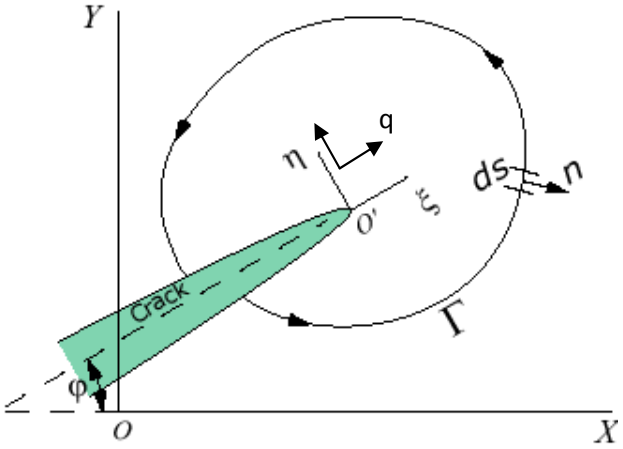

Figure 4-6, arbitrary contour around the tip of the crack.

The strain energy density is defined as:

$$w = \int_0^{\varepsilon_{ij}} \sigma_{ij}\, d\varepsilon_{ij} \qquad 4\text{-}15$$

where σ_{ij} and ε_{ij} are the stress and strain tensors, respectively.

In 2004 Courtin et al. (93) presented the advantages of the J-contour integral in the calculation of the stress intensity factor by using the method in the commercial FE software Abaqus. The study compares the value of SIF calculated from the J-Integral approach with those from an analytical solution and several other techniques including the displacement extrapolation technique and the singular element technique. It was shown that SIFs calculated from the J-contour integral provided good accuracy whilst also requiring a lower computational resource than the other two methods. One of many unique properties of the J-integral is path independency. Nevertheless, according to the Abaqus documentation (40), variation in J-integral values when taken along different contours may occur in the analysis of an elastic-plastic problem. This is due to the fact that each integral contour may consist of a different number of elements with plastic deformation. The error and variation can be lessened with the use of a higher mesh density. Also the use of singularity elements in a small strain analysis case can improve the accuracy of the J-integral from the first few contours.

In Abaqus, the integral domain for a J-contour integral analysis is defined a ring of elements around the crack tip. The first contour contains only the node at the crack tip. The following contours are created by the elements that share their nodes with the elements in the previous contour. The parameters needed by Abaqus for the J-integral calculation in two-dimensional crack initiation problems are: the definition of the node at the cracktip, the direction normal to the crack, η, or the vector in the virtual crack extension direction (q) (shown in Figure 4-6) and the number of contours to be used. In many cases, J values from the first few contours may be inaccurate and a larger number of contours will be required for the result to be consistent.

4.4.1.2 Virtual crack closure method

According to the review by Kruger(90), the energy release rates (*G*) in the VCCT are evaluated as the amount of elastic work that is required to close the crack by a small amount, *Δa*, separately for each mode. An illustration of the method for both 4-node and 8-node elements is shown in Figure 4-7a and Figure 4-7b, respectively, and the expressions for G_I and G_{II} are given by equations 4-16 and 4-17.

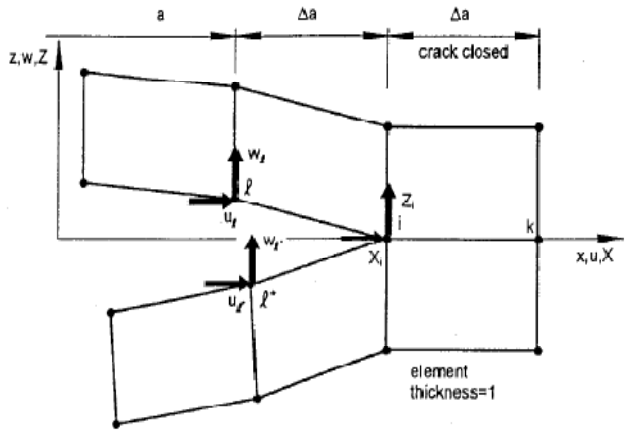

$$G_I = -Z_i (w_I - w_{I*}) / (2\Delta a)$$

$$G_{II} = -X_i (u_I - u_{I*}) / (2\Delta a)$$

4-16

a)

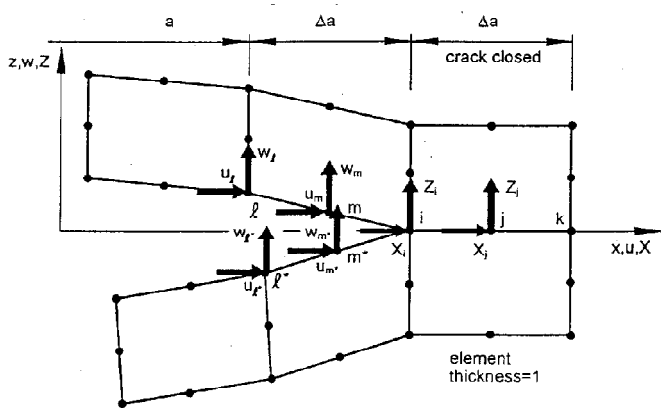

$$G_I = -[Z_i (w_I - w_{I*}) + Z_j (w_m - w_{m*})] / (2\Delta a)$$

$$G_{II} = -[X_i (u_I - u_{I*}) + X_j (u_m - u_{m*})] / (2\Delta a)$$

4-17

b)

Figure 4-7, VCCT calculation; a) for 4-node element, b) for 8-node element (90).

where

G_I = Energy release rate for mode I

G_{II} = Energy release rate for mode II

w_i, w_{i*}, w_m, w_{m*} = displacements in perpendicular direction to the crack at nodes i and m

u_i, u_{i*}, u_m, u_{m*} = displacements in parallel direction to the crack at nodes i and m

Z_i, Z_j = Reaction Force in y-direction at nodes i and j, respectively

X_i, X_j = Reaction Force in x-direction at nodes i and j, respectively

4.4.2 Crack growth simulation technique

There are several strategies that are currently being used in commercial finite element software for crack propagation simulations. One of the methods that is widely used is the application of special purpose cohesive elements along the crack front called a Cohesive Zone Model (CZM) proposed by Needleman (94). The traction-separation curve, Figure 4-10, has to be specified for the elements where the maximum traction (σ_{max}) is specified along with maximum displacement, δ_0, for the potential crack surfaces to reach total separation. The area under the curve is equal to the critical value of the strain energy release rate, G_C. A detailed discussion of cohesive zone modelling, including the implementation of this technique in Abaqus will be provided in chapter 6.

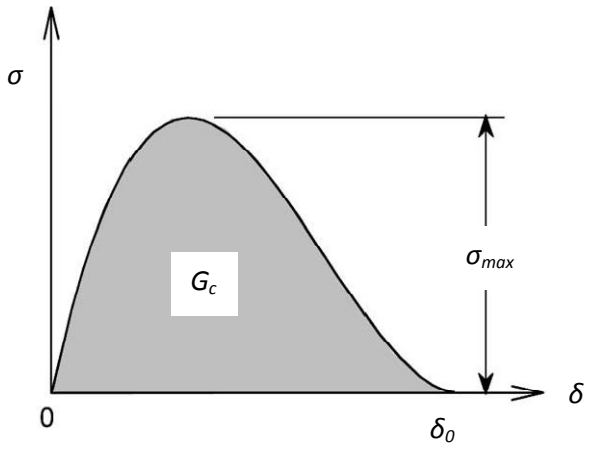

Figure 4-8, general form of cohesive law.

An alternative technique for the simulation of the crack propagation problem is the Node Releasing Technique. The capability to perform this technique is provided in Abaqus Version 6.8 (39) through the *Debond command with the option to choose from several failure criteria. This feature is only supported by the input file method, not by Abaqus CAE user graphic interface. In this project, the Virtual Crack Closure Technique (VCCT) and Low Cycle Fatigue criteria were selected to evaluate the crack propagation during monotonic and cyclic loading, respectively. The benefit of the VCCT criterion is that the method straightforwardly uses the critical energy release rate (G_C), which is a common material property.

4.4.3 Fatigue modelling in multi-layered coatings

This study aims to simulate fatigue cracking at the interface of polymeric coatings. Under cyclic loading, a material tends to build up damage from each loading cycle, which causes the crack to gradually propagate. In simulations, it is necessary to alter the material properties at the interface, such as the traction-separation curve, the value of fracture toughness, etc., between cycles, otherwise the material response will repeat in the same way in every cycle. Several studies have proposed algorithms to simulate the degradation of a material and interface properties during cyclic loading. A review of the available techniques is provided in this section.

Several finite element simulation techniques for interfacial fatigue fracture have recently been developed. Yang et al. (95) proposed an irreversible damage model, based on a damage locus derived from monotonic loading and the assumption that, for fatigue problems, damage from fatigue loading is accumulated cycle by cycle even though the load-displacement relationship is below the damage locus. Turon (96) and Robinson (97) proposed a modified cohesive zone model for high cycle fatigue, where the damage evolution of the element is controlled by a Paris law and a 'cycle skipping' scheme. Another technique, introduced by Roe and Siegmund (98), which is the most suitable for environmental, low cycle fatigue as in the current study, is the Irreversible Cohesive Zone Model. The technique was evaluated with the cases of a double cantilever beam (DCB), end load split (ELS) and mixed-mode beam specimen geometries.

Another option is the low cycle fatigue criterion. The technique uses the algorithm of the "Debond" feature mentioned in the previous section in conjunction with the direct cyclic algorithm and the damage extrapolation algorithm, similar to Paris Law, in order to simulate the damage due to cyclic loading. VCCT is used to calculate the relative fracture energy release rate, ΔG, during each cycle and a node is released during the cycle when ΔG reaches the user specified ΔG_C. With increasing number of cycles, ΔG_C is reduced following the Paris relationship. This technique is already implemented in Abaqus and was employed initially in this study but it was found that it could only model Mode I problems; under Mode II loading, the debonded surfaces interpenetrated which could not be avoided by a suitable contact definition.

A more detailed discussion regarding the direct cyclic method, the low cycle fatigue technique and the irreversible cohesive zone model including the author's own investigations on each technique will be provided later in chapter 6.

Thus far, a literature of analytical and numerical fracture mechanics techniques that were used in this work has been provided. The numerical techniques for fracture mechanics problems including crack initiation and propagation under monotonic and cyclic loading have been reviewed. The peel

test method described in section 4.2 was used in the determination of interfacial toughness between blue phthalo alkyd and acrylic gesso paint layers. Details of the experimental methods and summarised results are provided in chapter 5. In addition, the analytical solutions and the simulation techniques mentioned in this chapter were used in the development of the life prediction model for thin multilayer polymeric coatings under mechanical and environmental cyclic loading. These will be presented in chapters 6 and 7.

5. Mechanical Testing of Multilayer Paints : Method and Result

Mechanical tests of multilayer paints are documented in this chapter. Specifically the test method and results from the uniaxial tensile, relaxation and T-peel tests under controlled temperature, humidity, displacement rate and sample ages are reported. All the tests were conducted with a universal testing machine INSTRON 4301 with a 100N load cell and a built-in environmental control chamber which was developed in-house (11). The chamber was able to maintain the temperature within +/- 0.2°C and the humidity within +/-1% RH of the desired settings throughout the test. The details of the design and specification of the chamber can be found in (11).The tests data are used in the calibration of the hyper-viscoelastic material model described in chapter 3, the determination of the adhesive fracture toughness, G_C, and are also used in the environmental fatigue simulation study reported later in chapter 7.

This chapter will describe the following: sample preparation, the uniaxial tensile test, the relaxation test, the material model calibration, the T-peel test and the determination of fracture energy, G_C. Section 5.1 provides details of the sample preparation for the uniaxial tensile tests of the free paint films as well as for the T-peel tests. In section 5.2, the uniaxial tensile behaviours of Golden acrylic gesso and phthalo blue Windsor & Newton Griffin alkyd at the ages between 20 to 1600 days are reported, followed by the effect of environmental conditioning and strain rate. In section 5.3, the relaxation data of the paints for 2% and 10% applied strains are reported. The experimental results from sections 5.2 and 5.3 are used in the calibration of the visco-hyperelastic model presented in chapter 3, in section 5.4. Section 5.5 reports the T-Peel test results under several environmental conditions. The fracture toughness calculation and the G_C value calculated from the IC-Peel 2006 software available on the Department of Mechanical Engineering, Imperial College London, website (99), are also reported in section 5.5. The last section, 5.6, described the mode II fracture and environmental fatigue experiments that were attempted in this work.

5.1 Sample preparations

As already mentioned in section 2.3, two commercial paints were used in this work. They were chosen to be representatives of artist practice and because previous data had shown such combinations can result in cracking of the upper layer under bending (7). The first paint layer was an acrylic gesso primer manufactured by Golden. It is made from acrylic resin dispersed in water with $CaCO_3$ and TiO_2 white pigments. Acrylic gesso is recommended for use on solid and flexible supports, and is widely used as a base layer for painting on canvas. The second paint was an artist's alkyd (oil based polyester) with phthalocyanine blue pigment (Griffin series) manufactured by Winsor & Newton.

The two paints were cast as free films to enable their tensile properties to be determined, as well as in the form of overlaid layers for peel testing. The specimens had rectangular, thin film geometries. The procedure for specimen preparation outlined in (17),(28) and (29) was followed. The liquid paints were applied on a transparent polyester sheet (ordinary office transparencies) which served as a sample carrier. Electrical insulation tape, 19 mm wide and 0.12 mm thick, was used as a thickness gauge in order to control the thickness of the paint layer. Four overlaid tape layers produced an average dry film thickness of 0.25 mm for the alkyd and 0.15 mm for the acrylic gesso. The paint was applied using a plastic blade, dragging the liquid paint from one end of the sheet to the other. Care was taken to prevent bubble formation in the paint layer. The samples after paint application are shown in Figure 5-1a. After the paint is dry, the insulated tape was removed and the polyester sheet was cut to individual strips as shown in Figure 5-1b. The paint strips were left to dry for various periods in order to study the effect of sample age on the experimental data. The polyester backing was removed 24 hours before the dried paint samples were ready to be tested, by holding an ice pack on the back of the polyester sheet for a few seconds. The temperature drop reduced the adhesion between the paint and the polyester sheet, allowing the paint to be easily peeled off. The paint films were then cut to a size of 5 mm in width and 40 mm in length using a

sharp, ordinary blade. Paper tabs of 5 mm in length were attached to both ends of the sample, which left a 30 mm gauge length. The final samples ready to be tested are shown in Figure 5-1c.

The peel test samples consisted of a layer of phthalo blue Winsor & Newton Griffin alkyd on a white Golden acrylic gesso. These were prepared using a similar method to that used to make the tensile test samples. After the acrylic gesso was applied and left to dry for one week, a releasing agent (Freekote NC-55) was applied with a brush from one end to a distance of 35 mm on the dried gesso to prevent the adhesion between the gesso and the top alkyd layer. This served as the necessary 'precrack' in the peel tests. The insulation tapes that were used to control the thickness of the gesso were removed and replaced by new ones which overlapped the gesso layer. Phthalo blue alkyd was then applied as the second layer, using the same method. The insulation tape was removed one week after applying the alkyd. The finished strip before being cut to size is shown in Figure 5-2a. The samples were left to dry in an uncontrolled room environment. The polyester sheet was removed using an ice pack as explained above. The sample was cut to the size of 5 mm in width and 70 mm in length; 5 mm paper tabs were attached to the ends of both layers such that the final length of the peel arms was 30 mm, the same length as the tensile sample, as shown in Figure 5-2b.

It is important to emphasise that all paint samples used in this study were stored in an uncontrolled room temperature and humidity environment for two years. It is possible that the storage condition can significantly alter the adhesion and tensile properties as reported in (18) and (19).

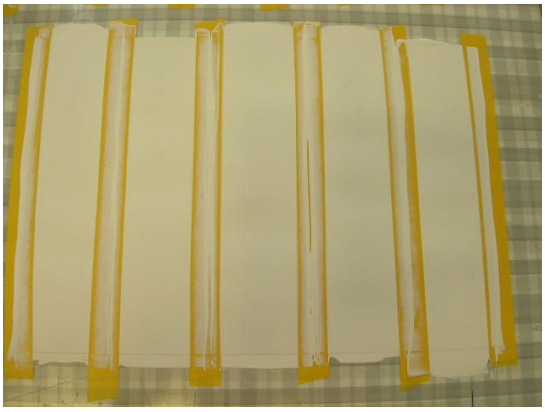
a)


b)

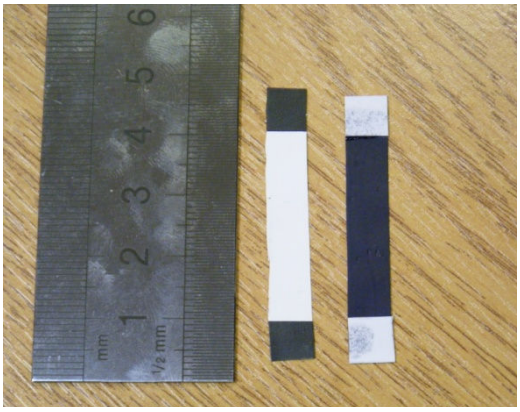

c)

Figure 5-1, a) strips of gesso with insulated tape after application(24), b) finished strip before cutting, c) finished sample after being cut to size before testing.

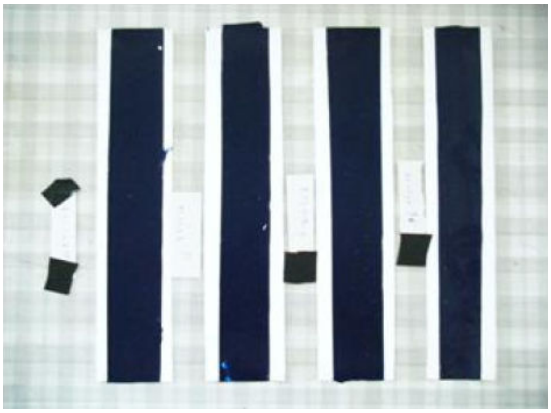

a)

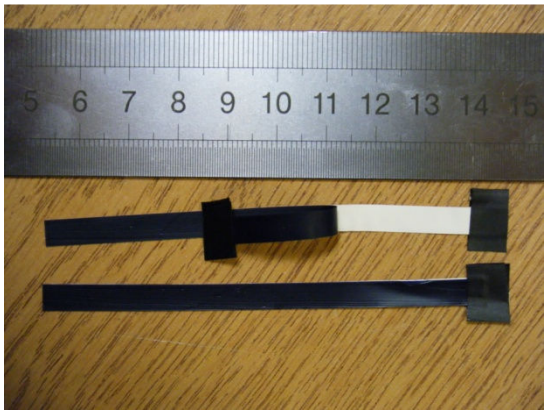

b)

Figure 5-2, a) finished strip of T-peel sample before cutting, b) finished T-peel test sample after cutting

5.2 Uniaxial tensile test of free paint film

The uniaxial tensile test method and the test results for the free blue phthalo alkyd and acrylic gesso layers are presented in this section. After the measurements of thickness, width and gauge length were made, one end of the sample is inserted into a metal grip. Care is taken to ensure that the sample is perpendicular to the grip's edge. The grip is tightened and then attached to the loading rod inside the environmental chamber which is fitted to the universal testing machine. The lower end of the sample is inserted into the bottom grip at the bottom of the chamber with the grip left un-tightened. The chamber door is closed and the sample is left inside until the humidity and temperature reaches the set condition. Five minutes after the environmental conditions in the

chamber reach the set values, an Allen key is used to tighten the bottom grip through a small hole drilled in the chamber door and the hole is then plugged with sticky putty. At least five repeats were performed for each test condition. The test configuration is shown in Figure 5-3 below.

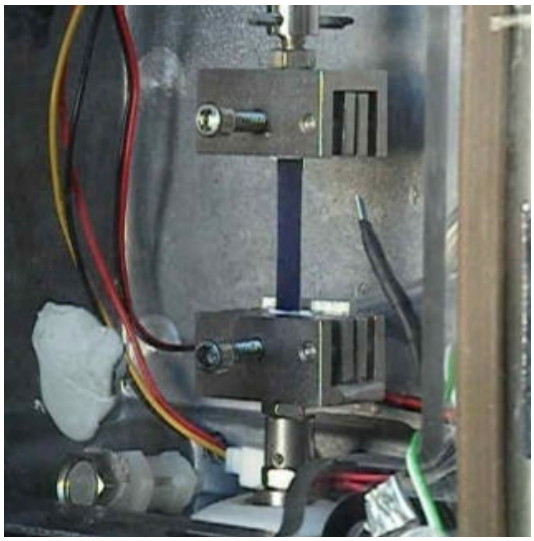

Figure 5-3, Tensile test configuration

The test is started whilst the load-displacement data is recorded at the sampling rate of five data points per second. The test continues until either the sample breaks or until the top grip nearly reaches the top of the chamber, whichever occurs first. The load-deflection data are converted to true stress, σ, and true strain, ε, using the following relations:

$$\sigma = \frac{PL}{L_0 A_0} \qquad 5\text{-}1$$

$$\varepsilon = \ln \frac{L}{L_0} \qquad 5\text{-}2$$

where P is applied load, L is current length and L_0 and A_0 are the initial length and cross sectional area respectively. Note that conservation of volume was assumed, based on the Poisson's ratio of acrylic paints reported in the work by Hagan (35) being approximately 0.5. The tensile test method outlined here was used for all the uniaxial tensile tests throughout this project.

Firstly the effect of sample age was investigated. The monotonic stress-strain data of the 20, 300, 500 and 1600 days-old gesso and 30, 180, 300, 700 and 1600 days-old alkyd at 25°C, 50% RH and a constant crosshead speed of 5 mm/min are presented in Figure 5-4. (5 repeat tests were performed for each sample age; the error bars are very small and obscured by the symbols, therefore are not visible in the plots). The 1600 days-old samples were obtained from the set of samples used in the earlier work by Valkana (25). The samples were made using the same method described in section 5.1. The initial stiffness, calculated from the slope of each stress-strain curve at 0.02 percent strain, versus age of the paints is shown in Figure 5-5. It can be observed that the stiffness of the alkyd paint (Figure 5-4a) increases over time even after four years of storage where Figure 5-5 shows that the initial stiffness of the alkyd increases by approximately 40 percent over 4 years. In contrast, the tensile properties of the acrylic gesso (Figure 5-4b) show a small change and the initial stiffness increases only by less than 10 percent. This is in agreement with the recent work by Hagan (11) who showed that the mechanical properties of acrylic paints remain relatively unchanged over time after approximately one month of application; on the contrary, the mechanical properties of alkyd paint are known to change overtime as reported in the work by Young (19) and Giannakopoulos (30). This is due to the increasing volume of cross-linking polymer chains with time (30).

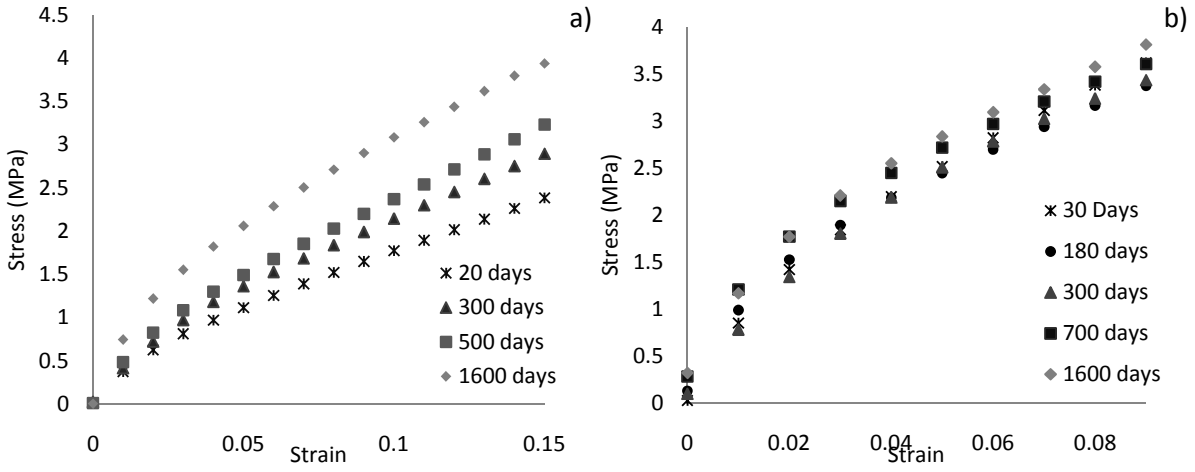

Figure 5-4, effect of age on tensile properties: a) Winsor & Newton Griffin phthalo blue alkyd, b) Golden acrylic gesso

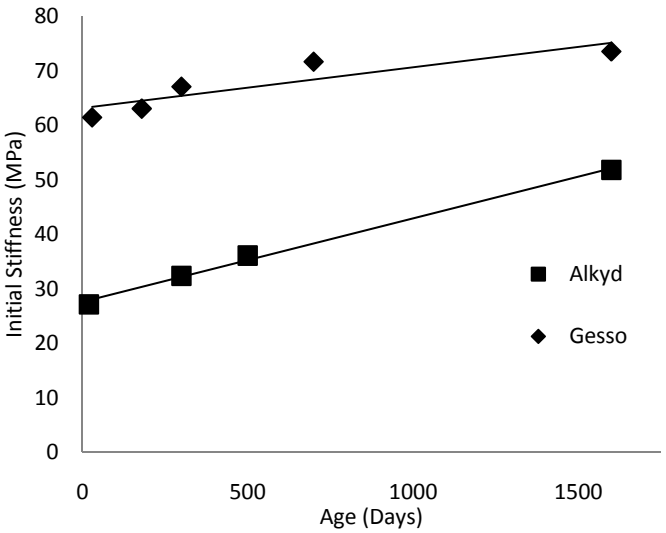

Figure 5-5, Initial stiffness versus age of the sample of acrylic gesso and blue pthalo alkyd.

The influence of temperature, in a range consistent with the experience of paintings in museum and conservation settings, on the stress-strain response of 300 day-old alkyd and 300 day-old gesso paints at 50% RH and 5 mm/min displacement rate is shown in Figure 5-6a and Figure 5-6b, respectively. It is observed that both paints are stiffer at lower temperatures with a high dependency on temperature. This is because the glass transition temperature of paints such as these is usually in the region of 0-25 °C as measured by the Differential Scanning Calorimetry technique (11), (35), leading to drastic changes in the stress-strain response for temperatures such as those shown in Figure 5-6.

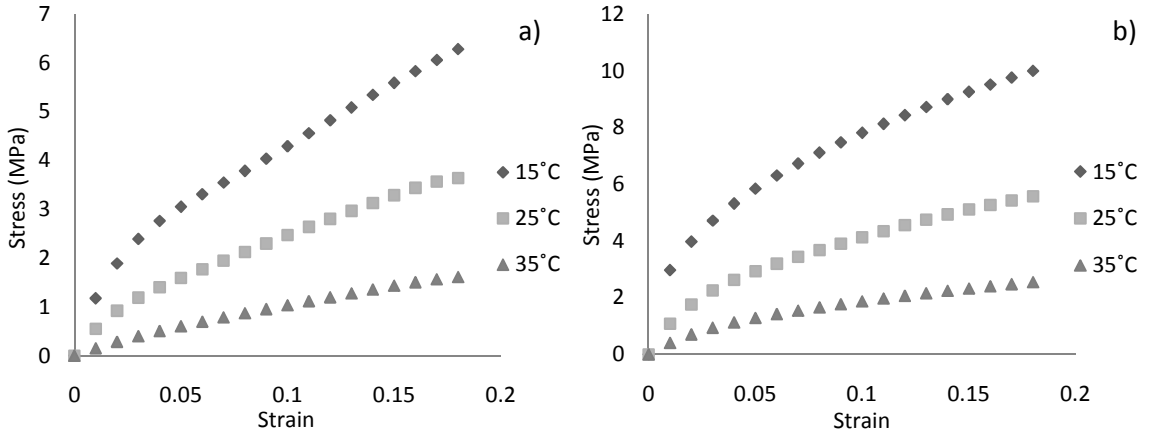

Figure 5-6, effect of temperature on tensile properties of 300 days old: a) Winsor & Newton Griffin Phthalo blue alkyd, b) Golden acrylic gesso.

Figure 5-7 illustrates the effect of the loading speed on 300 days-old alkyd (Figure 5-7a) and 300 days-old gesso (Figure 5-7b) paints at 25°C and 50% RH. The crosshead speed was varied between 0.05, 0.5, 5 and 50 mm/min which correspond to the initial strain rates of 0.00167, 0.0167, 0.167 and 1.67 min^{-1}, respectively. The data points are the experimental results whilst the solid lines show the calibrated visco-hyperelastic material model, to be explained later in this section. The experimental data highlights the time-dependent behaviour of both paints. It is known from the work of Hagan et al (17) that, for acrylic paints, increasing the strain rate has a similar effect as decreasing the temperature. This enabled a time-temperature superposition approach such that modelling the effect of both strain rate and temperature could be achieved. A time-temperature superposition was not performed in this study due to the extensive testing required; the modelling to be presented shortly is restricted to the median temperature in the expected range, i.e. 25˚C.

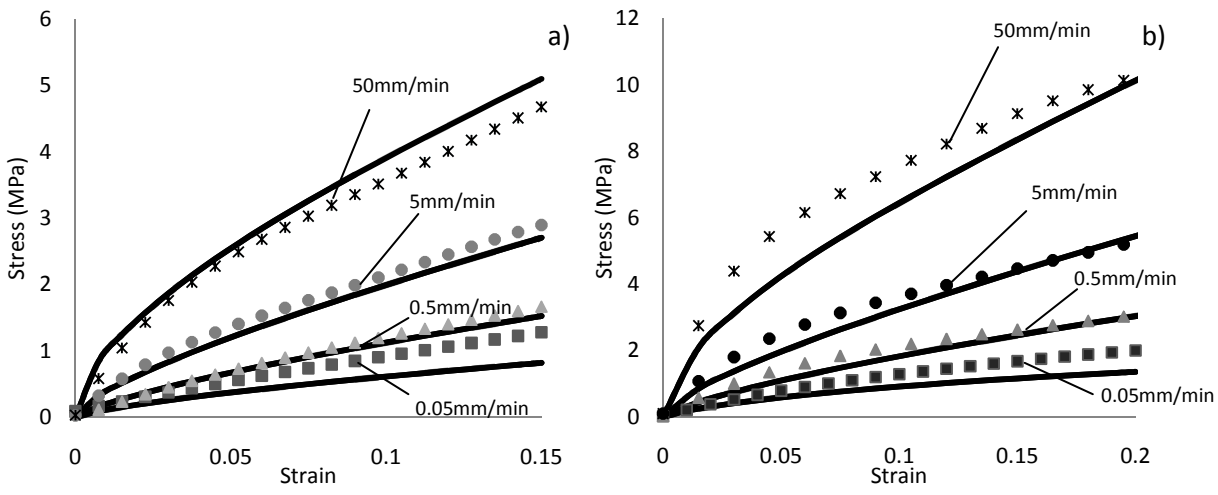

Figure 5-7, effect of displacement rate on tensile properties of 300 days old samples: a) Winsor & Newton Griffin phthalo blue alkyd, b) Golden acrylic gesso.

The stress-strain data at different strain rates for 1600 days-old gesso at 25°C and 35°C is shown in Figure 5-8 below. Figure 5-8a is comparable to those of the 300 days-old sample in Figure 5-7b for every speed. Similar test data for the alkyd was however not collected.

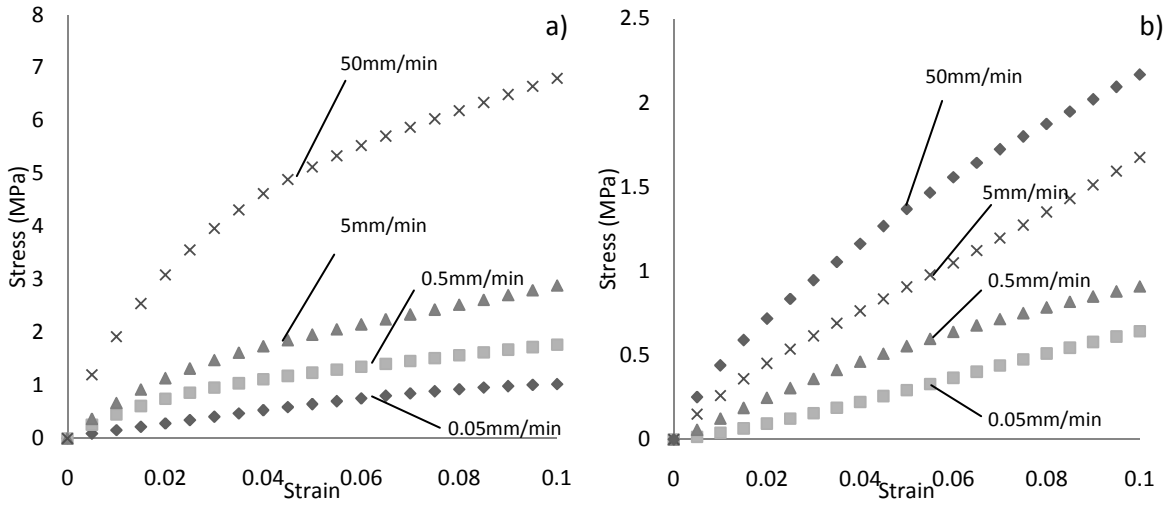

Figure 5-8, effect of displacement rate on tensile properties of 1600 days old Golden acrylic gesso: a) at 25°C, b) at 35°C.

5.3 Relaxation tests on free paint films

As a viscoelastic solid is held at a constant displacement, the stress that is required to maintain the strain in the sample decreases with time until it settles at an equilibrium value; this behaviour is called stress relaxation. The concept of the test is to keep the strain of the sample constant whilst the decrease in stress within the specimen is being monitored.

The relaxation tests have been carried out for both paints at 300 days-old, 25°C and 50% RH. Samples were initially loaded in tension at 5 mm/min to a strain of approximately 2% and 10%. The extension was then held constant under constant environmental conditions whilst the load data was recorded. It should be noted that it is not possible to instantly apply the maximum strain to the sample in practice; therefore the peak stress shown in the plot is significantly below the instantaneous value. The sample is left at the fixed displacement for 5000 seconds whilst the load versus time data is recorded. Figure 5-9a and Figure 5-9b show the stress-time response of the 300 days-old alkyd and 300 days-old gesso at 25°C and 50% RH. Data points shown are the experimental data whilst the solid line is the viscoelastic material model which will be explained in the following section.

It can be seen from Figure 5-9 that the stress decays rapidly after the crosshead displacement is fixed but the rate of decaying reduces over time. At longer periods the stress is significantly below the maximum value and is approaching equilibrium. At larger strain, the rate of decaying is shown to be faster than at smaller strain.

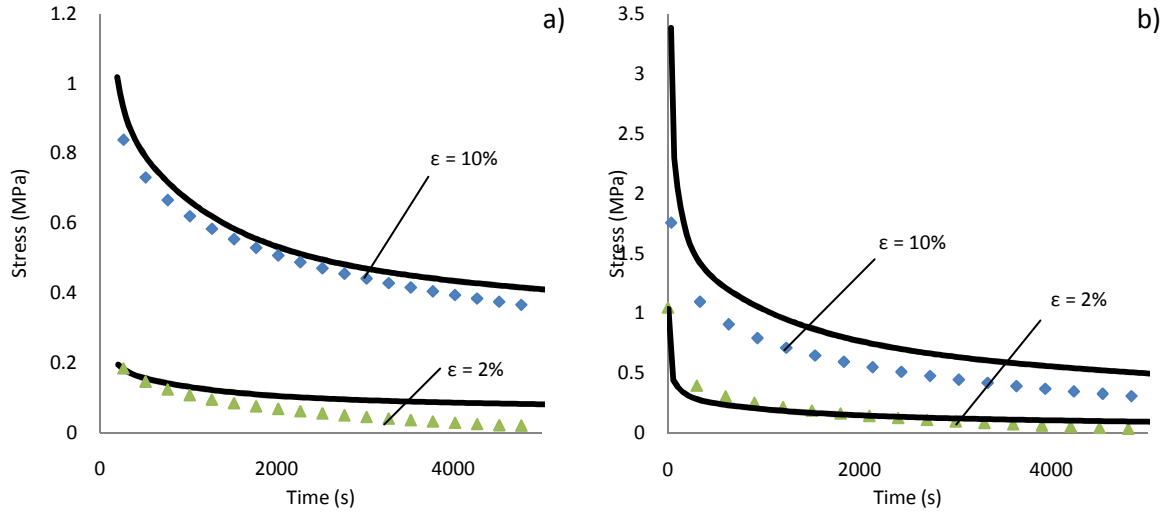

Figure 5-9, relaxation test data: a) Winsor & Newton Griffin Phthalo blue alkyd; b) Golden acrylic gesso.

The monotonic stress-strain and stress relaxation data shown in Figure 5-7 and Figure 5-9, respectively, will be used to calibrate the viscoelastic model in the next section. However, a question remains regarding which material model, a linear or nonlinear viscoelastic, is suitable to fit the data. Hagan et al. (17) have reported that the mechanical response of latex paints under uniaxial loading can be described using the hyperelastic model in conjunction with the time-dependent, viscoelastic Prony series, described earlier in chapter 3, an investigation to verify this has been carried out. The relaxation modulus, *G(t)*, calculated from the stress relaxation data in Figure 5-9 has been plotted as a function of time in Figure 5-10 through the relationship below

$$G(t) = \frac{\sigma(t)}{\varepsilon} \qquad 5\text{-}3$$

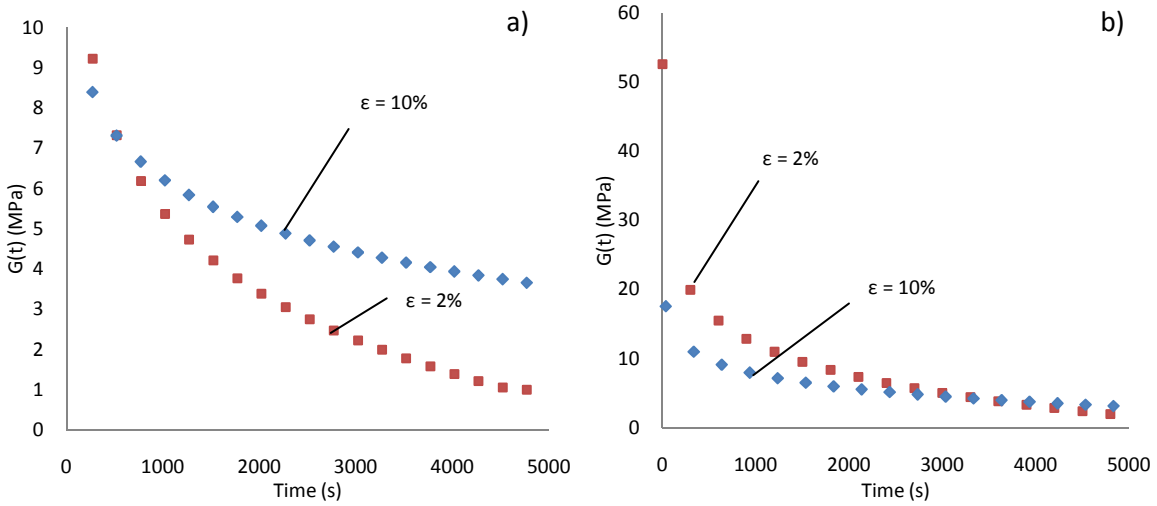

Figure 5-10, elastic modulus *G(t)* as a function of time from the relaxation test; a) Winsor & Newton Griffin Phthalo blue alkyd; b) Golden acrylic gesso.

The results show that the modulus of both paints are different at strains of 2% and 10%, hence it can be concluded that the tensile behaviour of both paints should be represented by nonlinear vicoelastic constitutive laws.

5.4 Material model calibration

The van der Waals hyperelastic and viscoelastic theory combination described in chapter 3 was selected as a material model for the acrylic gesso and the alkyd paint. The material constants of the model are calibrated using the uniaxial stress-strain data and the stress relaxation data in Figure 5-7 and Figure 5-9, using the least squares fitting method. The sum of the square relative errors, *SSPE,* defined in equation 5-4 was used to determine the relative difference between the model predictions, x_m, and the experimental data, x_i,.

$$SSPE = \sum_{i=1}^{n} \left(\frac{X_i - X_m}{X_i}\right)^2 \qquad 5\text{-}4$$

SSPE was minimised by using the solver algorithm embedded in a Microsoft Excel spread sheet by using Microsoft Office Macro Script (11). It is essential to use the relative error in order to eliminate the bias from the magnitude of stress at each point within the stress-strain curve. Also the stress-

strain curves have been re-plotted with the limit of 25 data points for each test speed using polynomial equations from the trend line. This technique makes it possible to control the weight ratio of the data from each test speed when fitting the model.

The calibrated time independent material parameters of the van der Waals model and the Prony series parameters for both paints are shown in Table 5-1 and Table 5-2.

Table 5-1 van der Waals time independent material parameters.

Time-independent parameters			
Paint	μ (MPa)	λ_m	α
Alkyd	75	8	0.5
Gesso	125	10	0.5

Table 5-2, time-dependent material parameters (Prony series)

Prony Series		
τ_i (s)	g_i (Alkyd)	g_i (Gesso)
1.00E-01	0.730	0.727
1.00E+00	0.145	0.150
1.00E+01	0.050	0.050
1.00E+02	0.032	0.030
1.00E+03	0.020	0.022
1.00E+04	0.013	0.020

So far, only the effect of strain rate has been modelled. The effect of age and temperature (and indeed relative humidity) on the constitutive model were not considered in this work. The effect of

temperature could possibly be accommodated through a shift in the relaxation times τ_i as suggested in (30) and (17).The effect of humidity and sample age are more problematic as time-humidity-age superpositions have not yet been demonstrated for such materials.

5.5 Peel experiments and analysis

Interfacial fracture toughness between the acrylic gesso and the alkyd is determined through the peel test. The test is commonly used in the determination of the adhesive energy release rate, G_C, of thin layer films on fixed rigid substrates (fixed arm peel test) or between two adjacent flexible laminates (T peel test). The aim of the test is to monitor the peel force and the peeling angle that are required to separate the film layer from the substrate or from another layer of flexible material. The steady state peel test data are used in conjunction with tensile stress-strain data of the peel arm materials for the determination of G_C, using the IC-Peel software available on the Department of Mechanical Engineering, Imperial College website (99).

The analytical solution for the determination of the adhesive fracture energy, G_C, of a peel arm was derived by Kinloch et al.(75) and Moore et al.(100). The energy balance principle was used:

$$G_C = \frac{1}{b}\left(\frac{dU_{ext}}{da} - \frac{dU_s}{da} - \frac{dU_{dt}}{da} - \frac{dU_{db}}{da}\right) \qquad 5\text{-}5$$

where b is the width of the peel arm, dU_{ext} is the external work, dU_s is the strain energy of the peel arm, dU_{dt} is the dissipated tensile energy and dU_{db} is the dissipated bending energy of the peel arm ahead of the peel front. Considering a peel arm of thickness h under a constant, steady state load P, at a peel angle Θ, the first three energy terms on the right hand side of equation 5-5 can be written as:

$$dU_{ext} = Pda(1 + \varepsilon_a - \cos\theta) \qquad 5\text{-}6$$

$$d(U_S + U_{dt}) = bhda\int_0^{\varepsilon_a} \sigma d\varepsilon \qquad 5\text{-}7$$

where ε_a is the tensile strain, σ is the tensile stress in the peel arm and a is the crack length.

Combining equations 5-5, 5-6 and 5-7 provides the corrected input energy per unit width per unit length, G, and the adhesion energy release rate, G_C, as shown in equations 5-8 and 5-9, respectively;

$$G = \frac{P}{b}(1 + \varepsilon_a - \cos\theta) - h\int_0^{\varepsilon_a} \sigma d\varepsilon \qquad 5\text{-}8$$

$$G_c = G - G_p \qquad 5\text{-}9$$

where G_p is the local plastic/viscoelastic work done per unit area defined as

$$G_p = \frac{1}{b}\frac{dU_{db}}{da} \qquad 5\text{-}10$$

The evaluation of G_p is summarized by Kinloch et al.(75). The derivation takes into account the deformation that occurs at the root of the peel arm, as shown in Figure 5-11. The deformation is modelled using a large deformation analysis for local bending given in (101) and the elastic plastic behaviour of the peel arm is modelled as a bilinear work-hardening material as illustrated in Figure 5-12 and equation 5-11.

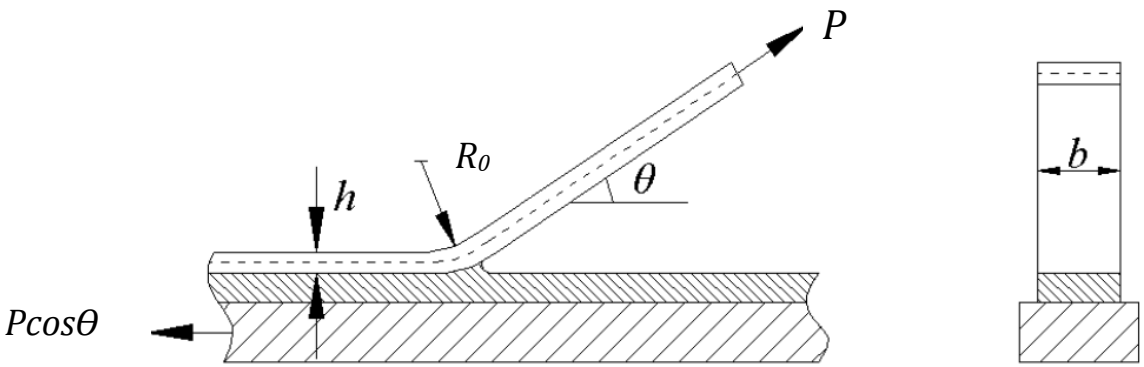

Figure 5-11 root rotation in the peel test

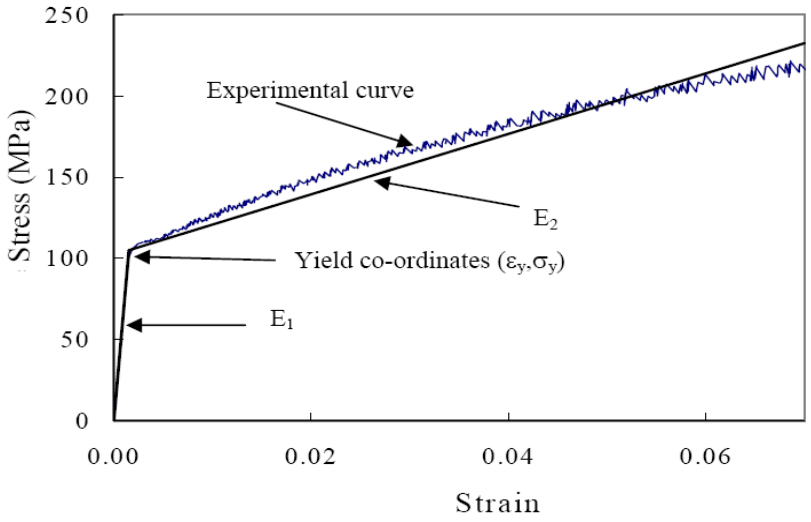

Figure 5-12, schematic of bilinear law (100)

$$\sigma = E_1\varepsilon \qquad \text{when } \varepsilon < \varepsilon_y$$

$$\sigma = \sigma_y + \alpha E_1(\varepsilon - \varepsilon_y) \qquad \text{when } \varepsilon > \varepsilon_y \text{ and } \alpha = E_1/E_2 \qquad 5\text{-}11$$

where E_1 is the elastic modulus, E_2 is the plastic modulus and σ_y is the yield stress.

G_p is expressed in the terms of α and k_0 which are, respectively, the work hardening parameter of the peel arm material, also known as the bilinear ratio, and the ratio R_0/R_1. R_0 is the actual radius of curvature corresponding to an angle Θ at the peel front and R_1 is the radius of curvature at the onset of plastic yielding, i.e.

$$k_0 = \frac{R_0}{R_1}$$

$$R_1 = \frac{h}{2\varepsilon_y} \qquad 5\text{-}12$$

where h and ε_y are the thickness of the peel arm and the plastic yield strain of the peel arm material, respectively. Three cases of deformation are considered:

Case 1 which occurs when $0<k_0<1$, is purely elastic during the initial bending of the peel arms, as well as the subsequent straightening and unloading. In this case G_p is obviously equal to zero.

$$G_p = 0 \qquad \text{5-13}$$

Case 2 which occurs when $1<k_0<2(1-\alpha)/(1-2\alpha)$ or $\alpha \geq 0.5$ corresponds to plastic deformation during the initial bending but elastic deformation during unloading and straightening,

$$G_p = \frac{1}{2}(E\varepsilon_y^2 h)(1-\alpha)\left[\frac{k_0^2}{3} + \frac{2(1-\alpha)^2}{3k_0} - 1\right] \qquad \text{5-14}$$

and Case 3 which occurs when $k_0>2(1-\alpha)/(1-2\alpha)$ and $\alpha < 0.5$ involves plastic deformations during both initial bending and subsequent straightening and unloading.

$$G_p = f_1(k_0)$$

where

$$f_1(k_0) = \frac{4}{3}\alpha(1-\alpha)^2 k_0^2 + 2(1-\alpha)^2(1-2\alpha)k_0 + \frac{2(1-\alpha)}{3(1-2\alpha)k_0}[1+4(1+\alpha)^3]$$

$$-(1-\alpha)[1+4(1-\alpha)^2] \qquad \text{5-15}$$

The set of equations above can be used in the determination of G_C for a fixed arm peel test. In the case of a T-peel test, such as the case in this project, the total adhesive fracture toughness is the sum of the adhesive fracture toughness of peel arms 1 and 2, that is:

$$G_c = (G_c)_1 + (G_c)_2 \qquad \text{5-16}$$

The IC-Peel software has been developed based on the analysis above and made publicly available on the Department of Mechanical Engineering, Imperial College London, website (99). The adhesive energy release rate can be calculated from experimental stress-strain curve data of the peeling materials, the steady state peel load, the peel angle and the sample dimensions. This software was used to determine the value of G_C at steady state peel of the alkyd and acrylic gesso paints.

A similar test set up method to the uniaxial tensile tests was used for the T-peel tests. Firstly, the alkyd layer is inserted into the top grip. The grip is attached to the metal rod which is connected to

the load cell and turned sideways which allows the peel angle to be measured during the test. The load cell is lowered and the gesso arm is inserted into the bottom grip with the grip left un-tightened. The chamber door is closed and the sample is left inside until the humidity and temperature reaches the set conditions. The set up is then left for a further five minutes and an Allen key is used to tighten the bottom grip through the small drilled hole in the chamber door. The hole is then plugged with sticky putty. The T-peel test configuration is shown in Figure 5-13 where the upper arm is the blue alkyd and the lower arm is the acrylic gesso.

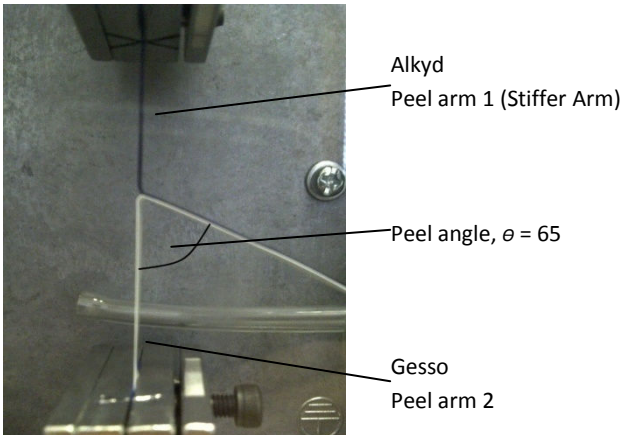

Figure 5-13, T-peel test configuration

The effects of speed and temperature on the fracture toughness of the interface were studied. Firstly, the test is performed at crosshead speeds of 0.5, 5 and 50 mm/min at 25°C, 50 %RH for 300 days old samples. The load versus displacement plots are shown in Figure 5-14a. Error bars are shown for the result at 5mm/min. It can be seen that the steady state peel force is higher under faster loading rate. Five repeats of successful peel tests were performed for each test speed, however, consistent failure of the gesso arm prior to interfacial failure occurred in nearly all samples for the test at 0.5 mm/min; only 1 sample out of 20 samples tested successfully peeled. The number of successful peel tests increased significantly at the higher rates: 5 out of 12 and 6 out of 10 successful peel tests at 5 mm/min and 50 mm/min, respectively.

Figure 5-14b shows the effect of temperature from tests at 5mm/min, 50%RH and 250 days old samples where the peel force increases with decreasing temperature. At least three repeats were conducted at each temperature however at the lower temperatures, the test success rate was found to decrease. Tests at 15°C were also performed but it was found that the gesso arm failed before peeling occurred in all samples.

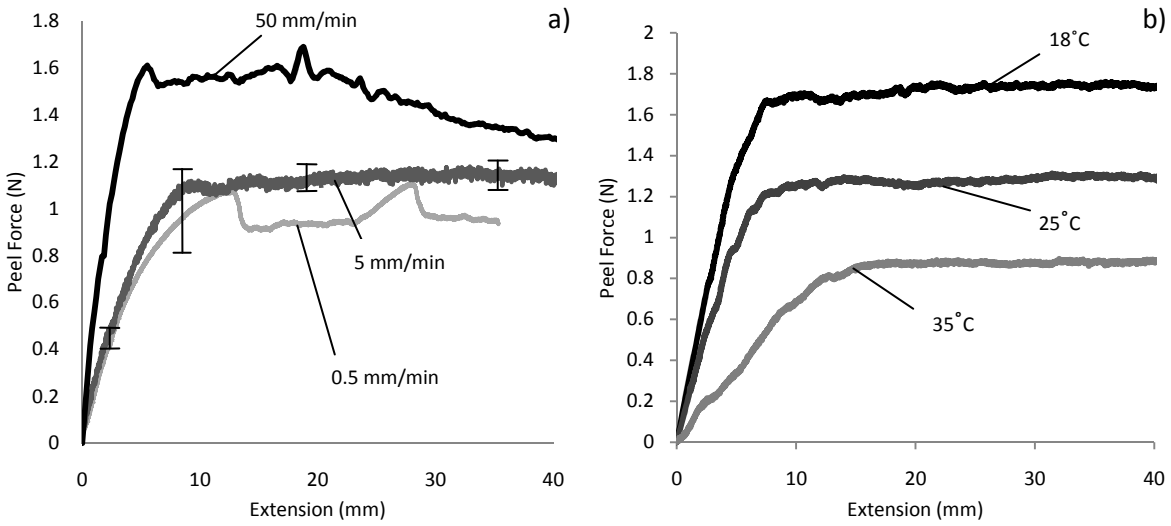

Figure 5-14, T-peel test a) effect of displacement speed of 300 days old samples at 25°C, 50%RH ; b) effect of temperature of 250 days old samples at 50%RH.

After the tests, the peeled surface of the acrylic gesso layer from the sample used in Figure 5-14b was examined. Figure 5-15 shows the blue colour remaining on the gesso surface which suggested that the peeling occurs cohesively in the alkyd layer. It can also be observed that the amount of blue pigment residue varied with the test temperature, the higher the test temperature the higher amount of the alkyd residue.

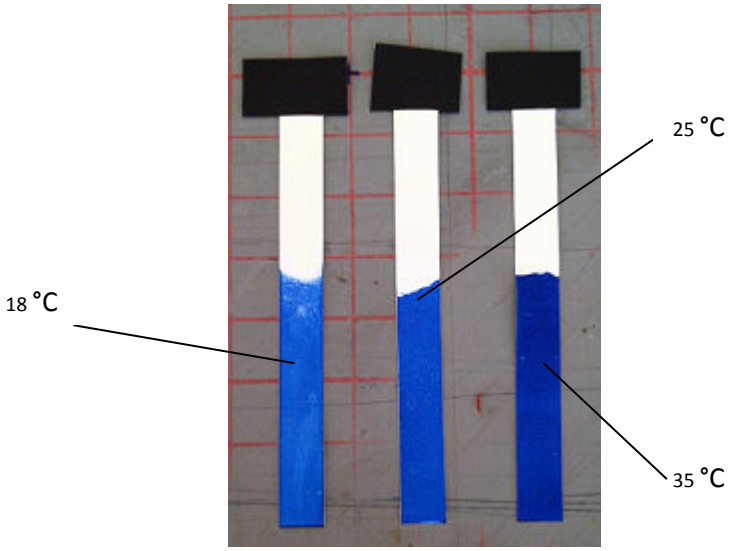

Figure 5-15, delamination surface of acrylic gesso from the 250 days old peel test samples tested at 50%RH at different temperatures.

The adhesive fracture toughness, G_C, was determined using the test results as a function of peel rate. The procedure is outlined for the 25°C, 50% RH at 0.5, 5 and 50 mm/min shown in Figure 5-14a. The ICPeel software version that was used for the calculations requires that the stress-strain curves of the peel arms are approximated by a bi-linear law representing linear elastic, work hardening behaviour. The bilinear approximations of the stress strain curves of alkyd at 25°C, 50% RH at 0.5, 5 and 50 mm/min displacement rate (0.0167, 0.167 and 1.67min^{-1} strain rate) are shown in Figure 5-16a, Figure 5-16c and Figure 5-16e, respectively, where as the corresponding approximations for the gesso are shown in Figure 5-16b, Figure 5-16d and Figure 5-16f. The curves were calculated analytically using the calibrated material models with the parameters shown in Table 5-1 and Table 5-2. Table 5-3 summarises the input parameters used in the calculation of G_C which was found to be equal to 250 N/m, 256 N/m and 264 N/m for speeds 0.5, 5 and 50 mm/min, respectively. It is worth mentioning that although, from Table 5-4 the gesso has higher initial shear stiffness than the alkyd, the peel angle of the Gesso arm, shown in Figure 5-13, is still larger due to the fact that the alkyd layer is approximately two times thicker and the stiffness of a peel arm is proportional to the flexural rigidity (EI) where E is the Young's modulus of the peel arm material and I is the second moment of area for rectangular specimens given by:

$$I = \frac{bh^3}{12} \qquad 5\text{-}17$$

where *h* is the thickness of the peel arm and *b* is the width. Therefore, flexural rigidity will be proportional to (Eh^3) for the peel arms.

Case 3 for the determination of G_p, explained in (75), was found to correspond to the experimental data (i.e. plastic deformation during initial bending and subsequent straightening and unloading). The detailed results are shown in Table 5-4. It is observed that the correction due to plastic bending effects is less than 50%. In addition, the peel rate does not lead to a significant effect on the G_C values.

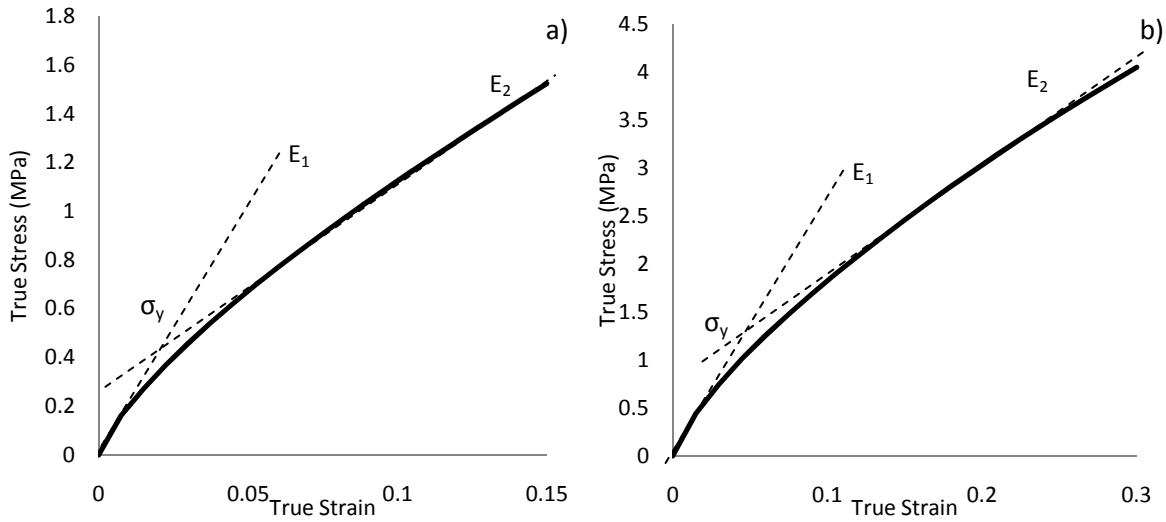

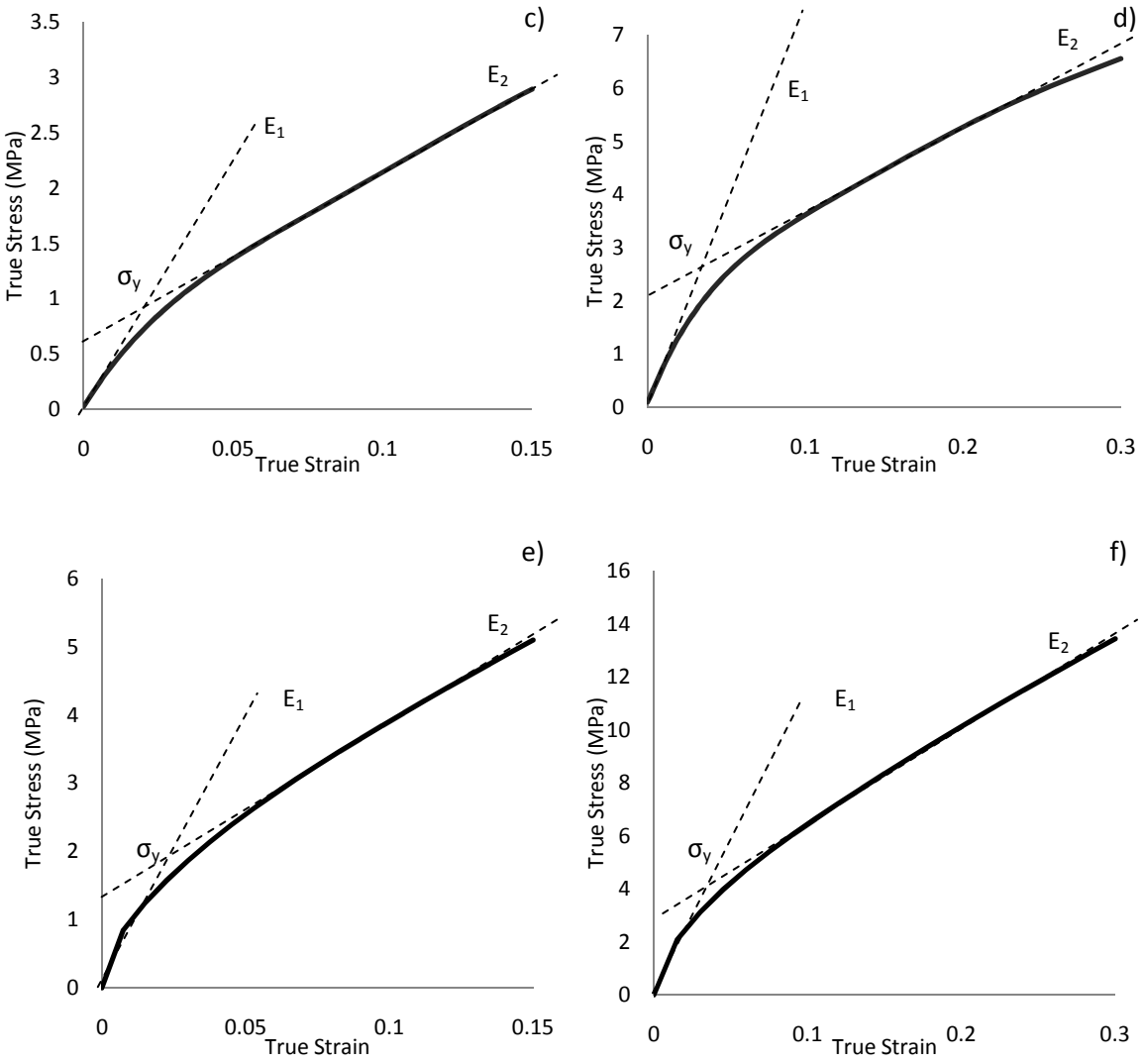

Figure 5-16, bilinear law fitting of stress strain curves at 25˚C and 50% RH of a) 300 day-old Griffin phthalo alkyd at 0.0167 min^{-1} strain rate, b) 300 day-old Golden acrylic gesso at 0.0167 min^{-1} strain rate, c) 300 day-old Griffin phthalo alkyd at 0.167 min^{-1} strain rate, d) 300 day-old Golden acrylic gesso at 0.167 min^{-1} strain rate, e) 300 day-old Griffin phthalo alkyd at 1.67 min^{-1} strain rate, f) 300 day-old Golden acrylic gesso at 1.67 min^{-1} strain rate.

Table 5-3, parameters for adhesive fracture toughness calculation.

Parameter	5mm/min		0.5mm/min		50mm/min	
	Gesso	Alkyd	Gesso	Alkyd	Gesso	Alkyd
Peel force (N)	1.14	1.14	0.94	0.94	1.4	1.4
Peel angle (°)	115	65	115	65	115	65
Thickness (mm)	0.11	0.2	0.11	0.2	0.17	0.22
Width (mm)	5	5	5	5	5	5
$\alpha\,(E_2/E_1)$	0.202	0.28	0.31	0.5	0.11	0.26
E_1 (GPa)	0.09	0.05	0.026	0.014	0.15	0.09
σ_y (MPa)	2.6	1	2.05	0.85	7.6	1.75

Table 5-4, values of G_C determined from peel tests.

	5 mm/min		0.5 mm/min		50 mm/min	
	Gesso	Alkyd	Gesso	Alkyd	Gesso	Alkyd
Corrected input energy, G (N/m)	325	130	276	112	375	152
Plastic bending energy, G_p (N/m)	155	50	106	33	192	74
Adhesive fracture energy, G_C (N/m)	170	80	173	83	185	79
Total adhesive fracture energy (N/m)	250		256		264	

The manual bilinear approach raises the issue whether errors in the material parameters shown in Table 5-3, could affect the accuracy of the calculation of G_C. Therefore, a parametric study on the effect of the chosen bilinear parameters on the calculated adhesive fracture toughness was conducted. Analytical calculations were performed whereby the elastic modulus, E_1, yield stress, σ_y, and bilinear ratio, α, of the peel arms were varied between 50% to 150% from the values shown in Table 5-3 and the corresponding adhesive fracture toughness, G_C, values were calculated. Figure 5-17, Figure 5-18 and Figure 5-19 shows the dependence of G_C on the elastic modulus, E_1, the yield stress, σ_y, and the work hardening parameter α, respectively. The data corresponding to the values in Table 5-3 are shown on each plot as a large data point at the middle of each curve. It can be seen that the inclining and declining trends in the adhesive fracture toughness, G_C, are within ±10% in all cases. However, for this small variation to occur the fitting error has to be large; hence the adhesive

fracture toughness is considered relatively insensitive to possible errors in these material parameters.

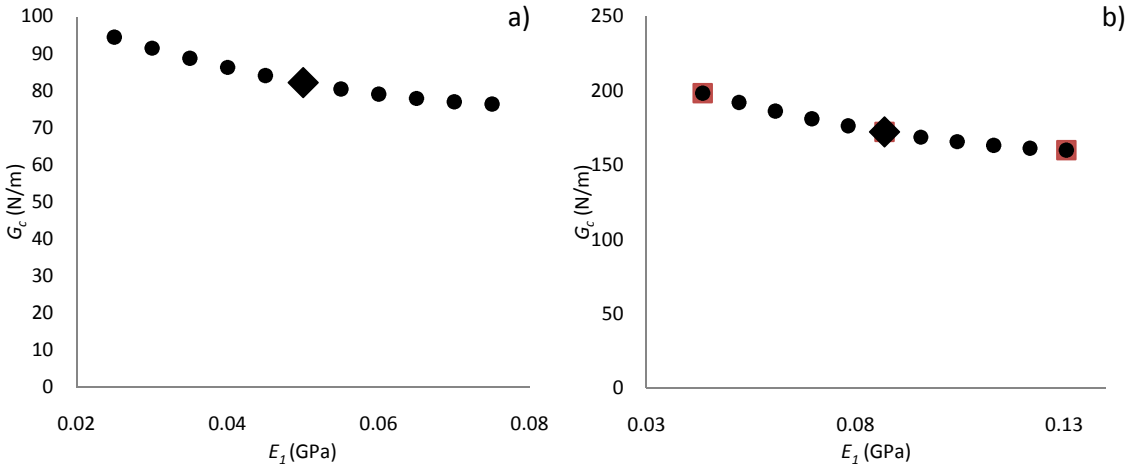

Figure 5-17, G_C dependence on the elastic modulus, E_1; a) for the alkyd peel arm, b) for the gesso peel arm

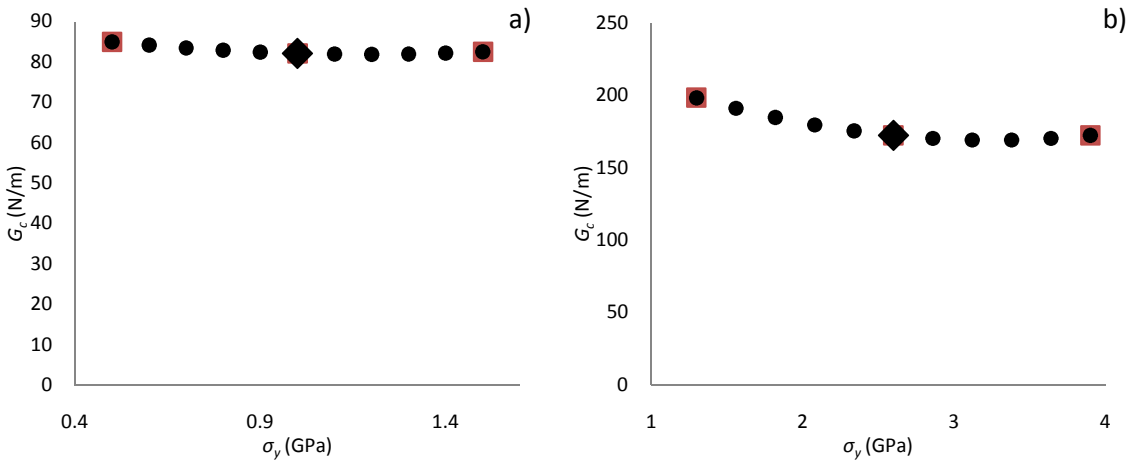

Figure 5-18, G_C dependence on the yield stress, $\sigma_.$; a) for the alkyd peel arm, b) for the gesso peel arm

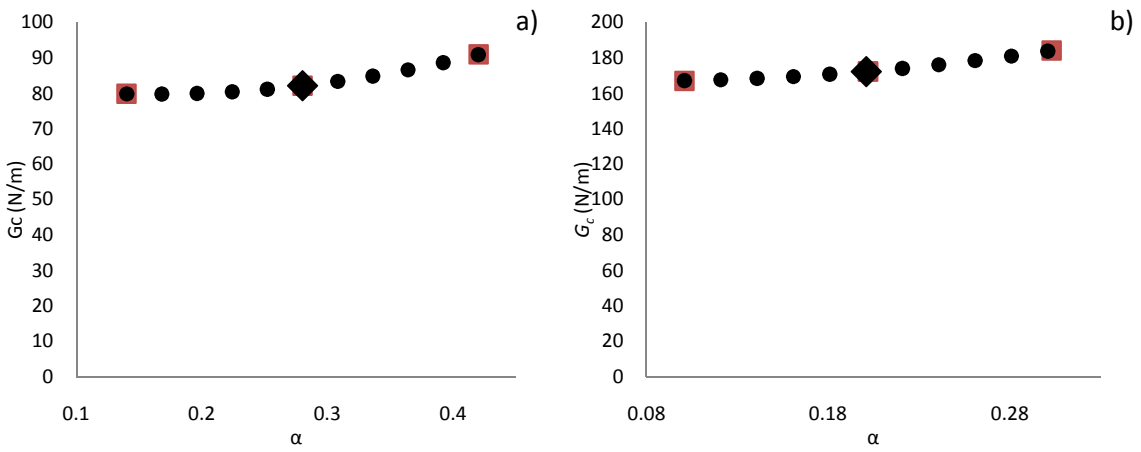

Figure 5-19, G_C dependence on the work hardening parameter, *α;* a) for the alkyd peel arm, b) for the gesso peel arm

5.6 Experimental attempts on mode II fracture and environmental fatigue delamination.

In an attempt to determine experimentally the G_C value for mode II loading several experiments were performed. Firstly, efforts to separate the two paint layers in well bonded samples, to make specimens for delamination tests were performed. A razor blade was used to make notches perpendicular to the pulling direction in the top (blue acrylic) layer without cutting into the bottom white layer as shown in Figure 5-20. The specimen was then tested in tension as shown; however, delamination did not occur. Instead, the failure mode was a fast fracture crack through the Gesso layer.

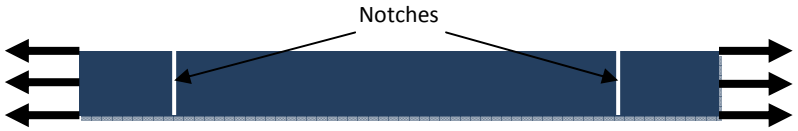

Figure 5-20, location of the notches perpendicular to the pulling direction in the top (blue acrylic) layer

The second attempt involved using a initially delaminated 3 year-old sample as shown in Figure 5-21. In order to reduce the chance of the gesso layer breaking prior to the delamination, the polyester sheet that was used as a base during the sample preperation stage was left attached to the back of the gesso. Furthermore, to increase the possibility of a delamination, a lower ambient temperature

at 4°C was used in the tests. This sample was loaded in the same test configuration as the previous sample. The load-displacement curves from the test are shown in Figure 5-22.

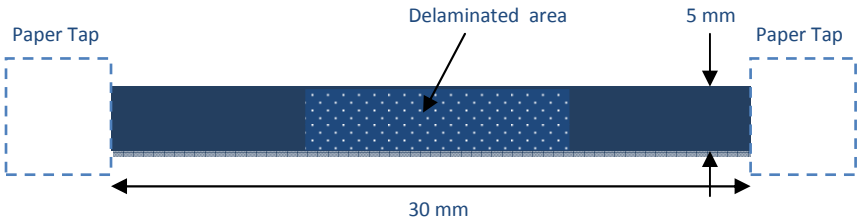

Figure 5-21, sample for mode II fracture toughness determination experiment with initial delamination.

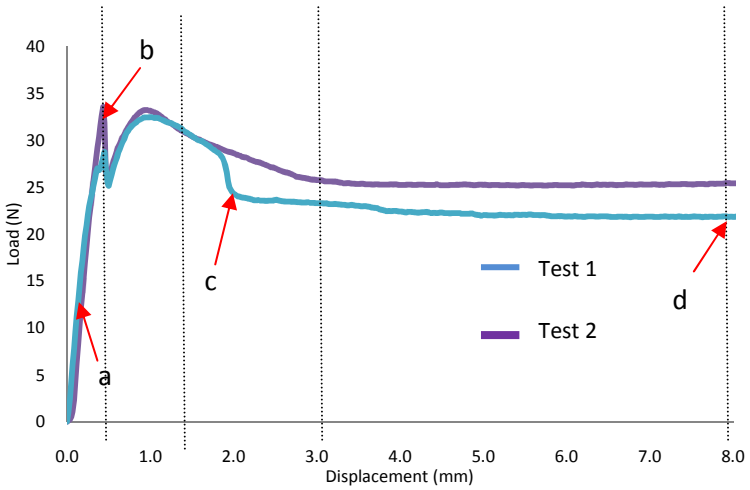

Figure 5-22, load-displacement curve of delaminated cracked sample under uniaxial tensile loading. Test at 4°C degree, RH=50%, 5mm/min; a = elastic deformation, b = crack propagation in blue alkyd layer, c = possible plastic deformation in the gesso, d = crack in white gesso

After the test there was no sign of a further delamination from the initial one in the sample. However, the sample behaviours during each state of the load-displacement curve was determine by synchronising the load-displacement curve to the video recording of the test. The labels a,b,c and d identify the regions of the curve corresponding to the images shown in Figure 5-23.

From Figure 5-22, the load-displacement curve shows several distinct regions. First the specimen is stretched elastically as in Figure 5-23a. Secondly, In Figure 5-23b, a crack through the alkyd layer occurs where a sudden drop in load magnitude can be observed. The load increases again after the

crack has run through the width of the specimen. Subsequently, in Figure 5-23c, yielding occurs in the bottom gesso layer and the load is gradually drops. Finally, after yielding, plastic deformation of the gesso occurs until the specimen breaks at the end of the test, Figure 5-23d.

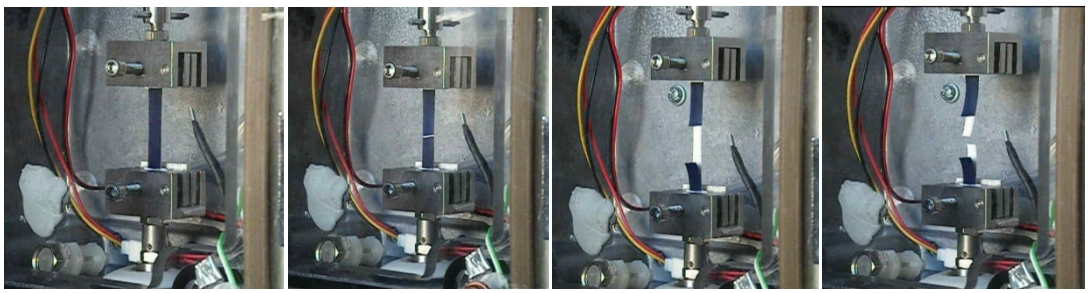

(a) (b) (c) (d)

Figure 5-23, behaviour of the initially delamination sample during loading; a = elastic deformation, b = crack propagation in blue alkyd layer, c = possible plastic deformation in the gesso, d = crack in white gesso

The final attempt was performed using the crack lap shear specimen geometry from (102) shown in Figure 5-23. where the top layer is the alkyd and the bottom layer is the gesso left attached to the polyester film for support and to avoid excessive tensile deformation. However, these test were also not successful due to the bottom layer breaking consistently before the delamination occurred, similarly to all the previous test.

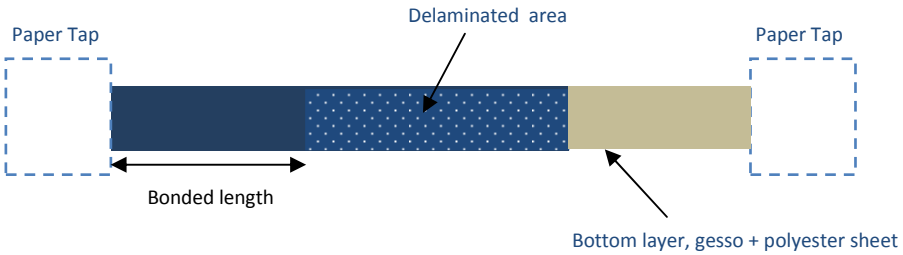

Figure 5-24, crack lap shear specimen

As delamination in paintings in museums takes decades of years to develop and performing mechanical tests on the actual painting is not possible, attempts were made to accelerate fatigue delamination in paint samples. Firstly, alkyd on gesso samples without pre-cracks were placed inside

a temperature-humidity controlled chamber with cyclic humidity conditions set as shown in Table 5-5 below.

Table 5-5, environmental condition of the accelerated fatigue delamination experiment

Low humidity condition Temperature = 45°C (Black panel temperature = 65°C) RH = 20% Light intensity = 0 W/m^2 Cycle time = 84 Hours
High humidity condition Temperature = 45°C (Black panel temperature = 65°C) RH = 70% Light intensity = 55 W/m^2 Cycle time = 84 Hours

The samples were left in the chamber for 6 weeks and were taken out for an examination. By observing with the naked eye, there was no sign of delamination however it was found the samples became stiffer than the unconditioned ones.

Later, the peel test samples were used instead of the un-precracked samples. To make the condition more severe, a weight of 20 grams was attached to the gesso layer of each sample and the samples were attached vertically. The same environmental conditions in the chamber were used but the cycle time was reduced to 12 hours per cycle. This test was however also unsuccessful after several attempts. This was mainly due to the chamber failing to continuously maintain the desired test condition and breaking down before the designed test period was reached. Also it is found that the gesso layer of several samples occasionally broke and some samples fell off the hanger due to the weight and air blowing inside the chamber.

In conclusion, the sample preparation method has been outlined in this chapter. The tensile behaviour of acrylic gesso and blue phthalo alkyd have been studied where the effects of age, temperature and speed were investigated. The results from the uniaxial tensile tests and the relaxation test have been used to calibrate the hyper-viscoelastic model for the acrylic gesso and the

blue alkyd. The peel test method and the analytical solution for the adhesive fracture toughness, G_C, have been presented. The fracture toughness at the interface of the gesso and alkyd has been evaluated using the T-peel test. The steady state peel force and peel angle were used in conjunction with the tensile stress-strain data of section 5.2 in the IC-Peel software to calculate the adhesive fracture toughness. Parametric studies for the bilinear law material parameters have been carried out as a validation of the calculated G_C. The results from this chapter will be used in a numerical model for the prediction of delamination under environment fatigue in chapter 7. Attempts have been made to determine experimentally the G_C value for mode II and to replicate the fatigue delamination under environment cycling condition however, thus far, both still unsuccessful.

6. Finite element techniques for environmental fatigue crack growth simulation

The development of the finite element model for simulating environmental fatigue crack growth is outlined in this chapter. The goal of the FE study is to build a life prediction model for thin multilayer polymeric coatings under mechanical and environmental cyclic loading. The options for fracture mechanics analysis in the commercial finite element software Abaqus were studied to assess their potential to analyse the fatigue problem in a multilayered material. The analysis techniques which were investigated include thermal and hygrothermal stress applications, viscoelastic and hyperelastic material analysis, J-contour integral, virtual crack closure method, cohesive zone model, the direct cyclic method and the irreversible cohesive zone model.

Seven test cases were designed in order to study capabilities in the Abaqus software which are relevant to this work. The first test case is a thermal expansion simulation of a linear elastic thin film specimen; this is presented in section 6.1. The second test case, discussed in section 6.2, is a uniaxial tensile test simulation of a hyperviscoelastic specimen using a single-element model. The third test case, presented in section 6.3, combines the simulation techniques from the first and second test case in the modelling of the hygrothermal expansion of a thin film of a hyperelastic material. Section 6.4 provides a discussion on crack initiation modelling using Abaqus' J-contour integral and the virtual crack closure technique, VCCT, which was introduced by Rybicki (88). A thin film on a rigid substrate and a single edge notched bend, SENB, geometry were selected in comparison tests between the two techniques and analytical solutions. Three material models were used including, linear elastic, elastic plastic and hyperviscoelastic. Techniques for crack propagation analysis are discussed in section 6.5. The SENB geometry and the linear elastic material model from section 6.4 were used in the study of crack propagation modelling using the "Debond" technique with the VCCT failure criterion. In the same section, a description and a parametric study of the cohesive zone

modelling technique are also presented. Cohesive contact and cohesive element techniques are both investigated. The discussion then moves on to the fatigue crack propagation simulation where section 6.6 presents the method of applying cyclic loading amplitude in Abaqus. The importance of a small time increment size is also addressed in this section. Finally, section 6.7 outlines the fatigue crack propagation modelling using Abaqus's direct cyclic method and the irreversible cohesive zone model using a thin film on a substrate model is discussed.

6.1 Thermal stress analysis

In Abaqus, temperature is one of the degrees of freedom in continuum elements. Firstly, an initial temperature is assigned to each node of the model and then the final temperature is specified by using the *temperature command. This study uses the film geometry model shown in Figure 6-1 with plane strain elements. The material properties of the film shown in Table 6-1 are of a typical brittle linear elastic polymer. To simulate the film being attached to a rigid substrate, all the nodes at the bottom of the film are constrained from moving in any direction. The temperature of the model was initially set at 21°C and was assigned to ramp up to the final temperature at 320°C. Several models with different mesh density were created using the plane strain element for a mesh convergence study.

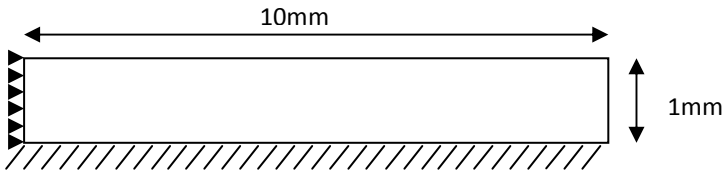

Figure 6-1, film on a rigid substrate model

Table 6-1, material properties of a linear elastic polymer for thermal stress analysis of a thin film on a substrate

Thermal Expansion Coefficient ($C^{\circ -1}$),	6.3×10^{-6}
Young's Modulus (MPa), *E*	20.7
Poison's Ratio, *v*	0.29

The contour plot of the stresses along the x-axis (S_{11}) is shown in Figure 6-2. S_{11} at the node at the middle of the top surface is plotted in Figure 6-3 as a function of temperature. The convergence study is shown in Figure 6-4 where the stresses at the maximum temperature (320°C) for every mesh density are plotted. The stress from the 80x8 mesh density model from Figure 6-4 at the maximum temperature was compared with the analytical solution, equations 4-1 and 4-2, in Table 6-2.

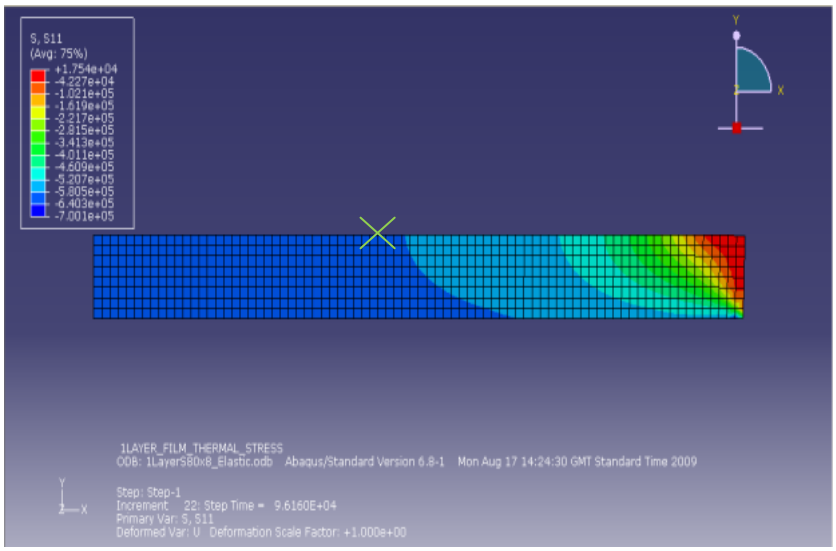

Figure 6-2, contour plot of stress in horizontal direction (σ_{11}), unit = Pa

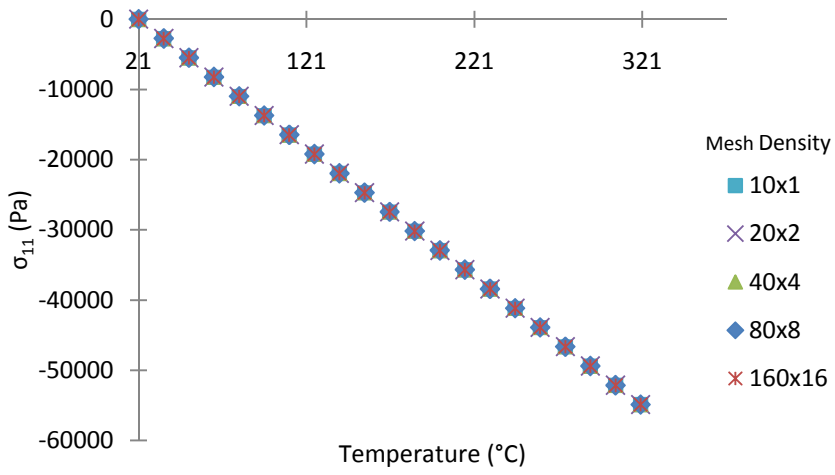

Figure 6-3, stress in longitudinal (σ_{11}) direction at the middle of the top surface of different mesh density models versus time

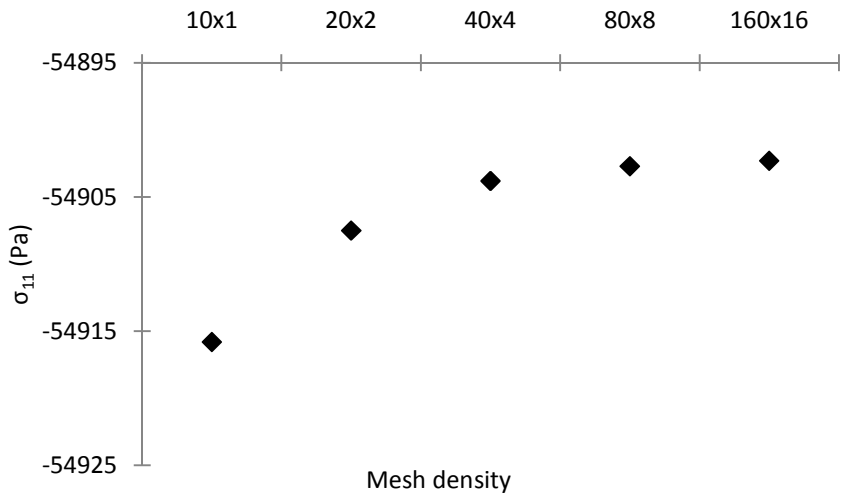

Figure 6-4, σ_{11} at the middle of the top surface at 320°C temperature versus Mesh Density

Table 6-2, stress at the middle of the top surface at the maximum temperature (320°C)

Model	σ_{11} at top Surface (Pa)	Analytical (Pa)	Percentage Different
80x8 Elements	-54907.5	-54912	0.008%

It can be seen from Figure 6-3 and Figure 6-4 that convergence is obtained with 80x8 elements. Nevertheless, the models with lower mesh density can also provide accurate results; at the maximum temperature the results are less than 0.04% different from the finer mesh model results. Also, from Table 6-2, the stress predicted from the numerical method is close to the analytical solution with the value from the FE model only 0.008% different from the analytical model. This thermal stress simulation capability will also be used in the fracture mechanics analysis in the later part of this chapter. It is worth mentioning that the same thermal stress analysis technique can also be applied to a hygrothermal stress problem in Abaqus, since the constitutive equations of both cases are written in the same manner.

6.2 Uniaxial tensile test simulation of a hyperelastic material model

A single-element, tensile test model, Figure 6-5, was used to investigate Abaqus' capability in simulating a time dependent hyperelastic material behaviour. The Prony Series and hyperelastic

parameters of Latex paint with 0% TiO_2 at 20°C under 5mm/minutes tension from Table 6-3 and Table 6-4 were used in the study. The Prony-Ogden model, equations 3-26 and 3-45, was used as the analytical solution to verify the FE result. The element has the dimensions of 3mm x 20mm. It was designed to have half the dimensions of the tensile specimen used in (11) in both vertical and horizontal directions. Half the loading speed (2.5mm/min) was used at the top surface and symmetry boundary conditions were specified on the left and bottom side of the element. After the analysis, stress-strain curves from the experiment by Hagan (11), analytical solution and FE analysis, were plotted together in Figure 6-6.

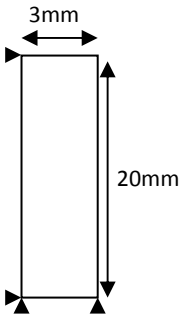

Figure 6-5, one element uniaxial tensile test model

Table 6-3, Prony series parameters for Ogden/Prony series models of latex paint. (11)

Element, I	Relaxation Time (log τ_i),	g_i
1	2.00E-06	0.095447
2	2.00E-05	0.177229
3	2.00E-04	0.236168
4	2.00E-03	0.225850
5	2.00E-02	0.155001
6	2.00E-01	0.076341
7	2.00E+00	0.026984
8	2.00E+01	0.004110
9	2.00E+02	0.001510
10	2.00E+03	0.000359
11	2.00E+04	0.000359
Equilibrium, e	-	0.000642

Table 6-4, hyperelastic parameters for the Prony series model. (11)

μ_o (MPa)	α
581	-5.70

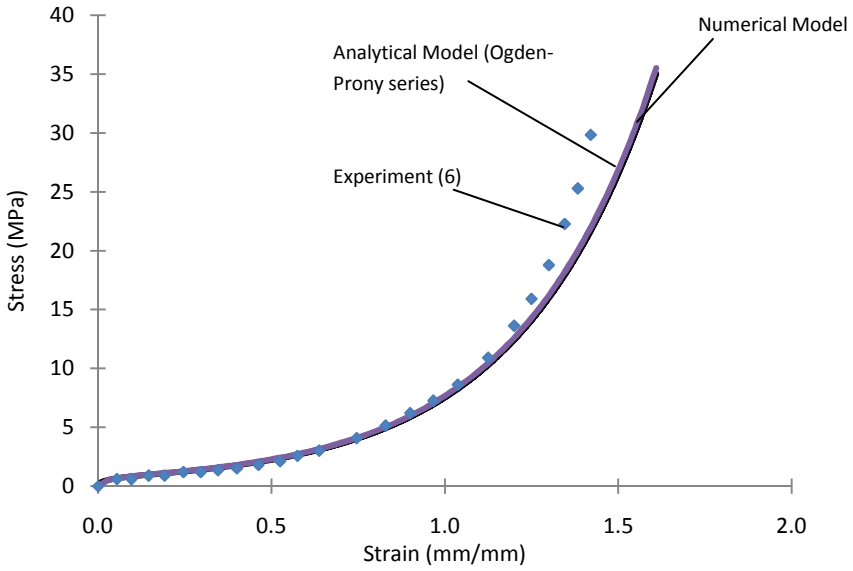

Figure 6-6, stress-strain curve for Latex with 0%TiO_2 at 20˚C and 5mm/min loading.

It can be seen that the stress-strain curve from the FE analysis exactly matches the analytical solution. Both results show very good agreement with the experimental results from Hagan's work, (11), at small and medium deformation up to approximately 120 percent strain. The discrepancy towards the final region of the curve could be due to the fact that the Ogden model only uses two parameters which are not enough to model the large deformation.

6.3 Hygrothermal stress simulation of film model

Aside from the temperature variation, humidity change can also cause expansion in paints. The relationship between hygrothermal (swelling) strain and humidity is known to have the same characteristic as that between thermal strain and temperature. This experiment employs the simulation technique for thermal stress analysis into a hygrothermal stress analysis problem. The material properties of the visco-hyperelastic material, Table 6-3 and Table 6-4, were used in this model.

The hygrothermal strain of paints was defined by using the hygrothermal expansion coefficient (β) which is taken from Hagan's work (35), shown in Figure 6-7. The coefficient was obtained from

experiments where a gesso paint film was clamped in the grips of a tensometer within a sealed chamber containing silica gel. Changing the mixing ratio between wet and dry silica gel enables the control of the relative humidity inside the chamber. The expansion of the paint film was measured as the RH is increased. The effective expansion coefficient, β, calculated from the slope of the strain versus RH plot.

Humidity was assigned to rise from 0 %RH to 65 %RH which is within the range of β_1, shown in Figure 6-7. The FE model is the same as the one used in section 6.1. After the analysis, the stress in the parallel direction to the film (σ_{11}) at the same middle position of the top film surface as shown in Figure 6-2, was plotted against humidity in Figure 6-8. Different mesh density models were created and the stresses at the maximum %RH of each model were plotted for a convergence test in Figure 6-9.

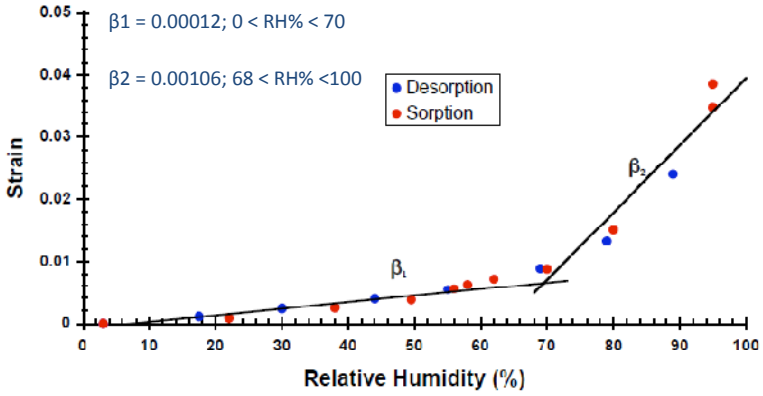

Figure 6-7, hygrothermal strains for the Golden TiO2 emulsion paint at 23°C (35).

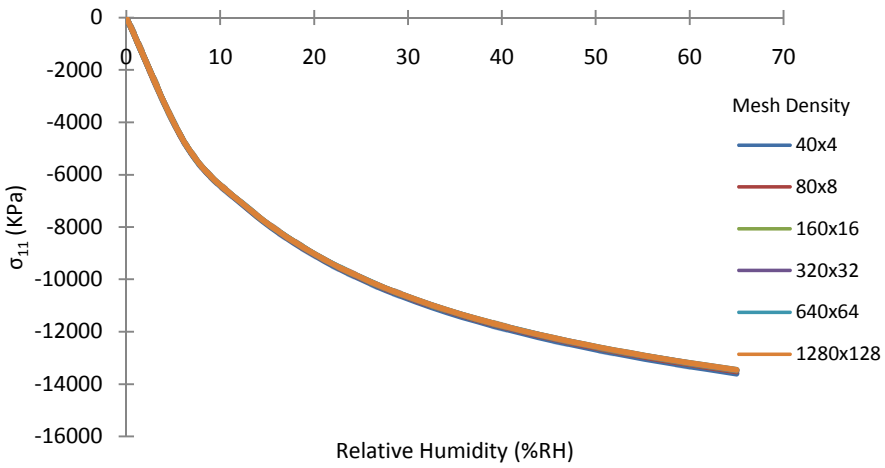

Figure 6-8, stress in longitudinal (σ_{11}) direction at the middle of the top surface versus Relative Humidity (%RH) for different mesh density models.

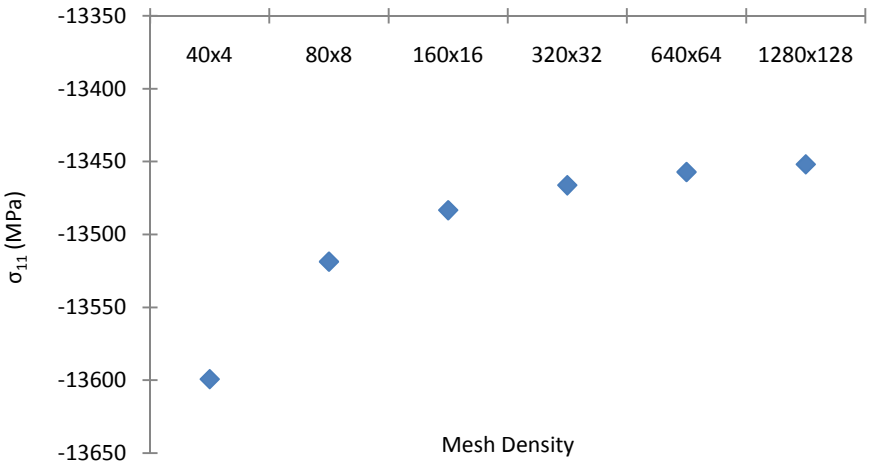

Figure 6-9, σ_{11} at the middle of the top surface at 65 %RH humidity versus mesh density (Convergence Test)

It can be seen from Figure 6-9 that convergence is reached with a 640 x 64 mesh density. However, the difference between the results from the lowest and the highest mesh density is only within 1.1%.

Therefore, so far it is established that ABAQUS can be used to calculate the hygrothermal expansion behaviour of time-dependent hyperelastic materials. In addition, the experiments also show that a low mesh density model can be used in the analysis of a relatively simple geometry, such as a film on a substrate, with the result from a low mesh density model being within a 2% difference from the higher mesh density models.

6.4 Crack initiation analysis: J-contour integral and Virtual Crack Closure Technique

Analysis tools for fracture mechanics are provided in ABAQUS for both crack initiation and crack propagation problems. This part of the chapter will summarise several techniques used in simulating the fracture behaviour of a hyperelastic material with time-dependent behaviour. Two specimen geometries were used in the studies. The first one is the thin film on a rigid substrate geometry shown in Figure 6-1. This geometry is used in a mesh convergence study and also in the evaluation of the agreement between J-integral and VCCT under Mode-II loading. The second geometry is the Single Edge Notched Bend (SENB), shown in Figure 6-10, which is used in the evaluation of the agreement between the J-Integral technique and the VCCT under mode-I loading and also in crack propagation studies.

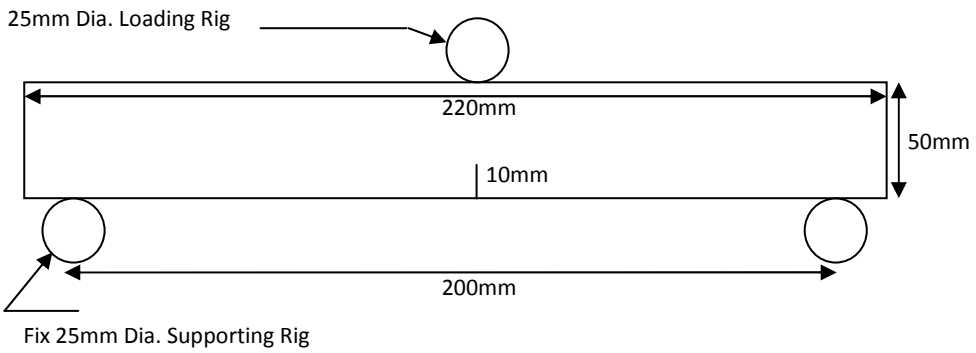

Figure 6-10, single edge notched specimen, SENB, model

6.4.1 Mode-II study: thin film on a rigid substrate geometry model

The VCCT method evaluation for Mode-II crack initiation for a linear elastic fracture mechanics, LEFM, problem was studied using the model in Figure 6-1 with the material properties shown in Table 6-5. The model was created with plane strain elements which ignores out of plane, Mode-III, fracture. Thermal loading was created by specifying the temperature of the model to rise from 70˚C to 1900˚C. Values of *G* calculated from the modified VCCT using equations 4-16 and 4-17 were compared with the values from the J-contour integral from Abaqus as well as from the analytical solution, equation 4-6. The studies were performed with both 4-node and 8-node elements.

Table 6-5, material properties of a linear elastic polymer for fracture mechanics problem of a thin film on a substrate

Thermal Expansion Coefficient ($C°^{-1}$), α	7.5×10^{-6}
Young's Modulus (MPa), E	30.0
Poison's Ratio, ν	0.3

Initially, a good agreement is observed between VCCT and the other two techniques (see Figure 6-11). However, the agreement was reduced as the mesh density of the model was increased. It was found later that the reason was due to the Δa value that was used in the calculations. During the simulation, the difference between Δa values of the element in front and the value of Δa for the element behind the crack tip is increased as the model deforms. The element deformation at the local area at the cracktip is shown in Figure 6-12, where the arrow indicates the cracktip node.

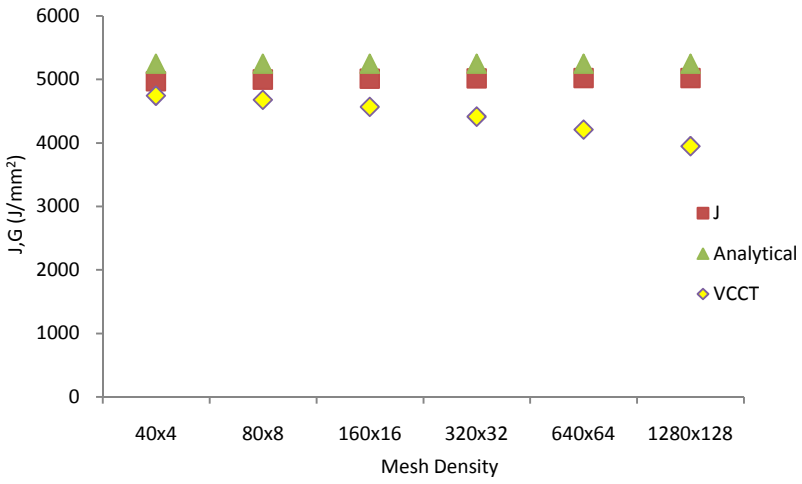

Figure 6-11, liner (4-node) elements, mesh convergence test for mode-II VCCT (G_{II}) versus J-integral (J) and analytical solution at the maximum analysis temperature (1900˚C) using Δa values from the deformed model in the calculation.

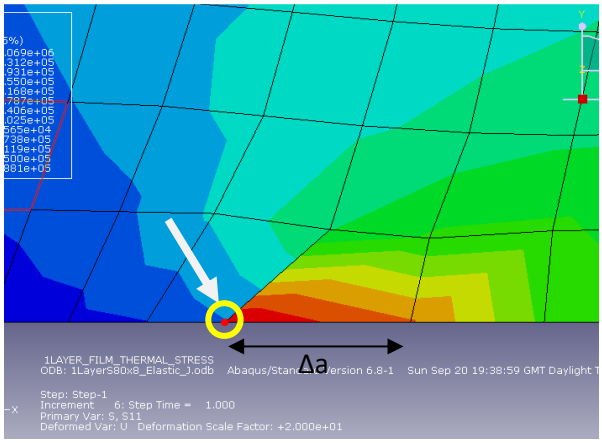

Figure 6-12, element deformation around cracktip.

The agreement of VCCT with the other two techniques for the higher element density models was improved by using the value of Δa of the undeformed element. After this modification, it is found that the differences between VCCT and the other two techniques were reduced to almost zero percent as the mesh density is increased, as shown in Figure 6-13, Figure 6-14 and Figure 6-15.

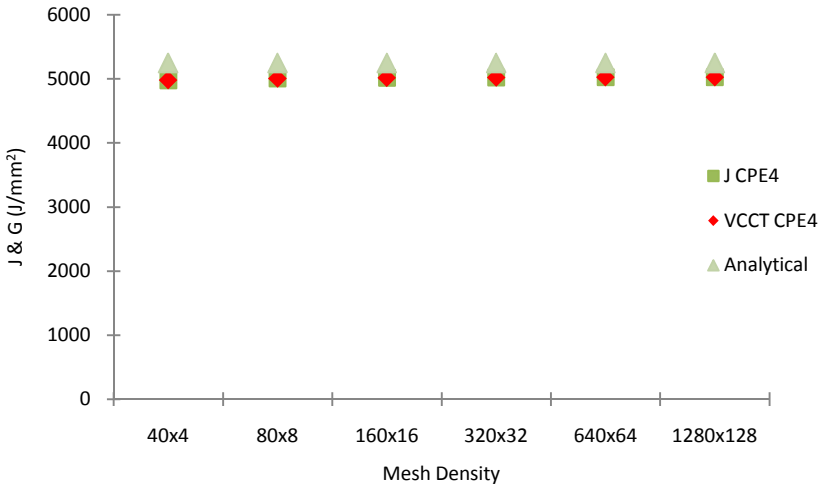

Figure 6-13, linear (4-node) elements, mesh convergence test for mode II VCCT (G_{II}) versus J-integral (J) and analytical solution at maximum analysis temperature (1900˚C)

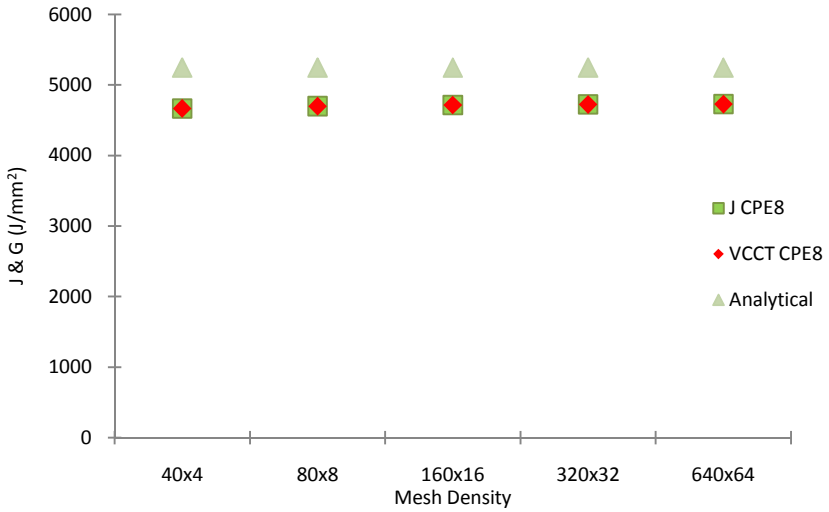

Figure 6-14, quadratic (8-node) elements, mesh convergence test for mode II VCCT (G) versus J-integral (J) and analytical solution at maximum analysis temperature (1900˚C)

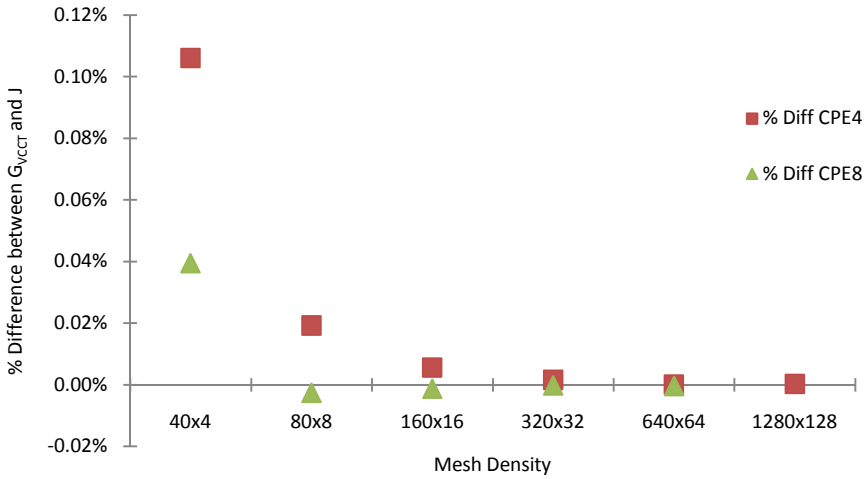

Figure 6-15, percentage differences between J-contour integral value and G-value from VCCT at maximum temperature (1900˚C), plotted versus mesh density.

Figure 6-13 and Figure 6-14 show that the energy release rates predicted by the J-contour integral method and the VCCT using the 4-node elements model are within 5% of the analytical solution and within 10% of the analytical solution when using the 8-node element model. Therefore, it is established that the J-contour integral method and the VCCT can accurately predict the energy release rate of plane strain, Mode-II crack initiation problems for a linear elastic material.

It is worth noting that, even though the agreement between the J-contour integral and the VCCT for the 8-node element model is closer than the 4-node element model for the same mesh density (see Figure 6-15), the agreement between the methods and the analytical solution for the 8-node models is lower than those of the 4-node model. This could be due to the fact that the simplified analytical solution does not include the geometry effect of the initial crack length (Δa). Therefore, the calculated G_C can be higher than the actual value which turns out to be closer to those predicted by the 4-node elements model.

6.4.2 Mode I study: SENB specimen

The standard SENB specimen, shown in Figure 6-10, was used in crack initiation studies. Two studies were performed using this geometry. The first study is the investigation of the effect of material properties on the agreement between J-contour integral and VCCT. Three material models were used which are 1) a linear elastic model (properties shown in Table 6-6), 2) an elastic plastic model (properties shown in Table 6-7) and 3) a visco-hyperelastic model (Table 6-3 and Table 6-4). The second study was the effect of time-dependence on the agreement between J-contour integral and VCCT. This effect was investigated by varying the loading speed in the model.

Table 6-6, material properties of a linear elastic polymer for SENB crack initiation modelling.

Young's Modulus (MPa), E	600
Poison's Ratio, ν	0.3

Table 6-7 input parameters for Abaqus of an elastic plastic polymer for SENB simulation

Elastic Modulus E (MPa)	v
445	0.3

Stress (MPa)	Plastic Strain
0	0
2.23	0.00000
3.57	0.00411
4.82	0.00782
5.71	0.01193
6.52	0.01561
7.23	0.01968
7.95	0.02374
8.66	0.02778
9.11	0.03140
9.64	0.03541
10.00	0.03940
10.45	0.04338
10.80	0.04695
11.16	0.05090
11.43	0.05483
12.59	0.07002
14.29	0.09030
15.45	0.10832
16.79	0.12602

In the first analysis, the values of *J* from the J-contour integral and *G* from VCCT were plotted against analysis time to observe the agreement between the two methods. The results for the linear elastic problem and the visco-hyperelastic problem at 5mm/min loading speed show very good agreement between *J* and *G*, as shown in Figure 6-16 and Figure 6-18, respectively. However, the result from the elastic plastic fracture mechanics, EPFM, analysis shows that the agreement is reduced as the plastic deformation increases, as shown in Figure 6-17. This is as expected because VCCT was originally derived for linear elastic problems, according to (88); therefore the solution may be inaccurate if plastic deformation is involved.

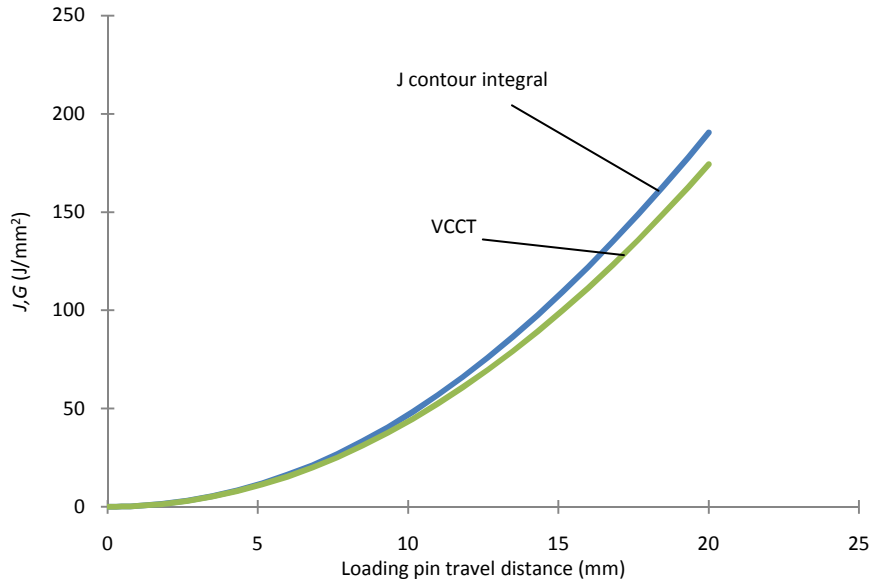

Figure 6-16, energy release rate from J-contour integral and VCCT versus loading pin travel distance in SENB model with linear elastic material.

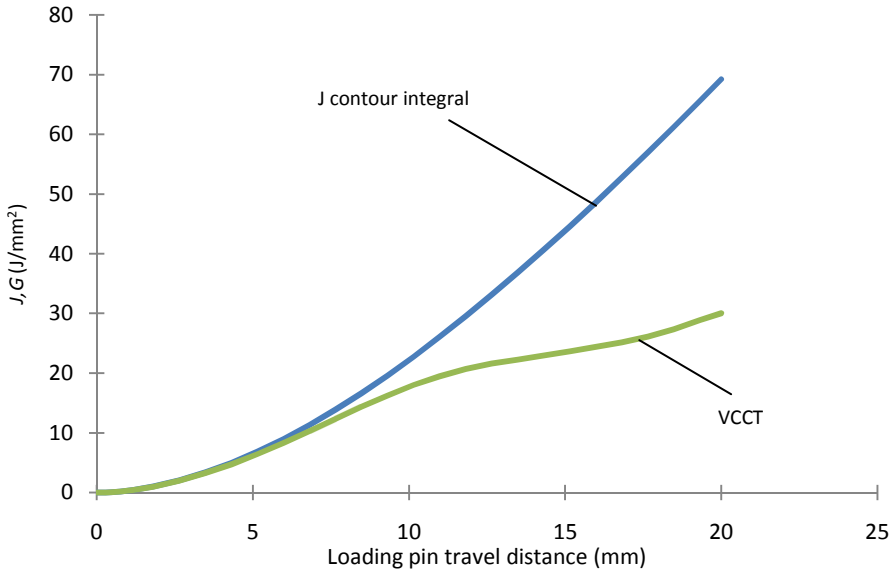

Figure 6-17, energy release rate from J-contour integral and VCCT versus loading pin travel distance in SENB model with elastic plastic material.

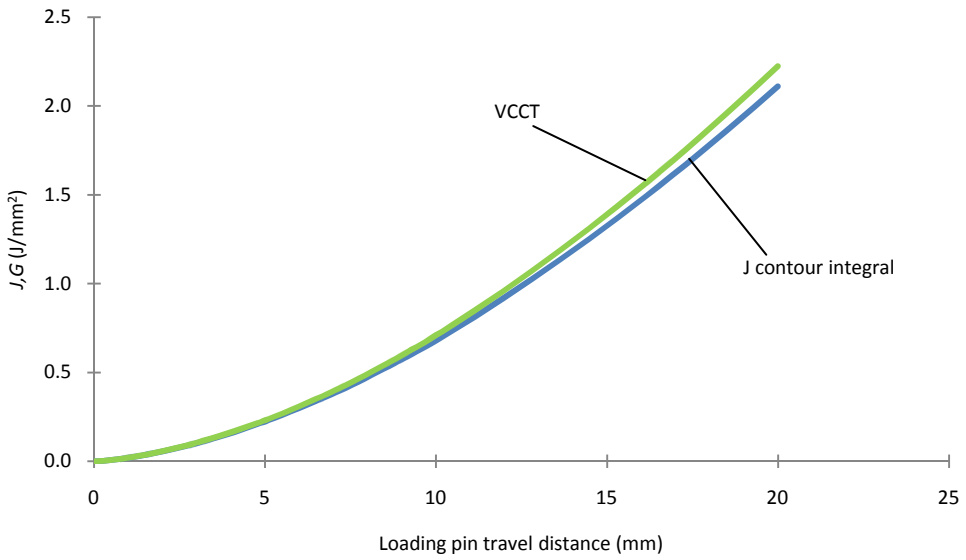

Figure 6-18, energy release rate from J-contour integral and VCCT versus loading pin travel distance in SENB model with visco-hyperelastic material at 5mm/min loading speeds.

The second analysis is the comparison between the J-contour integral and the VCCT from the analysis using a visco-hyperelastic material at different loading speeds. The energy release rates from both techniques at 0.5mm/min, 5mm/min and 50mm/min loading speed are plotted against the loading pin travel distance, shown in Figure 6-19.

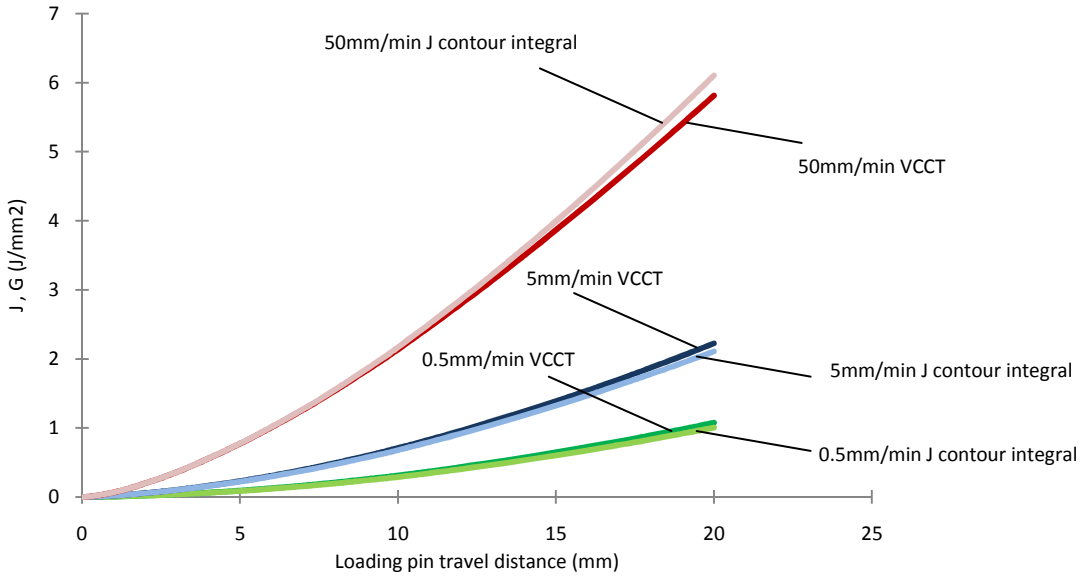

Figure 6-19, energy release rate from J-contour integral and virtual crack closure technique versus loading pin travel distance of visco-hyperelastic material in SENB test at different loading speed

The difference between the results from the two methods is less than 10%. However, the percentage difference is slightly increased as the loading speed is decreased.

From the results, it can be concluded that the J-integral and VCCT methods agree when used in the analysis of linear elastic or visco-hyperelastic materials. For the latter, there is no significant effect of the deformation rate on the agreement between the two methods.

6.5 Crack propagation analysis

So far crack initiation simulation techniques have been investigated as presented in the previous section. In the remaining parts of this chapter, simulation techniques for crack propagation problems available in Abaqus will be reviewed in order to find a suitable simulation technique(s) for the peel test and fatigue delamination in multilayered films.

6.5.1 Node releasing technique using VCCT fracture criteria

In this section, crack propagation analyses using the Node Releasing Technique with the VCCT fracture criterion in ABAQUS were conducted. The SENB geometry, shown in Figure 6-10, was used in this analysis. The J-integral value at the cracktip was plotted against analysis time and was compared with the analysis without crack propagation. The aim is to verify the accuracy of the first node releasing at the predefined G_{Ic} values in the code under the *Fracture Criteria section. Theoretically, the first node should be released exactly when the J-value equals to G_{Ic} divided by the specimen thickness, which in this case is 20mm. Analyses were conducted using three material models, linear elastic from Table 6-6, elastic plastic from Table 6-7 and hyper-viscoelastic from Table 6-3 and Table 6-4. Figure 6-20 and Figure 6-22 show the comparison of the J-contour integral values and the load-displacement data obtained from the crack propagation simulation and the model with no crack propagation using linear elastic, and visco-hyperelastic material properties respectively. The results indicate that the crack first starts to propagate at the time when the specified G_{IC} value is reached. A spike in the value of J is observed at the points where the first node is released in the

linear elastic analysis. This is assumed to be due to numerical instabilities. It should be mentioned that there is a numerical convergence problem with the hyperviscoelastic analysis too which causes the simulation to terminate if the increment time is not kept low enough i.e. lower than 1/100 of the total analysis time. Attempts to further reduce the increment time have been made however this significantly increases the analysis time. On the other hand, the comparison results from the model using elastic plastic material properties, Figure 6-21, show that the crack starts to propagate later than the time where the specified G_{IC} is reached.

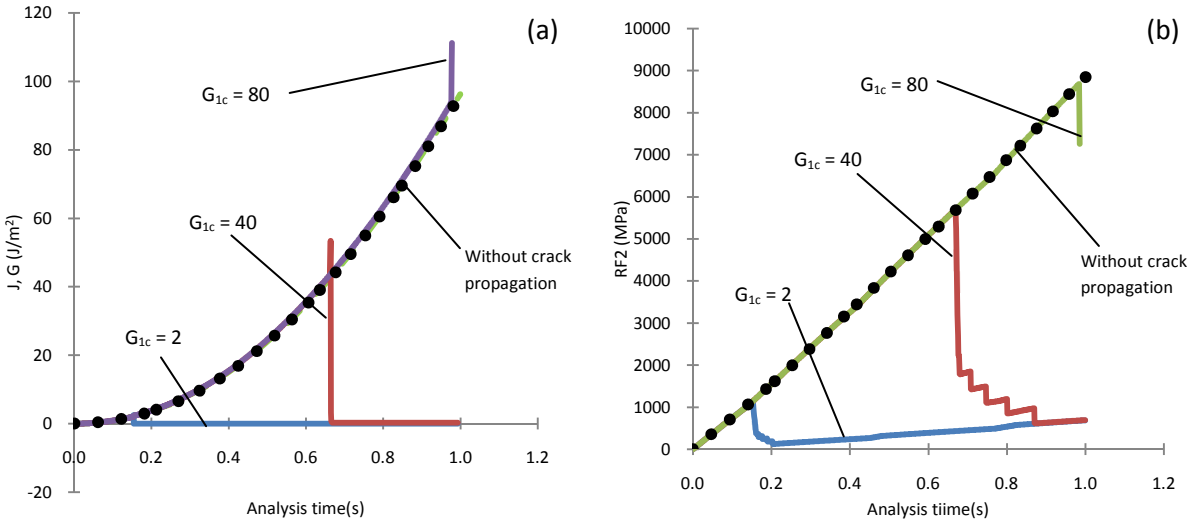

Figure 6-20, SENB simulation result for LE material, (a) J at cracktip versus analysis time, (b) Reaction force (RF2) at loading pin versus analysis time.

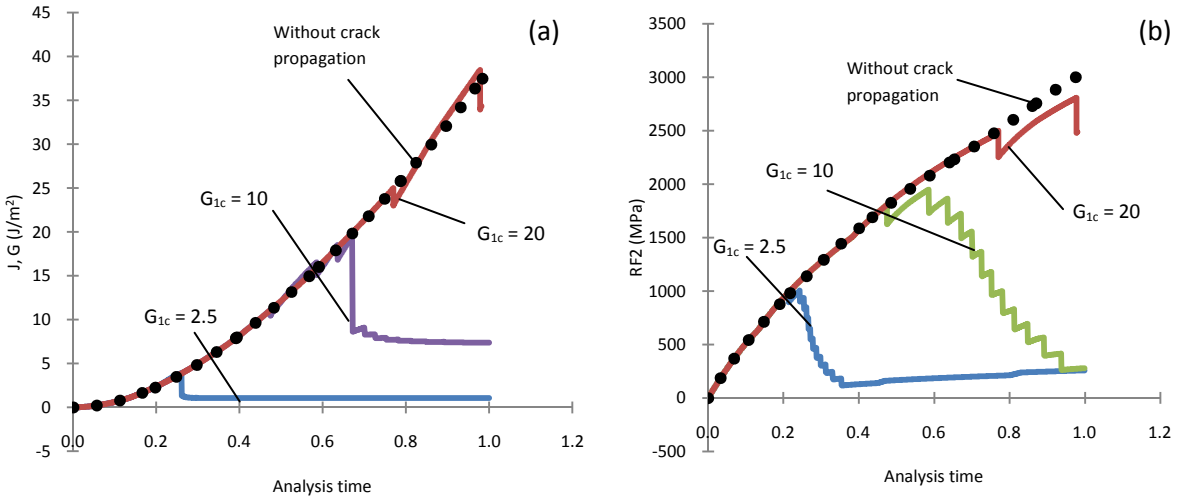

Figure 6-21, SENB simulation result for EP material, (a) J at cracktip versus analysis time, (b) Reaction force (RF2) at loading pin versus analysis time

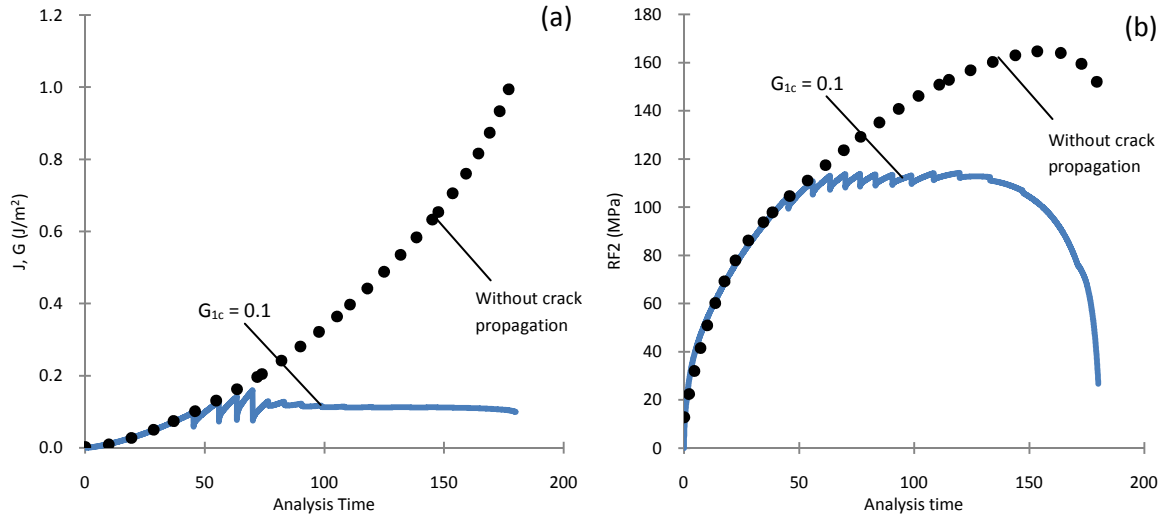

Figure 6-22, SENB simulation result for visco-hyperelastic material, (a) J at cracktip versus analysis time, (b) Reaction force (RF2) at loading pin versus analysis time

A further attempt to improve the accuracy of the hyperviscoelastic analysis by increasing the mesh density was performed. The test with the value of G_{Ic} equal to 0.1 J/mm^2 was repeated by using a mesh of 20x88 and 40x176 elements. Figure 6-23, shows the process of crack propagation during loading of the 40x176 elements and the contour plot of Mises-stress. The load-displacement curves of both mesh models are shown in Figure 6-24. It was found that the convergence study could not be taken further due to numerical problems for even higher mesh densities the model.

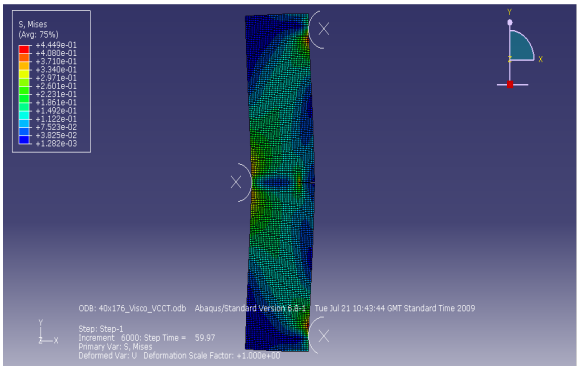

a

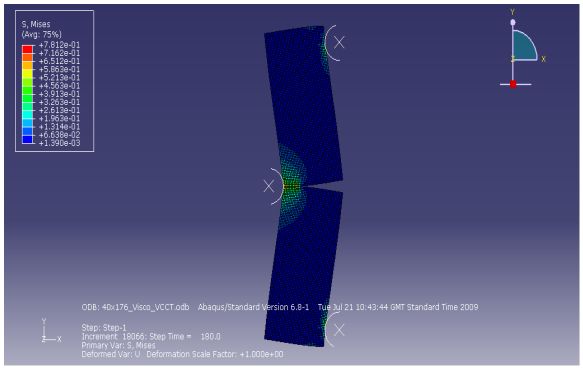

b

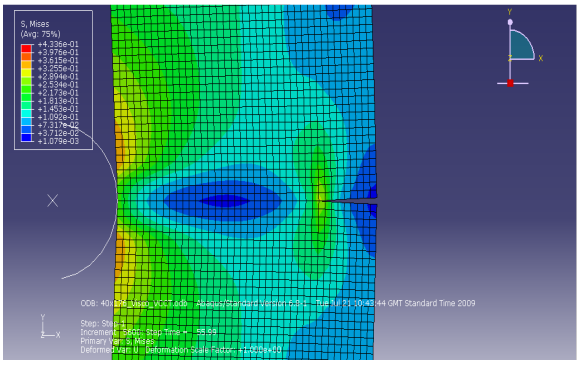

c

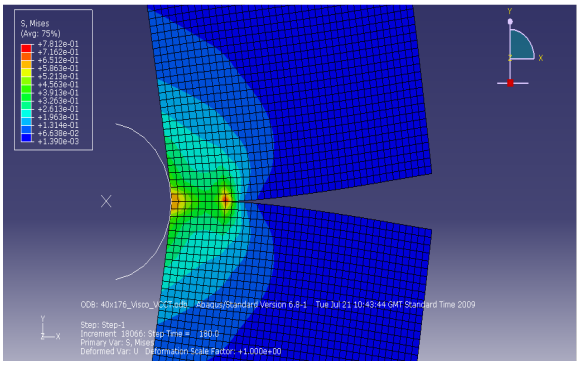

d

Figure 6-23, contour plot of three-point bending crack propagation simulation using VCCT fracture criteria, 40x176 elements, Hyper-Viscoelastic Material. a and b, screen captures of the whole model. c and d, captures of the cracktip area.

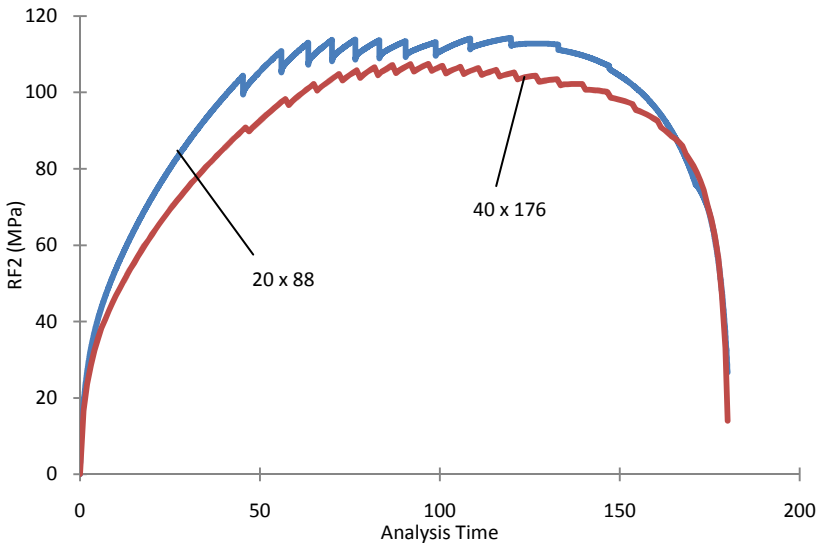

Figure 6-24, load versus displacement plot of SENB crack propagation simulation using VCCT fracture criteria, 40x176 elements, Hyper-Viscoelastic Material and G_{IC} = 0.1.

To summarise, the node releasing technique is suitable for modelling crack propagation under monotonic loading where energy release rate obtained from experiments can be used directly as a failure criterion in the model. The technique is also proven to be accurate in predicting load at the crack initiation point. However, it is shown that convergence problem can occur in the simulation with complicated material models such as the visco-hyperelastic model.

6.5.2 Cohesive zone model

An alternative method of modelling crack propagation is through the Cohesive Zone modelling (CZM) technique. This technique, (94),(103),(104), is increasingly being employed to describe the local fracture processes in engineering materials. In the CZM, the local fracture process is accounted for by a local traction-separation law which describes the decrease in stress transfer in the material due to the formation of the fracture zone. The traction-separation curve is a material property and is defined by the critical energy release rate which is equal to the area under the curve. The attraction of this technique is that it provides a means of describing material damage without the need to model individual failure micro-mechanisms within the zone [29, 30]. Wei and Hutchinson [31] and

Williams and Hadavinia [32] introduced the traction-separation law for fracture toughness analysis of the peel test for elastic and elastic plastic materials. Thouless [33] later included the effect of transverse stress to the analytical solution of the traction-separation law. In order to use the CZM, data for the traction-separation law is required. Direct measurements of the traction-separation curves have been achieved for engineering polymers using the circumferentially deep notched tensile test [30, 34] but these are not always possible as in the case of the current study, where peel tests were used instead.

in Abaqus, there are two ways of adding cohesive behaviour into a model, first is by using the cohesive element and the second is to use the recently introduced surface based cohesive behaviour; also called cohesive contact method. In both techniques, the constitutive or so-called cohesive response is usually defined with a bilinear traction (*t*) – separation (*δ*) law shown schematically in Figure 6-25 as an example. The law consists of two parts. The first part is prior to the damage initiation. This part is governed by a linear elastic traction-separation relationship, described by equation 6-1 and equation 6-2.

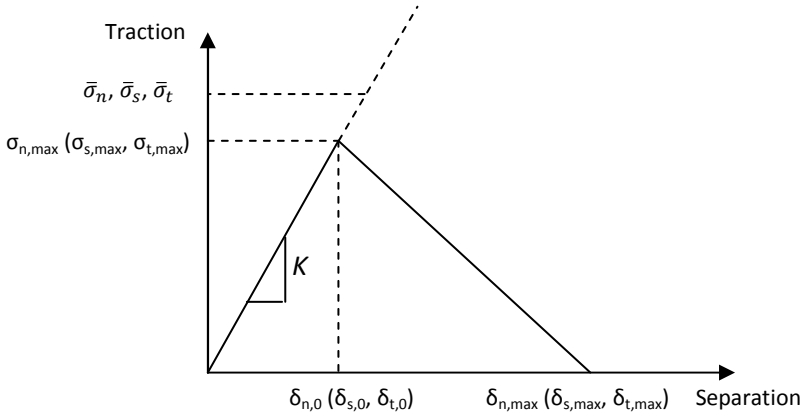

Figure 6-25, traction-separation law

$$\sigma = \begin{Bmatrix} \sigma_n \\ \sigma_s \\ \sigma_t \end{Bmatrix} = \begin{bmatrix} K_{nn} & K_{ns} & K_{nt} \\ K_{ns} & K_{ss} & K_{st} \\ K_{nt} & K_{st} & K_{tt} \end{bmatrix} \begin{Bmatrix} \varepsilon_n \\ \varepsilon_s \\ \varepsilon_t \end{Bmatrix} = K\varepsilon \qquad 6\text{-}1$$

where $\varepsilon_n = \frac{\delta_n}{T_0}$, $\varepsilon_s = \frac{\delta_s}{T_0}$, $\varepsilon_t = \frac{\delta_t}{T_0}$ 6-2

σ^n, σ^s and σ^t are the stresses related to Mode-I, Mode-II and Mode-III fracture respectively. The penalty stiffness, *K*, is the elastic stiffness, *E*, of the cohesive element divided by the element length, *L* whilst ε is the cohesive strain and T_0 is the original thickness of the cohesive element. For cohesive contact, T_0 is always 1 which makes the cohesive strain values always equal to the separation, δ.

As the traction increases with load, a damage initiation criterion is used to determine whether the node has reached the crack initiation condition or not. Four damage initiation criteria are available in Abaqus which are

Maximum nominal stress, MAXS,:

$$max\left\{\frac{\sigma_n}{\sigma_{n,max}}, \frac{\sigma_s}{\sigma_{s,max}}, \frac{\sigma_t}{\sigma_{t,max}}\right\} = 1 \qquad 6\text{-}3$$

Maximum nominal strain, MAXE, for the cohesive element technique and MAXU for the cohesive contact technique

$$max\left\{\frac{\varepsilon_n}{\varepsilon_{n,max}}, \frac{\varepsilon_s}{\varepsilon_{s,max}}, \frac{\varepsilon_t}{\varepsilon_{t,max}}\right\} = 1 \qquad 6\text{-}4$$

Quadratic nominal stress, QUADS, :

$$\left\{\frac{\sigma_n}{\sigma_{n,max}}\right\}^2 + \left\{\frac{\sigma_s}{\sigma_{s,max}}\right\}^2 + \left\{\frac{\sigma_t}{\sigma_{t,max}}\right\}^2 = 1 \qquad 6\text{-}5$$

and Quadratic nominal strain, QUADS, :

$$\left\{\frac{\varepsilon_n}{\varepsilon_{n,max}}\right\}^2 + \left\{\frac{\varepsilon_s}{\varepsilon_{s,max}}\right\}^2 + \left\{\frac{\varepsilon_t}{\varepsilon_{t,max}}\right\}^2 = 1 \qquad 6\text{-}6$$

The superscript *max* in the criteria denotes the cohesive traction or cohesive strain at the maximum traction point of the user defined cohesive law.

Once the damage initiation criterion is met, the stiffness of the cohesive behaviour is degraded with respect to the scalar damage variable *D* which reduces the magnitude of stresses predicted by the elastic cohesive response as shown in equation 6-7

$$\sigma_n = \begin{cases} (1-D)\bar{\sigma}_n;\ \bar{\sigma}\ \geq 0 \\ \bar{\sigma}_n\ ; otherwise \end{cases}$$

$$\sigma_s = (1-D)\bar{\sigma}_s \qquad 6\text{-}7$$

$$\sigma_t = (1-D)\bar{\sigma}_t$$

where $\bar{\sigma}_n$, $\bar{\sigma}_s$ and $\bar{\sigma}_t$ are the tractions predicted by the cohesive stiffness *K* and the current separation without damage.

The value of *D* for the linear damage evolution is calculated from the effective displacement, δ_m, defined as

$$\delta_m = \sqrt{\langle\delta_n\rangle^2 + {\delta_s}^2 + {\delta_t}^2}$$

where

$$\langle\delta_n\rangle = \delta_n\ ;\ \delta_n\ \geq 0 \quad \text{and}$$

$$\langle\delta_n\rangle = 0\ \ ;\ \delta_n < 0 \qquad 6\text{-}8$$

For the bilinear traction-separation law i.e. cohesive law with linear damage evolution as shown in Figure 6-25, the damage parameter is calculated using equation 6-9 below.

$$D = \frac{\delta_{m,max}(\delta_{m,eff}-\delta_{m,0})}{\delta_{m,eff}(\delta_{m,max}-\delta_{m,0})} \qquad 6\text{-}9$$

where $\delta_{m,max}$ is the effective displacement at complete failure, $\delta_{m,0}$ is the effective displacement at damage initiation and $\delta_{m,eff}$ is the maximum effective displacement attained during the loading history.

For the calculation of the damage parameter *D*, described by equation 6-8, if the displacement based approach is used, the term ($\delta_{m,max} - \delta_{m,0}$) must be specified by the user. If the energy approach

is used, the critical energy release rate G_C is required where Abaqus calculates $\delta_{m,max}$ and $\delta_{m,0}$ from G_C.

In dealing with mixed-mode fracture, two approaches are used by Abaqus, energy based and traction based. Three mixed mode fracture criteria for the calculation of the mode dependent ratio are available for the user, “power law”, “Benzeggagh-Kenane or BK” and “tabular”. The first two only work with the energy based approach whilst tabular criteria can be used in both approaches.

In the energy based approach, the mode dependent ratio is determined from G_n, G_s and G_t which are the energy release rate in normal, first shear and second shear directions, respectively. When this approach is used in conjunction with the power law criterion the failure of the cohesive element or cohesive interaction is governed by

$$\left\{\frac{G_n}{G_{n,C}}\right\}^{\alpha} + \left\{\frac{G_s}{G_{s,C}}\right\}^{\alpha} + \left\{\frac{G_t}{G_{t,C}}\right\}^{\alpha} = 1 \qquad 6\text{-}10$$

where α is the user defined parameter. $G_{n,C}$, $G_{s,C}$ and $G_{t,C}$ are the critical energy release rates in the normal, first shear and second shear modes. They also need to be defined by the user. If the energy approach is used with the Benzeggagh and Kenane criterion, the mixed-mode failure is governed by:

$$G_{n,C} + (G_{s,C} - G_{n,C})\left\{\frac{G_S}{G_T}\right\}^{\eta} = G_C \qquad 6\text{-}11$$

where $G_S = G_s + G_t$ and $G_T = G_n + G_S$. The parameter η is a cohesive property parameter. $G_{n,C}$, $G_{s,C}$, $G_{t,C}$ and η have to be specified by the user.

The last criterion is the tabular parameter, m, which can be used with both the energy and traction based approaches. In the case of the energy based approach, m is used to define the ratio between the normal and shear energies (mode-II and mode-III) to the total energy G_T. The equations can be written as:

$$m_1 = \frac{G_n}{G_T}, m_2 = \frac{G_s}{G_T}, m_3 = \frac{G_t}{G_T} \qquad 6\text{-}12$$

where G_T is the total, G_n is the normal, G_s is the mode II shear, and G_t is the mode III shear energy release rates. It can be seen that $m_1+m_2+m_3 = 1$ therefore only two parameters are needed.

Rewriting the equation with this relationship results in

$$m_2 + m_3 = \frac{G_S}{G_T}, \qquad 6\text{-}13$$

$$\frac{m_3}{m_2+m_3} = \frac{G_t}{G_S}, \qquad 6\text{-}14$$

The ratio G_s/G_T is the shear fracture energy (mode-II and mode-III) fraction of the total fracture energy. The ratio G_t/G_S is the second shear fracture energy (mode-III) fraction of the total shear fracture energy. These two ratios must be specified by user.

If the tabular mixed mode criterion is used with the traction based approach, the mixed-mode ratio is defined as a function of the tractions using the angular measures shown in Figure 6-26 and equations 6-15 and 6-16.

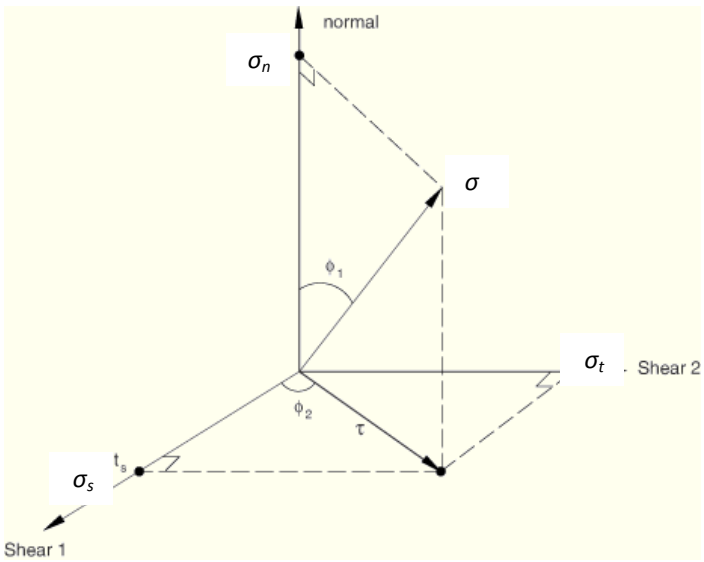

Figure 6-26, tabular mode mix criterion based on traction (40)

$$\phi_1 = \left(\frac{2}{\pi}\right) tan^{-1}\left(\frac{\tau}{\langle\sigma_n\rangle}\right) \qquad 6\text{-}15$$

$$\phi_2 = \left(\frac{2}{\pi}\right) tan^{-1}\left(\frac{\sigma_t}{\sigma_s}\right) \qquad 6\text{-}16$$

Where τ is the effective shear traction defined by $\tau = \sqrt{\sigma_s^2 + \sigma_t^2}$ and

$$\langle \sigma_n \rangle = \sigma_n \; ; \; \sigma_n \geq 0$$

$$\langle \sigma_n \rangle = 0 \; ; \; \sigma_n < 0 \qquad \text{6-17}$$

Φ_1 represents the ratio of the normal and the total shear traction whilst Φ_2 represents the ratio of the first and second shear traction. The values of $\tau/\langle\sigma_n\rangle$ and σ_t/σ_n must be specified by user where they are normalised by the factor $2/\pi$.

The mixed mode behaviour in every cohesive zone simulation in this work is defined as "mode independent" (40). The total fracture toughness varies with the mixed-mode ratio along the mixed-mode fracture locus, which is assumed to be a straight line as shown in Figure 6-27 below.

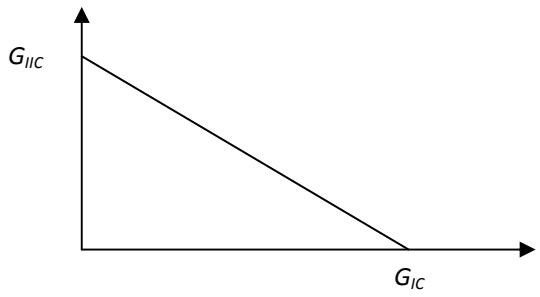

Figure 6-27, mixed-mode fracture locus of the mode independent behaviour

However, in case 6 of the fatigue simulation in chapter 7, the "power law" criterion, equation 6-10, is used with the parameter α set equal to 1. This results in the same mixed-mode fracture locus as shown in Figure 6-27. The reason for changing to the "power law" criterion is that this allows a separate definition of G_{IC} and G_{IIC}; in the "mode independent" case, G_{IIC} is automatically set equal to G_{IIC}.

The next section will outline the study of the simulations using the cohesive law explained in this section. Both cohesive element and cohesive contact technique were evaluated. Parametric studies are conducted to investigate the agreement among the two techniques and the experimental data.

6.5.3 Cohesive contact versus cohesive element

As mentioned previously, there are two ways of implementing cohesive zone modelling techniques in Abaqus: either using cohesive elements or a cohesive contact definition. In this section, the cohesive contact and cohesive element techniques were evaluated through a SENB test model. The material properties of Polyethylene (PE1) shown in Figure 6-28, the traction-separation law in Figure 6-29, and the SENB specimen geometry in Figure 6-30, are obtained from the work by Ivankovic et al (105). Table 6-8 and Table 6-9 show the input parameters for the material model and cohesive zone law, respectively. The finite element model, shown in Figure 6-31 was created according to dimensions shown in Figure 6-30. Area 1 and Area 2 of the model were filled with uniform 0.1mm x 0.1mm and 0.1mm x 1mm mesh, respectively. The reduced integration plane strain element was used in both areas. A row of 0.1mm x 0.1mm elements was added to the crack region to enable the model to accurately capture the crack propagation behaviour. Two rigid bodies were used as a loading pin and support as shown.

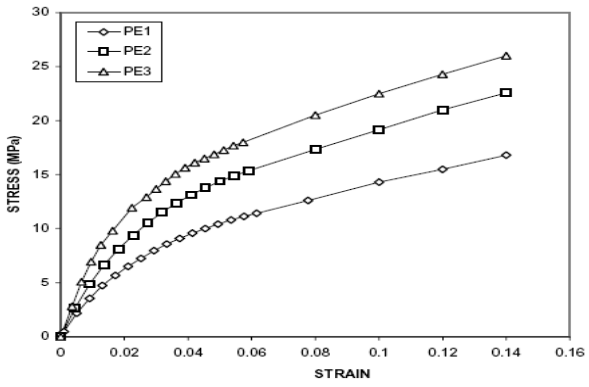

Figure 6-28, material Properties (PE1) from (105)

Table 6-8, Abaqus Input for material properties of Polyethylene (105)

E	350 (MPa)
Poison's ratio	0.3

Stress (MPa)	Plastic Strain
11.43	0.0000000
12.59	0.0151899
14.29	0.0354699
15.45	0.0534885
16.79	0.0711880

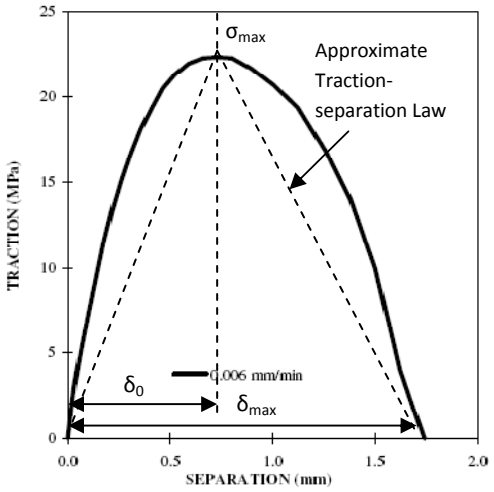

Figure 6-29, traction-separation Law from (105)

Table 6-9, parameters of traction-separation law.

Cohesive *stiffness, K*	30 (MPa/mm)
Maximum Traction, t^0	22.5 (MPa)
Displacement at Failure, δ^f	1.75 (mm)
Displacement at t^0, δ^0	0.875 (mm)

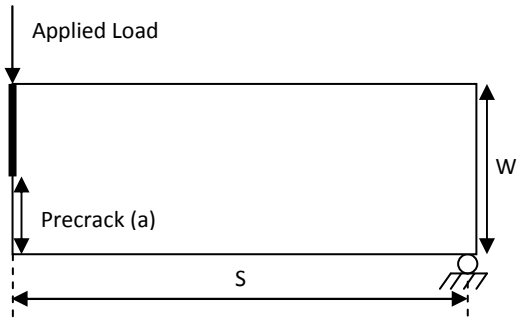

TPB Dimensions (mm)	
Span (S)	100
Width (W)	25
Out of plane thickness (B)	15
a/W ratio	0.55

Figure 6-30, dimensions of the SENB model from (105)

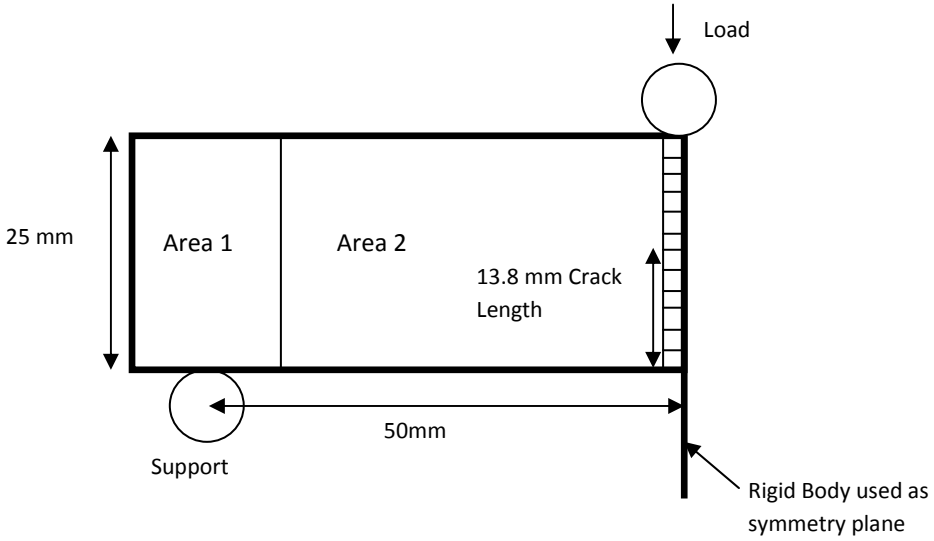

Figure 6-31, FE model of SENB test

Firstly, simulations using cohesive elements were carried out. The effect of the cohesive element thickness on the sample's response is shown by comparing the result from two simulations defined as Case 1 and Case 2. Case 1 uses the cohesive thickness taken from the nodal coordinates which is 0.1mm whilst in Case 2 the cohesive thickness is Abaqus' default value which is 1mm. The cohesive parameters of the two simulations are listed in . The displacement criterion for damage evolution is used in this simulation.

Table 6-10, material properties of the cohesive element in each simulation

Simulation	K (MPa/mm)	σ_{max} (MPa)	δ_{max} - δ_0 (mm)	Cohesive Element Thickness (mm)
Case 1	30	22.5	0.875	1
Case 2	30	22.5	0.875	0.1

Load-displacement curves were exported from the simulations and compared in Figure 6-32 with the experimental result and simulation result from (105). The latter was obtained using the finite volume technique. The traction-separation response of the cohesive element at the crack tip for each simulation was plotted in Figure 6-33 to verify them against the input parameters.

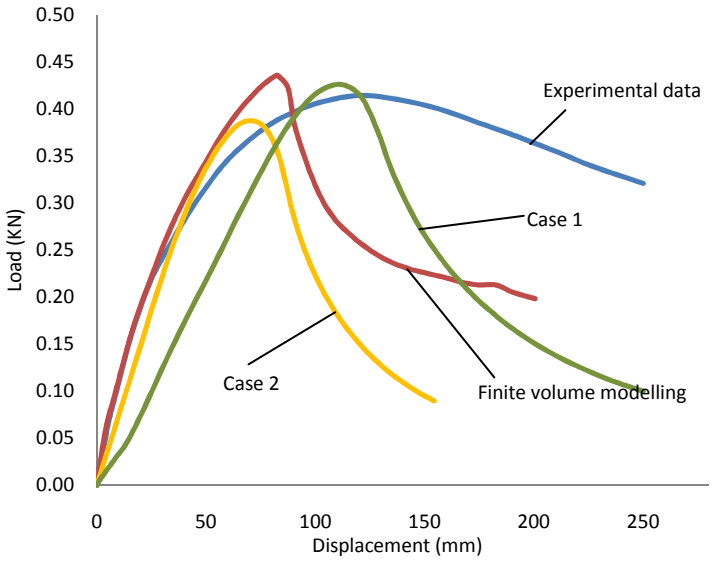

Figure 6-32: load-displacement curves from SENB simulation the using Cohesive Element Technique. A comparison is made with experimental and finite volume results (105)

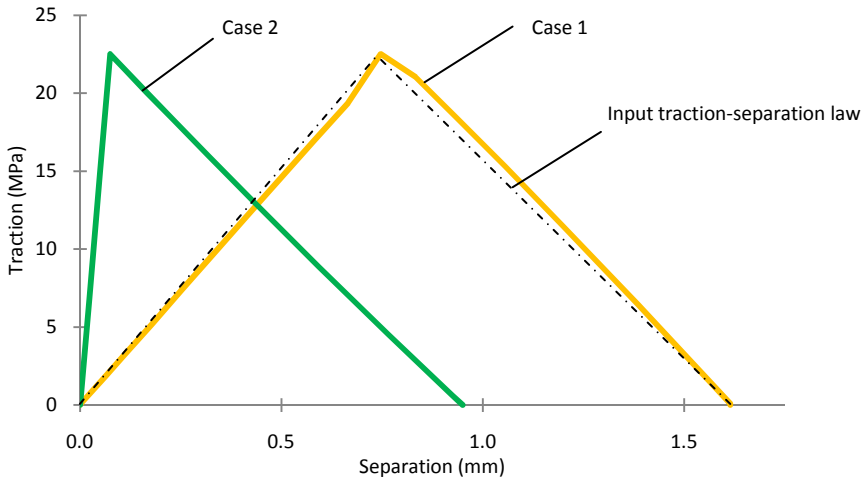

Figure 6-33: traction-separation response of the cohesive element at the cracktip for case 1 and 2.

The deformed geometry at the crack initiation stage and final stage are shown in Figure 6-34 and Figure 6-35 respectively.

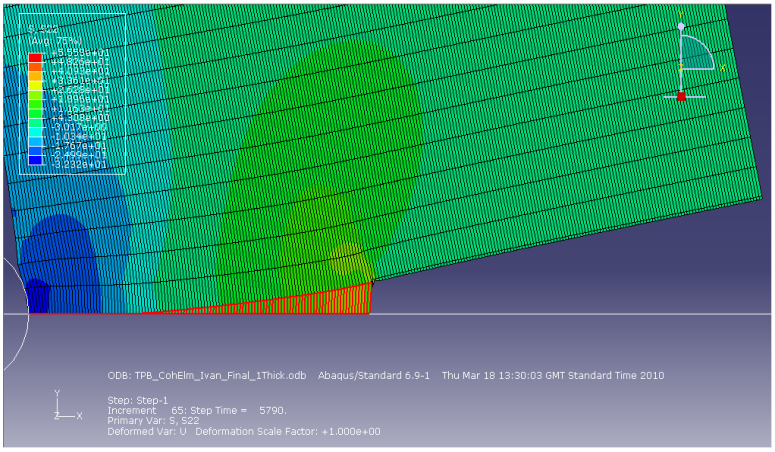

Figure 6-34: σ_{22} (stress in y-direction) plot during crack initiation, red highlighted area shows the cohesive elements

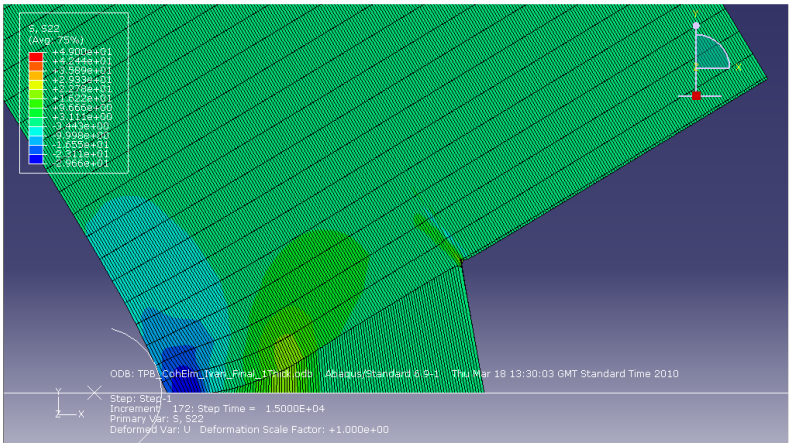

Figure 6-35: σ_{22} (stress in y-direction) plot at the final stage of the simulation (at 200mm loading pin travel distance)

It can be seen from Figure 6-32 that the load-displacement curve from simulation case 2 shows a better agreement to the simulation results from (105) than case 1. However, Figure 6-33 shows that the traction-separation response of case 2 does not match the input traction-separation curve whilst the response from case 1 does. This is due to the traction prior to damage initiation being affected by the cohesive element thickness as shown in equations 6-1 and 6-2. It is worth noting that the degradation rate of the element stiffness from both simulations are similar which shows that the damage evolution parameter, *D*, does not depend on the cohesive thickness.

Similar simulations were conducted with the cohesive contact technique. By default, the cohesive "thickness" of the cohesive contact is equal to 1 which makes *K* the only input parameter that controls the stiffness of the cohesive behaviour prior to damage initiation. Two simulations with different values of *K* were performed. The first one (case 3) has a *K* value equal to that used in the cohesive element simulation i.e. 30 MPa/mm. The second one (case 4) has a *K* value of 30 divided by the cohesive thickness of the previous model, i.e. case 2, 0.1mm. The list of parameters for both simulations is shown in Table 6-11.

Table 6-11, cohesive contact properties in each simulation

Simulation	*K* (MPa/mm)	σ_{max} *(MPa)*	$\delta_{max} - \delta_0$ *(mm)*
Case 3	30	22.5	0.875
Case 4	300	22.5	0.875

Load-displacement curves were obtained from the simulation results and are compared with the experimental and simulation results from (105) in Figure 6-36. The traction-separation response of the cohesive element at the crack tip of each simulation was plotted in Figure 6-37 to verify then against the input parameters.

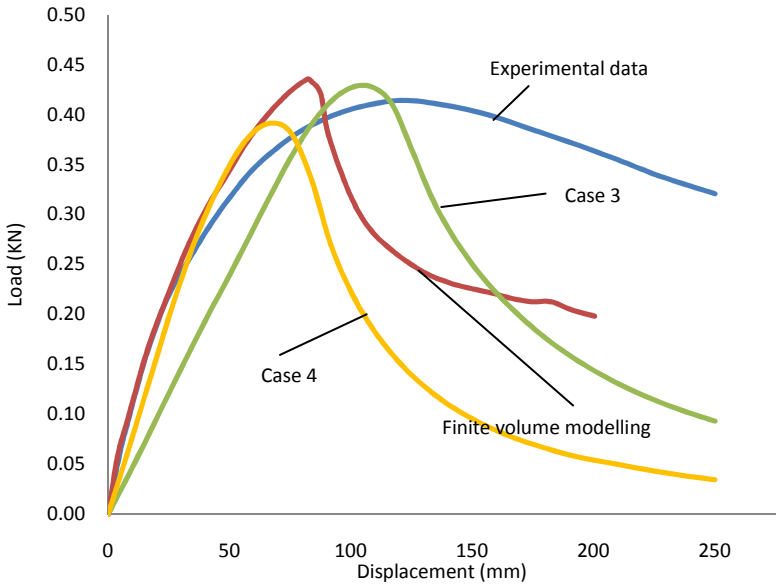

Figure 6-36, load-displacement curves from SENB simulation using the cohesive contact technique. A comparison is made with experimental and finite volume results from (105).

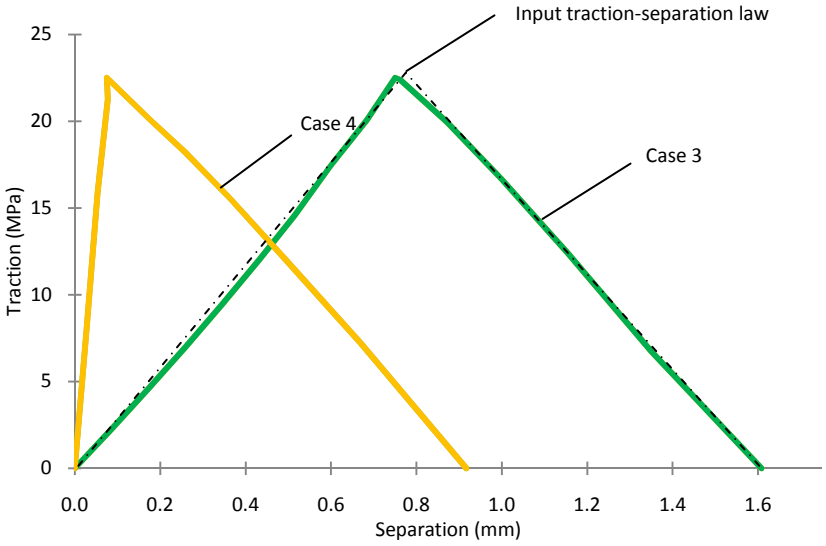

Figure 6-37, traction-separation response of the node at the cracktip

The deformation plots at the crack initiation stage and final stage are shown in Figure 6-38 and Figure 6-39 respectively. The length of the cohesive contact is also shown in Figure 6-38.

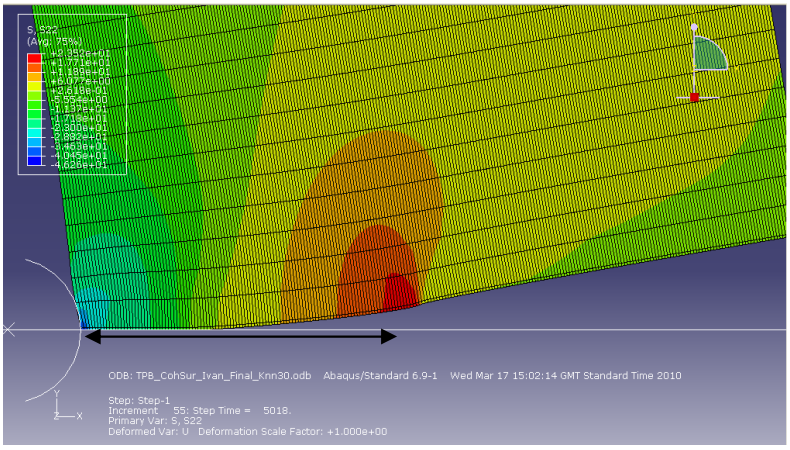

Figure 6-38, σ_{22} plot during crack initiation step with indicated cohesive contact length

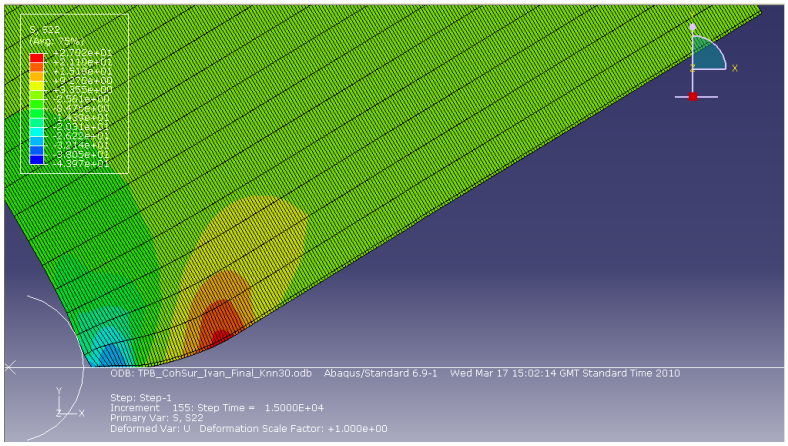

Figure 6-39, σ_{22} plot at the final stage of the simulation (at 200mm loading pin travel distance)

In Figure 6-36, the load-displacement curve from case 3 is closer to the results from (105) than case 4. As expected, the traction-separation response in Figure 6-37 shows case 4 does not match the input traction-separation curve whilst the response from case 3 does. This is identical to the results obtained from the cohesive element technique.

The results from the cohesive contact and cohesive element models are compared in Figure 6-40 and Figure 6-41 below. Figure 6-40 shows the load displacement curves and Figure 6-41 shows the

cohesive response at the crack tip from all four simulations, i.e. case 1 to case 4 as outlined in Table 6-10 and 6-11.

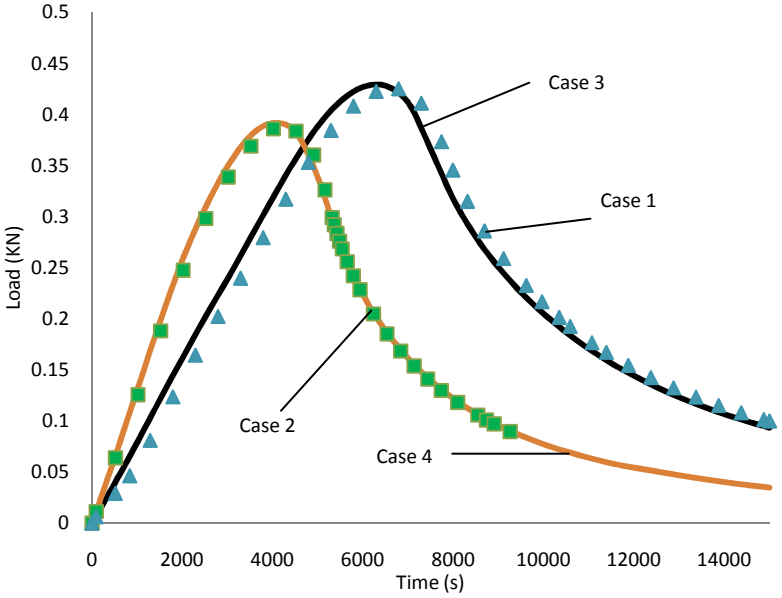

Figure 6-40: load- displacement curves from SENB simulations using Cohesive Contact and Cohesive Elements

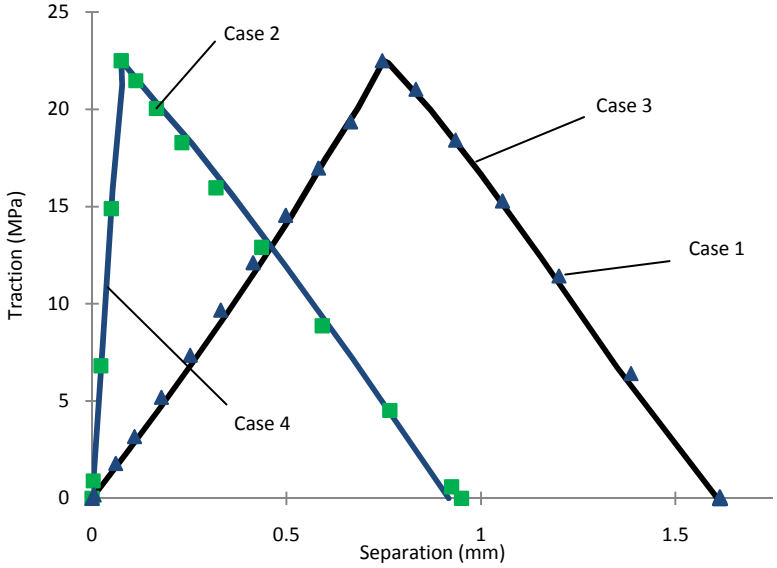

Figure 6-41: traction-separation response of the node at the cracktip from Cohesive Contact simulation and Cohesive Element simulation

It can be seen that case 1 generates results that are identical to the results from case 3. Similarly, case 2 is identical to case 4. It can be concluded that if the cohesive thickness of the element is set to

1 and the rest of the cohesive parameters are the same, cohesive contact and cohesive element techniques will produce identical results.

6.6 Cyclic loading simulation

So far, all the simulations involving fracture using cohesive zones used a monotonic loading boundary condition. This section studies the behaviour of a cohesive element and a cohesive contact under cyclic loading at three different stages which are loading, unloading and reloading. A simple tensile test model consisting of two 1mm x 1mm plane strain elements joined with either a cohesive element or cohesive contact, as shown in Figure 6-42, were used for this study. The Young's modulus and Poisson's ratio of the plane strain element are 70 GPa and 0.3 respectively. Four sets of cohesive properties were used as shown in Table 6-12.

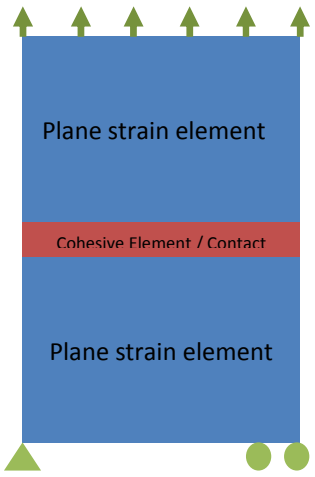

Figure 6-42, model of two elements with a cohesive zone under cyclic loading

Table 6-12, cohesive parameters for two element cyclic models

Simulation	Technique	Damage initiation criterion	K (MPa/mm)	Abaqus Thickness (mm)	σ_{max} *(MPa)*	δ_0 (mm)	Displacement at failure, δ_{max} (mm)
Case 5	Element	MAXE	17.5	1		0.203	0.812
Case 6	Contact	MAXU	17.5	1		0.203	0.812
Case 7	Contact	MAXS	17.5	1	3.5322		0.812
Case 8	Element	MAXS	17.5	1	3.5322		0.812

Cyclic loading, with two different displacement amplitudes (0.15mm and 0.25mm) are used to study the cohesive response, both with and without damage. The first amplitude of 0.15mm keeps the traction below the damage initiation criterion and the second one, 0.25 mm, is beyond the damage initiation point. The loading curves of the two displacement amplitudes are shown in Figure 6-43 whilst the traction-separation responses of all four cases of are shown in Figure 6-44. It can be seen that the results from cases 5-8 are identical and the loading, unloading and reloading curves coincide. Similarly, when the displacement amplitude us set to 0.25mm, as shown in Figure 6-45, there is no difference in the response of the four models corresponding to cases 5-8.

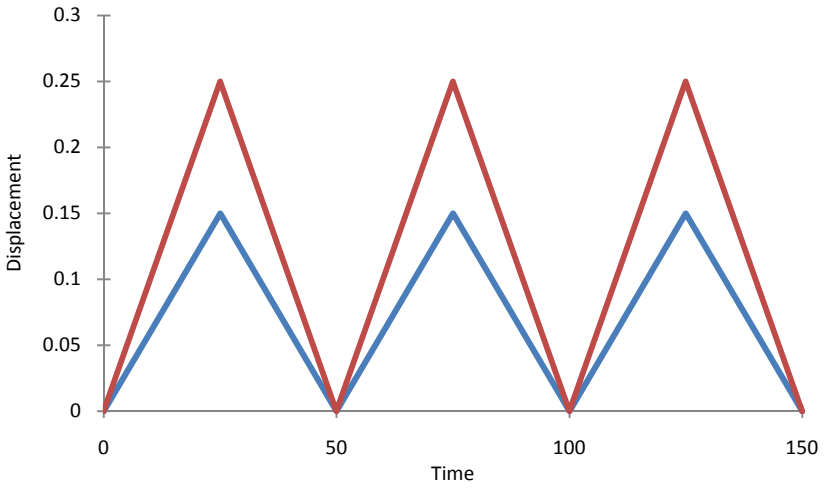

Figure 6-43, tabulate cyclic loading amplitude

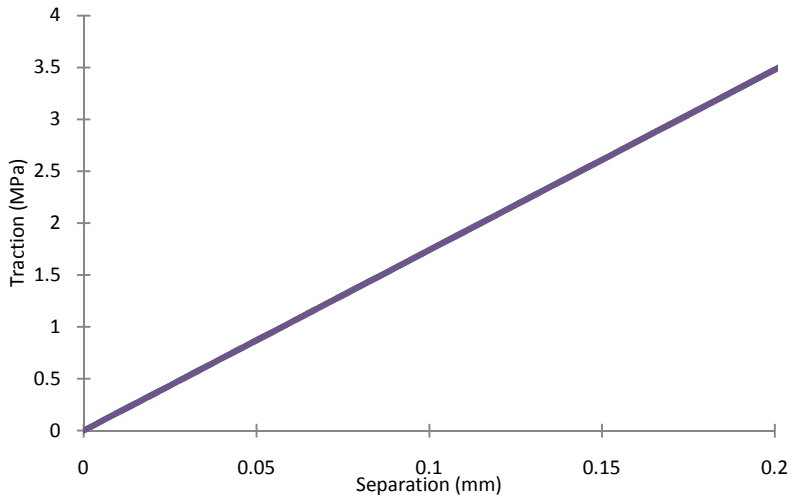

Figure 6-44, traction-separation response of cohesive element and cohesive contact at a displacement amplitude of 0.15mm. The four curves corresponding to cases 5-8, coincide.

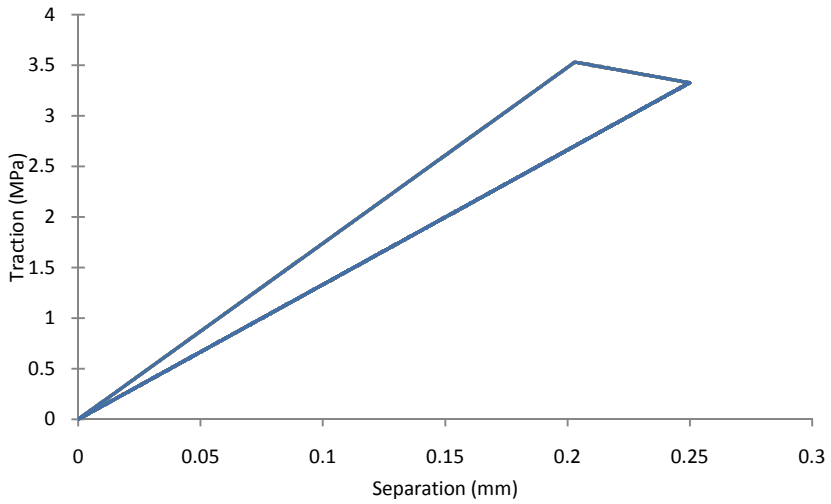

Figure 6-45, traction-separation response of cohesive element and cohesive contact at a displacement amplitude of 0.25mm. The four curves corresponding to cases 5-8, coincide.

In a multi-cycle loading situation with 10^3 to 10^6 cycles, a tabular amplitude definition as was prescribed above is not suitable. Abaqus provides an option that allows a periodic amplitude definition using the Fourier series where the amplitude, a, is defined as shown in equation 6-18

$$a = A_0 + \sum_{n=1}^{N}[A_n cos\, n\omega(t - t_0) + B_n sin\, n\omega(t - t_0)] \;;\; \text{for } t \geq t_0 \qquad 6\text{-}18$$

where t_0, N, ω, A_0, A_n and B_n are user-defined constants and are summarised below:

N = the number of terms in the Fourier series.

ω = the circular frequency, in radians.

t_0 = the start time.

A_0 = the constant term in the Fourier series.

A_n , B_n = Coefficients of cos and sin terms respectively

In order to investigate how the periodic definition works in Abaqus, a parametric study with the simple model shown in Figure 6-42 was carried out. The maximum displacement of the model was assigned to be 0.03mm. The user defined constants were $N = 1$, $A_0 = 0.5$, $A_n = 0$, $B_n = 0.5$. Three circular frequencies (ω), 0.2π, π and 2π, are used where t_0 is changed in correlation with ω to shift the displacement to zero at $t = 0$. The displacement at the loading edge of the model was plotted against time for each frequency, and it is shown in Figure 6-46 below.

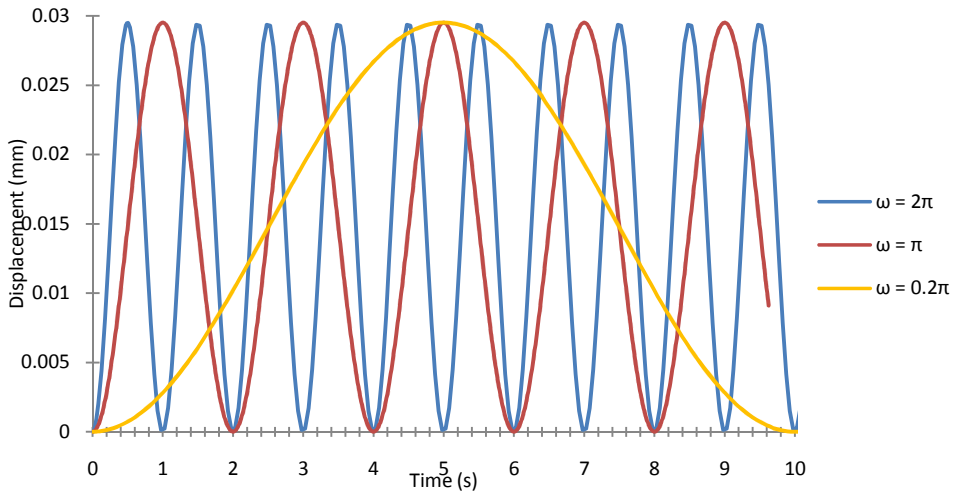

Figure 6-46, displacement versus time at the loading face of the two element model under periodic amplitude loading

In cyclic loading situations, especially at higher frequencies, it is crucial that the time increment within a step is small enough to capture the evolution of the load. Therefore, a convergence test was conducted to determine the optimal time increment for the cyclic loading simulation.

A model of a film with dimensions of 20m X 0.1mm attached to a 25mm rigid substrate as shown in Figure 6-48 was used for the convergence study. Note that this is also the geometry that will be used in the fatigue simulations in chapter 7. The film is meshed with 0.25mm X 0.25mm linear, plane strain, elements. A layer of cohesive elements with a length of 0.25mm is placed at the interface between the film and the substrate from the left end of the film the right, leaving 2.5mm from the right end as a cracktip. The cohesive law parameters used were arbitrarily chosen and are shown in Table 6-13 below.

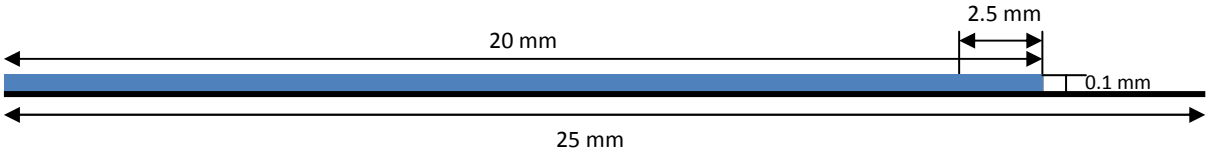

Figure 6-47, Model of a film attached to a rigid substrate for convergence and fatigue crack growth simulation

Table 6-13, cohesive law parameters for film on a substrate under cyclic loading model.

K (MPa/mm)	σ_{max} *(MPa)*	$\delta_{max} - \delta_0$ *(mm)*
17.4	0.04	0.1

A boundary condition with the periodic amplitude (for ω=2π) from Figure 6-46 is applied at the right end of the film. Fixed time increments of 0.01s, 0.05s and 0.1s are used in the study which makes the number of calculation points within each cycle equal to 100, 20 and 10 respectively.

The traction-separation response of the cohesive element at the cracktip was plotted to determine the optimal time increment for the analysis. It can be seen that an insufficiently small time increment results in a shift of the response from the input traction-separation behaviour. Only the time increment size of 0.01 is small enough to capture accurately the damage initiation point.

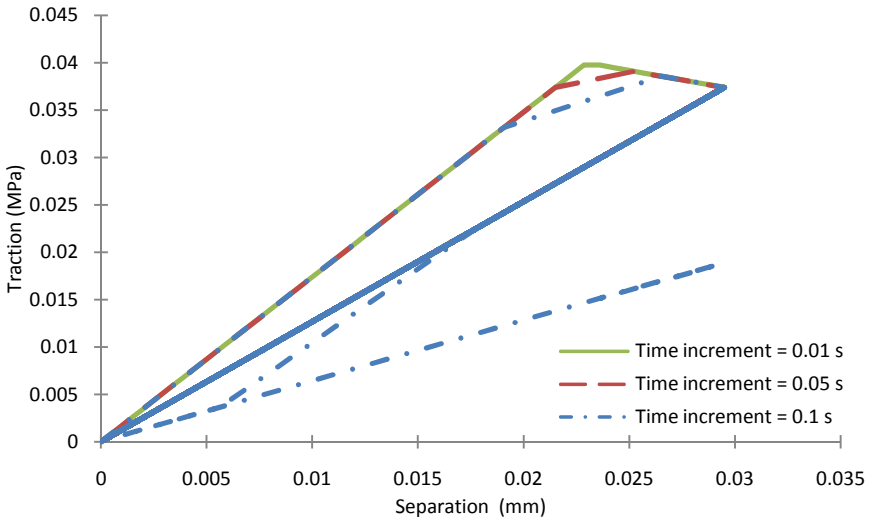

Figure 6-49, effect of time increment on traction-separation of the cohesive element at cracktip.

Thus far, the methods for applying cyclic loading for several cycles up to the order of 10^6 cycles in Abaqus have been reviewed. The next section will investigate the techniques for fatigue simulation available in Abaqus including the low cycle fatigue simulation using the direct cyclic method and the use of the user defined field (USDFLD) subroutine.

6.7 Fatigue crack growth analysis

6.7.1 Low cycle fatigue simulation using the "debond" technique with a direct cyclic algorithm

A built-in simulation technique for interfacial fatigue fracture in Abaqus is the low cycle fatigue analysis using the direct cyclic approach in conjunction with the "debond" feature (40). It was firstly introduced in Abaqus 6.8. In this method, the direct cyclic approach which will be explained below is used in conjunction with a Paris Law type material degradation definition to simulate material behaviour under cyclic loading.

The direct cyclic approach provides an efficient ways of modelling the response of a material under repeated loading by using a truncated Fourier series to describe the displacement versus cycle time within a cycle of each node instead of recording the displacement at every time increment. The equation is shown below:

$$u(t) = u_0 + \sum_{k=1}^{n}[u_k^s \sin k\omega t + u_k^c \cos k\omega t] \quad \text{6-19}$$

where $u(t)$ describes the response of the structure whilst u_0, u_k^s and u_k^c represent unknown displacement coefficients. Under cyclic loading, the stress-strain response of a time-independent linear elastic material is the same in every cycle. Therefore equation 6-19 can be used to describe the displacement-time response of the material. In the case of a time-independent elastic plastic material, the mechanical response normally reaches a steady state after a number of hysteresis loops in the stress-strain response. In order to find the steady state response, Abaqus creates a residual vector for in the same form as the Fourier series of the displacement.

$$R(t) = R_0 + \sum_{k=1}^{n}[R_k^s \sin k\omega t + R_k^c \cos k\omega t] \quad \text{6-20}$$

where *R* represents the residual vector in each degree of freedom. The Fourier coefficients are obtained from

$$R_0 = \frac{2}{T}\int_0^T R(t)dt$$

$$R_k^s = \frac{2}{T}\int_0^T R(t) \sin k\omega t \, dt \quad \text{6-21}$$

$$R_k^c = \frac{2}{T}\int_0^T R(t) \cos k\omega t \, dt$$

The coefficients of these residual vectors as well as the displacement coefficients in equation 6-19 were used to determine convergence. By increasing the number of terms (*n*) in equations 6-19 and 6-20, convergence is more likely to be achieved as shown in Figure 6-49 below.

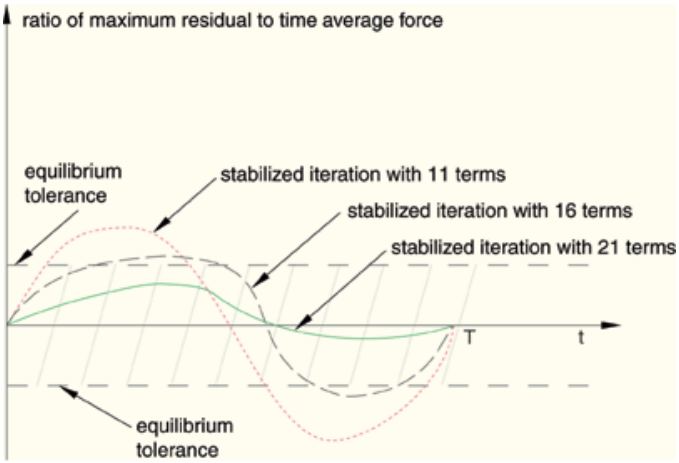

Figure 6-49, stabilized iterations with different Fourier terms (40)

Once the direct cyclic method obtains a converged i.e. a steady state result, Abaqus will determine whether delamination will initiate and grow using a fatigue damage criterion. The latter needs to be defined for two stages. The first one is the criterion for the onset of delamination growth which is a phenomenological model defined as:

$$\frac{N}{c_1 \Delta G^{c_2}} \geq 1 \qquad 6\text{-}22$$

where c_1 and c_2 are user defined material constants, ΔG is the relative energy release rate which is the difference between the energy release rate at maximum loading and minimum loading. ΔG is calculated by Abaqus using the VCCT, which is the same technique that was used in the monotonic loading crack propagation analysis of section 6.4. The node at the crackfront will not be released unless equation 6-22 is satisfied. Also the value of the energy release rate at maximum loading, G_{max}, is required to be larger than the $G_{threshold}$ which is also set by the user.

The second required criterion described the propagation of the delamination. A damage variable, D, is introduced through the Paris' law. The relative energy release rate ΔG is related to the damage parameter, D, via

$$\frac{dD}{dN} = \frac{c_3 \Delta G^{c_4}}{L} \qquad 6\text{-}23$$

where *D* is the accumulated damage, *N* is the number of the extrapolated cycles, c_3 and c_4 are material constants and, *L* is the element characteristic length. This relationship is used to calculate the damage variable for the next cycles. The damage parameter is then used to modify the interfacial stiffness, *K*, which is used in the next direct cyclic calculation. The calculations of the damage variable, *D*, and material stiffness, *K*, are shown in equations 6-24 and 6-25 below, respectively.

$$D_{N+\Delta N} = D_N + \frac{\Delta N}{L} c_3 \Delta G^{c_4} \qquad 6\text{-}24$$

$$K_{N+\Delta N} = K_N(1 - D_N) \qquad 6\text{-}25$$

This model was employed initially in this study to the hygrothermal expansion simulation of a film on a substrate shown in Figure 6-50. The same model geometry as shown in Figure 6-1 and the material properties in Table 6-1 were used. The fracture criterion parameters were arbitrarily chosen and are shown in Table 6-14 below.

Table 6-14, failure criterion parameter for direct cyclic fatigue simulation of a film on substrate model.

C_1	C_2	C_3	C_4	$G_{threshold}/G_C$	G_C
0.5	-0.1	4.87×10^{-6}	1.15	0.01	0.8

It was found that after the first node was released, the contact definition at the interface was ignored by the Abaqus algorithm. This resulted in the elements in front of the cracktip interpenetrating as they swell due to hygrothermal strain as shown in Figure 6-51.

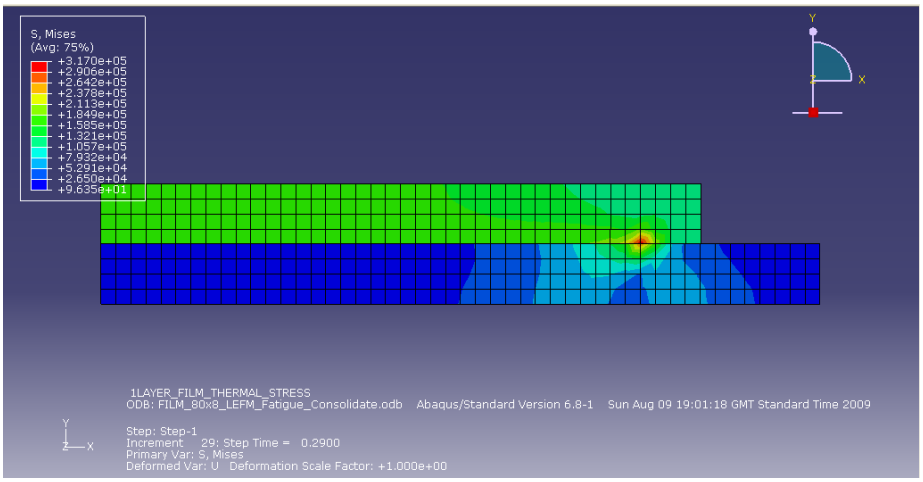

Figure 6-50, contour plot of Mises stress at the first cycle of direct cyclic fatigue simulation

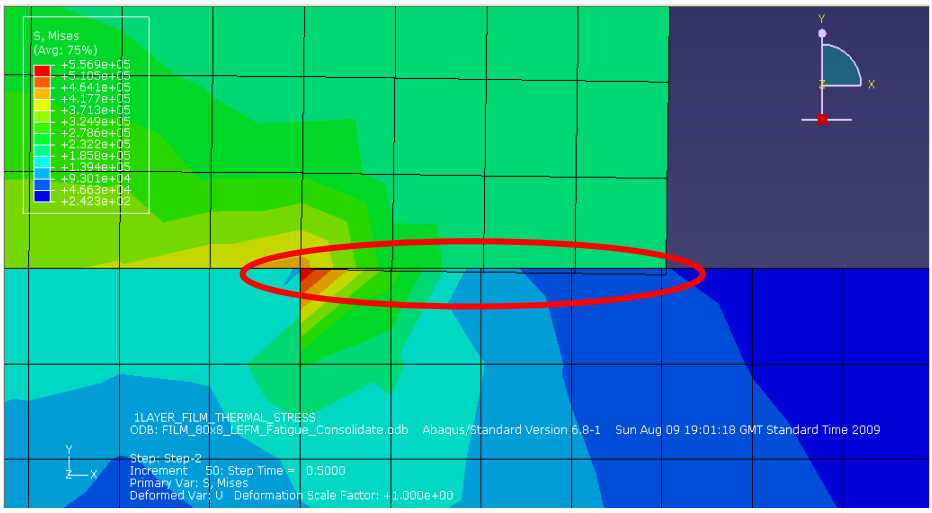

Figure 6-51, elements interpenetration in the crack opening area

To summarise, although the low cycle fatigue technique in Abaqus is suitable for low to medium cycle fatigue of materials with a Paris law type behaviour, the interpenetration of elements that occurs in shear fracture mode due to the contact definition being ignored once the first node is debonded, makes this technique unsuitable for the current study. Another concern regarding this technique is that the Paris law material parameters are required. The parameters must be obtained from experiments.

6.7.2 Irreversible Cohesive Zone Model

A recent technique for low cycle fatigue simulation is the irreversible cohesive zone model, ICZM, proposed by Roe and Siegmund (98) . Whilst previous literature relied on Paris Law to define material degradation, this technique uses a damage evolution algorithm based on strain history to decrease the stiffness, *K*, and the damage initiation traction, σ_{max}, of the cohesive elements.

Consider the traction-separation model shown in Figure 6-25. It does not account for the effect of cyclic loading on the stress response of the cohesive elements. For example, consider the case when the separation δ is such that $\delta < \delta_0$, i.e. *D* is equal to zero. The cohesive stress would follow the initial line with slope, *K*. If the element is unloaded and then loaded again to the same value of δ, the cohesive stress would unload and reload with the same slope *K*. In other words, *K* remains unchanged as a result of the cyclic loading. Let K_0 be the initial stiffness of the cohesive law without damage, the stress is given by

$$\sigma = K_0 \delta \qquad 6\text{-}26$$

What is required, therefore, is to introduce a modification which allows the stiffness to change with cyclic loading. For this purpose a variable, D_c, is introduced which is the damage due to cyclic loading. This allows the stiffness, *K*, to degrade with cyclic loading, therefore the stress equation becomes:

$$\sigma = K\delta \qquad 6\text{-}27$$

An equation is now needed to define how the damage variable, D_c, evolves with time during fatigue loading. The evolution equation used in this work was the one introduced by Roe & Siegmund, (98) which is defined as:

$$\Delta D_c = \frac{\Delta\delta}{\delta_{max} - \delta_0} \frac{\sigma}{\sigma_{max}} \qquad 6\text{-}28$$

where D_c is the fatigue damage evolution parameter, σ_{max} is the damage initiation stress of the cohesive law and

$$\Delta D_c = D_c(t) - D_c(t - \mathrm{d}t) \quad \text{6-29}$$

$$\Delta\delta = \sqrt{(\Delta\delta_n)^2 + (\Delta\delta_s)^2} \quad \text{6-30}$$

$$\sigma = \sqrt{{\sigma_n}^2 + {\sigma_s}^2} \quad \text{6-31}$$

where

$$\Delta\delta_n = \delta_n(t) - \delta_n(t - \mathrm{d}t) \quad \text{6-32}$$

$$\Delta\delta_s = \delta_s(t) - \delta_s(t - \mathrm{d}t) \quad \text{6-33}$$

$$\sigma_n = \sigma_n(t)H(\Delta\delta) \quad \text{6-34}$$

$$\sigma_s = \sigma_s(t) \quad \text{6-35}$$

with the *n* and *s* subscripts denoting normal and shear components respectively. Note that for mode I, damage only accumulates while the normal separation is positive (this is controlled by the Heavyside step function $H(\Delta\delta)$, whereas in shear loading, damage occurs for both shear displacement directions. In addition, since the value of $\Delta\delta$ in equation 6-30 is always positive, damage occurs during loading as well as the unloading phases of the cycle. The above modification is implemented to the simulation by using the USDFLD user defined subroutine in conjunction with the GETVRM utility routine. The latter is used to access the current values for σ_n, δ_n and δ_s. Equations 6-28 and 6-29 are then specified in the USDFLD subroutine and the change in the damage variable D_c is determined. By defining the variable D_c as a field variable, the cohesive stiffness and the traction at damage initiation at every time increment are then modified through:

$$\sigma_{max} = \sigma_{max_0}(1 - D_c) \quad \text{6-36}$$

$$K = K_0(1 - D_c) \quad \text{6-37}$$

Equation 6-37 is coupled to equation 6-27, and in so doing gives rise to cyclic damage. Note that in cases where the separation is larger than the values at damage initiation, i.e. $\delta \geq \delta_0$, the monotonic variable D is given by equation 6-9. On unloading, the cohesive stress response in the absence of this USDFLD subroutine would be:

$$\sigma = (1 - D)K_0\delta \qquad 6\text{-}38$$

When the subroutine is used, equation 6-37 will modify the stress response to:

$$\sigma = (1 - D)K\delta = (1 - D)(1 - D_c)K_0\delta \qquad 6\text{-}39$$

Therefore, this method allows the introduction of solution-dependent cohesive properties. The traction-separation responses of the irreversible cohesive element for normal and shear loading modes are shown in Figure 6-53 and Figure 6-54, respectively. Figure 6-53a and Figure 6-54a correspond to $\delta < \delta_o$ whereas Figure 6-53b and Figure 6-54b correspond to $\delta > \delta_o$ where δ is less than the final separation, δ_{max}. The cohesive parameters used for these calculations are shown in Table 6-15 below. The results were obtained by using the model of two elements with a cohesive element in the middle, the same geometry to the one shown in Figure 6-42. The cohesive element is loaded in tension and shear as shown in Figure 6-52a and Figure 6-52b, respectively.

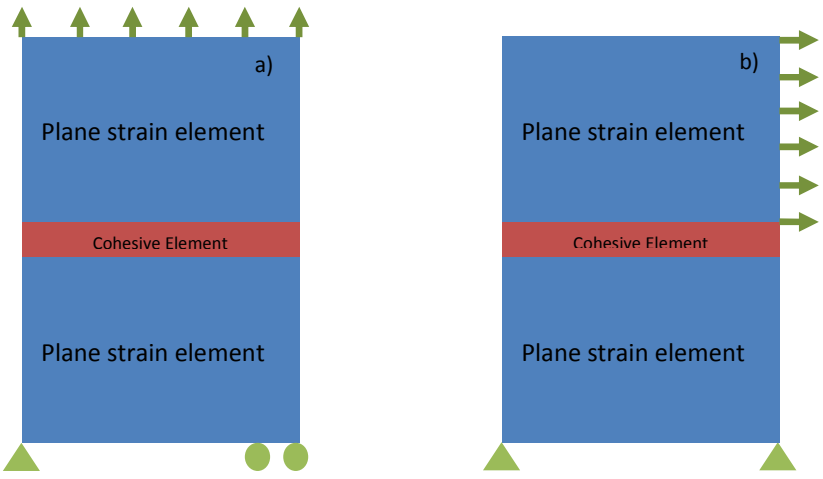

Figure 6-52, models of two elements with a cohesive zone a) loaded in tension, b) loaded in shear.

Table 6-15, cohesive parameters fatigue of thin film simulation using irreversible cohesive zone model

K (MPa/mm)	σ_{max} (MPa)	δ_{max} - δ_0 (mm)	δ_0 (mm)	Cohesive Element Thickness (mm)
6666	80	0.05	0.012	1

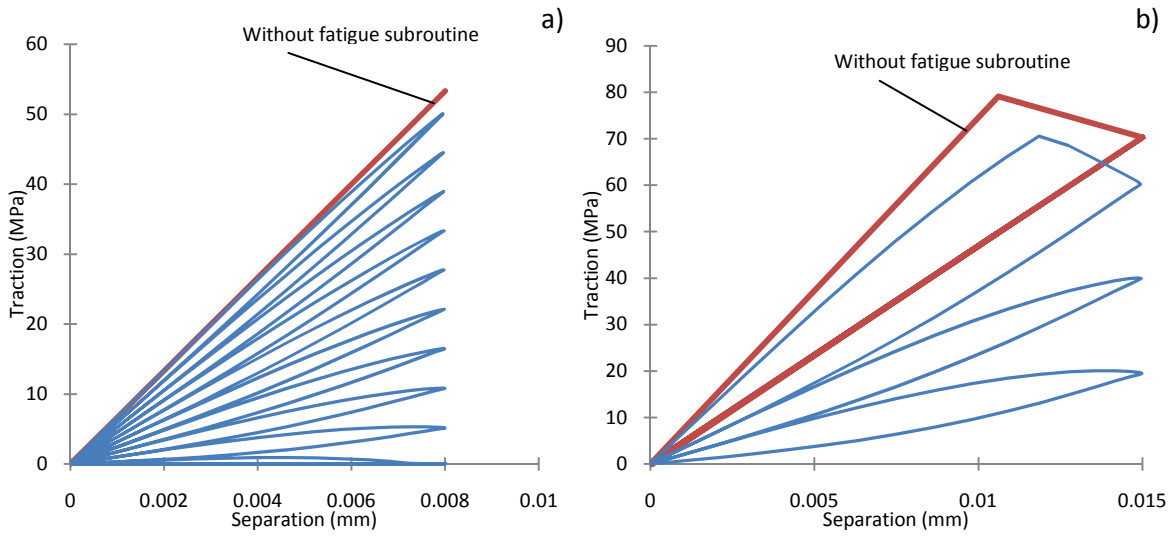

Figure 6-53, traction-separation response using the parameters in under mode I loading with: a) maximum loading less than the damage initiation, δ = 0.08 mm, b) maximum loading greater than damage initiation, δ_{max} = 0.15 mm.

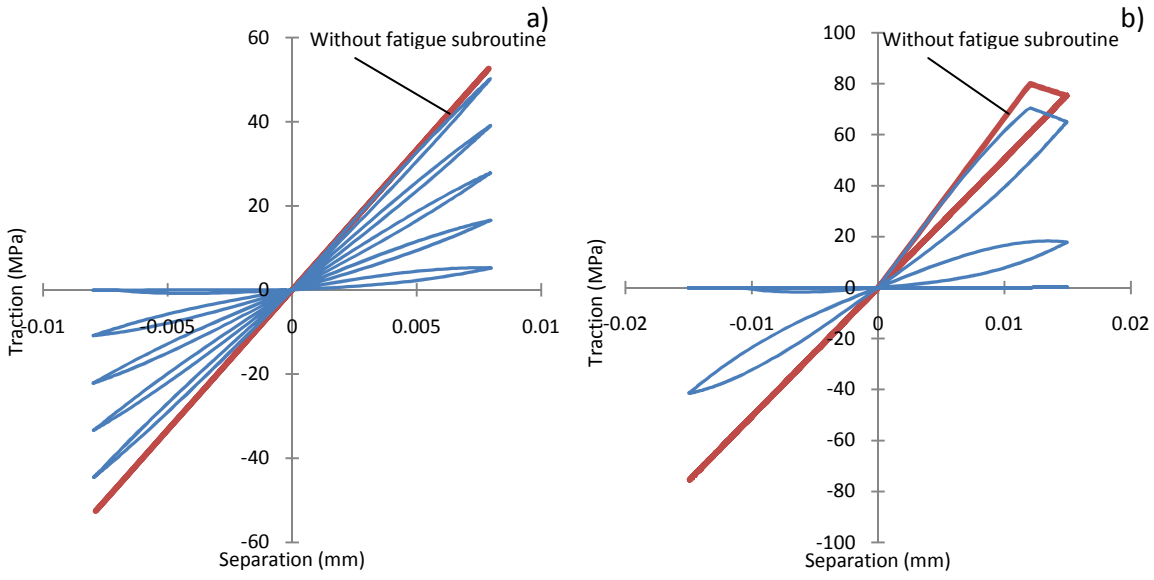

Figure 6-54, traction-separation response using the parameters in under mode II loading with: a) maximum loading less than the damage initiation, δ = 0.08 mm, b) maximum loading greater than damage initiation, δ_{max} = 0.15 mm.

A preliminary study of the capability of this modelling technique has been carried out using the thin film model shown in Figure 6-48 with the viscoelastic material properties summarised in Table 6-3 and Table 6-4. The film is loaded with a cyclic change in relative humidity from 45 to 55 %RH with the hygrothermal expansion coefficient of 0.00012 RH^{-1} taken from Figure 6-7 and the cohesive parameters at the interface shown in Table 6-15.

The contour plot of the von Mises stress at the first cycle, Figure 6-55a, is compared to that of the 50^{th} cycle, Figure 6-55b. It is evident that the cracktip has moved from the initial point. The shear stress and shear strain history plots of the cohesive element at the original cracktip are shown in Figure 6-56. It is observed that the stiffness of the element gradually degrades and loses the ability to withstand any stress after several cycles. At that point, the crack initiates and the cracktip moves on to the neighbouring node.

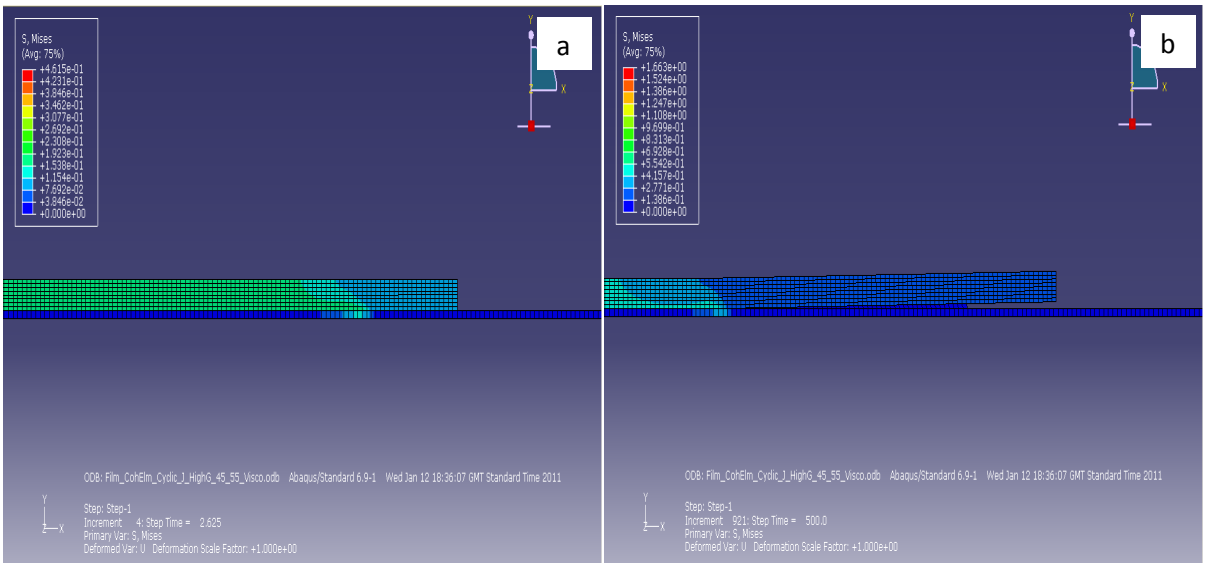

Figure 6-55 Mises Stress contour plot at 55%RH at a) the first loading, b) the 50th loading cycle

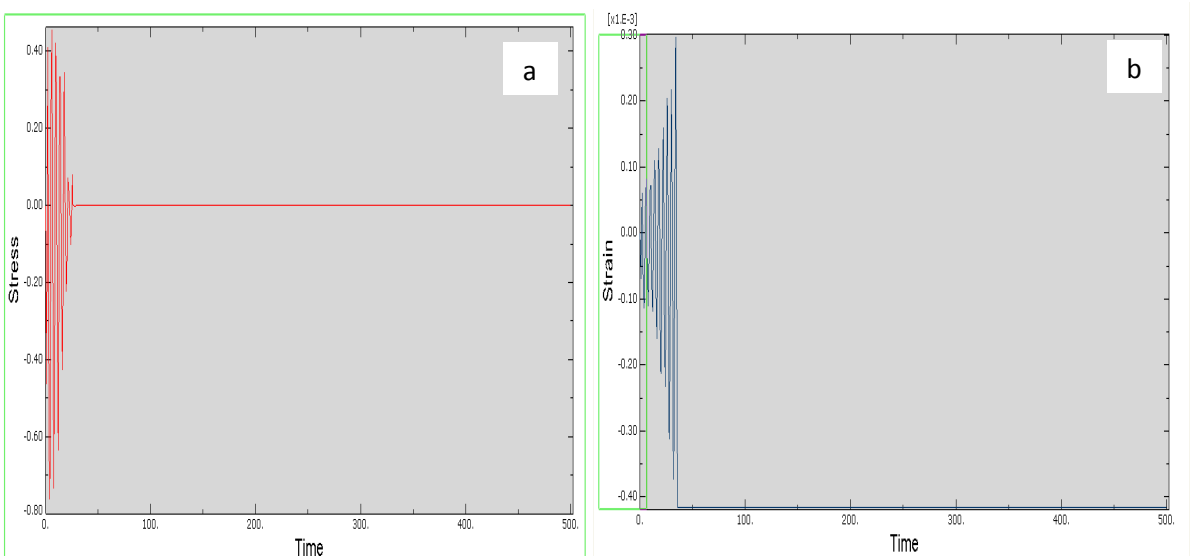

Figure 6-56, a) shear stress and b) shear strain history plot of the cohesive element at the original cracktip

A similar simulation was conducted without the fatigue damage subroutine. It is shown by comparing the Mises stress contour plots at the 1st and 50th cycles, that the crack has not extended from its initial position (see Figure 6-57a and Figure 6-57b). Also, it is shown in Figure 6-58 that the stress and strain response of the cohesive element remains the same after 50 loading cycles.

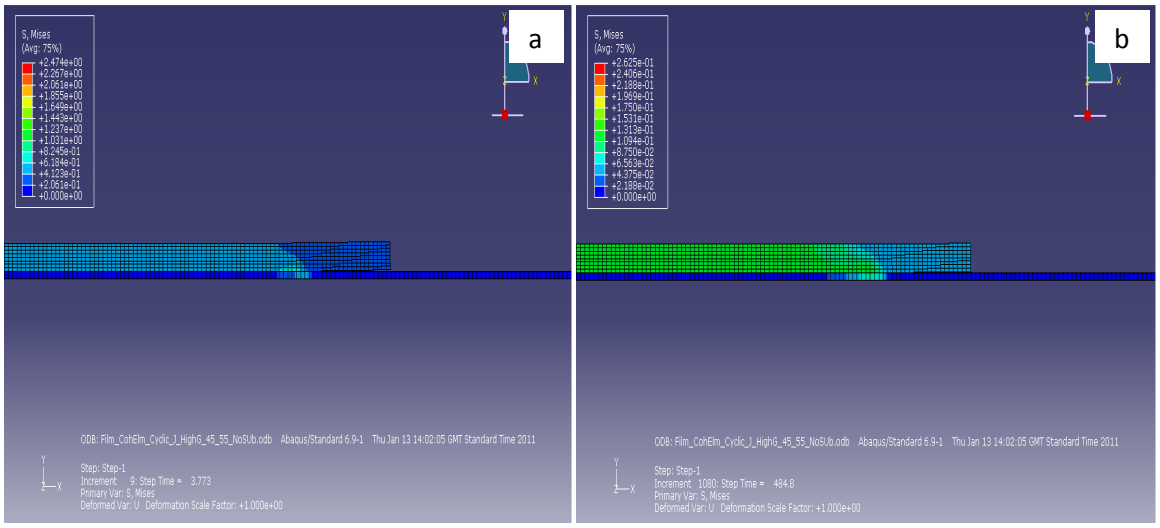

Figure 6-57, Mises Stress contour plot of the film model without the fatigue damage subroutine at 55%RH at a) the first loading, b) the 50th loading cycle

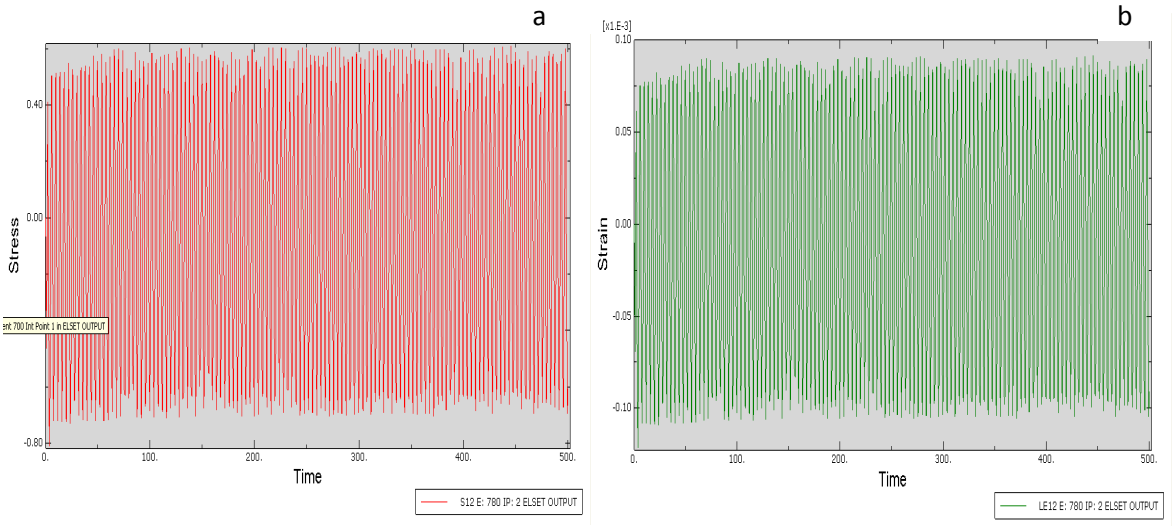

Figure 6-58, a) shear stress and b) shear strain of the cohesive element at the cracktip of the film model without the fatigue damage subroutine

In conclusion, the development of an environmental fatigue model has been outlined in this chapter. The simulation techniques available in the commercial finite element software Abaqus including, thermal stress analysis, hyperviscoelastic analysis, J-contour integral, VCCT, direct cyclic fatigue simulation and the cohesive zone modelling, including cohesive element and cohesive contact, have all been comprehensively studied. The irreversible cohesive zone modelling technique has examined regarding its capability to simulate environmental fatigue in a multi layered film. The evolution of the cohesive stiffness and damage initiation traction degradation due to the introduction of the ICZM subroutine has been shown. This technique will also be used in chapter 7 in conjunction with hygrothermal and hyperviscoelastic modelling in the simulation of fatigue crack growth in acrylic gesso and blue phthalo alkyd paint combinations.

7. The T-Peel test and the environmental fatigue modelling

Thus far, the mechanical properties of the two paints (blue phthalo alkyd and acrylic gesso) and the fracture toughness of the interface between the two paints have been determined. The finite element techniques related to hygrothermal stress analysis, hyperviscoelastic, fracture mechanics and fatigue modelling have been studied. The last objective of this project is to develop a numerical model that is suitable for the prediction of delamination in multi layer viscoelastic paint film due to cyclic loading that could arise because of fluctuating humidity.

This chapter outlines the finite element simulation of the T-Peel test and the environmental fatigue loading of multilayered, thin film. A T-Peel model has been created with respect to the dimensions and the material properties of the paints in chapter 5. The cohesive zone modelling technique was used to define the adhesive behaviour between the two peel arms. The traction-separation parameters of the elements were calibrated by comparing experimental and numerical T-peel data. The calibrated traction-separation law is next used in the modelling of environmental fatigue delamination of the blue alkyd from an artists' canvas which is primed with acrylic gesso. The irreversible cohesive zone model technique, as discussed in chapter 6, was implemented into the model of an alkyd film on a primed canvas substrate. The technique introduces fatigue damage to the cohesive behaviour of the interface. Eventually, the initiation time of the delamination was predicted for various painting storage conditions. The propagation of the delamination was also predicted for the most severe environmental case.

7.1 The T-Peel simulation

A finite element model of the peel test, shown in Figure 7-1, was created using the commercial finite element software Abaqus(40). The dimensions of the model are the same as the actual peel sample

with the thickness of the top arm (alkyd) being 0.20 mm and the bottom arm (acrylic gesso) 0.10 mm.

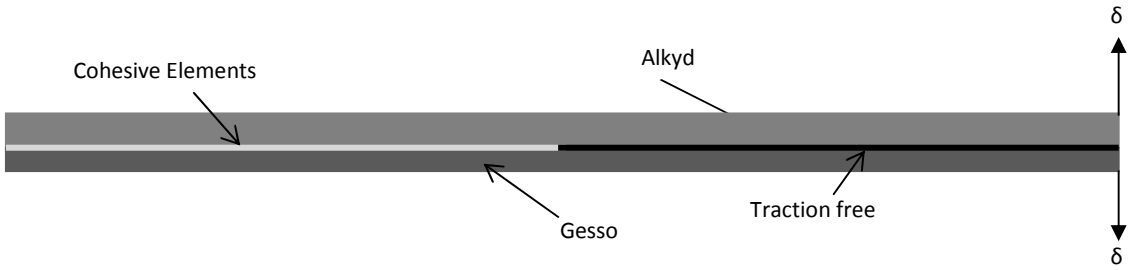

Figure 7-1, T-Peel Model.

A rigid pad of 4x4 elements is created at the end of each peel arm where the displacement is applied. The pads are constrained from moving in the horizontal direction. The material parameters from Table 5-1 and Table 5-2 in chapter 5 are used to define the materials' behaviour. The top peel arm is assigned to move upwards at 5mm/min which creates the same boundary condition as in the actual experiment. Cohesive zone elements were defined between the peel arms half way from the loading end to define the path of delamination as shown in Figure 7-1. The value of 250 N/m for the fracture toughness obtained from the peel test at 5mm/min, 25˚C, 50%RH of a 300-days old sample in Figure 5-13a was used in the calibration of the cohesive law described next.

First, a suitable CETOL parameter was determined through convergence tests. The CETOL value is the maximum allowable creep strain within a time step which is used in controlling the accuracy of viscoelastic analysis. Two separate cohesive laws with damage initiation traction values of 1 MPa and 4 MPa, labelled 1 and 2 respectively as shown in Figure 7-2, were used in these tests. The area under the curve is kept equal to the fracture toughness at 250 N/m and the ratio between the damage initiation separation, δ_0, and final separation, δ_{max}, was set at 1:4. Note that a ratio of 4 is the value used in the irreversible cohesive zone modelling by Roe (98). This gives the cohesive initial stiffness of 8 MPa/m and 128 MPa/m for the cohesive laws 1 and 2, respectively. The CETOL value was varied from $0.0001s^{-1}$ to $0.1s^{-1}$ in the order of a decade apart for each traction-separation law.

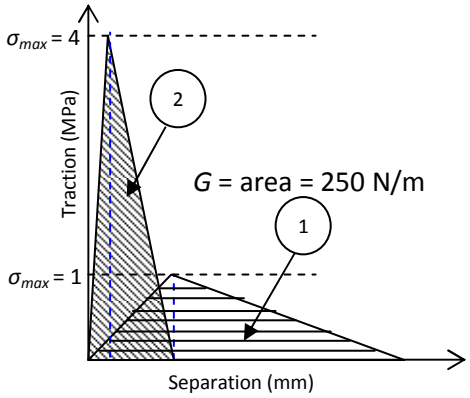

Figure 7-2, traction separation law for the determination of CETOL value

Full integration hybrid plane strain elements, CPE4H, were used. The mesh density of each peel arm is 4 x 1200 (thickness x length) elements. This mesh density was chosen based on the general criteria for simulating bending problems which requires at least four linear elements throughout the thickness of a beam, however, this mesh density was also found to be accurate following mesh sensitivity studies which will be discussed later in this section.

The load-displacement curves from the CETOL tests are shown in Figure 7-3. The load and displacement are those corresponding to the reference point of the rigid pad, at the end of the top peel arm. It is observed that the results converge at a CETOL value of 0.01 in both cases. Therefore, the value of 0.01 is used in all the peel test models in this chapter. It is also observed in Figure 7-3a that the curves from the simulations using the cohesive law number 1 fits the experimental data very well.

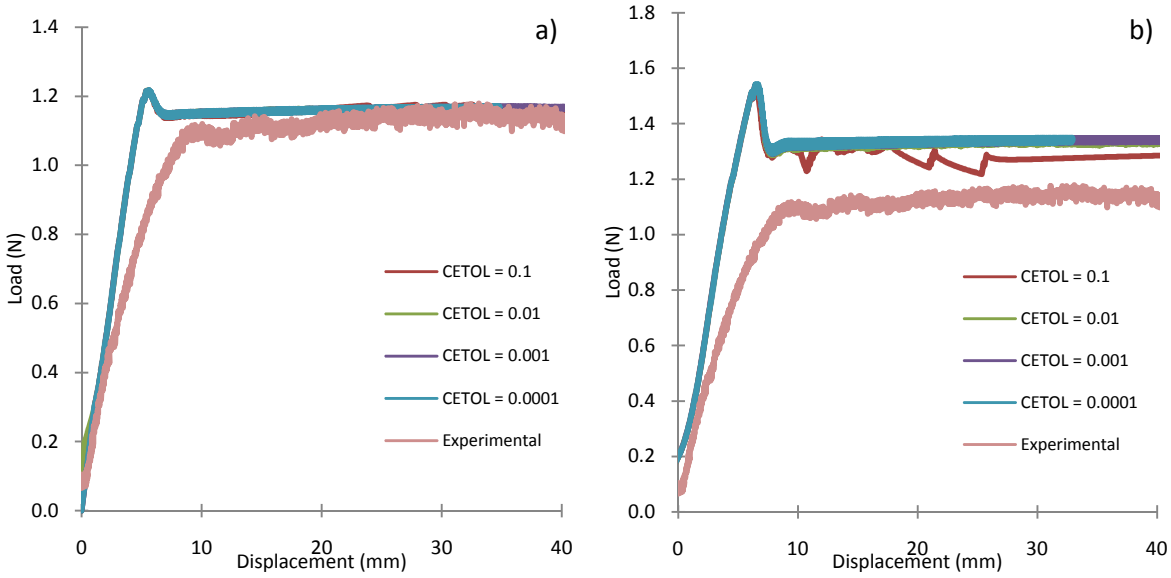

Figure 7-3, load-displacement curves of CETOL calibration test with a) cohesive law number 1, b) cohesive law number 2.

A mesh convergence study was performed using the same model with the cohesive law number 1 in Figure 7-2. The rows of elements through the thickness of the peel arms were varied until the corresponding steady state peel loads were shown to converge as shown in Figure 7-4. The difference in load between each mesh density is small, less than 3%, therefore the model with 4x1200 elements will be used for all the following T-Peel simulations.

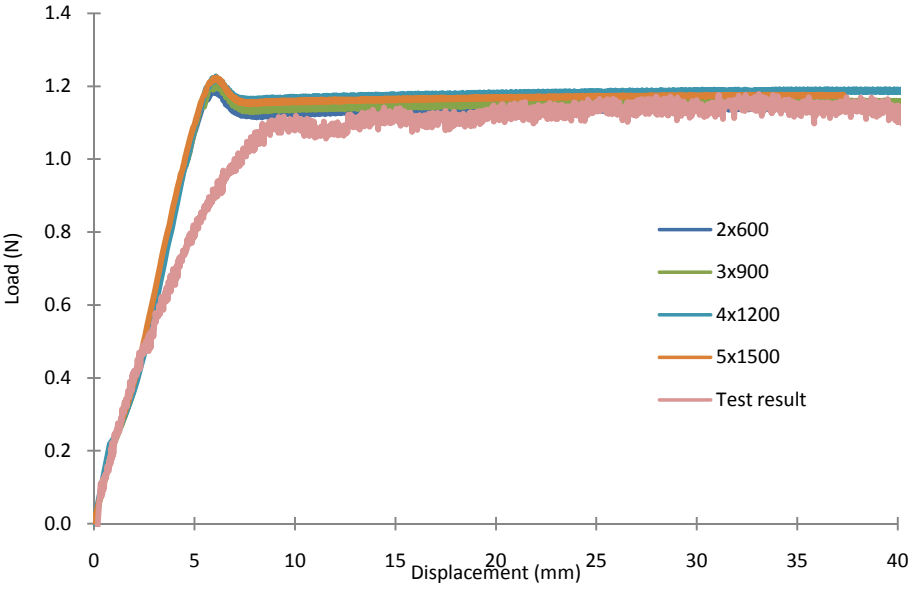

Figure 7-4, load versus displacement of mesh convergence study. σ_{max} = 1, G = 0.25 MPa/mm.

The next step in the calibration of the cohesive law regards the shape of the traction-separation law which is determined by the ratio between the separation at damage initiation, δ_0, and final separation, δ_f. This ratio was varied through a parametric study from 2:1 to 5:1 where σ_{max} and G_C were kept constant at 1 MPa and 250 N/m, respectively. The corresponding load displacement curves from the simulations are plotted in Figure 7-5 together with the experimental result at 5mm/min, 25˚C, 50%RH of a 300-days old sample from Figure 5-13a. It was found that the resulting load-deflection response of the numerical model varied by only 1% for the range of δ_{max}/δ_o 3:1 to 5:1. Therefore the ratio was set to 4:1.

The final calibration was for the maximum traction, σ_{max}. The fracture energy is still fixed at 250 N/m and the δ_{max} : δ_0 ratio was kept at 4:1 as determined from the previous parametric tests. The value of σ_{max} was varied from 0.01 to 5 MPa and the corresponding load displacement curve of each simulation is plotted in Figure 7-6. It is observed that the value of σ_{max} below 0.1 MPa results in a variation of the stiffness in the initial part of the curve. At higher σ_{max}, the initial part of the curve, prior to the steady state peel, stays constant irrespective of the δ_{max} value. However, as the σ_{max} is increased, the average load during steady state peel also becomes higher. If the value of σ_{max} is set too high, in this case over 5MPa, the analysis will terminates before the steady state peel condition are reached. This is due to the fact that the maximum stress at the cracktip does not reach the set σ_{max}. The value of σ_{max} at 1MPa gives a steady state peel load that is closest to the experimental value, therefore it is selected as the correct estimate. It is worth noting that the chosen σ_{max}, is roughly equal to the yield stress values shown in Figures 5.6a and 5.6b This finally gives an initial elastic stiffness, K_0, of 8 GPa/mm. A summary of the cohesive parameters is given in Table 7-1.

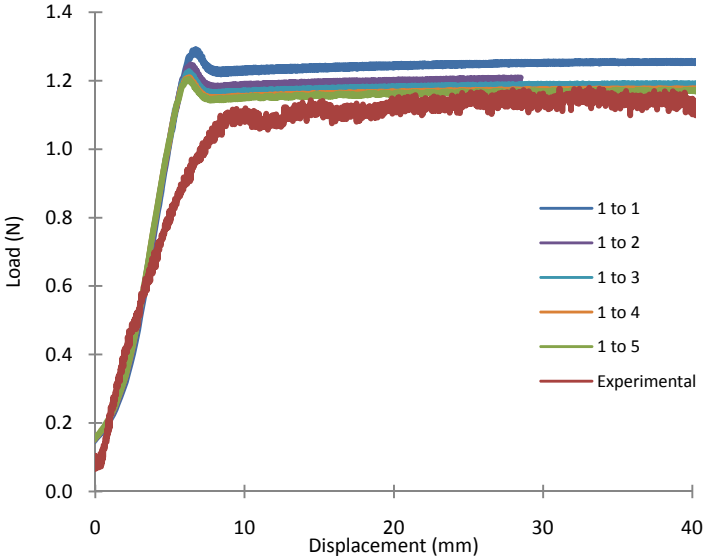

Figure 7-5, load versus displacement for the calibration of $\delta_f : \delta_0$ ratio, σ_{max} = 1, G = 250 N/m

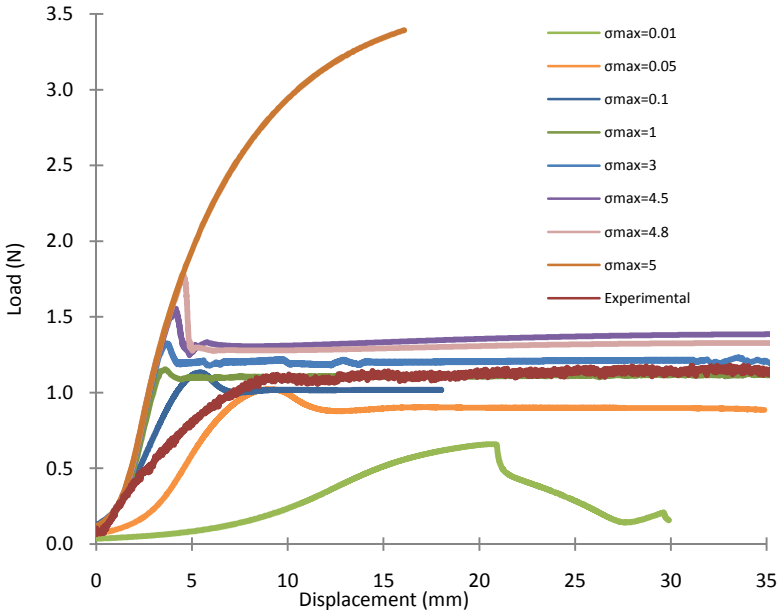

Figure 7-6, load versus displacement for the calibration of σ_{max}. $\delta_f : \delta_0$ ratio = 4:1, G = 250 N/m

Table 7-1, the cohesive parameters of peel test simulation at 5 mm/min.

Parameters	
G_0	0.25 (MPa.mm)
K_0	8 (MPa/mm)
σ_{max}	1 (MPa)
δ_0	0.125
δ_{max}	0.5

The final resulting force-displacement curve from the viscoelastic simulations is compared to the experimental result in Figure 7-7. A good agreement is observed during the initial loading and the steady state regions of the curve. A maximum is observed in the numerical result which is absent in the experimental data. There is a discrepancy between the experimental result and the FE result at the region prior to the steady state peel. This could be because of slipping of the sample in the grip during the experiments or the fact that the experiments are started with the samples already in the T-peel position whereas in the FE, the sample starts off in the flat position and gradually the edge of the top arm is lifted so that the sample attains the T-peel position. However, the only region of concern in the curve is the steady state peel load. The discrepancy in the steady state value is less than 6 %. The deformed plot is shown in Figure 7-8. From this, the peel angle is measured as 70°. The experimental value for this test was 65°. It is believed that the difference in the peel angle is mainly due to the weight which causes the sample to 'drop' and hence reduce the peel angle in the actual experiment. This is not thought to be a significant effect, as changing the angle from 65° to 70° results in only 3% change in the value of G_C, as calculate by IC-Peel (99).

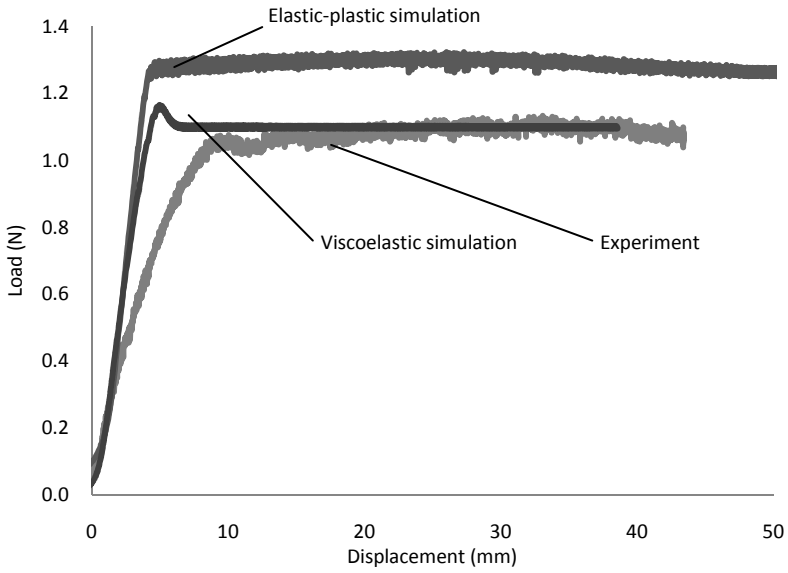

Figure 7-7, peel force versus displacement from the experiments, at 5mm/min, 25˚C and 50%RH, and simulations.

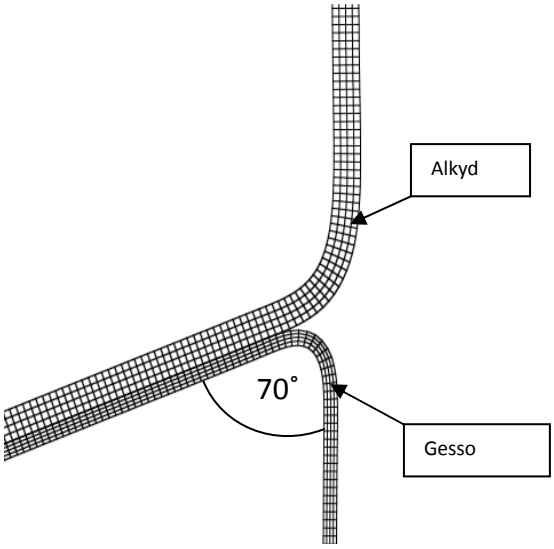

Figure 7-8, deformation plot of T-peel model.

Further investigations on the capability of the model to simulate the peel test at different displacement rates were performed. The cohesive law in Table 7-1 was used in peel test simulations at 0.5 and 50 mm/min. The model dimensions and material definitions were kept the same as in the 5mm/min simulation. Load-displacement curves from the simulations versus the experimental ones from Figure 5-13a are shown in Figure 7-9. It can be seen that slope of the initial part of the curve, prior to crack initiation, becomes higher as the displacement rate increases. However in the second part of the curve, the same steady state peel load is observed from all the simulations rates. This is different from the experimental result where the steady state peel force increases with the displacement rate. The result demonstrates that the damage initiation stress is rate dependent and a calibration of cohesive law is needed for each test speed in order to create a simulation result that matches the experimental data.

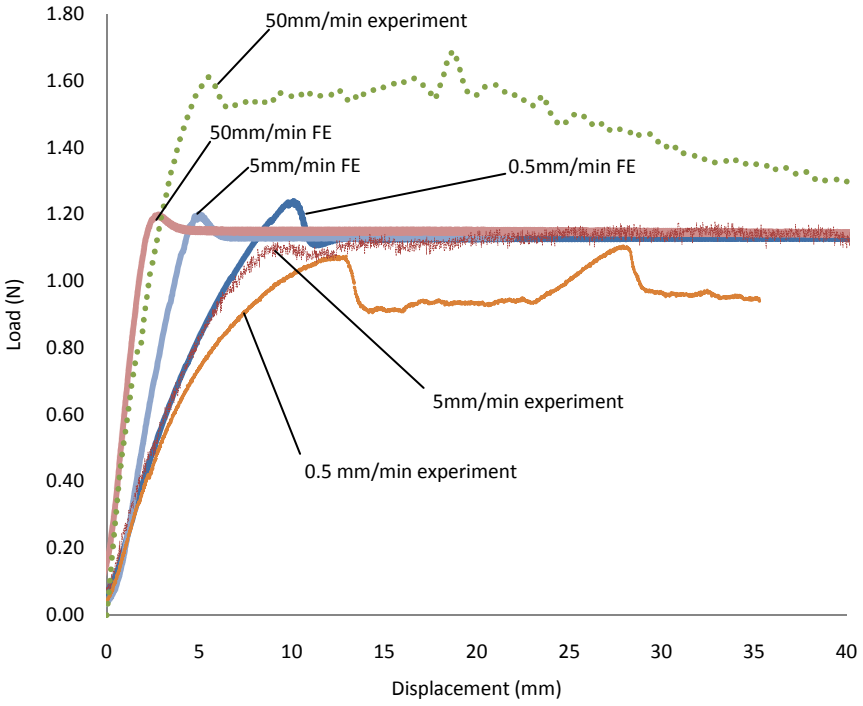

Figure 7-9, load-displacement curves from peel test simulations versus experiments at different speed

Thus far, the material parameters of the two paint layers have been determined and a conventional cohesive zone model simulating the interface has been calibrated for the peel test of the 300 day-old sample at 25°C, 50% RH and 5mm/min. The calibration of the cohesive zone model was obtained from peel tests, therefore the parameters, strictly speaking, should only be valid for normal, mode I loading conditions. Attempts were made to determine experimentally the G_C value for mode II loading through tensile loading of samples as reported in (102) (the geometry was similar to the one illustrated in Figure 7-11) but these were not successful as the gesso layer broke consistently before the delamination occurred. Other standard mode II test geometries including End Notched Flexure (ENF) and End Loaded Split (ELS) cannot be used because the paints are too soft and flexible. In the absence of mode II experimental data, we assumed therefore that the cohesive zone parameters for mode I and mode II are identical. This assumption makes the numerical prediction conservative, as mode II toughness is generally greater than or equal to that of mode I. For some material combinations, e.g. glass/epoxy, mode II toughness can be considerably larger than that of mode I

(106). However, for combinations of softer materials, mode I and mode II toughness values are more often nearly the same as reported in (107) and (108). This information will be used in conjunction with a fatigue damage accumulation algorithm, in order to predict delamination due to environmental fatigue loading in multilayered paints.

7.2 Modelling of the delamination in paints due to environmental fatigue

The usual structure found in art paintings is illustrated in the simplified diagram in Figure 7-10. Decorative paint layers are painted on canvas which is usually commercially available already 'primed', i.e., one of its surfaces is painted with a preparation layer (gesso). The finished work of art is stretched on the support frame as shown in the diagram. In order to mimic this structure, a numerical model shown in Figure 7-11 was developed. This shows a 25 mm long, 0.25 mm thick and 5 mm wide alkyd film attached to a 30 mm long, 0.4 mm thick and 5 mm wide primed canvas substrate. The length of 30 mm was chosen after parametric investigations by comparing the thermal stress at the middle of the film from the simulation to the analytical solution which showed 30 mm to be sufficiently large compare to the initial crack length that end effects do not affect the global stress of the model. In addition, (63) states that for a linear elastic coating, as long as the bond length is at a distance longer that several times the film thickness from the edges, the results are valid in the generic sense and can be assumed to apply for this geometry. The properties of the primed canvas (Belgian superfine linen) were already investigated in (109) and their results were used in the current study. Similar to the peel tests, a layer of cohesive elements is defined between the film and the substrate along a line from the middle of the film to the left end of the model. The aim was to develop a method for predicting crack initiation times under various cyclic temperature and relative humidity conditions. In order to achieve this, the irreversible cohesive zone model explained in chapter 6 was implemented to the model.

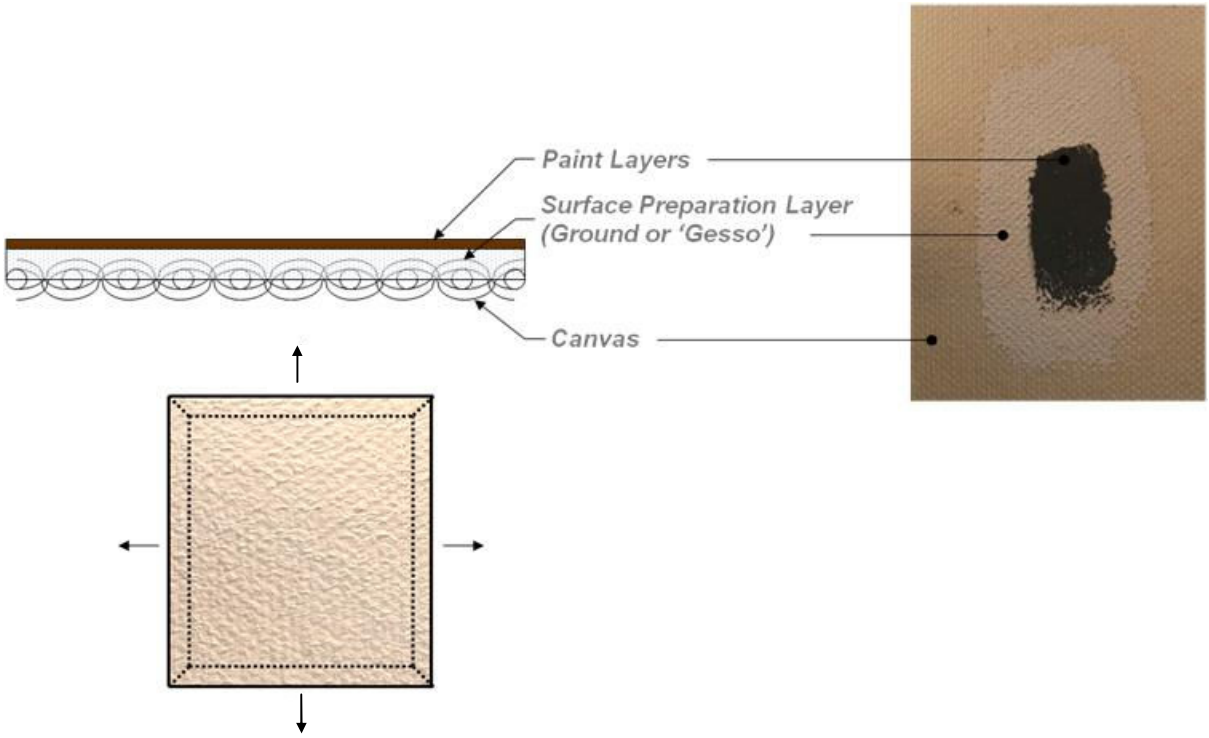

Figure 7-10, schematic of structure in art paintings (35).

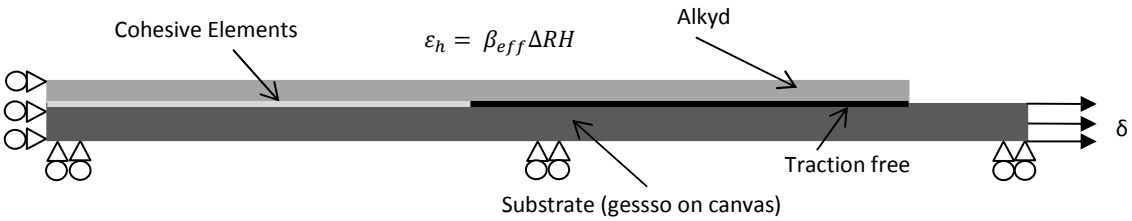

Figure 7-11, finite element model of alkyd on primed canvas.

The models with two rigid elements and a cohesive element in the middle used in chapter 6, (see Figure 6-52a and Figure 6-52b) were used to create similar plots of traction-separation responses of the modified cohesive element using the calibrated cohesive parameters shown in Table 7-1. Note that the parameters for normal and shear loading modes were set equal. The results are shown in Figure 7-12 and Figure 7-13 for mode I and mode II, respectively. Figure 7-12a and Figure 7-13a correspond to the case where $\delta<\delta_o$ whereas Figure 7-12b and Figure 7-13b correspond to the case of $\delta>\delta_o$ but δ less than the final separation, δ_{max}. The bold lines in Figure 7-12 and Figure 7-13

represent the traction-separation response of the cohesive elements without the use of the fatigue subroutine which of course results in an infinite fatigue life.

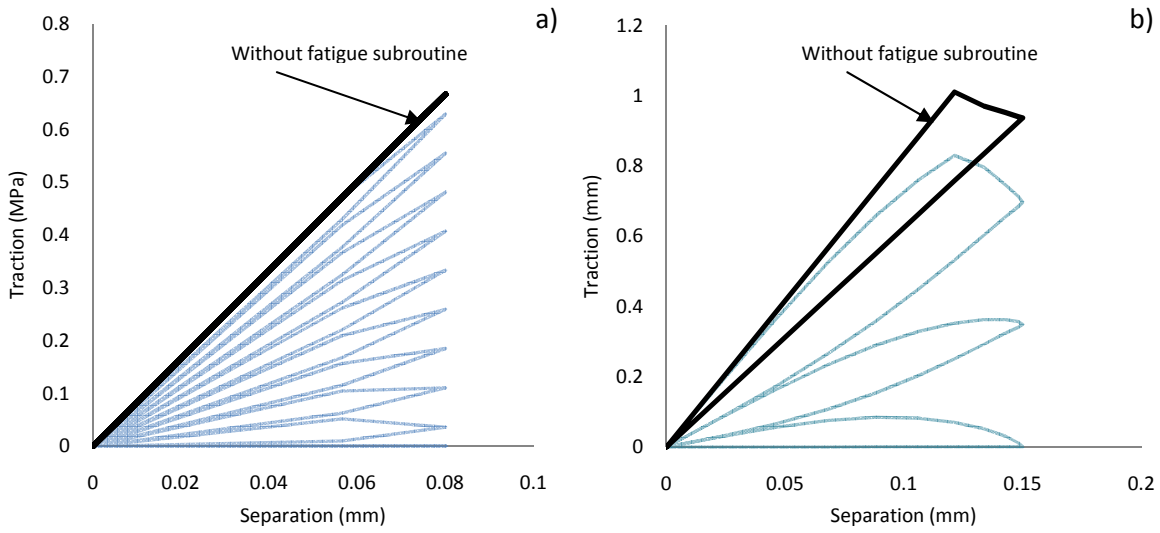

Figure 7-12, traction-separation response under mode I loading with: a) maximum loading less than the damage initiation, δ = 0.05 mm, b) maximum loading greater than damage initiation, δ = 0.15 mm.

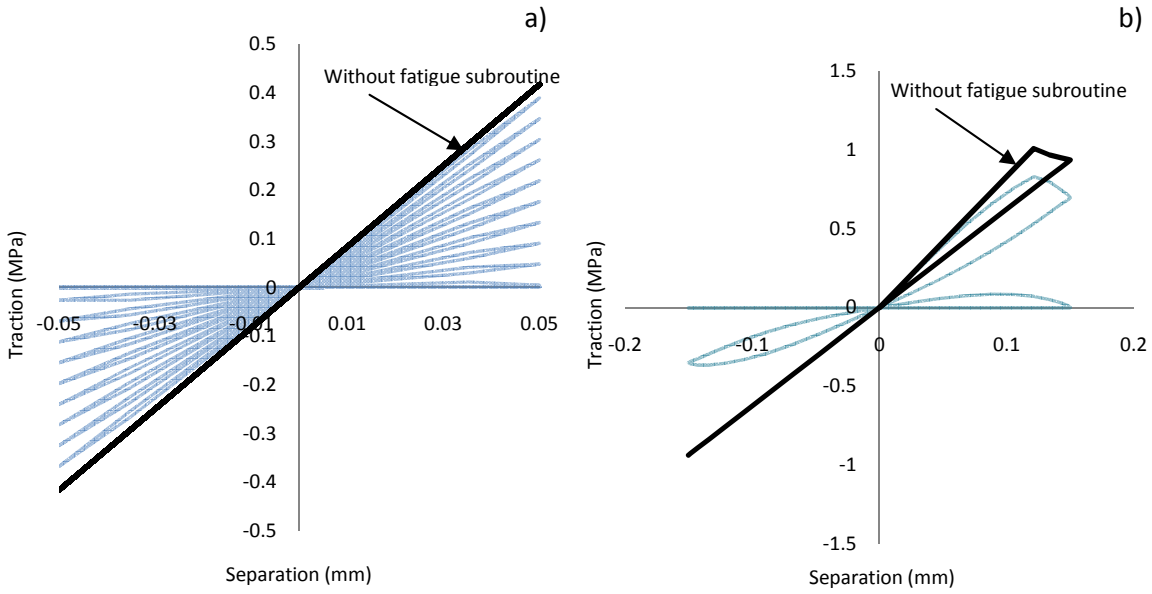

Figure 7-13, traction-separation response under mode II loading where: a) maximum loading less than the damage initiation, δ = 0.05 mm, b) maximum loading greater than damage initiation, δ = 0.15 mm

A layer of the modified cohesive elements was used in the finite element model of the painting as shown in Figure 7-11. Symmetric boundary conditions were specified at the left end of the model and the bottom of the substrate is prevented from moving in the vertical direction. The material parameters in Table 5-1 and Table 5-2 were used for the alkyd film whilst the material properties of the substrate are taken from Young (109), which assume the primed canvas to be linear elastic with a Young's modulus and a Poisson's ratio equal to 3.6 GPa and 0.3, respectively. In addition, the expansion of the alkyd paint due to moisture absorption was measured experimentally in this project by soaking an identical paint sample in water. Firstly, free films of alkyd and gesso paint were cut into the same size of 15cm long and 1 cm wide as shown in Figure 7-14a. The relative humidity in the room was measured before the samples were soaked in water as shown in Figure 7-14b and left for 1 hour. It can be seen from the figure that the white gesso samples expand in water more than the alkyd. Afterwards, the samples were taken out and their lengths were measured immediately. A transparent glass plate was placed on the samples during measurement to make them flat and improved the accuracy of the measurement.

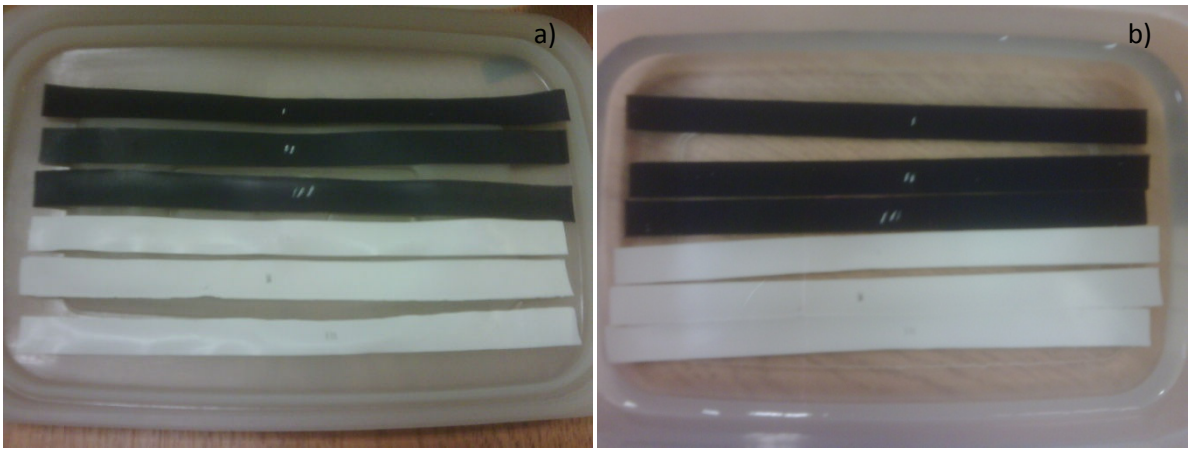

Figure 7-14, moisture expansion experiment: a) the dried samples before soaking, b) the samples soaking in water

The resulting change in sample length was then recorded which allowed the swelling strain, ε_h, to be determined. An 'effective' expansion coefficient, β, was then calculated from:

$$\beta = \frac{\varepsilon_h}{100-36} \qquad 7\text{-}1$$

where the denoniminator is the difference in the relative humidities that the sample was exposed to (100% corresponding to soaking and 36% to room storage conditions). In this way, the 'effective' expansion coefficient was therefore determined to be to 3.05 x 10^{-4} $\%RH^{-1}$. Similar experiments on canvas showed that it underwent no significant expansion due to moisture absorption, so this was neglected

Calibrations for the optimum time increment size and the value CETOL have been carried out. Both test use the model with three rows of 75 linear plane strain elements for the alkyd film and two rows of 120 linear plane strain elements modelling the canvas substrate The time increment size was determined through a convergence test using plots of output cyclic stress versus time as shown in Figure 7-15a. The increment size was varied from 2160 to 34560 seconds. It can be observed that there are very small differences among the data however, only time increment sizes smaller than 4320 seconds is small enough to accurately capture the peak stress therefore the time increment of 4320 seconds were used in the model.

A similar method was used to determine the optimum value of CETOL. The stress versus time plots from simulations with CETOL values ranging from 0.0001 to 0.1 are shown in Figure 7-15b. It is observed from the result that only the simulation with CETOL set to 0.0001 is able to accurately predict the peak stress; therefore this value is used in all the following models.

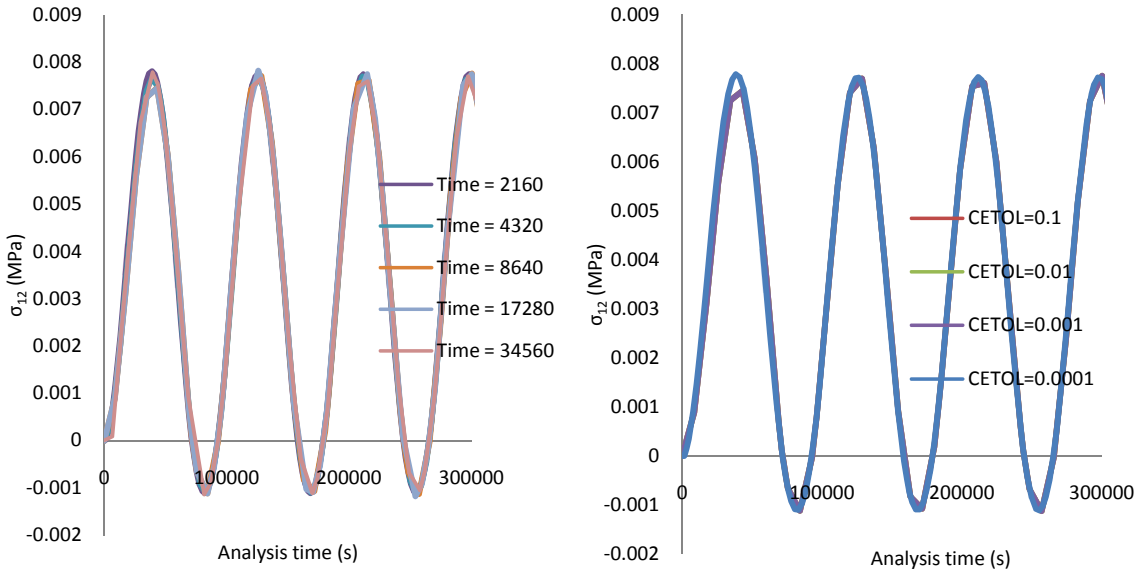

Figure 7-15, convergence test using for optimum: a) time increment b) CETOL value

A mesh convergence test was carried out using the envelopes of oscillation of the shear traction at the cracktip, as shown in Figure 7-16. The environmental cyclic loading of 25 to 75 %RH at one cycle per day was used in the test. The end point of the envelope, where the traction reduces to zero, is where the cohesive element is fully damaged and is considered as the crack initiation time. The mesh densities of the alkyd film were varied from 2 elements through the thickness x 50 elements in length to 5 elements through thickness x 125 elements along the length. The legend label of each curve shows the number of elements through thickness x the number of elements through the length for both the alkyd and the canvas layers. The difference in the predicted crack initiation time between the model with the 3 x 75 alkyd film mesh density and the 5 x 125 mesh density is approximately 8 percent whilst the difference between the model with the 4 x 100 alkyd film mesh density and the mode with 5 x 125 mesh density is approximately 4 percent. In order to keep the computational cost low, it was decided to represent the alkyd film with three rows of 75 elements whereas the substrate was modelled with two rows of 120 linear plane strain elements; this mesh density was considered to be accurate enough and was used as the final mesh for the environmental fatigue study which will be reported shortly. In the case of low environmental stress, the model

takes almost one month for the analysis to reach the crack initiation point on a computer with a dual core 1.98 GHz processor and 3.48 GB of RAM. A higher mesh density will require over 50% more analysis time and could drain the computer's processing capability and memory storage which would causes the analysis to terminate before completion.

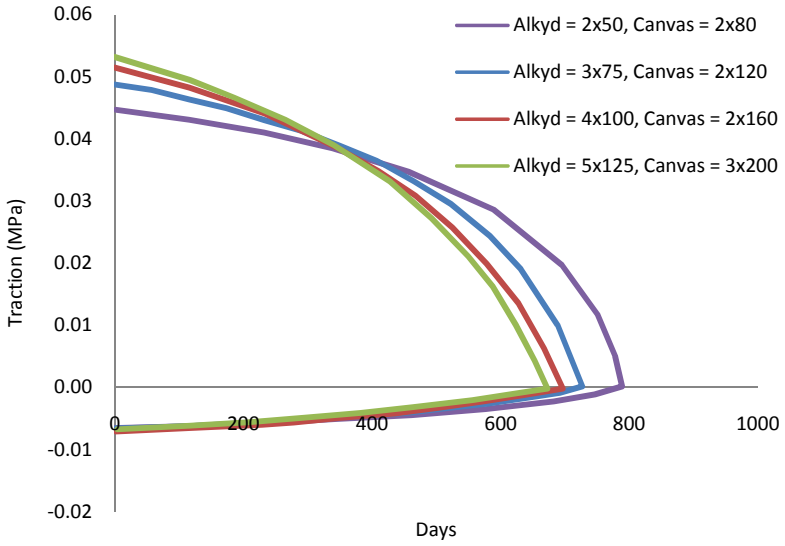

Figure 7-16, mesh convergence study

Six simulation cases were performed as shown in Table 7-2. In case 1, the extreme environmental cyclic loading of 25 to 75 %RH at one cycle per day was imposed. In the second case, boundary conditions similar to those kept in art museums (4) were applied, i.e. 50 +/- 5 % RH at one cycle per day. The third and fourth simulations used the extreme environmental cyclic loading of the first simulation and the standard museum humidity conditions in the second simulation, respectively, but also introduced a static horizontal mechanical load of 0.6 N/mm width (110).This represents the stretch in the canvas by the support frame Figure 7-10. The width, being the out of plane dimension in Figure 13, was set to 5 mm. The magnitude of the displacement was determined by making use of the effective cross-section of (72 mm^2 per metre width) and the modulus (3.6 GPa) of the a 0.4mm thick superfine linen canvas; both values are reported in (109), which resulted in a static strain of approximately 0.25%. This boundary condition was implemented in the simulation by imposing a

horizontal, constant (non cyclic) displacement. As a result of the very low frequency and low amplitude of the loading, the strain rates that are imposed in the model are extremely low, i.e. on the order of $2x10^{-6}$ min^{-1} (calculated using the median slope of the prescribed sinusoidal loading curve as shown in Figure 7-17).

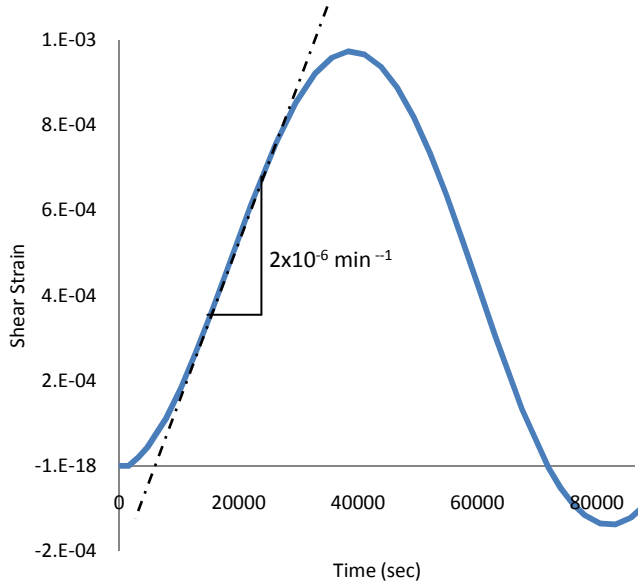

Figure 7-17, maximum strain rate of the environmental fatigue simulation of alkyd paint on canvas, *ΔRH* = 50%

However, the material model of the alkyd layer was calibrated from experimental data with a minimum displacement rate at 0.005 mm/min (0.00167 min^{-1} initial strain rate). Therefore the material behaviour at the very slow rates of the fatigue simulations are in effect extrapolated from the mechanical test data available and are very close to the equilibrium response of the viscoelastic model as shown in Figure 7-18

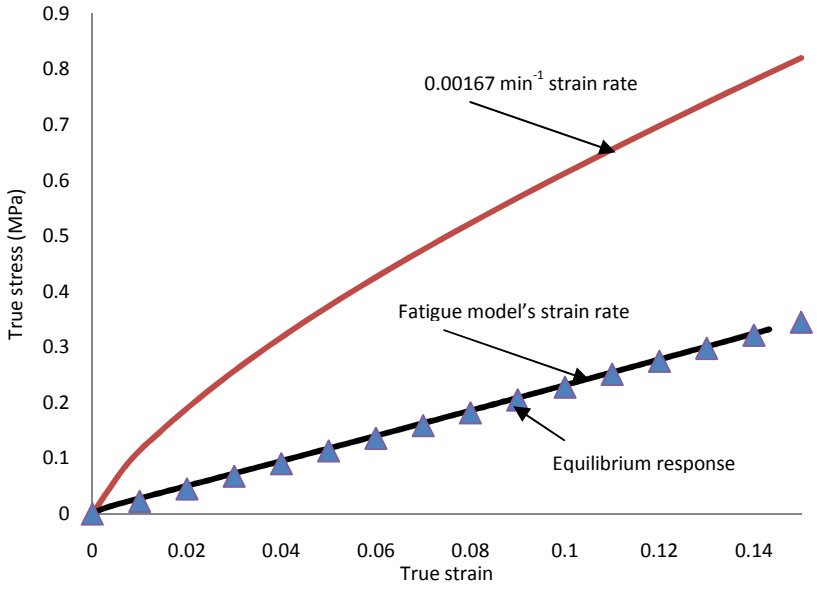

Figure 7-18, stress strain plot at very low strain rates of the calibrated van der Waals model of the alkyd paint

In addition, the cohesive law used in the model was calibrated using data from a 5 mm/min (0.167 min^{-1} initial strain rate) peel test. Therefore, all the experimental data were collected at much higher strain rates. This raises the question of the validity of the cohesive material parameters used. Therefore, an attempt to quantify this effect was made in case 5 by repeating the simulation in case 1 but decreasing the G_C value from 250 N/m to 150 N/m. Finally, in order to justify the effect of the ratio between G_{IIC} and G_{IC} on the life prediction, the value of G_{IIC} was set to twice the value of G_{IC} in case 6.

The predicted crack initiation times are shown in Table 7-2. The predictions seem reasonable and are of the order that one would expect when comparing the initiation time to the age of earliest paintings on canvas. It is predicted that the paint can start to delaminate within 3 years under severe environmental conditions. The prediction of the initiation time for delamination in paintings under normal museum conditions is greater than 100 years which is approximately $1/6^{th}$ of the age of earliest oil paintings on canvas and 2.5 times the number of years passed since the artists' alkyd paint line was introduced in 1974. Cases 3 and 4 show that the static loading speeds up the crack initiation time by approximately 170% under extreme conditions and by 300% under museum

conditions. (This also indicates that the more severe the environmental condition, the less is the effect of the static load on the damage initiation). Case 5 shows the effect of the value of G_C where the predicted initiation time is reduced by 49%. Case 6 shows that the increasing of G_{IIC} also results in slower crack initiation time. The trends of the predictions from case 5 and 6 are of course as expected.

Table 7-2, crack initiation times obtained from environmental fatigue simulations, * decreasing the G_C value to 150 N/m, ** $G_{IIC} = 2G_{IC}$,

Case	Static Mechanical Loading (strain %)	Hygrothermal Loading (Δ%RH) at 1 cycle/day	Initiation Time of Delamination (Years)
1	0	25-75	2.4
2	0	45-55	101
3	0.25%	25-75	1.7
4	0.25%	45-65	36.5
5*	0	25-75	1.24
6**	0	25-75	4.4

To illustrate the characteristics of the damage accumulation, the envelopes of oscillation of the shear traction versus time at the cracktip for cases 1, 2 and the cases 3, 4, are plotted in Figure 7-19a and Figure 7-19b, respectively. Note that the time was normalised by dividing by the initiation time of delamination. The end point of the envelope, where the normalised time equals 1 and the traction reduces to zero, is where the cohesive element is fully damaged and is considered the crack initiation point. The high nonlinearity in damage accumulation can be observed in these plots.

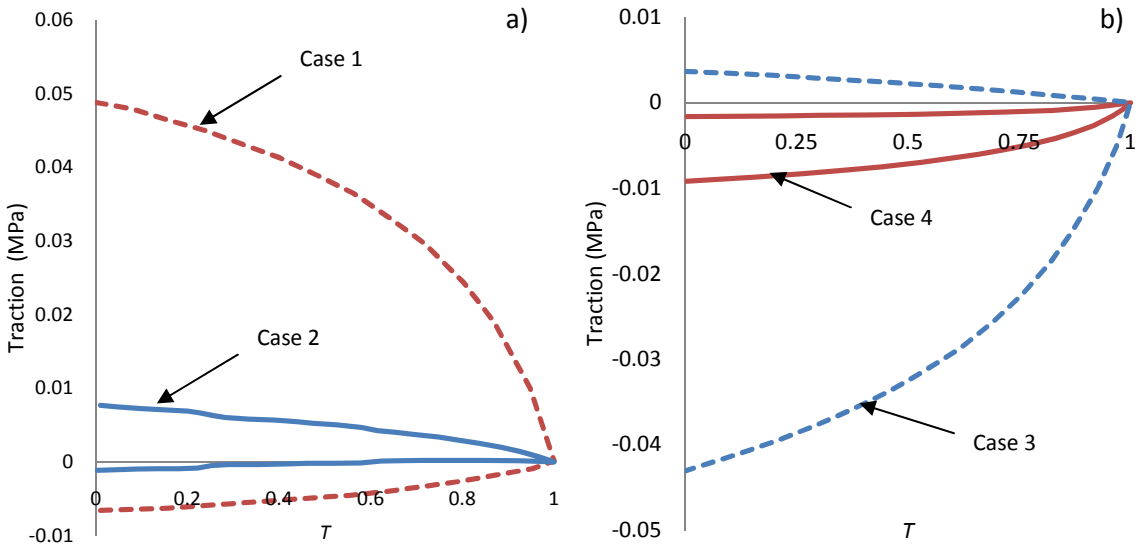

Figure 7-19, traction versus normalised time, T, at the crack tip for the fatigue simulations: a) without mechanical loading b) with 0.2% strain mechanical loading

A further study was performed in order to determine the propagation rate of the delamination. Figure 7-20 shows the crack extension versus time from the simulation of case 1. Each data point is obtained by recording the time at the point when the cohesive element at the current cracktip is fully damaged, the crack is then considered to be extended by one element length. It can be seen that, after initiation, the relationship of the crack extension versus time is found to be linear with the constant extension rate of approximately 0.1 mm per year. The crack extension per year is relatively small even under extreme humidity variations. However, it should be noted that this prediction is based on the effect of the humidity change alone. The crack extension rate may be increased in the real situation due to the addition of other factors such as temperature change, intensity of UV light, chemical damage etc.

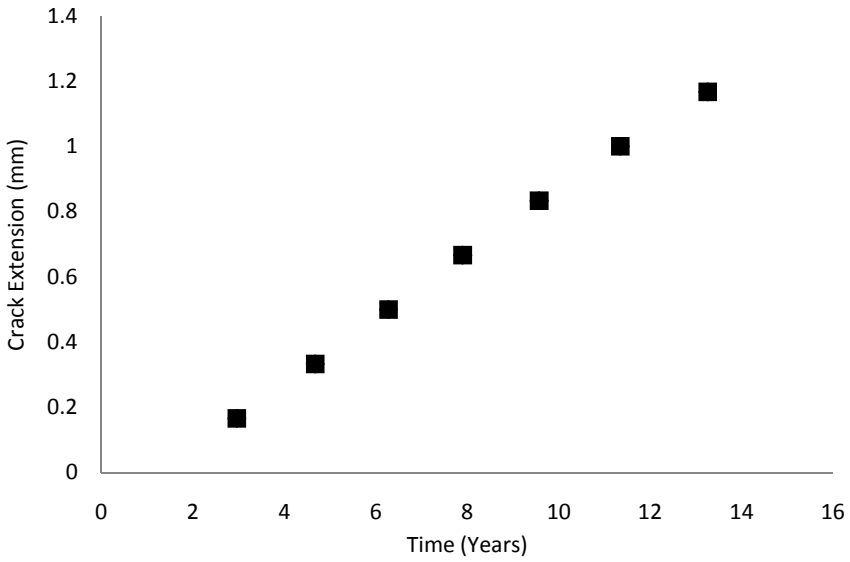

Figure 7-20, crack extension versus time for fatigue simulation case 1.

To summarise, in this chapter the development of a life prediction model of multilayered paint films under environmental fatigue has been outlined. The peel test simulation using CZM was carried out which provided the calibration of the cohesive parameters for the modelling of the delamination between the alkyd and acrylic gesso. A model of alkyd paint on primed canvas was created using the commercial finite element software Abaqus where the irreversible cohesive zone model was implemented to introduce fatigue damage to the calibrated cohesive law through a user subroutine. Life predictions for the delamination of alkyd from acrylic gesso primed canvas under several storage conditions including normal museum environment, extreme humidity condition and under tension caused from the stretch in the canvas, have all been considered.

8. Discussion

This chapter will give a discussion on the results provided in chapters 5, 6 and 7. It will include a discussion and conclusions drawn from experimental results presented in chapter 5, a justification for the selection of the simulation techniques chosen for the environmental fatigue modelling in chapter 6, and remarks on the fatigue life prediction of the alkyd on a primed canvas model in chapter 7.

8.1 Discussion on the experimental results

Tensile properties of the acrylic gesso and the blue alkyd paints as well as the delamination behaviour between the two paints were investigated in this work. This information is necessary for the finite element simulation of the peel test and fatigue life prediction model, outlined in chapter 7.

The test results provided in chapter 5 include results from tensile tests, relaxation tests and T-Peel tests. The tensile test results at different strain rate of the acrylic gesso and the blue alkyd shown in Figure 5-7 suggest that the materials are time dependent. Also the results suggest that the time-temperature superposition principle could be applied to the tensile behaviour of both paints. The relaxation tests, shown in Figure 5-9 and 5-10, further proved that both paints are nonlinear viscoelastic materials. Therefore the van der Waals hyperelastic model, in conjunction with the Prony series was used for the material model calibration of both paints.

The fracture toughness of the interface between the two paints was determined using the T-peel experiment. The average steady state peel force and peel angle were used in conjunction with the bilinear fit of the tensile stress-strain data from section 5.2 as input to the IC-Peel software to calculate the adhesive fracture toughness. The analytical model for the T-Peel test, described in section 5.5, has been developed for laminates which show linear elastic – plastic behaviour, not visco-elastic. There is currently no analytical visco-elastic derivation for the peel problem. Since it is the only analytical model available, in order to determine the estimates for the adhesive fracture

toughness, G_c, case 3 for the determination of the local plastic bending work, $G_{p,}$ explained in (75), was found to correspond to the experimental data (i.e. plastic deformation during initial bending and subsequent straightening and unloading) and the stress-strain curves for gesso and alkyd corresponding to the strain rate seen in the peel test, were approximated with the elastic-plastic curves using a bilinear law as shown in Figure 5-16. It is observed from the result in Table 5-4 that the correction due to plastic bending effects is less than 50%. This is below the range recommended in (111) which suggested that the correction can be allowed up to 70%.

The manual way of fitting the bilinear parameters raises the concern over the correctness of the output strain energy release rate from the IC-Peel, therefore the parametric studies in Figures 5-17, 5-18 and 5-19 were performed to address this concern. The studies show that even though each bilinear parameter was varied between 50% and 150%, the inclining and declining trends in the adhesive fracture toughness, G_C, stay within a ±10% variation.

The value of G_c we obtained through the analytical elastic-plastic peel model has led to a good agreement between the numerical predictions and experimental peel data, shown in Figure 7-7, further justifying the use of this analytical model, even though it was not derived specifically for viscoelastic materials. Also in (75), it is stated that the term G_c calculated by the analysis, represents the energy needed to break the interfacial bonding forces as well as the energy dissipated locally at the current peel front, whether the latter is plastic and/or viscoelastic in nature.

Apart from the peel test, which is considered a Mode-I fracture test, attempts were made to artificially accelerate the delamination between the two paint layers as well as to perform a mode-II fracture test on the sample; however these studies were unsuccessful.

8.2 Discussion on the development of an environmental fatigue model

The development of an environmental fatigue model was outlined in chapter 6. The model was designed to accurately predict three important aspects of the material behaviour which are 1) the

expansion due to humidity change, 2) the hyperviscoelastic behaviour and 3) the interfacial fatigue fracture. The review study on the available simulation techniques in Abaqus provided the information needed for the selection of the technique that was suitable for the fatigue model of the present work.

In sections 6.1, 6.2 and 6.3, it was shown that a thermal stress analysis, with temperature as one of the degrees of freedom of each node, can be used in the hygrothermal stress simulation of a hyperviscoelastic material in a similar manner. The numerical analysis is fairly simple and an accurate solution can be obtained even with an unrefined mesh. This was confirmed through the convergence tests and the comparisons of the numerical results with both analytical solutions (presented in chapter 3) as well as experimental results from published literature (6). Therefore it became apparent that the first two material behaviours, the hygrothermal expansion and hyperviscoelastic deformation, could easily be modelled using available modelling tools in the Abaqus library.

Simulation techniques for fracture mechanics were then reviewed and several techniques were shown to be suitable for modelling fracture in hyperviscoelastic material and interfacial fracture problems. These included the J-contour integral and the VCCT for crack initiation problems in section 6.4. A good agreement was observed between the two techniques for both linear elastic and hyperviscoelastic problems. Even though these two techniques were proven to be appropriate for studying fracture in hyperviscoelastic materials, their use is limited to crack initiation problems; therefore further investigations were performed in order to develop techniques suitable for crack propagation simulations. Comprehensive crack propagation studies using the Debond feature with the VCCT fracture criterion as well as cohesive zone modelling, CZM, were carried out. Whilst the former technique requires only the strain energy release rate input and a predefined crack path, the latter also requires a predefined traction separation law. However, in a more complex model such as a hyperviscoelastic simulation, the Debond technique was shown to suffer from convergence problems. The cohesive zone modelling studies showed that both cohesive elements and cohesive

contact modelling options gave the same numerical results when the original thickness of the elements was set equals to 1. Therefore it was convenient to define the cohesive thickness as unity in every model using the cohesive zone modelling technique. The CZM was suitable for crack propagation under monotonic loading such as the T-peel simulation outlined in chapter 7, however without a modification, it could not be used to model fracture under cyclic loading. This led to a further investigation to determine a suitable technique for a low cycle fatigue fracture problem.

Two simulation techniques for fatigue fracture propagation were reviewed. The first was the direct cyclic fatigue method. There are several advantages of using this technique which are 1) it is a built-in feature in Abaqus, 2) the technique is suitable for modelling a Paris law type fatigue fracture and 3) the direct cyclic algorithm and the cycle skipping scheme help reduce the computational cost. Nevertheless, the fact that this technique is based on a Paris law coefficient (which is currently unavailable from experiments) and the interpenetration of the top and bottom crack surfaces as explained in Section 6.7 rendered this technique unsuitable to be used in the final model. The second technique considered was the Irreversible Cohesive Zone Model (ICZM), (98). The latter technique can be applied to low cycle fatigue of interfacial crack problems. Most importantly, unlike the direct cyclic fatigue method, it does not require a Paris Law definition. The technique was also proven to be suitable for both Mode-I and Mode-II fracture problems. The implementation of this technique required the use of a user defined subroutine; however, this was fairly simple and did not significantly increase the computational cost. Even so, it should be noted that in the case of very long periods of cyclic loading i.e. when the fatigue loading is in the order of hundreds of years, the computational cost without a cycle skipping scheme in place is high and it could take up to several weeks for the simulation to complete. The investigation on this technique also showed that a proper definition of the time step is required in order to attain an accurate result.

From sections 6.5 to section 6.8, it was concluded that the ICZM was the most suitable technique for modelling environmental fatigue in multilayer paints. By implementing this technique into a

hygrothermal expansion model of a hyperviscoelastic material, a suitable model for environmental fatigue simulation in paint layers could be constructed.

8.3 Discussion on the fatigue life prediction of the blue alkyd and acrylic gesso paint on canvas

In chapter 7 it was shown that the life prediction of multilayered paint films can be achieved using the information obtained from several experiments including: (i) the hyperviscoelastic material model parameters calibrated from tensile tests, (ii) the fracture toughness from the peel test, (iii) material properties of the primed canvas from published literature, (iv) the swelling coefficient of the alkyd paint and (v) the cohesive law determined inversely from the peel test simulation. This procedure as well as remarks on each of the five necessary pieces of information listed above is outlined below.

Firstly, the peel test numerical model was created based on the geometry of the T-Peel experiments outlined in Chapter 5. The material parameters of the alkyd and the acrylic gesso from Table 5-1 and 5-2 were used for each peel arm. The strain energy release rate in Table 5-4 was used as the cohesive fracture energy of the cohesive elements whereas as the cohesive stiffness, k, and the maximum traction, σ_{max}, parameters were calibrated through parametric tests. The latter involved comparing the steady state region of the load-displacement curves from the simulation with the experimental T-peel data corresponding to 5mm/min. The fact that the constitutive law of the paint used in this model is time dependent increased the complexity and computational cost. This, however, was deemed to be necessary as it was shown in an additional simulation of the peel test where the viscoelastic material model was replaced with an elastic-plastic, rate-independent, stress strain curve corresponding to 5mm/min for both paints, that the predictions did not agree as well as the viscoelastic analysis did with the experimental data .

Secondly, the calibrated cohesive law was used to describe the interface behaviour between the alkyd and a gesso primed canvas. The material model of the alkyd was obtained from Tables 5-1 and

5-2, whereas the material properties of the primed canvas were obtained from published literature (109).

Thirdly, the swelling strain of the alkyd paint in the model is captured by using the effective expansion coefficient obtained from equation 7-1. The swelling strain was measured experimentally by soaking the paint film into water. It should be noted that the coefficient was only used to apply the effective swelling strain into the model but it does not fully represent the actual hygrothermal strain coefficient. Nevertheless, the coefficient value was compared to the hygrothermal coefficient of alkyd paint reported in literature (35) and it was found that it was within the same order of magnitude.

Finally, life prediction analyses for crack initiation time were carried out. It should be noted that the strain rate of the fatigue model is far below the slowest strain rate in the actual experimental data used to calibrate the material model. It was found that the stress-strain response at this low strain rate is close to the equilibrium response. The simulation takes approximately 24 hours to complete the calculation corresponding to a three years loading period which is considered a very time consuming simulation. An attempt to reduce the analysis time by increasing the size of the time step was proven to be unsuccessful as it resulted in an inaccurate prediction and a termination of the model due to non-convergence.

9. Conclusions

The significant findings from this study are summarised in this chapter and some possible areas for future work are discussed.

9.1 Experimental work

The experimental work primarily involved studying the tensile properties of acrylic gesso and pthalo blue alkyd. Uniaxial tensile tests and relaxation tests were performed on free films of the alkyd and gesso paints where the effects of displacement rate, environment and age on the mechanical properties were considered. The tensile test results show that the higher the strain rate, the higher the stiffness of the paints; also, the higher the temperature, the lower the stiffness. The effects of these two factors on the tensile properties show that the time-temperature superposition approach could be applied in a further study of these paints. The tensile tests of the paints at different ages, varying from 20 to 1600 days old, show that storage life only affects the tensile properties of the alkyd not the properties of the gesso. The relaxation tests show that the relaxation modulus of the paint films varies with both strain and time; therefore, the tensile properties of the paints were modelled with a nonlinear viscoelastic material model. The tensile test results at different strain rates were used in conjunction with the relaxation test data to calibrate the material models based on the van der Waals hyperelastic model, and the Prony series.

Peel tests on the alkyd/gesso paint combination were performed at different temperatures. It is found that the higher the test temperature, the lower the initial slope and the steady state peel force in the load-displacement curve. The effect of strain rate was also studied where it is shown that a higher displacement rate results in an increase in the steady state peel force and the initial slope of the curve. The adhesive fracture energy was determined through the analytical model reported by Kinloch et al (75) using a bilinear fit to the stress-strain curves of the paints under the same strain rates as those used in the peel test. The fracture toughness from the test at higher

speed, 50mm/min, was found to be higher than that from the test at lower speed, 0.5mm/min, but only by 5%. Finally, parametric studies were conducted to address the effect of the bilinear stress strain approach on the analytical calculation of G_C. The result shows that by varying each parameter of the bilinear law from 50% to 150% of its original value will result in less than 10% change in the calculated fracture toughness.

9.2 Finite element analysis and fatigue life prediction model

Fracture mechanics simulation techniques in Abaqus suitable for nonlinear-viscoelastic materials were reviewed. Each technique was investigated by parametric study, and by comparing the numerical results from the simulations using standard test geometries to known analytical solutions, and the results of previous findings. The limitations, advantages and the possibility of using each simulation technique in modelling environmental fatigue in films were addressed. The capability to determine the energy release rate of the VCCT technique has been studied using the SENB geometry. It was found that the prediction is in agreement with that obtained using the J-contour integral technique for the linear elastic and viscoelastic cases, however not for the elastic-plastic case. A parametric study was carried out to evaluate the agreement between the cohesive element and cohesive contact techniques. It was found that with a cohesive thickness of unity, both techniques give the same numerical result. After the review of techniques, the following were included in the peel test simulations and the environmental fatigue life prediction models: thermal stress analysis, nonlinear viscoelastic analysis, cohesive element modelling and a USDFLD user-defined subroutine for the Irreversible cohesive zone.

A cohesive zone was used in a finite element model of the peel test such that the cohesive parameters could be calibrated. The calibration was performed using peel test data of materials aged for 300 days, tested at 5 mm/min, 50 %RH and 25°C. The predicted load-displacement curve from the simulation shows good agreement with the one from the test result, especially at the steady state peel load. The calibrated cohesive law was also used in the simulation of the peel test at

higher and lower displacement rates. However, it was found that the predicted steady state peel forces are the same as those from the test at 5mm/min.

The calibrated constitutive and traction-separation laws were implemented in an Abaqus user-defined subroutine employing the Irreversible Cohesive Zone Modelling such that the effect of cyclic loading on damage was taken into account. The initiation of delamination for alkyd on primed Belgian superfine linen under extreme and museum standard conditions was predicted. The predictions seem reasonable and are of the order that one would expect when comparing to the ages of the earliest paintings on canvas. Also, delamination growth is predicted for the same paint combination under extreme humidity change. The growth rate is on the order of 0.1mm per year, which is relatively small.

9.3 Implications for conservation and future work

Predicting fatigue life for paint combinations such as the ones studied in this work is very complex as there are many variables that need to be taken into account. The purpose of this work is to provide museum information on addressing the potential risks in art conservation, and to provide guidelines for upcoming research on fracture in valuable artists' paintings.

In the experimental work, the effects of temperature, age and strain rate on the tensile behaviour have been investigated. However, the effects of humidity, composition of the paints (surfactant and pigment content) and UV light have not been examined. Peel tests at the lower test speed, i.e. at 0.5 mm/min, were not very reliable as only one sample out of 20 reached steady state peel conditions. Since the thermal and hygrothermal deformation of paints under museum conditions occurs at extremely low rates and is very small, more experiments at lower strain rates are needed. The time-temperature superposition principle will be useful in dealing with this issue.

Attempts were made to create an accelerated fatigue delamination in paint samples using a temperature-humidity controlled chamber, however these were unsuccessful. This was mainly due

to the chamber failing to continuously maintain the desired test condition and breaking down before the tests were complete. Also, the samples, which were suspended inside the chamber with a hanging weight, occasionally broke and fell off the hanger due to air currents inside the chamber. For future attempts, it is recommended to make samples of paint layers on a framed stretched canvas or a primed wooden board to reduce sample movement.

Regarding the numerical work, the effect of strain rate on the material behaviour has been modelled in the peel test simulation. However, the traction-separation laws were defined as time independent. Therefore, the steady state peel load from the simulation does not change with the loading speed and this does not correlate with the experimental results. Additional variables, namely the effect of relative humidity, temperature and material age on both the constitutive and the cohesive behaviour need to be investigated. In the fatigue life predictions, the effect of strain rate and humidity/temperature on the cohesive parameters also needs to be implemented as well as the anisotropic behaviour of the canvas. Due to the fact that there was no “cycle skipping” scheme involved, the fatigue simulation, especially the one corresponding to the museum environmental conditions, took up to one month to complete and occasionally terminated prior to the crucial stage of the simulation, i.e. the crack initiation point. This also prevented the use of a finer mesh and more complex geometries, i.e. more layers.

The current work is merely an initial attempt towards predicting the fatigue life of precious art paintings such that these can be conserved for future generations. However, a methodology has been defined for further work in this area.

10. References

1. Gottsegen MD. *The painter's handbook, revised and expanded.* New York : Watson Guptill Publication, 2006.

2. Sands S. *Using oils with acrylics. Just Paint, Golden Artist Aolors Inc. Issue 24.* 2011.

3. Crook J, Learner TJS. *The impact of modern paints.* Tate Gallery Publishing, 2000.

4. Thomson G. *The museum environment 2nd edition. Oxford: Butterworth.* 1986.

5. Hagan EWS. *The viscoelastic properties of latex artist paints.* PhD Thesis, Imperial College, 2009.

6. Young CRT. *Department of Conservation & Technology, Courtauld Institute of Art, London, UK, Private conversation.* 2010.

7. Digney-Peer S, Burnstock A, Learner TJS, Khanjian H, Hoogland F, Boon J. *The migration of surfactants in acrylic emulsion paint films Modern art; .* New Museums, Contributions to the Bilbao Congress, 2004; 202-7.

8. Jones FN, Mao W, Ziemer PD, Xiao F, Hayes J, Golden M. *Artist paints—an overview and preliminary studies of durability.* 2005. pp. 52:9-20.

9. Scalaron D, Chiantor O. *Separation techniques for the analysis of artists' acrylic emulsion paint.* journal of Separation Science, 2004;27:263-74.

10. Brown GL. *Formation of films from polymer dispersions.* Journal of Polymer Science, 1956;22:423-34.

11. Hagan EWS. *The viscoelastic properties of latex artist paints.* PhD Thesis, Imperial College, 2009.

12. http://www.britannica.com/EBchecked/topic/15764/alkyd-resin. [Online] [Cited: 2012-12-12.]

13. Lack CM. *Performance and Working Properties of Artists' AlkydPaints, .* M.A.C. thesis, Queen's University, Canada, 1988.

14. Ploeger R, Scalarone D, Chiantore O. *The characterization of commercial artists' alkydpaints.* Journal of Cultural Heritage, 2008;9:4:412-9.

15. Goldsmith HA. *Alpha- and beta-hydroxyls of glycerol in preparation of alkyd resins.* Industrial Engineering Chemistry, 1948;40:7:1205-11.

16. Morgans WM. *Outlines of paint technology 3rd. ed.* London : Edward Arnold, 1990.

17. Hagan EWS, Charalambides MN, Young CRT, Learner TJS, Hackney S. *Tensile properties of latex paint films with TiO2 pigment.* Journal of Mechanics of Time-Dependent Materials, 2009;13:149-61.

18. Mecklenburg MF. Determining the acceptable ranges of relative humidity and temperature in museums and galleries, part 2, structural response to temperature. [Online] Museum Conservation Institute. [Cited:] http://hdl.handle.net/10088/7055; 2007; 2012.

19. Young CRT. *Interfacial interactions of modern paint layers, Modern paints uncovered.* Postprints Tate/Getty NGA Symposium, 2006:247-56.

20. Kim SR, Nairn JA. *Fracture mechanics analysis of coating/substrate systems: II. Experiments in bending,.* Engineering Fracture Mechanics, 2000;65:595-607.

21. Kim SR, Nairn JA. *Fracture mechanics analysis of coating/substrate systems: I. analysis of tensile and bending experiments.* Engineering Fracture Mechanics, 2000;65:573-93.

22. Nichols ME, Darr CA, Smith CA, Thouless MD, Fische ER. *Fracture energy of automotive clearcoats-I, experimental methods and mechanics.* Polymer Degradation and Stability, 1998;60:29I-9.

23. Nichols ME, Gerlock JL, Smith CA, Darr CA. *The effects of weathering on the mechanical performance of automotive paint systems.* Progress in Organic Coatings, 1999;35:153–9.

24. Song MC. *Adhesion in modern artists' paints.* MSc thesis, Imperial College London (2007).

25. Valkana G. *Measuring the adhesion properties of modern artists' paints.* MSc Thesis, Imperial College London (2006).

26. Mecklenburg MF, Tumosa CS. *An introduction into mechanical behaviour of paintings under rapid loading conditions. Art in Transit: Studies in the Transport of Paintings,.* Washington D.C. : National Gallery of Art , 1991;137-72.

27. Erlebacher JD, Mecklenburg MF, Tumosa CS. *The mechanical behaviour of artists' acrylic paints with changing temperature and relative humidity.* AIC Paintings Speciallity Group Postprints, 1992.

28. Hagan EWS, Charalambides MN,Young CRT ,Learner TJS, Hackney S. *Influence of the inorganic phase concentration and geometry on the viscoelastic properties of latex coatings through the glass-transition.* Polymer, 2011, 52:7:1662-73.

29. Hagan EWS, Charalambides MN,Young CRT ,Learner TJS, Hackney S. *Viscoelastic properties of latex paint films in tension: Influence of the inorganic phase and surfactants.* Progress in Organic Coatings, 2010;69:73–81.

30. Giannakopoulos I. *The mechanical properties of polyester-based coil coatings, correlations with chemical structure.* PhD thesis, Imperial College London, Department of Mechanical Engineering, 2012.

31. Ogden RW. *Large Deformation Isotropic Elasticity - On the Correlation of Theory and Experiment for Incompressible Rubberlike Solids, Proceedings of the Royal Society of London. Series A, Mathematical and Physical Sciences,.* 1972;326:1567:565-84.

32. Enderle HF, Kilian HG. *General deformation modes of a van der Waals network. Progress in Colloid and Polymer Science.* 1987;75:55-61.

33. Marckmann E, Verron G. *Comparison of hyperelastic models for rubberlike materials. Rubber Chemistry and Technology .* 2006;79:5:835-58 .

34. Mooney M. *A Theory of Large Elastic Deformation. Journal of Applied Physics.* 1940;11:582-92.

35. Hagan EWS. *The Mechanical Properties of Paints used by Modern Artists.* MPhil-PhD Transfer Report, Imperial College London, Department of Mechanical Engineering, 2006.

36. Rivlin, RSl. *Large elastic deformations of isotropic materials. I. Fundamental concepts. Philosophical Transactions of the Royal Society of London. SeriesA, Mathematical and Physical Sciences.* 1948;240:822:459-90.

37. Gent AN. *A new constitutive relation for rubber, Rubber Chemistry and Technology.* 1996;69:59.

38. Ogden RW. *Non-Linear Elastic Deformations.* 1984 Chichester: Ellis Horwood. 532.

39. ABAQUS version 6.8 Documentation, ABAQUS, Inc., Dassault Systemes, 2008.

40. ABAQUS version 6.9 Documentation, ABAQUS, Inc., Dassault Systemes, 2009.

41. Wall FT. *Statistical thermodynamics of rubber, Journal of Chemical Physics.* 1942;10:132.

42. Treloar LRG. *The elasticity of a network of long-chain molecules I, Transactions of the Faraday Society.* 1943;39:36-41.

43. Boyce MC and Arruda EM. *Constitutive models of rubber elasticity: A review. Rubber Chemistry and Technology.* 2000;73:3:504-23.

44. Cohen A. *A Padé approximant to the inverse Langevin function. Rheologica Acta.* 1991;30: 270-3.

45. Kilian HG. *Thermo-elasticity of networks. Colloid & Polymer Science.* 1982;260:10:895-910.

46. Enderle HF, Kilian HG. *General deformation modes of a van der Waals network. Progress in Colloid and Polymer Science.* 1987;75:55-61.

47. Williams JG. *Stress Analysis of Polymers. 2nd ed. 1980, New York: Halsted Press. 360.*

48. Goh SM, Charalambides MN and Williams JG. *Determination of the constitutive constants of non-linear viscoelastic materials. Mechanics of Time-Dependent Materials.* 2004;8:255-68.

49. Goh SM, Charalambides MN and Williams JG. *Large strain time dependent behavior of cheese. Journal of Rheology.* 2003;47:3:701-16.

50. Charalambides MN, Wanigasooriya L, Williams JG, Goh SM, Chakrabarti S. *Large deformation extensional rheology of bread dough. Rheologica Acta.* 2006:46:239-48.

51. Wiechert E. *Gesetze der elastischen Nachwirkung für constante Temperatur. Annalen der Physik, .* 1893. 50: p. 335-348; 546-570.

52. Leaderman H. *Elastic and creep properties of filamentous materials and other high polymers. Washington, D.C.: The Textile Foundation.* 1943.

53. Taylor RL, Pister KS and Goudreau GL. *Thermomechanical analysis of viscoelastic solids, International Journal for Numerical Methods in Engineering, .* 1970;45.

54. Mohammed MAP. *Mechanical characterisatio, processing and microstructure of wheat flour dough, PhD Thesis, Department of Mechanical Engineering, Imperial College London.* 2012.

55. Tobolsky RD, Andrews AV. *Systems manifesting superposed elastic and viscous behavior. Journal of Chemical Physics.* 1945;13:1:3-27.

56. Leaderman H. *Elastic and creep properties of filamentous materials and other high polymers, Washington, D.C.: The Textile Foundation.* 1943.

57. Williams ML, Landel RF, and Ferry JD. *The temperature dependence of relaxation mechanisms in amorphous polymers and other glass-forming liquids. Journal of the American Chemical Society.* 1955;77:14:3701-07.

58. Ferry, JD. *Viscoelastic Properties of Polymers. 3rd ed. 1980, New York: Wiley.*

59. Paris PC. *The growth of fatigue cracks due to variations in load, Ph.D. Thesis, Lehigh University.* 1962.

60. Paris PC, Gomez MP, Anderson WE. *A rational analytic theory of fatigue, The trend in Engineering, 1961;13:9-14.*

61. Rice JR. *Elastic Fracture Mechanics Concepts for Interfacial Cracks. Journal of Applied Mechanics (Trans. ASME).* 1988;55:11:3:98-103.

62. Hutchinson JW. *Mixed mode fracture mechanics of interfaces, Metal-ceramic interfaces; Proceedings of an International Workshop, Santa Barbara, CA, UNITED KINGDOM,.* 1989;295-306.

63. Suo Z. *Fracture in Thin Films, Encyclopedia of Materials: Science and Technology.* 2008;3290-3296.

64. Schapery RA. *A theory of crack initiation and growth in viscoelastic media; I. theoretical development, International Journal of Fracture .* 1975:11:141-59.

65. Liang RY, Zhou J. *Energy based approach for crack initiation and propagation in viscoelastic solid, Engineering Fracture Mechanics .* 1997;58:I/2:71-85.

66. Moore DR, Pavan A, Williams JG. *, Fracture mechanics testing methods for polymers, adhesives and composites. London, Elsevier Science.* 2001.

67. Johnson WS. *Stress Analysis of the Cracked Lap Shear Specimen: An ASTM Round Robin, Journal of Testing an Evaluation.* 1987;25:6:303-324.

68. Poursartip A, Chinatambi N. *, Fatigue Growth, Deflection, and Crack Opening Displacement in Cracked Lap Shear Specimen; Composite Material: Testing and Materials, Philladelphia.* 1990;301-323.

69. Chang T, Sproat EA, Lai YH, Sherphard NE, Dillard DA,. *A Test Method for Accelerating Humidity Conditioning and Estimation of Adhesive Bond Durability, The Journal of Adhesion .* 1995;60:1:153-162.

70. Dillard DA, Chen B, Chang T, Lai YH. *Analysis of the Notched Coating Adhesion Test, The Journal of Adhesion.* 1999;69:1:99–120.

71. Nichols ME, Darr CA, Smith CA, Thouless MD , Fische ER. *, Fracture energy of automotive clearcoats-I, Experimental methods and mechanics, Polymer Degradation and Stability.* 1998;60:291-299.

72. Nichols ME, Gerlock JL, Smith CA, Darr CA. *The effects of weathering on the mechanical performance of automotive paint systems, Progress in Organic Coatings .* 1999;35:153–159.

73. *Standard test method for peel or stripping strength of adhesive bonds, ASTM D903-98.* 1998.

74. *Standard test method for peel resistance of adhesives (T-Peel), ASTM D 1876-95.* 1995.

75. Kinloch AJ, Lau CC, Williams JG. *Peeling of flexible laminates.* International Journal of Fracture,1994;66:45-70.

76. Thouless MD, Yang QD. *A parametric study of the peel test, International Journal of Adhesion & Adhesives .* 2008;28:176–184.

77. Mars WV, Fatemi A. *A literature survey on fatigue analysis approaches for rubber, International Journal of Fatigue.* 2002;24:949–61.

78. Mecklenburg MF. *Determining the acceptable ranges of relative humidity and temperature in museums and galleries, part 2, structural response to temperature. Museum Conservation Institute, http://hdl.handle.net/10088/7055; 2007; Accessed July 2012.*

79. Dowling NE, Begley JA. *Fatigue crack growth during gross plasticity and the J-integral, Mechanics of crack growth, ASTM STP.* 1976;590:80-103.

80. Anderson TL. *Fracture Mechanics Fundamental and Applications, 3rd Edition, Taylor & Francis.* 2005.

81. Hellen TK. *The finite element calculations of stress intensity factors using energy techniques, 2nd International Conference on Structural Mechanics in Reactor Technology, Berlin .* 1973;Paper G5/3.

82. Benzley SE, Parks DM. *Fracture Mechanics, Structural Mechanics Computer Programs, University Press of Virginia .* 1974;85-102.

83. Wilson WK, Yu IW. *The use of the J integral in thermal stress crack problem; International Journal of Fracture.* 1979;15:377–87.

84. Shih CF, Moran B, Nakamura T. *Energy release rate along three dimension crack front in a thermally stress body; International Journal of Fracture.* 1986;30:79–102.

85. Stern M. *The numerical calculation of thermally induced stress intensity factor, Journal of Elasticity.* 1979;9:91–95.

86. Chen WH, Chiang CR, Chen KT. *An integral Jr for a crack perpendicular to the interface of a bonded composite, Engineering Fracture Mechanics.* 1987;28:3:301-307.

87. Khandelwal R, Chandra Kishen JM. *The use of conservative integral in bi-material interface crack problems subjected to thermal loads, International Journal of Solids and Structures .* 2008;45:2976–2992.

88. Rybicki EF, Kanninen MF. *A finite element calculation of stress intensity factors by a modified crack closure integral.* Engineering Fracture Mechanics;1997:9:931-8.

89. Viswanath S, Lakshminarayana HV, Ravindranath DJ. *A Modified Crack Closure Integral Method for Calculating Stress Intensity Factors for Cracked Plates subject to Bending Loads; International Journal of Fracture, Kluwer Academic Publis.* 1989;41:45-50.

90. Krueger R. *Virtual crack closure technique; History, approach, and applications, American Society of Mechanical Engineers, Appl Mech Rev.* 2004;57:2:109-143 .

91. Rice JR. *A Path Independent Integral and the Approximate Analysis of Strain Concentration by Notches and Cracks, Journal of Applied Mechanics.* 1968;35:35:379-86.

92. Cherepanov GP. *The propagation of cracks in a continuous medium, Journal of Applied Mathematics and Mechanics.* 1967;31:3:503-512.

93. Courtin S, Gardin C, Bezine G. *Advantages of the J-integral approach for calculating stress intensity factors when using the commercial finite element software ABAQUS, Engineering Fracture Mechanics .* 2005;72:2174–2185.

94. Needleman A. *A continuum model for void nucleation by Inclusion debonding.* Journal of Apply Mechanics 1987;54: 525.

95. Yang B, Mall S, Ravi-Chandar K. *A cohesive zone model for fatigue crack growth in quasi-brittle materials, International Journal solids and structure .* 2001;38:3927-3944.

96. Turon A, Costa J, Camanho PP, Da´vila CG. *Simulation of delamination in composites under high-cycle fatigue. Composites: Part A .* 2007;38:2270–82.

97. Robinson P, Galvanetto U, Tumino D, Bellucci G, Violeau D. *Numerical simulation of fatigue-driven delamination using interface elements. International Journal for Numerical Methods in Engineering.* 2005;63:1824–48.

98. Roe KL, Siegmund T. *An irreversible cohesive zone model for interface fatigue crack growth simulation.* Engineering Fracture Mechanics 2003;70:209-32.

99. IC Peel. [Online] [Cited: 2012-08-September.] http://www3.imperial.ac.uk/meadhesion/testprotocols/peel.

100. Moore DR, Williams JG. *A Protocal for determination of the adhesive fracture toughness of flexible laminates by peel testing: fixed arm and t-peel methods.* An ESIS Protocal, 2010.

101. Kim KS, Aravas N. *Elastoplastic analysis of the peel test.* International Journal of Solids and Structures, 1988;24:417-435.

102. Johnson WS. *Stress analysis of the cracked lap shear specimen: An ASTM round robin, Journal of Testing and Evaluation.* 1987:15:6;303-24.

103. Tvergaard V, Hutchinson JW. *The relation between crack growth resistance and fracture process parameters in elastic-plastic solids.* Journal of the Mechanics and Physics of Solids 1992;40:1377.

104. Bao G, Suo Z. *Remarks on crack-bridging concepts.* Applied Mechanics Review 1992;45:355-66.

105. Ivankovic A, Pandya KC, Williams JG. *Crack growth predictions in polyethylene using measured traction–separation curves.* Engineering Fracture Mechanics, 2004;71:657–68.

106. Liechti KM, Chai YS. *Asymmetric shielding in interfacial fracture under In plane shear. Journal of Applied Mechanics .* 1992;59:295-304.

107. Maccagno TM, Knott JF. *The fracture behaviour of PMMA in mixed modes I and II. Engineering Fracture Mechanics .* 1989;34:1:65-86.

108. Hashemi S, Kinloch AJ, Williams JG. *The analysis of interlaminar fracture in uniaxial fibre-polymer composites. Proceeding of the Royal Society London .* 1990;427:173-199.

109. Young CRT. *Measurement of the biaxial tensile properties of paintings on canvas. PhD Thesis, Imperial College, University of London.* 1996.

110. Idelson AI. *About the choice of tension for canvas paintings. Les dilemmes de la restauration.* 2009:4.

111. Moore DR, Williams JG. The determination of adhesive fracture toughness for laminates by the use of different test geometry and consideration of plastic energy correction factors, Fracture of Polymers, Composites and Adhesives II, ESIS. 2003;32:341-53

11. Appendix

The Abaqus input files for the peel test and the environmental fatigue simulation, described in chapter 7 are provided in this chapter. Also, the Irreversible Cohesive Zone user define subroutine used in the fatigue simulations is presented here.

11.1 Abaqus input file for the peel test simulation

The Abaqus Standard input file for the peel test simulation at 5mm/min using visco analysis is shown below.

```
*HEADING
**
** Fatigue crack growth in Film, use with file af_film.for
**
*PREPRINT,ECHO=YES,HISTORY=YES,MODEL=YES,CONTACT=YES
*NODE
1,0,-0.1
1201,60,-0.1
40001,0,0
41201,60,0
50001,0,0
51201,60,0
90001,0,0.2
91201,60,0.2
*NGEN, NSET=LBOT
1,1201,1
*NGEN, NSET=LTOP
40001,41201,1
*NFILL, NSET=LOWER
LBOT,LTOP,4,10000
*NGEN, NSET=UBOT
50001,51201,1
*NGEN, NSET=UTOP
90001,91201,1
*NFILL, NSET=UPPER
UBOT,UTOP,4,10000
*NSET, NSET=GRIP
21199,71199
*NSET, NSET=UPPERARM, GENERATE
61201,81201,10000
*NSET, NSET=LOWERARM, GENERATE
11201,31201,10000
*NSET, NSET=CRACKFRONT, GENERATE
50001,50601,1
*NSET, NSET=OUTPUT
50600,50601,40600,40601
**
************************************************************
**
```

```
*ELEMENT,TYPE=CPE4H,ELSET=ELOWER
 1, 1, 2, 10002, 10001
*ELGEN, ELSET=ELOWER
 1,1200,1,1,4,10000,10000
**
*ELEMENT, TYPE=CPE4H, ELSET=EUPPER
 70001, 50001, 50002, 60002, 60001
*ELGEN, ELSET=EUPPER
 70001, 1200,1,1,4,10000,10000
**
*ELSET,ELSET=OUTPUT
 10600,80600
*ELSET, ELSET=LARM, GENERATE
 1,1196,1
 10000,11196,1
 20000,21196,1
 30000,31196,1
*ELSET, ELSET=TARM, GENERATE
 70000,71196,1
 80000,81196,1
 90000,91196,1
 100000,101196,1
*ELSET, ELSET=TGRIP, GENERATE
 71197,71200,1
 81197,81200,1
 91197,91200,1
 101197,101200,1
*ELSET, ELSET=LGRIP, GENERATE
 1197,1200,1
 11197,11200,1
 21197,21200,1
 31197,31200,1
**
************************************************************
*SOLID SECTION, ELSET=ELOWER, MATERIAL=GESSO
5
*MATERIAL,NAME=GESSO
*HYPERELASTIC, VAN DER WAALS, MODULI=INSTANTANEOUS
125,10,0.5
*VISCOELASTIC,TIME=PRONY
 0.727,, 1e-1
 0.15,, 1e0
 0.05,, 2e1
 0.03,, 2e2
 0.022,, 2e3
 0.02,, 2e4
 **
*SOLID SECTION, ELSET=EUPPER, MATERIAL=ALKYD
5
*MATERIAL,NAME=ALKYD
*HYPERELASTIC, VAN DER WAALS, MODULI=INSTANTANEOUS
75, 8, 0.5
*VISCOELASTIC,TIME=PRONY
 0.73,, 1e-1
 0.145,, 1e0
 0.05,, 1e1
 0.032,, 1e2
 0.02,, 1e3
 0.013,, 1e4
**
************************************************************
```

```
*RIGID BODY, REF NODE=71199, ELSET=TGRIP
*RIGID BODY, REF NODE=21199, ELSET=LGRIP
*ELSET, ELSET=SUPPER, GENERATE
70001,70600,1
*ELSET, ELSET=SLOWER, GENERATE
30001,30600,1
*SURFACE, NAME=SUPPER
SUPPER, S1
*SURFACE, NAME=SLOWER
SLOWER, S3
**
*CONTACT PAIR, INTERACTION=COHESIVE
SUPPER, SLOWER
*SURFACE INTERACTION, NAME=COHESIVE
5
*COHESIVE BEHAVIOR,ELIGIBILITY=SPECIFIED CONTACTS
8, 8, 8
*DAMAGE INITIATION,CRITERION=MAXS
1,1,1
*DAMAGE EVOLUTION,TYPE=displacement
0.375
**
************************************************************
*BOUNDARY
21199,1,1
71199,1,1
*INITIAL CONDITIONS, TYPE=CONTACT
SUPPER, SLOWER, CRACKFRONT
************************************************************
*STEP,NLGEOM,INC=100000000
*VISCO, CETOL=0.0001, STABILIZE, FACTOR=0.01
2,2160,1E-9,2
*BOUNDARY
21199,2,2,0
71199,2,2,180
**
*OUTPUT, FIELD, VARIABLE = PRESELECT, FREQUENCY=20
*ELEMENT OUTPUT, ELSET = EUPPER
E, S
*NODE OUTPUT, NSET = GRIP
U,RF
*OUTPUT, HISTORY
*NODE OUTPUT, NSET = GRIP
RF2, U2
*NODE OUTPUT, NSET = OUTPUT
U
*ELEMENT OUTPUT, ELSET = OUTPUT
E22, S22
*END STEP
**
```

11.2 Abaqus input file of the peel test simulation

The input file of the environmental fatigue simulation corresponding to case 1 in is given below:

```
*HEADING
**
** Fatigue crack growth in Film, use with file af_film.for
**
*PREPRINT,ECHO=NO,HISTORY=NO,MODEL=NO,CONTACT=NO
*NODE
1, 0, 0
76, 25, 0
30001, 0, 0.25
30076, 25, 0.25
100001,0,0
100121,40,0
80001,0,-0.40
80121,40,-0.40
*NGEN, NSET=BOT
1,76,1
*NGEN, NSET=TOP
30001,30076,1
*NFILL, NSET=FILM
BOT,TOP,3,10000
*NGEN, NSET=NUNDER
80001,80121,1
*NGEN, NSET=NCOH
100001,100121,1
*NFILL, NSET=CANVAS
NUNDER,NCOH,2,10000
*NSET, NSET=LOAD, GENERATE
80121,100121,10000
*NSET, NSET=cracktip
38
*NSET, NSET=OUTPUT
38
*NSET, NSET=SYMM, GENERATE
1,30001,10000
*NSET, NSET=SYMM, GENERATE
90001,100001,10000
**
************************************************************
**
*ELEMENT,TYPE=CPE4H,ELSET=EFILM
 1001, 1, 2, 10002, 10001
*ELGEN, ELSET=EFILM
 1001,75,1,1,3,10000,10000
**
*ELEMENT,TYPE=COH2D4
 1, 100001, 100002, 2, 1
*ELGEN, ELSET=INT
 1, 37,1,1,
**
*ELEMENT, TYPE=CPE4H, ELSET=ESUBSTRATE
 70001, 80001, 80002, 90002, 90001
*ELGEN, ELSET=ESUBSTRATE
 70001, 120,1,1,2,10000,10000
*ELSET, ELSET=OUTPUT
 19,37
*ELSET, ELSET=MIDFILM
 1001
**
************************************************************
*SOLID SECTION, ELSET=EFILM, MATERIAL=ALKYD
5,
```

```
*MATERIAL,NAME=ALKYD
*EXPANSION
3.05E-4,
*HYPERELASTIC, VAN DER WAALS, MODULI=INSTANTANEOUS
75, 8, 0.5
*VISCOELASTIC,TIME=PRONY
 0.73,, 1e-1
 0.145,, 1e0
 0.05,, 1e1
 0.032,, 1e2
 0.02,, 1e3
 0.013,, 1e4
**
*SOLID SECTION, ELSET=ESUBSTRATE, MATERIAL=ESUB
5,
*MATERIAL,NAME=ESUB
*ELASTIC
 4500., .3
*EXPANSION
1.32736E-5
**
*COHESIVE SECTION,ELSET=INT,MATERIAL=CZ1,RESPONSE=TRACTION SEPARATION
1,5
*MATERIAL,NAME=CZ1
*ELASTIC,TYPE=TRACTION, DEPENDENCIES=2
8,8,8,,0.0,1.0
0.008,0.008,0.008,,0.9999,1.0
8,8,8,,0.0,2.0
8,8,8,,0.9999,2.0
*DAMAGE INITIATION, CRITERION=MAXS, DEPENDENCIES=1
1,1,1,,0.0
0.001, 0.001, 0.001,,0.99999
*DAMAGE EVOLUTION,TYPE=displacement
0.375
*****SPECIFY NUMBER OF USER DEFINED FIELD VARIABLES, USER OUTPUT VARIABLES
*USER DEFINED FIELD
*DEPVAR
2
**********************************************************
*ELSET, ELSET=CFILM, GENERATE
1001,1150,1
*ELSET, ELSET=CSUB, GENERATE
80001,80240,1
*SURFACE, NAME=CFILM
CFILM, S1
*SURFACE, NAME=CSUB
CSUB, S3
**
*SURFACE INTERACTION, NAME=DB
5,
*FRICTION
*CONTACT PAIR, INTERACTION=DB
CFILM, CSUB
**
*INITIAL CONDITION, TYPE=TEMPERATURE
FILM, 25
**********************************************************
*AMPLITUDE, NAME=CYCLE, TIME=STEP TIME, DEFINITION=PERIODIC
1,7.2722e-5,-64800,50
0,25
*STEP,NLGEOM,INC=2147483647
```

```
*VISCO, CETOL=0.0001, STABILIZE
1080,864000000,1e-5,1080
*BOUNDARY
NUNDER,1,2
SYMM,1,1
*TEMPERATURE, AMPLITUDE=CYCLE
FILM, 1
**
*OUTPUT, FIELD, VARIABLE=PRESELECT, FREQUENCY=0
*OUTPUT, HISTORY
*ELEMENT OUTPUT, ELSET = OUTPUT
MAXSCRT, E12, S12
*ELEMENT OUTPUT, ELSET = MIDFILM
TEMP, S11
*NODE OUTPUT, NSET = OUTPUT
U1,RF1
*END STEP
```

11.3 User defined subroutine (Irreversible Cohesive Zone Modelling Technique)

The irreversible cohesive zone user subroutine for the environmental fatigue simulation corresponding to cases 1-4 in is given below.

```
      SUBROUTINE USDFLD(FIELD,STATEV,PNEWDT,DIRECT,T,CELENT,
     1 TIME,DTIME,CMNAME,ORNAME,NFIELD,NSTATV,NOEL,NPT,LAYER,
     2 KSPT,KSTEP,KINC,NDI,NSHR,COORD,JMAC,JMATYP,MATLAYO,
     3 LACCFLA)
C
C Implementation of fatigue model for cohesive zone elements
C following Roe & Siegmund, Engineeringg Fracture Mechanics 2001
C
      INCLUDE 'ABA_PARAM.INC'
C
      CHARACTER*80 CMNAME,ORNAME
      CHARACTER*3  FLGRAY(15)
      DIMENSION FIELD(NFIELD),STATEV(NSTATV),DIRECT(3,3),
     1 T(3,3),TIME(2)
      DIMENSION ARRAY(15),JARRAY(15),JMAC(*),JMATYP(*),
     1 COORD(*)
CC
C     FIELD(1)=DAMAGE in Cohesive Zone Elements
C     FIELD(2)=1 for Tension in Cohesive Zone Elements
C     FIELD(2)=2 for Compression in Cohesive Zone Elements
C
C     Begin DAMAGE accumulation in Cohesive Zones
C     Maximum Initial Strength is 80MPa
CC
      real MAXS0
      real MAXS
      real DELTAT
      real DELTAN
      real DELTATNEW
      real DELTANNEW
      real TEFFN
```

```
      real TEFFT
      real EFFT
      real EFFN
      real DELTATTEMP
      real DELTANTEMP
CC
            MAXS0=1
CC
CC
C     If DAMAGE is greater than or equal to 1, then:
C     The previous effective separation was stored as STATEV(2)
C     The maximum strength is equal to 0
C     The accumulated DAMAGE equals 1
C     The current DAMAGE equals 1
C
            OLDDELTA=STATEV(2)
            OLDDAMAGE=STATEV(1)
            MAXS=(1-OLDDAMAGE)*MAXS0
C     WRITE (6,*) 'MAXSCAL',MAXS, MAXS0, OLDDAMAGE
CC
C     Call the stress tensor
CC
      CALL GETVRM('S',ARRAY,JARRAY,FLGRAY,JRCD,JMAC,JMATYP,
     1     MATLAYO,LACCFLA)
CC
C     TRACTIONT is equal to the shear traction in the cohesive element
C     TRACTIONN is equal to the normal traction in the cohesive element
CC
      TRACTIONN=ARRAY(1)
      TRACTIONT=ARRAY(4)
CC
C     Calculate the effective traction and only use if greater than 0
CC
      EFFN=TRACTIONN
      IF(EFFN.LT.0) THEN
        TEFFN=0
      ELSE
        TEFFN=EFFN
      END IF
      EFFT=TRACTIONT
      TEFFT=EFFT
      TEFF=(TEFFN**2+TEFFT**2)**0.5
CC
C     WRITE (6,*) 'TEFFN', TEFFN
C     WRITE (6,*) 'TEFFT', TEFFT
C     WRITE (6,*) 'TEFF', TEFF
CC
C     Call the strain tensor
CC
      CALL GETVRM('E',ARRAY,JARRAY,FLGRAY,JRCD,JMAC,JMATYP,
     1     MATLAYO,LACCFLA)
CC
C    DELTATNEW is equal to the current shear separation in the cohesive
element
C    DELTANNEW is equal to the current normal separation in the cohesive
element
CC
      DELTANNEW=ARRAY(1)
      DELTATNEW=ARRAY(4)
C      WRITE (6,*) 'DELTATNEW', DELTATNEW
C      WRITE (6,*) 'DELTANNEW', DELTANNEW
```

```
CC
C     FIELD(2) equals 1 if current normal separation is tensile
C     FIELD(2) equals 2 if current normal separation is compressive
CC
      DELTANTEMP=DELTANNEW
      IF (DELTANTEMP.LT.0) THEN
             DELTAN=0
      ELSE
             DELTAN=DELTANTEMP
      END IF
CC
      DELTATTEMP=DELTATNEW
      DELTAT=DELTATTEMP
      DELTA=(DELTAN**2+DELTAT**2)**0.5
      FIELD(2)=1
CC
C      WRITE (6,*) 'DELTAN', DELTAN
C      WRITE (6,*) 'DELTAT', DELTAT
C      WRITE (6,*) 'DELTA', DELTA
CC
C     Calculate the current effective separation
C     Calculate the incremental effective separation
CC
      DDELTA=DELTA-OLDDELTA
CC
C     IF the current maximum strength is greater than 0 AND
C     the ratio of effective traction to maximum strength is
C     greater than the fatigue limit, then:
C     Calculate the incremental DAMAGE as
C     DDAMAGE=(DDELTA/CCLENGTH)*((TRACTIONN/MAXS)-(ELIMIT/MAXSO))
C     Add incremental DAMAGE to accumulated DAMAGE
C     DAMAGE=DAMAGE+DDAMAGE
CC
            IF (MAXS.GT.0) THEN
            RATIO=(TEFF/MAXS)-0
C     WRITE (6,*) 'RATIO', RATIO
            IF (RATIO.GT.0) THEN
                  DDAMAGE=((ABS(DDELTA))/0.375)*((TEFF/MAXS)-(0))
            ELSE
                  DDAMAGE=0.0
            END IF
            ELSE
            DDAMAGE=0.0
            OLDDAMAGE=1.0
            END IF
                  DAMAGE=OLDDAMAGE+DDAMAGE
c      WRITE (6,*) 'DDAMAGE',DDAMAGE
CC
C     IF accumulated DAMAGE is greater than 1, then:
C     set STATEV(1) equal to 1
C     IF accumulated DAMAGE is less than 1, then:
C     set STATEV(1) equal to DAMAGE
CC
            IF (DAMAGE.GE.1) THEN
                  STATEV(1)=1.0
            ELSE
                  STATEV(1)=DAMAGE
            END IF
c      WRITE (6,*) 'DAMAGE',DAMAGE
CC
C     Set FIELD(1) equal to STATEV(1) which is the current DAMAGE
```

```
C     Set STATEV(2) equal to the current effective separation in order
C     to calculate incremental effective separation in the next increment
CC
            FIELD(1)=STATEV(1)
            STATEV(2)=DELTA
C
C       IF (NOEL.EQ.1001) THEN
c       WRITE (6,*) 'TIME',TIME
c       WRITE (6,*) 'OLD',OLDDELTA,OLDDAMAGE
c       WRITE (6,*) 'NEW',DELTA,DAMAGE
c       WRITE (6,*) 'DELTAS',DDELTA,DDAMAGE
c       WRITE (6,*) 'MAXSTEFF',MAXS,TEFF
C       END IF
CC
CC
CC
      RETURN
      END
C
C
```